About Journal

The University of Sistan and Baluchestan entered into strategic partnership with Iranian Association of Electrical and Electronic Engineers (IAEEE) to publish the **International Journal of Industrial Electronics Control and Optimization (IECO)**. The IECO is a refereed international journal which presents to the international scientific community important results of work in these fields, whether in the form of modeling simulation, analysis, fundamental research, development, application, design or real-time implementation. The scope of IECO is broad, encompassing all aspects of Industrial Electronics, Control and Optimization.

Note: International Journal of Industrial Electronics, Control and Optimization (IECO) has qualified to **ACADEMIC RESEARCH JOURNAL (ELMI-PAJOHESHI)** status certified by the ministry of Science, Research and Technology of Iran (No. 231566/3/18 dated 1396/10/09), and is published by the University of Sistan and Baluchestan through a formal partnership (No. 952/2/1500 dated 1395/11/04) with Iranian Association of Electrical and electronic Engineers (IAEEE) in order to develop scientific and research cooperation.

Aims and Scope

International Journal of Industrial Electronics, Control and Optimization (IECO) is a Peer reviewed journal of advanced and state-of-the-art in the science and engineering of Industrial Electronics, Control and Optimization. Its Scope encompasses the applications of Industrial Electronics, power systems, control, optimization and computational intelligence for the enhancement of industrial and manufacturing system and processes. The scope of the journal include the following:

I. Industrial Electronics

- *Low and high power converters*
- *Renewable energy*
- *Drive control techniques*
- *Techniques for advanced power semiconductor devices*
- *Power quality and utility applications*
- *Communications*
- *Flexible AC Transmission Systems (FACTS)*
- *Control in power electronics*
- *Electromagnetic and thermal performance of electronic power converters*
- *Motion control, robotics, sensors and actuators*
- *Fault detection and diagnosis*
- *Power systems*
- *Factory automation, communication, and computer networks*

II. Control

- *Adaptive control*
- *Control of process systems*
- *Control theory*
- *Data processing*
- *Design of control systems*
- *Hybrid systems*
- *Identification and observation*
- *Intelligent systems*
- *Model-predictive control*
- *Optimal control*
- *Robust control*
- *Fractional order systems*

III. Optimization

- *Ant Colony*
- *Chaos Theory*
- *Evolutionary Computing*
- *Fuzzy Computing*
- *Hybrid Methods*
- *Immunological Computing*
- *Neuro Computing*

- *Particle Swarm*
- *Probabilistic Computing*
- *Rough Sets*
- *Wavelet*

International Journal of Industrial Electronics, Control and Optimization © 2022 IECO
Vol. 5, No. 1, pp. 1-9 , Jan (2022)

Introducing a New Optimized Emergency Demand Side Management Method to Restore the Power System Frequency

Pezhvak Sheikhzadeh-Baboli[1], and Mohsen Assili[2,†]

[1,2] Department of Electrical Engineering, Shahrood University of Technology, Shahrood, Iran

ABSTRACT

Emergency demand response (EDR) and under frequency load shedding (UFLS) are used as two separate methods for frequency restoration of power systems after the common methods of frequency control fail to maintain the frequency stability of the system. This paper proposes an optimized emergency demand side management (OEDSM) method that improves the performance of previous methods by integrating UFLS and EDR methods along with introducing new critical status detection and optimization modules. The proposed method is characterized by simultaneous operation of EDR and UFLS processes, the high speed of critical condition detection using the proposed emergency index, higher speed of the algorithm with parallel operation of modules, and optimal load shedding by providing a separate optimization module. To validate and evaluate the performance of the proposed method, a power system was tested under different scenarios using DIgSILENT software. The results indicate the better performance of the proposed method in frequency restoration, as well as the higher utilization and power quality of the system compared to previous methods.

Article Info

Keywords:
Adaptive Control, Emergency demand response, Frequency restoration, Optimal load shedding, Under frequency load shedding.

Article History:
Received 2021-10-22
Accepted 2021-10-23

I. INTRODUCTION

In stable conditions of a power system, the total power generation is equal to the total power consumption (i.e., demand and losses), so that the system frequency operates within its allowable range. Any disturbance or incident in the network can reduce the network generation capacity and cause a frequency drop in the power system [1]. Once the critical situation of the system frequency drop happens, frequency control systems such as automatic generation control (AGC) start operating to return the system frequency to its allowable range [2]. However, when these systems are unable to restore the frequency and the frequency is less than a certain limit, their set point relays are adjusted to disconnect generators and sensitive devices from the grid to prevent damage to power system elements such as generators. Consequently, hierarchical and sequential generators and power transmission lines tripping will further reduce the frequency and increase the probability of cascading blackouts in the power system [3]. Various methods have been proposed to prevent the collapse of a power system and then ensure the return of its frequency to its nominal value. These methods are all based on creating a balance between the total power generation and the power consumption of the power system. Now, depending on whether the power system is conventional or modern and intelligent, the methods of creating power balance and recovery will be different. In older power systems, under frequency load shedding (UFLS) methods are used, but modern and intelligent systems use, in addition to UFLS, the emergency demand response (EDR) method, which is a type of contracted interruption demands (CIRs) with spinning reserves (SRs).

The UFLS methods are generally divided into three

[†]**Corresponding Author:** m.assili@shahroodut.ac.ir
Tel: +98-23-32392204, Shahrood University of Technology
Department of Electrical and Computer Engineering, Shahrood University of Technology, Shahrood, Iran.

categories of conventional methods, computational intelligent algorithms, and adaptive methods [4], among which adaptive methods are more appropriate than the other two due to efficiency, up-to-datedness and the practicality. Recent researches have improved the performance of adaptive UFLS algorithms by making some modifications in the main algorithm and optimizing interruptible loads selection. Accordingly, new methods are introduced in [5] and [6] for adaptive UFLS that use state estimators. In [7] and [8] adaptive UFLS methods are presented in the presence of sources using wide-area measurements. Based on voltage and frequency data and the use of phasor measurement units (PMUs), an adaptive algorithm considering UFLS and UVLS has been proposed in [9], which improves frequency and voltage stability. In [10], a semi-adaptive method is used for multi-stage UFLS using the rate of change in frequency value to recover the frequency. In [11], a continuous UFLS method is used to control the adaptive frequency of the power system. The loads to shed are calculated based on the event signal. In [12], different loads are prioritized to optimize the adaptive algorithm, and in selecting the priorities, a combination of loads is selected that the amount of load shedding is closer to the calculated values.

Demand response (DR) programs include methods of demand side management (DSM) that refer to any changes in customer consumption due to changes in electricity prices in the market. It is worth mentioning that some of such programs are used in the traditional power systems in the form of multi-tariff meters, but in the restructured power systems, these programs have taken on a new form and are reviewed and revised according to the economic and competitive approach of the market [13-14].

Accordingly, to improve the operation of the power grid when an imbalance occurs between power generation and consumption, the power system can delay UFLS and forced interruption by the power system operator as much as possible. In the DR program, due to the importance of decision speed to create a balance between production and consumption, an operational subdivision at the moments and seconds time range, namely physical-DR and SRs is used. This part of the DR is called EDR. The process of frequency control by the EDR method is such that after the AGC system is unable to control the frequency and prevent its reduction, in the first stage, the emergency EDR system is activated [15]. Physical-DR programs are applied to control and prevent excessive frequency reduction. Then, at the moment when the frequency is less than a certain level, to prevent the operation of the under frequency relays, fast-spinning reserves are entered in the second stage to increase the frequency by a certain amount. In the last step, to return the frequency to its nominal value, the lower speed SRs or fast non-spinning reserves such as hydropower plants enter. Most EDR devices can start quickly as soon as they receive signals of an event. Participants in EDR programs contract to commit to a certain amount of capacity. They will be charged for their presence and may face a fine if they do not attend. In another type of contract, load shedding is optional and will not be penalized if the customer does not interrupt the loads. Also in another contract, the telecommunications company interrupts the demand by a controlled switch and pays a fee in return [16].

In [17], a comprehensive central demand-based response algorithm is presented for frequency regulation by minimizing the amount of load manipulation in a smart microgrid. Simulation studies in a standard 13-bus distribution system have been performed considering the effect of producing a variable wind unit. The results, show that the proposed control strategy is effective in regulating the frequency and consequently the voltage. In [18], a responsive end-user is used that can change power such as solar cells and electric vehicles connected to the grid by an inverter to support the power system in the transmission system. The paper shows how the power sources that are connected to these buses are controlled.

This paper presents a new method for optimal frequency restoration of the power system and prioritization of interrupts in the process of the proposed method. Accordingly, in Section 2, the emergency demand side management (EDSM) method is proposed as an alternative method for frequency restoration of the power system, which is the result of a combination of UFLS and EDR methods. The tasks of its sections and modules is described in the following. One of the advantages and innovations of this method is the simultaneous performance of UFLS and EDR methods, which has improved the speed of frequency restoration performance. Modulation of the proposed method and separate and parallel operation of the modules are also effective in improving the speed of frequency restoration. Also, by creating an emergency index module (EIM), it has contributed to timely detection of the critical situation, the frequency decline, and the minimization of the possibility of power system collapse. Then in Section 3, presents the optimized emergency demand side management (OEDSM) method by optimizing the EDSM method and presenting a module called the optimization module (OM). This optimal algorithm can improve the frequency restoration process and power quality indices by using the dynamic programming method. The OM optimally controls the process of disconnecting or connecting resources by forming sub-sections for each of the UFLS and EDR sections. Section 4 performs simulations on the New England 39-bus standard grid to validate and evaluate the performance of the proposed method. Section 5 also reviews the results and presents the achievements of the proposed method.

II. EMERGENCY DEMAND SIDE MANAGEMENT (EDSM)

A. EDSM algorithm

To improve the performance and efficiency of the EDR and UFLS frequency restoration algorithms, which operate separately in the power system, by integrating them and applying changes and adding modules, the emergency demand side management (EDSM) method is proposed. Accordingly, the modules available in the EDSM frequency restoration method are suggested as follows:

1) Center Of Inertia Frequency Module (COIFM): calculates the instantaneous frequency of the system at the center of inertia of the power system [12]:

$$f_{COI} = \frac{\sum_{i=1}^{N} H_i f_i}{\sum_{i=1}^{N} H_i} \quad (1)$$

where:

f_{COI} frequency of center of inertia (in Hz);
H_i inertia constant of *i*-th generator (in seconds);
f_i frequency of *i*-th generator (in Hz);
N number of generators;

2) Power Deficit Estimation Module (PDEM):

The power deficit estimated at each stage based on the equation in [12] is considered as follows:

$$P_{deficit} = \left(\left(2 \times \sum_{i=1}^{N} \frac{H_i}{f_n} \right) \times \frac{d}{dt} f_{COI} \right) \quad (2)$$

where:

$P_{deficit}$ power deficit (in MW);
$\frac{d}{dt} f_{COI}$ rate of change of center of inertia (in Hz/s);
f_n rated frequency (in Hz);

3) Emergency Index Module (EIM):

A new diagnostic index called Emergency Index (EI) has been unveiled. By defining frequency first-order derivative (FFD) and frequency second-order derivative (FSD) and determining the sign of each of the two characteristics, we have the following:

$$FFD = \frac{d}{dt} f_{COI} \quad (3)$$

$$FSD = \frac{d^2}{dt^2} f_{COI} \quad (4)$$

$$EI = FFD \times FSD \quad (5)$$

where:

FFD Frequency First-order Derivative (FFD);
FSD Frequency Second-order Derivative (FSD);
EI Emergency Index (EI);

Table I shows an example of different values of the indicators in the form of stable and unstable frequency response waveforms.

TABLE I
AN EXAMPLE OF DIFFERENT VALUES OF THE INDICATORS IN THE FORM OF STABLE AND UNSTABLE FREQUENCY RESPONSE WAVEFORMS.

Index / Stability	Stable	Unstable
FFD	-0.0937	-0.19880
FSD	+0.0181	- 0.05016
EI	-0.00169	+0.00997

4) Frequency Emergency Condition Identity Module (FECIM):

It is a module to identify the critical frequency state of the frequency and start the proposed frequency restoration algorithm. The operation of the algorithm is such that the three indexes EI, *f*, and FFD are constantly monitoring and receiving data from their respective modules. Therefore, as soon as the frequency drops and the FFD index becomes negative, assuming that the EI is positive, which is an indication of the acute state and the movement of the frequency curve towards divergence and instability (Table II), the command is immediately sent to the frequency restoration module (FRM) and announce the acute condition. Now, if the frequency decreases and the FFD index are negative, assuming the negative EI, it indicates that the frequency converges to a certain value (Table II). In this case, only if the frequency is less than a certain limit ($f_{threshold}$), by announcing the non-acute status, the command is sent to activate the FRM module.

TABLE II
DIFFERENT SITUATIONS OF EI INDEX.

Stability / Indexes	*f*	*FFD*	*EI*
Stable	Decreasing	-	-
Unstable	Decreasing	-	+
Stable	Increasing	+	-
Unstable	Increasing	+	+

5) Frequency Restoration Module (FRM):

When a severe disturbance occurs in the power system, as soon as the critical situation is detected, the command will be sent to the FRM module and the module will perform the frequency restoration process as shown in Fig. 1.

The operation of each module is separate and in each step, the data and outputs of each section are sent to the next section and are related to each other. The COIFM, PDEM, and EIM modules, which are responsible for calculating the frequency of center of inertia, the estimated power deficit, and the emergency index, respectively, constantly calculate and record the values. In a critical situation, the most important point at the first stage is to know the extent of the crisis so that the system can react appropriately. The frequency response behavior of the system can be detected by analyzing the EI index and determining the acute or non-acute critical state that will occur in the stability (convergence) or instability (divergence) of the curve, respectively.

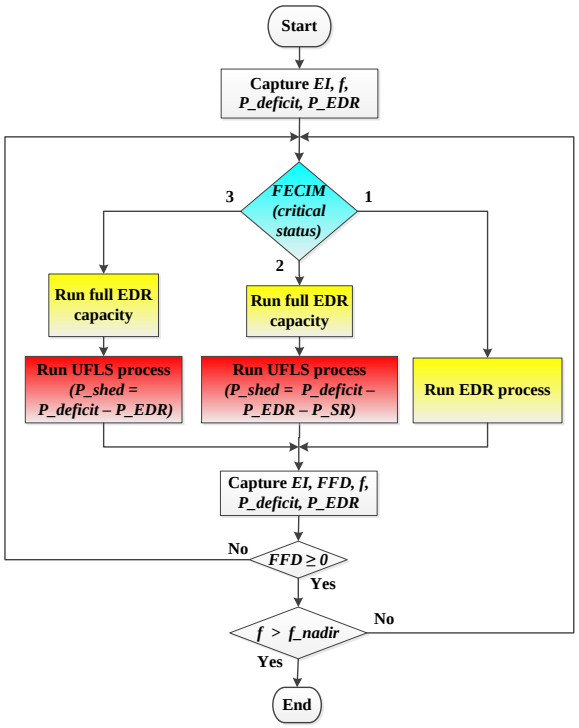

Fig. 1. Frequency Restoration Module (FRM).

In general, for non-acute cases, we will have:

$$P_{shed} = P_{deficit} - P_{EDR} - P_{FSR} \quad (6)$$

where:

P_{shed} UFLS's share of total power deficit (in MW);

$P_{deficit}$ Power deficit (in MW);

P_{EDR} EDR's share of total power deficit (in MW);

P_{FSR} Fast SR's share of total power deficit (in MW);

Also, this equation for the acute situation will be as follows:

$$P_{shed} = P_{deficit} - P_{EDR} \quad (7)$$

B. *Performance of UFLS and EDR algorithms in EDSM compensation algorithm*

As was mentioned in the previous section, after the amount of power deficit ($P_{deficit}$) is calculated by the PDEM module, this value is compensated by the UFLS and EDR algorithms in the corresponding module (FRM). Therefore, to improve the quality of customer service, the load related to each of the UFLS and EDR sections can be classified into different categories. Accordingly, in the UFLS section, loads will be divided into two parts of without priority and with priority, and they eill be divided by the type of contract and their nature in the EDR section. Therefore, the UFLS share of power deficit will be equal to:

$$P_{shed} = P_{NO} + P_{WO} \quad (8)$$

where P_{NO} represents the no order-interruption priority of loads and P_{WO} represents the with-order interruption priority of loads that will participate in the UFS.

Also, EDR's share of power deficit will be equal to:

$$P_{EDR} = P_{CD} + P_{CG} \quad (9)$$

where P_{CD} represents the sum of contracted demands and P_{CG} represents the sum of contracted generations with the ability to inject power that will participate in the EDR process.

Therefore, the different states that occur in each step of the algorithm will include the following:

1) Type 1 critical situation:

In this case, the existing P_{EDR} capacity is estimated to be greater than the power deficit and the EI is less than zero, so the frequency drop is in the non-acute state, where only the EDR process will operate in the algorithm and no UFLS will need to be performed, so we will have:

$$P_{shed} = 0 \quad (10)$$

$$P_{EDR} = P_{deficit} - P_{FSR} \quad (11)$$

2) Type 2 critical situation:

In this case, the EI is less than zero, so the frequency drop trend is non-acute, but the P_{EDR} -capacity that is ready to participate is less than the estimated power deficit. In this case, the EDR process alone will not be responsible and the UFLS process needs to start. In this case, because the network is not in an unstable condition and the existing SRs may be activated with a slight delay to restore the frequency, the amount of load to be shed is equal to:

$$P_{EDR}: in \ \ full \ \ capacity \quad (12)$$

$$P_{shed} = P_{deficit} - P_{EDR} - \ \ P_{FSR} \quad (13)$$

3) Type 3 critical situation:

Under this condition, the EI coefficient is greater than zero and the frequency response curve is in an unstable condition. Therefore, the frequency drop is in an acute state, in which the EDR process algorithm is activated with all its capacity and at the same time, the UFLS process will be executed regardless of the SRs, so we will have:

$$P_{EDR}: in \ \ full \ \ capacity \quad (14)$$

$$P_{shed} = P_{deficit} - P_{EDR} \quad (15)$$

After the first stage of EDR or UFLS is performed, additional monitoring and analysis are needed to determine the frequency restoration process and make the appropriate decision to achieve the desired result. Therefore, the required indexes and variables are received from the relevant modules again. The index that will help the proposed restoration algorithm at this stage is the FFD index. Thus, if the rate of frequency change with respect to time is positive (ascending frequency curve) and the acceptable frequency value (f_{nadir}) is reached, the operation of the FRM module ends. However, if it has not yet reached the desired frequency if the EI index is negative (convergent frequency curve), the EDR or UFLS residue will be used for the second time, otherwise, the FRM module will stop. However, if at the end of the first stage the FFD index is positive (descending frequency curve), in terms of positive or negative EI index, the first stage will be repeated according to

the mentioned situation and will be implemented depending on the EDR and UFLS algorithm. This process continues until the system frequency is within the acceptable range.

III. Optimization Module Design and Presentation of OEDSM Algorithm

As was mentioned in the previous section, the UFLS and EDR processes involve divisions in terms of power deficit supply. Hence, different combinations of different parts can be formed. Extendable combinations can be considered in terms of operating priority, cost of operation, fines, and so on. Therefore, by defining different objective functions, the most appropriate combination can be found according to the respective objects.

The sum of the various UFLS combinations are divided as follows:

$$\begin{cases} Comb(P_{NO}) = \sum_{j=1}^{J} s_j \cdot p_{NO_j} \\ s.t. \\ j = 1, 2, 3, \dots, J \\ s_j = 0 \ \ or \ \ 1 \end{cases} \quad (16)$$

where

j number of no-order loads;

s_j coefficient of the j-th no-order load;

p_{NO_j} no-order load's share of total UFLS (in MW);

$Comb(P_{NO})$ sum of the combinations of no-order loads;

$$\begin{cases} Comb(P_{WO}) = \sum_{k=1}^{K} s_k \cdot p_{WO_k} \\ s.t. \\ k = 1, 2, 3, \dots, K \\ s_k = 0 \ \ or \ \ 1 \end{cases} \quad (17)$$

where

k number of with-order loads;

s_k coefficient of the k-th with order load;

p_{WO_k} with-order load's share of total UFLS (in MW);

$Comb(P_{WO})$ sum of the combinations of with-order loads;

Also, the sum of different EDR combinations can be distinguished as follows:

$$\begin{cases} Comb(P_{CD}) = \sum_{l=1}^{L} s_l \cdot p_{CD_l} \\ s.t. \\ l = 1, 2, 3, \dots, L \\ s_l = 0 \ \ or \ \ 1 \end{cases} \quad (18)$$

where

l number of contracted demands;

s_l coefficient of l-th contracted demand;

p_{CD_l} contracted demand's share of total EDR (in MW);

$Comb(P_{CD})$ sum of the combinations of contracted demands;

$$\begin{cases} Comb(P_{CG}) = \sum_{m=1}^{M} s_m \cdot p_{CG_m} \\ s.t. \\ m = 1, 2, 3, \dots, M \\ s_m = 0 \ \ or \ \ 1 \end{cases} \quad (19)$$

where

m number of contracted generations;

s_m coefficient of the m-th contracted generation;

p_{CG_m} contracted generation's share of total EDR (in MW);

$Comb(P_{CG})$ sum of the combinations of contracted generations;

The process of selecting the right combination to participate in power deficit compensation follows the pattern that the load shedding process starts from no-order loads in the UFLS algorithm. If the amount of no-order loads is not enough to shed, with-order loads will also participate. Also, in the EDR algorithm, at first, the process of participation from contracted generations starts, and then, if it is necessary, contracted demands will also participate. The process is summarized as follows:

- If $P_{Shed} \leq \sum_{j=1}^{J} p_{NO_j}$ then:
  $Comb(P_{NO}) = P_{Shed}$ (20)
- If $P_{Shed} > \sum_{j=1}^{J} p_{NO_j}$ then:
  $\sum_{j=1}^{J} p_{NO_j} + Comb(P_{WO}) = P_{Shed}$ (21)
- If $P_{EDR} \leq \sum_{m=1}^{M} p_{CG_m}$ then:
  $Comb(P_{CG}) = P_{EDR}$ (22)
- If $P_{EDR} > \sum_{m=1}^{M} p_{CG_m}$ then:
  $\sum_{m=1}^{M} p_{CG_m} + Comb(P_{CD}) = P_{EDR}$ (23)

Now according to the previous equations, after selecting the different combinations, the error values will be defined as follows:

$error_{P_{Shed}} = |P_{Shed} - (Comb(P_{NO}) + Comb(P_{WO}))|$ (24)

$error_{P_{EDR}} = |P_{EDR} - (Comb(P_{CD}) + Comb(P_{CG}))|$ (25)

Now a combination must be selected for each equation to create a minimum error. So, to achieve this purpose, the optimal values must be found. There are various methods derived from optimization algorithms and mathematical methods, among which the dynamic programming method, which is a practical mathematical method, has been used to find optimal values due to the specificity of the problem variables and the need for an accurate (not approximate) response and the proper response speed [19].

To achieve the purpose of minimizing UFLS and EDR errors, an OM has been designed which finds the answers in interaction with the FRM module based on the dynamic

programming method and sends the data to execute the EDSM algorithm. Fig. 2 shows an overview of the optimal EDSM algorithm and related modules and the location of the OM. The objectives of the proposed OM are:

$$\begin{cases} \min(error_{P_{Shed}}) \\ and \\ \min(error_{P_{EDR}}) \end{cases} \quad (26)$$

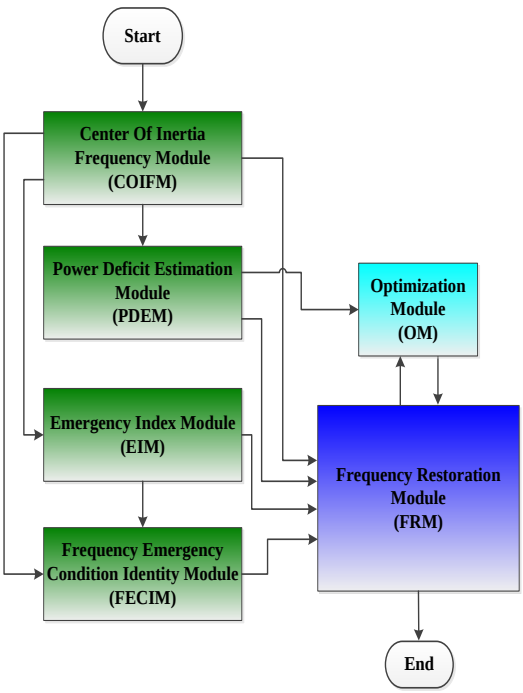

Fig. 2. The block diagram of the OEDSM algorithm and its related modules.

IV. TEST OF THE OEDSM ALGORITHM

The frequency restoration process of the OEDSM method was tested to confirm the performance. One of the purposes of frequency restoration with this method is to reduce UFLS participation and increase EDR participation in the frequency restoration process. Another purpose is the participation of each of the sections mentioned in the previous section optimally and with the least error. Accordingly, the standard New England 39 bus grid was selected to validate the proposed frequency restoration method. The network has a nominal frequency of 60 Hz and is composed of 10 main power plants, 19 feeders, and 34 lines at the transmission level, which has a generation capacity at a nominal load of about 6140 MW. The total load in the current operation of the network is about 6098 MW, of which 30% is of no-order interruption priority type and 70% is with-order interruption priority type. The total EDR capacity is about 305 MW composed of about 260 MW EDR with contracted demand and 45 MW EDR with contracted generation. Also, fast SRs and slower SRs have been considered with a capacity of about 50 and 100 MW, respectively. This power system is simulated in DIgSILENT software under the following scenarios. Based on this, the simulations were performed once using the conventional frequency restoration method and then using the OEDSM method.

A. Turbulence with a power deficit of 250 MW

In this part, the system is faced with a power deficit of 250 MW, which is a small disturbance for the studied system. Now the performance of the conventional and proposed frequency restoration methods is examined in the face of this turbulence. When the conventional method [12,15] is used for restoration, with the occurrence of turbulence and the beginning of the frequency reduction process when its value reaches 59.7 Hz, the EDR algorithm starts working and after a delay of a few seconds, the system frequency returns to the nominal value.

Since the EDR capacity of this method is 305 MW and the power deficit is 250 MW, the EDR algorithm will be able to fully return the frequency to its nominal value, which is well demonstrated in Fig. 3. In the other case, the system is evaluated under the proposed method. In this method, as soon as the frequency reduction process is identified by the FECIM diagnostic module, the FRM, and then the OM modules start working. Therefore, after detecting the critical state of type 1, only the EDR algorithm starts working and returns the frequency to its nominal value well. One of the advantages of the proposed method compared to the conventional method is faster performance and consequently less frequency drop, which is well shown in Fig. 3.

Table III is compares the results of the two methods. As can be seen, in both methods the value of UFLS is zero, a lower EDR value is applied in the proposed method than in the conventional method. Based on the comparison of the minimum frequency and the duration of the frequency convergence, it is clear that the proposed method is in a more favorable situation. But both methods could bring the final frequency to the nominal value of 60 Hz. Another advantage of the proposed method is optimal load shedding. The details of the operation of the OM in the optimal classification of load shedding are presented in Table IV. As it is known, out of the total 207.27 MW EDR, the amount of 162.27 MW is the share of the contracted demands, and 45 MW EDR is the share of the contracted generations. Also, the share of each UFLS segment in load interruption is zero. This means that there is no need to share load shedding with no-order and with-order loads.

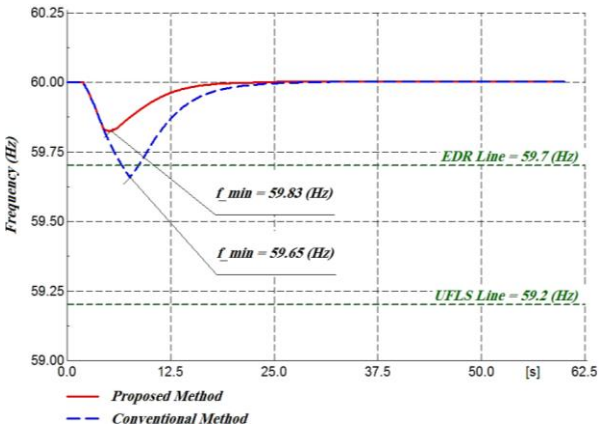

Fig. 3. The frequency response of the network with a power deficit of 250 MW.

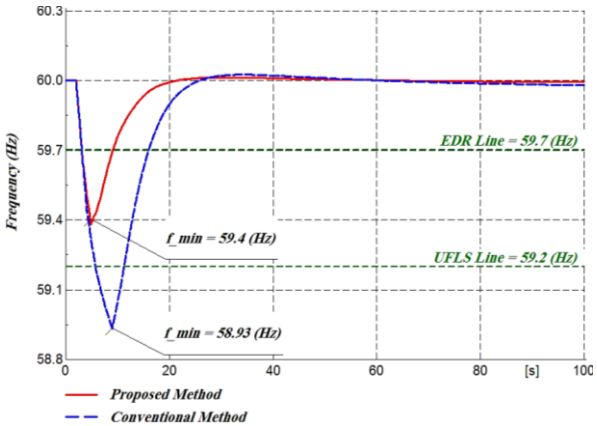

Fig. 4. The Frequency response of the network with a power deficit of 830 MW.

TABLE III

A COMPARISON OF THE RESULTS OF THE VARIABLES BETWEEN THE CONVENTIONAL AND PROPOSED METHODS IN SCENARIO 1.

Variable	Conventional Method [12,15]	Proposed method
Total Load Shedding (MW)	0	0
Total EDR (MW)	253.23	207.27
Minimum Frequency (Hz)	59.65	59.83
Convergence Time (s)	23	17
Steady-State Frequency (Hz)	60	60

TABLE IV

A COMPARISON OF SHED COMBINATIONS IN THE PROPOSED METHOD IN SCENARIO 1.

Variable	UFLS [12]	EDR [15]
Total P_{NO} (MW)	0	-
Total P_{WO} (MW)	0	-
Total P_{CD} (MW)	-	162.27
Total P_{CG} (MW)	-	45

B. Turbulence with a power deficit of 830 MW

In the next scenario, we evaluate the system under 830 MW turbulence. Accordingly, after this turbulence, the conventional algorithm [12,15] is implemented first. As shown in the system frequency response in Fig. 4, after the system frequency becomes less than 59.7 Hz, the EDR algorithm starts to return the system frequency to its nominal value. Since the generated power deficit is 830 MW and the maximum EDR capacity is 305 MW, EDR will not be able to restore the system frequency and the frequency will continue to decrease until it reaches the UFLS limit of 59.2 Hz. As soon as the frequency reaches 59.2 Hz, the UFLS algorithm starts working and compensates for the remaining power deficit, and after a while, brings the system frequency closer to the nominal value. The results are shown in Table V.

In the next case, the system is evaluated under the proposed algorithm scheme. In this case, as soon as the disturbance occurs and after the system frequency starts to decrease and the emergency status and its type are announced by the FECIM, the frequency restoration process starts operating. In this case, the FECIM module detects type 2 critical situation, in which both EDR and UFLS algorithms are started. As can be seen in Fig. 4, the algorithm performed the restoration process faster and the system frequency decreased less, which minimized the possibility of tripping the under-frequency relays of generators.

As shown in Table V, the comparison of the frequency restoration process related to the two methods clearly reveals the superiority of the proposed method in terms of fewer loads shedding amount, less frequency reduction, less convergence time, and the steady-state frequency closer to the nominal value.

TABLE V

A COMPARISON OF THE RESULTS OF THE VARIABLES BETWEEN THE CONVENTIONAL AND PROPOSED METHODS IN SCENARIO 2.

Variable	Conventional Method [12,15]	Proposed method
Total Load Shedding (MW)	500.47	467.25
Total EDR (MW)	305	305
Minimum Frequency (Hz)	58.93	59.40
Convergence Time (s)	77	46
Steady-State Frequency (Hz)	59.98	59.99

Table VI also shows the results of the OM performance in the optimal share segmentation of each of the EDR and UFLS segments. As it is known, out of the total 305 MW from the share of the EDR algorithm, 260 MW is the share of contracted demands and 45 MW EDR is the share of the contracted generations. Also, 467.25 MW, which is the total share of the UFLS, is provided by no-order loads, and there is no need to be shared by with-order loads.

TABLE VI
A COMPARISON OF SHED COMBINATIONS IN THE PROPOSED METHOD IN SCENARIO 2.

Variable	UFLS [12]	EDR [15]
Total P_{NO} (MW)	467.25	-
Total P_{WO} (MW)	0	-
Total P_{CD} (MW)	-	260
Total P_{CG} (MW)	-	45

C. Turbulence with a power deficit of 2490 MW

In the third scenario, the system is severely disturbed by 2490 MW. For frequency restoration, the system has been evaluated once under the conventional algorithm [12,15] and then under the proposed algorithm.

Under the conventional algorithm, when the power deficit is 2490 MW, its frequency decreases sharply. Therefore, as soon as the system frequency exceeds 59.7 Hz, the EDR algorithm starts working, which will not be effective in practice due to the large difference in the capacity of this algorithm owing to the lack of power. When the system frequency reaches 59.2 Hz, the UFLS algorithm starts working and tries to return the system frequency to its acceptable level. The implementation process of the mentioned algorithm is due to the high speed of system frequency drop to such an extent that the system frequency is reduced to 56.97 Hz.

Since the system frequency was set at frequencies below 57 Hz for about 1.3 seconds, which is close to the critical level, and in case of further delay in the operation of UFLS relays in real systems, the under-frequency turbine relays allow tripping. Generators will not be allowed to stay at this frequency for more than 2.4 seconds [20]. (IEEE Std C37.117 will be allowed for frequencies below 57 Hz for a maximum of 2.4 seconds.) Therefore, the generators may be disconnected from the power grid and prevent their turbines from twisting and breaking down.

The system is then evaluated under the proposed frequency restoration method. Accordingly, as soon as the system frequency began to decrease and the emergency status and type were announced by the FECIM module, the frequency restoration process began. In this case, the module detected critical state 3, and both EDR and UFLS algorithms started working. As can be seen in Fig. 5, the proposed algorithm copes well with the frequency restoration and could bring the system frequency to an acceptable level close to the nominal value by dropping a frequency much lower than the conventional method. As it turned out, the network frequency is always kept above 58 Hz, which is a safe area in terms of the performance of under-frequency relays of turbines.

Table VII also provides a comparison of conventional [12,15] and proposed methods. As it turns out, the proposed method is in a better position both in terms of the amount of load shedding in the UFLS algorithm and the larger frequency and the shorter convergence time.

Table VIII also shows the share of each of the EDR and UFLS segments in the proposed algorithm. As it is known, out of the total 305 MW from the share of the EDR algorithm, an amount of 260 MW is the share of contracted demands and 45 MW EDR is contracted generations. Also, out of the total 2101.43 MW which is the total share of UFLS, 1829.4 MW is supplied by no-order loads and 272.03 MW by with-order loads.

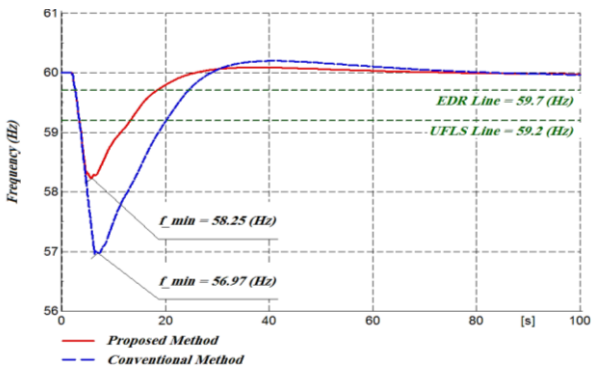

Fig. 5. The Frequency response of the network with a power deficit of 2490 MW.

TABLE VII
A COMPARISON OF THE RESULTS OF THE VARIABLES BETWEEN THE CONVENTIONAL AND PROPOSED METHODS IN SCENARIO 3.

Variable	Conventional Method [12,15]	Proposed method
Total Load Shedding (MW)	2129.10	2101.43
Total EDR (MW)	305	305
Minimum Frequency (Hz)	56.97	58.25
Convergence Time (s)	81	60
Steady-State Frequency (Hz)	59.98	59.98

TABLE VIII
A COMPARISON OF SHED COMBINATIONS IN THE PROPOSED METHOD IN SCENARIO 3.

Variable	UFLS [12]	EDR [15]
Total P_{NO} (MW)	1829.40	-
Total P_{WO} (MW)	272.03	-
Total P_{CD} (MW)	-	260
Total P_{CG} (MW)	-	45

V. CONCLUSIONS

When a power system encounters a serious disturbance that results in an imbalance between power generation and consumption and a drastic change in system frequency, it needs a comprehensive and flexible system for frequency restoration to the nominal value in the minimum time and with the least frequency drop. This paper presents the OEDSM method, which consists of various modules with specific tasks.

This method improves the reliability of previous methods. The method is formed by integrating EDR and UFLS algorithms and then adding diagnostic, control, and OMs. The results of the simulations under different scenarios with different turbulence sizes well show the high capability of the proposed algorithm in the system frequency restoration process. As the results show, this method leads to the simultaneous operation of EDR and UFLS algorithms, which in itself increases the speed of critical state detection in the process of frequency restoration. Other desirable results of the proposed method include lower network frequency drop, lower load shedding amount, higher convergence speed, optimal load shedding, and load classification based on interruption priority that increases consumer satisfaction, improves the power quality of the system, and minimizes the possibility of network blackouts.

REFERENCES

[1] Y. Y. Hong, M. C. Hsiao, Y. R. Chang, Y. D. Lee, and H. C. Huang, "Multiscenario underfrequency load shedding in a microgrid consisting of intermittent renewables," *IEEE Trans. Power Deliv.*, Vol. 28, No. 3, pp. 1610-1617, July 2013.

[2] A. Ketabi, M. Hajiakbari. Fini, "An underfrequency load shedding scheme for islanded microgrids," *Int. J. Electr. Power Energy Syst.*, Vol. 62, No. 1, pp. 599-607, Nov. 2014.

[3] A. J. Wood and B. F. Wollenberg, *Power generation, operation, and control*, Wiley, Chap. 3, Dec. 2013.

[4] J. Laghari, H. Mokhlis, A. Bakar, and H. Mohamad, "Application of computational intelligence techniques for load shedding in power systems: A review," *Energy Convers. Manag..*, Vol. 75, No. 1, pp. 130-140, Nov. 2013.

[5] G.S. Grewal, J.W. Konowalec and M. Hakim, "A new centralized adaptive underfrequency load shedding controller for microgrids based on a distribution state estimator," *IEEE Trans. Power Deliv.*, Vol. 32, No. 1, pp. 370-380, Feb. 2017.

[6] V. Terzija, "Case study: Adaptive underfrequency load shedding based on the magnitude of the disturbance estimation," *IEEE Trans. Power Syst.*, Vol. 21, No. 3, pp. 1260-1266, July 2006.

[7] A. Chandra and A. K. Pradhan, "An Adaptive Underfrequency Load Shedding Scheme in the Presence of Solar Photovoltaic Plants," *IEEE Syst. J.*, Vol. 15, No. 1, pp. 1235-1244, May 2020.

[8] T. Shekari, F. Aminifar, and M. Sanaye-Pasand, "An analytical adaptive load shedding sheme againts severe combinational disturbances," *IEEE Trans. Power Syst.*, Vol. 31, No. 5, pp. 4135-4143, Sept. 2016.

[9] J. Tang, J. Liu, F. Ponci, and A. Monti, "Adaptive load shedding based on combined frequency and voltage stability assessment using synchrophasor measurements," *IEEE Trans. Power Syst.*, Vol. 28, No. 2, pp. 2035-2047, May 2013.

[10] S.S. Banijamali and T. Amraee, "Semi-adaptive setting of under frequency load shedding relays considering credible generation outage scenarios," *IEEE Trans. Power Deliv.*, Vol. 34, No. 3, pp. 1098-1108, June 2019.

[11] Ch. Li, Y. Wu, Y. Sun, H. Zhang and Y. Liu, "Continuous under-frequency load shedding sheme for power system adaptive frequency control," *IEEE Trans. Power Syst.*, Vol. 35, No. 2, pp. 950-961, Mar. 2020.

[12] J.A. Laghari, H. Mokhlis, M. Karimi, A.H. Abu Bakar and H. Mohamad, "A new under-frequency load shedding technique based on combination of fixed and random priority of loads for smart grid applications," *IEEE Trans. Power Syst.*, Vol. 30, No. 5, pp. 2507-2515, Sept. 2015.

[13] L. Zhang, S. Zhou, J. An and Q. Kang, "Demand-side management optimization in electric vehicles battery swapping service," *IEEE Access*, Vol. 7, pp. 95224-95232, July 2019.

[14] P. Herath, V. Fusco and M. Navarro, "Computational Intelligence-Based Demand Response Management in a Microgrid," *IEEE Trans. Ind. Appl.*, Vol. 55, No. 1, pp. 732-740, Jan. 2019.

[15] L. R. Chang-Chien, L. N. An, T. W. Lin, W. J. Lee, "Incorporating demand response with spinning reserve to realize an adaptive frequency restoration plan for system contingencies," *IEEE Trans. Smart Grid*, Vol. 3, No. 3, pp. 1145-1153, Sept. 2012.

[16] M. Collotta and G. Pau, "An Innovative Approach for Forecasting of Energy Requirements to Improve a Smart Home Management System Based on BLE," *IEEE Trans. Green Commun. Netw.*, Vol. 1, No. 1, pp. 112-120, Feb. 2017.

[17] S. A. Pourmousavi and M. H. Nehrir, "Real-time central demand response for primary frequency regulation in microgrids," *IEEE Trans. Smart Grid*, Vol. 3, No. 4, pp. 1988-1996, Mar. 2012.

[18] K. M. Rogers, R. Klump, H. Khurana, A. A. Aquino-Lugo, and T. J. Overbye, "An authenticated control framework for distributed voltage support on the smart grid," *IEEE Trans. Smart Grid*, Vol. 1, No. 1, pp. 40-47, June 2010.

[19] M. Sankur, D. Arnold, and D. Auslander, "Dynamic programming for optimal load-shedding of office scale battery storage and plug-loads," *IEEE Power and Energy Society General Meeting*, pp. 1-5, 2015.

[20] *IEEE Guide for the Application of Protective Relays Used for Abnormal Frequency Load Shedding and Restoration*, IEEE Std C37.117, 2007.

Pezhvak Sheikhzadeh-Baboli received his B.Sc. degree in electrical engineering at the Noshirvani University of Technology, Babol, Iran in 2008 and his M.Sc. degree in power engineering at the K.N. Toosi University of Technology, Tehran, Iran in 2012. Now, he is pursuing a Ph.D. degree in power engineering at the Shahrood University of Technology, Shahrood, Iran. His research interests include the stability of power systems and power quality.

Mohsen Assili received his B.Sc., M.Sc., and Ph.D. degrees in power engineering at the Ferdowsi University of Mashhad, Mashhad, Iran in 1996, 1999 and 2009, respectively. Since 2009, he has been in the Department of Power Engineering at the Shahrood University of Technology, Shahrood, Iran. His research interests include power system operation and analysis, particularly in dynamics and stability, power system economics, and restructuring and generation technologies.

IECO

This page intentionally left blank.

International Journal of Industrial Electronics, Control and Optimization © 2022 IECO
Vol. 5, No. 1, pp. 11-22 , Jan (2022)

Event-Triggered Predictive Networked Control Systems with Network Imperfections and External Disturbance

Beheshte Sadeghi Sabzevari [1], Mohammad Haddad Zarif [2,†], and Seyed Kamal Hosseini Sani [3]

[1,2]Faculty of Electrical and Robotic Engineering, Shahrood University of Technology, Shahrood, Iran
[3]Faculty of Electrical Engineering, Ferdowsi University of Mashhad, Mashhad, Iran.

ABSTRACT

This paper presents a novel event-triggered predictive control (ETPC) approach for the stabilization of discrete-time output- feedback networked control systems (NCSs). The studied NCS is considered to be subject to both random external input and output disturbances, and network imperfections including random communication delay, random packet dropout, packet disorder, limitation of network bandwidth, and network resources. In the proposed algorithm, an observer-based event detector is designed for reducing the number of sent packets through the communication network using the estimated system states by the Luenberger observer. In this way, the system's energy resources are saved and network-induced effects are skipped. A switched predictive controller with multiple gains are used to compensate for network-induced effects. Controller gains are designed compatible with different possible values of delays and packet dropouts. A novel augmented representation of the state-space equations of the system is derived to design observer gain and controller gains. The asymptotic stability of the system is guaranteed by designing the observer and controller based on the Lyapunov function through solving linear matrix inequalities (LMIs). Putting all the aforementioned points together has made the whole framework presented in this paper a comprehensive one. The effectiveness of the proposed approach is demonstrated by comparative simulation results.

Article Info

Keywords:
Event-triggered control, Networked control system, Network imperfections, Predictive controller, Switched controller

Article History:
Received 2020-07-19
Accepted 2020-10-12

I. INTRODUCTION

Networked control systems (NCSs) are systems that utilize the communication network for data exchange between different parts of the system. The insertion of the communication network in traditional control systems has led to more flexible systems with easier maintenance [1]. Robot networks [2], intelligent transportation systems [3], laparoscopy [4], and cyber-physical systems [5] are some of the applications of NCSs. On the other hand; since there are always imperfections in real networks; the use of the communication network has introduced new challenges to conventional control systems. Some of these challenges are network bandwidth limitation, delay, packet dropout, congestion, and packet disorder. Dealing with these issues has received noticeable attention in the last decade. Readers are referred to surveys [6]-[8] and the references therein. Delay and packet dropout are the most important challenges among all the network-induced effects. Therefore, researchers have paid considerable attention

†Corresponding Author: mhzarif@shahroodut.ac.ir
Tel: +98-9121733730, Fax: +98-2332300250, Shahrood University of Technology
Faculty of Electrical and Robotic Engineering, Shahrood University of Technology, Shahrood, Iran

to different compensation methods for these two challenges.

An effective method for confronting with delay and the packet dropout effect; after their occurrence; is using the predictive control method which can be either centralized or decentralized. Paper [9] is an example of the decentralized predictive control method in which a robust decentralized model predictive control scheme for systems subject to state and input constraints is introduced. Papers [10] and [11] are examples of the centralized predictive control method. In [10], a switched predictive control method for NCSs exposed to both delay and packet dropout is investigated. In [11], an algorithm based on Kalman filter for systems exposed to time delay is introduced.

Another method is reducing the number of sent packets by confining them to those which are critically necessary for maintaining the system's performance at the desired level. This approach is called the event-triggered control (ETC) method. In conventional time-triggered control method system state(s)/output(s) are sampled periodically and all of them are sent through the network. However, in the ETC method, the sampled data is sent only if a predetermined inequality is violated. Readers are referred to the survey [12] and the references therein.

By combining predictive control and ETC in networked control systems, an effective approach called the event-triggered predictive control (ETPC) method was introduced. Controlling spacecraft rendezvous hovering phases [13], freeway traffic [14], and embedded artificial pancreas system [15] are some of the wide applications of the ETPC method.

In [16], a cost function is proposed for calculating the required control signal for the stabilization of the system using an ETPC method, but neither delay nor packet dropout is considered. In [17], an ETPC method is investigated for output feedback NCSs exposed to delay and packet dropout, but no disturbance is considered. Reference [18] addresses the ETPC problem for NCSs subject to communication delay, in which either the value of the communication delay is less or more than the sampling time are discussed separately. In [19], the ETPC method is studied using a fuzzy predictive controller for NCSs with packet dropout. Reference [20] discusses the ETPC method for NCSs subject to communication delay while using two event-detector blocks, one in the sensor side and the other on the controller side.

In [21], an ETPC strategy is proposed for solving the existence of an unsynchronized delay in both sensor-to-controller and controller-to-actuator channels. Paper [22] uses a Luenberger observer for estimating the system states and utilizes an event-triggered mechanism for saving network resources. Moreover, an augmented model and a piecewise linear model are introduced to derive the stability condition in the presence of network delay.

In [23], a state-feedback NCS under delay, packet loss, and limited network resources is studied. An ETPC scheme is proposed in which, similar to the current paper, a switched controller is deployed; however, unlike the present paper, no disturbance is considered. A gain scheduled extended state observer is employed in the ETPC scheme proposed in [24] which stabilizes the NCS in the presence of delay, packet dropout, packet disorder, and input disturbance. Unlike the present paper, [24] has not considered output disturbance and has not used a switched controller.

The system studied in this paper is a linear time-invariant system exposed to random input and output external disturbances. Network-induced delay, packet dropout, and packet disorder along with the limitation of network bandwidth and resources are taken into account. Since system states are required for calculating the control signal, an observer is utilized for estimating the system state based on the system output sampled by the sensor. The estimated system state is then passed to the "event detector" block which determined whether a pre-determined event has occurred. If the event has happened, the last estimated system state is sent to the predictive controller through the feedback network channel. The "event detector" block determines the necessity of each piece of data for transmitting to the controller and, thus, significantly saves network bandwidth and resources.

The data sent to the controller is exposed to network-induced delay, packet dropout, and packet disorder. Therefore, a predictive controller along with a buffer is utilized for compensating the network effects. The data sent through the feedback channel is first received by the "Buffer 1" block which decides whether the received data is newer than the data already in the buffer. The buffer block keeps the newest data and passes it to the "controller" block. For increasing the compatibility of the controller with different values of network delay and packet dropout, multiple gains are considered for the controller, so the resultant controller is a switching predictive controller.

The control signal sent to the actuator side is also subject to delay and packet dropout, so a data packet is created by the controller which contains different values of control signal compatible with different possible values of delay and packet dropout. This data packet is then received on the actuator side by the selector block. This

block is designed such that it can deal with packet disorder in addition to delay and packet dropout. The data packet first entered the "Buffer 2" block which acts similarly to "Buffer 1". It keeps the newest data packet and passes it to the "control signal selector" block which chooses the appropriate control signal among different control signals in the data packet and passes it to the actuator to be applied to the plant. The event detector condition and controller and observer gains are designed based on the Lyapunov function, so that the asymptotic stability of the system in the presence of the aforementioned network imperfections is guaranteed.

Unlike many other papers in which the disturbance effect is either neglected or compensated through specific blocks in the system's architecture; which leads to more complexity and energy consumption in the NCS; in this paper the disturbance effect problem is resolved while designing the ETPC method. Furthermore, in order to take into account external disturbances and network imperfections, a novel augmented representation of the state-space equations of the system is derived. The augmented representation of the system can be used as a suitable base for analyzing systems with different control methods in other works.

The remainder of this paper is organized as follows: The investigated system and the structure for the implementation of the proposed ETPC method are described in Section 2. In section 3 the main results are explained in which two derived theorems for the asymptotic stability of the proposed ETPC method are included. Section 4 is dedicated to presenting the effectiveness of the proposed method by two comparative simulation results. Finally, the conclusions are included in Section 5.

Notation. Throughout this paper, $\Re^n$ and $\Re^{n\times m}$ are the n-dimensional and $n \times m$-dimensional Euclidean space, respectively. The superscript "-1" denotes the inverse of an invertible matrix, and the superscript "T" denotes the transpose of a matrix or a vector. "I" and "0" represent the identity matrix and the zero matrix with appropriate dimensions, respectively. The inequality $P < 0$ indicates the negative-definiteness of the symmetric matrix P. The symbol "$*$" denotes a term induced by symmetry in a symmetric matrix. $\|v\|_2$ represents the second Euclidean norm of the vector v.

II. System Description

The studied networked control system is described as

$$x(k+1) = Ax(k) + Bu(k) + E_1 w_1(k) \quad (1)$$

$$y(k) = Cx(k) + E_2 w_2(k) \quad (2)$$

$$x(0) = x_0 \quad (3)$$

where $x \in \Re^n$, $u \in \Re^m$ and $y \in \Re^l$ denote the state vector, control input, and system output, respectively; $w_1 \in \Re^p$ and $w_2 \in \Re^q$ are input disturbance and output disturbance, respectively, and both of them belong to $L_2(0,+\infty)$; A, B, C, E_1 and E_2 are known constant matrices with appropriate dimensions; and the initial value of the system state is denoted by x_0.

The proposed structure of the event-triggered predictive NCS in this paper is depicted in Fig. 1. At each instant k, the observer estimates the system state; then, the event detector decides whether an event has happened or not. If an event has happened, $\hat{x}(k)$ is sent to the controller through the network; if not, $\hat{x}(k)$ is discarded. The predictive controller generates a data packet containing predictive control signals based on the last received data and sends the sequence to the actuator. On the actuator side, first, a selector selects the appropriate control signal among the received predictive control signals based on the delay imposed on the last received data packet. Then, the selected control signal is sent to the actuator in order to be applied to the plant.

The following assumptions are considered for the NCS in this paper:

Assumption 1. [17] The sensor, controller and actuator are time-driven with the same sampling period T and the packets sent through the network are with time stamps.

Assumption 2.[17] The number of network-induced packet losses in the feedback and feedforward channels are denoted by L_{fb} and L_{fw}, respectively, and both are random numbers. The upper bounds of L_{fb} and L_{fw} are L_1 and L_2, respectively.

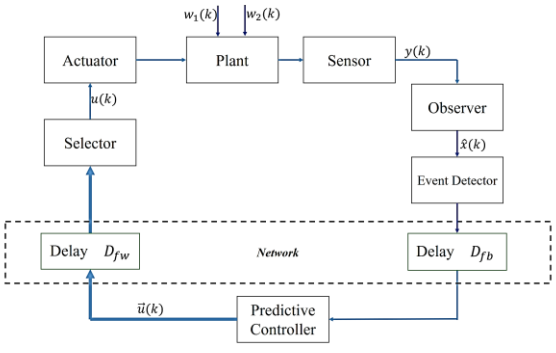

Fig. 1. The proposed structure of the event-triggered predictive NCS.

Assumption 3.[17] The random network-induced delay in the feedback and feedforward channels are denoted by D_{fb} and D_{fw}, respectively. The upper bounds of D_{fb} and

D_{fw} are D_1 and D_2, respectively.

Assumption 4. Without loss of generality, it is considered that

$$\alpha_1\|w_1(k)\|_2^2 \le \beta_1\|x(k)\|_2^2 \quad (4)$$

$$\alpha_2\|w_2(k)\|_2^2 \le \beta_2\|x(k)\|_2^2 \quad (5)$$

in which α_i and β_i, $i = 1,2$, are four constant values.

Assumption 5. Without loss of generality, it is assumed that the sizes of w_1, w_2, and y are the same, which means that $l = p = q$. This can happen by adding enough '0's to those vectors with a smaller size.

A. *Observer-based Event Detector*

The proposed observer for the NCS is the Luenberger observer which is described as

$$\hat{x}(k+1) = A\hat{x}(k) + Bu(k) + L(y(k) - C\hat{x}(k)). \quad (6)$$

$\hat{x}$ and u are the observed state and the input of the observer at instant k, respectively. Matrix L is to be designed such that the asymptotic stability of the system is guaranteed.

In order to reduce unnecessary data transmission in the feedback network, an event detector is considered. Using an ETC scheme saves network bandwidth and energy resources. At each instant, a triggering condition is checked. If the condition is violated, the last sampled data is sent through the network; otherwise, it is discarded. In this paper, the triggering condition is as

$$k_{i+1} = \begin{cases} \min\{k \mid (\hat{x}(k) - \hat{x}(t_i))^T \Phi_1 (\hat{x}(k) - \hat{x}(t_i))\} > \hat{x}^T(k)\Phi_2\hat{x}(k), & k < k_i + R + 1 \\ k_i + R + 1, & k \ge k_i + R + 1 \end{cases} \quad (7)$$

where Φ_1 and Φ_2 are known positive definite symmetric matrices; t_i is the last instant a data packet was sent through the network. The condition states that, after a data packet is sent at k_i, for R instants, the inequality is checked. If no violation occurs during these R instants, the newest sampled data at $k_i + R + 1$ is sent, whether a violation occurs or not.

Thereby, at each sampling instant k, the sensor samples the system output ($y(k)$) and passes it to the observer. The observer estimates the system states ($\hat{x}(k)$) using Equ. (4). The estimated state is then sent to the "event detector" block. The "event detector" block decides based on Equ. (7) whether $\hat{x}(k)$ must be sent to the controller or not.

B. *Predictive Controller*

Fig. 2 demonstrates the internal architecture of the predictive controller in the NCS. A buffer is used to store the latest packet received through the feedback channel. In order to deal with the packet disorder, at each instant, only that packet with the newest timestamp is kept and the older packets are discarded.

Fig. 2. The internal structure of the predictive controller

For the system without time delay, the control signal is generated based on the equation

$$u(k_i) = K_0\hat{x}(k_i) \quad (8)$$

where $K_0 \in \Re^{m\times n}$ is the control gain matrix which will be designed later.

Each sent data may be affected by network delay and packet loss. A suitable approach for generating the proper control signal by the predictive controller is using a controller with different constant gains, as

$$u_{k_i-f+i|k_i-f} = K_i\hat{x}(k_i - f) \quad (9)$$

where $i = 1,2,\dots,f, f \in \{1,\dots,D_{fb} + L_{fb}\}$. $u_{k_i-f+i|k_i-f}$ is the predictive control signal for instant $k_i - f + i$ based on the available data from instant $k_i - f$. K_i is the corresponding controller gain in order to predict the control signal i step(s) ahead.

Generated control signals are supposed to be sent to the actuator and are exposed to delay and packet loss in the feedforward channel. If the generated control signal based on a sent packet by event detector at instant k_i is not lost during the transmission, then it will be used at instant $k_i + D_{fb} + L_{fb} + D_{fw} + L_{fw}$ on the actuator side. Thus, by setting $N = D_{fb} + L_{fb} + D_{fw} + L_{fw}$, $N + 1$ different controller gains must be considered.

The packet generated by the predictive controller is as

$$\vec{u}(k) = [u_{k|k_i}^T \; u_{k+1|k_i}^T \; u_{k+2|k_i}^T \; \dots \; u_{k+l|k_i}^T]^T. \quad (10)$$

k_i denotes the instant in which the newest data ($\hat{x}(k_i)$) available on the controller side was sent by the event detector. l is as $l = D_{fw} + L_{fw}$ and $k \ge k_i$.

Consequently, the state space equations of the system can be rewritten as

$$x(k+1) = Ax(k) + BK_i\hat{x}(k-i) + E_1w_1(k) \quad (11)$$

and the observer equation is as

$$\hat{x}(k+1) = A\hat{x}(k) + BK_i\hat{x}(k-i) + L\big(Cx(k) + E_2w_2(k) - C\hat{x}(k)\big)$$

$$= (A - LC)\hat{x}(k) + BK_i\hat{x}(k-i) + LCx(k) + LE_2w_2(k) \quad (12)$$

Therefore, the resultant augmented state-space equations of the NCS are

$$\bar{x}(k+1) = \bar{A}_j \bar{x}(k+1) + \bar{E}_1 \bar{w}_1(k) \quad , j = 1, \dots, N, \tag{13}$$

$$y(k) = \bar{C}\bar{x}(k+1) + \bar{E}_2 w_2(k) \tag{14}$$

in which

$$\bar{x}(k) = [x^T(k), x^T(k-1), \dots, x^T(k-N), \hat{x}^T(k), \hat{x}^T(k-1), \dots, \hat{x}^T(k-N)]^T$$

$$\bar{E}_1 = \begin{bmatrix} E_1 & 0_{(N+1)n\times q} \\ 0_{(2N+1)n\times q} & LE_2 \\ & 0_{Nn\times q} \end{bmatrix}, \qquad \bar{E}_2 = [E_2 \quad 0_{l\times q}],$$

$$\bar{C} = [C \quad 0_{l\times(2N+1)n}],$$

$$\bar{w}_1(k) = \begin{bmatrix} w_1(k) \\ w_2(k) \end{bmatrix}, \qquad \bar{A}_j = \begin{bmatrix} A_1 & A_{2j} \\ A_3 & A_{4j} \end{bmatrix}$$

where

$$A_1 = \begin{bmatrix} A & 0_{n\times Nn} \\ I_{Nn} & 0_{Nn\times n} \end{bmatrix},$$

$$A_{2j} = \begin{bmatrix} 0_n & BK_j & 0_{n\times(N-j)} \\ 0_{(N+1)n\times(N+1)n} \end{bmatrix}, \quad A_3 = \begin{bmatrix} LC & 0_{n\times Nn} \\ 0_{Nn\times(N+1)n} \end{bmatrix},$$

$$A_{4j} = \begin{bmatrix} A-LC & 0_{n\times(j-1)n} & BK_j & 0_{n\times(N-j)} \\ & I_{Nn} & 0_{Nn\times n} \end{bmatrix}.$$

C. Selector

Fig. 3 presents the internal structure of the selector block. Buffer 2 is the block solving packet disorder problem. This buffer compares the timestamp of the newly received packet through the feedforward channel with the one already existing in the buffer. If the received packet has newer timestamp, it is stored in the buffer and used by the actuator; otherwise, it is ignored and the existing one in the buffer is used by the actuator until a newer packet becomes available.

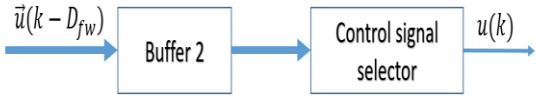

Fig. 3. The internal structure of the selector block

Then, the control signal selector selects the appropriate control signal among different elements of the packet received from the controller.

III. Main Results

Lemma 1.[10] (Schur complement): For a symmetric matrix $L = \begin{bmatrix} L_{11} & L_{12} \\ L_{12}^T & L_{22} \end{bmatrix}$, the following statements are equivalent:

(1) $L < 0$

(2) $L_{11} < 0, L_{22} - L_{12}^T L_{11}^{-1} L_{12} < 0$

(3) $L_{22} < 0, L_{11} - L_{12} L_{22}^{-1} L_{12}^T < 0$

Theorem 1. The system described by Equs. (13) and (14) is asymptotically stable if the following LMI holds:

$$\Omega(A_j, P) = \begin{bmatrix} \bar{A}_j^T P \bar{A}_j - P + \beta_1 I & \bar{A}_j^T P \bar{E}_1 \\ * & \bar{E}_1^T P \bar{E}_1 - \alpha_1 I \end{bmatrix} < 0, \quad j = 1,2,\dots,N. \tag{15}$$

Proof. The following Lyapunov functions are considered for the system described by Equs. (11) and (12)

$$V_j(x(k)) = \bar{x}^T(k) P \bar{x}(k). \quad j = 1,2,\dots,N$$

Based on Assumption 4, $\alpha_1 \|w_1(k)\|_2^2 \le \beta_1 \|x(k)\|_2^2$; then,

$$\Delta V_j - \alpha_1 \|w_1(k)\|_2^2 + \beta_1 \|x(k)\|_2^2$$

$$= V_j\big(x(k+1)\big) - V_j\big(x(k)\big) - \alpha_1 \|w_1(k)\|_2^2 + \beta_1 \|x(k)\|_2^2$$

$$= \bar{x}^T(k+1) P \bar{x}(k+1) - \bar{x}^T(k) P \bar{x}(k) - \alpha_1 w_1^T(k) w_1(k) + \beta_1 x^T(k) x(k)$$

$$= (\bar{A}_j \bar{x}(k) + \bar{E}_1 w_1(k))^T P \left(\bar{A}_j \bar{x}(k) + \bar{E}_1 w_1(k)\right) - \bar{x}^T(k) P \bar{x}(k) - \alpha_1 w_1^T(k) w_1(k) + \beta_1 x^T(k) x(k)$$

$$= [\bar{x}^T(k) \quad w_1^T(k)] \begin{bmatrix} \bar{A}_j^T P \bar{A}_j - P + \beta_1 I & \bar{A}_j^T P \bar{E}_1 \\ * & \bar{E}_1^T P \bar{E}_1 - \alpha_1 I \end{bmatrix} \begin{bmatrix} \bar{x}(k) \\ w_1(k) \end{bmatrix}$$

so if $\Omega(A_j, P) < 0$, then $\Delta V_j - \alpha_1 \|w_1(k)\|_2^2 + \beta_1 \|x(k)\|_2^2 < 0$, and it is concluded that $\Delta V_j < 0$. Thus, based on the Lyapunov function theorem, the asymptotic stability of such system is guaranteed.

After determining the sufficient condition for the asymptotic stability of the system, the controller gains must be designed. For this purpose, matrices $\bar{A}_j$ and $\bar{E}_1$ are rewritten in new forms.

By defining matrices

$$\tilde{B} = \begin{bmatrix} B \\ 0_{Nn\times m} \\ B \\ 0_{Nn\times m} \end{bmatrix}, \qquad \tilde{I} = \begin{bmatrix} 0_{(N+1)n\times n} \\ I_n \\ 0_{Nn\times n} \end{bmatrix},$$

$$\tilde{C} = [C \quad 0_{l\times Nn} \quad -C \quad 0_{l\times Nn}],$$

$$\bar{I}_j = [0_{n\times(N+j+1)n}\ I_n\ 0_{n\times(N-j)n}],$$

$$\tilde{A} = \begin{bmatrix} A_1 & 0_{(N+1)n} \\ 0_{(N+1)n} & A_1 \end{bmatrix}$$

$\bar{A}_j$ can be written as

$$\bar{A}_j = \tilde{A} + \tilde{B}K_j\bar{I}_j + \tilde{I}L\tilde{C}, \tag{16}$$

and by defining

$$\tilde{E}_1 = \begin{bmatrix} E_1 \\ 0_{(2N+1)n\times q} \end{bmatrix}, \quad 0_{2(N+1)n\times q}],$$

$$\hat{I} = \begin{bmatrix} 0_{(N+1)n\times n} \\ I_n \\ 0_{Nn\times n} \end{bmatrix}, \qquad \tilde{E}_2 = [0_{l\times q} \quad I_q]$$

$\bar{E}_1$ can be written as

$$\bar{E}_1 = \tilde{E}_1 + \hat{I}L\tilde{E}_2. \tag{17}$$

Theorem 2. Suppose that there exist positive definite matrix P and matrices L and $K_j, j \in \bar{N}, \bar{N} = \{0,1,\dots,N\}$ such that matrix inequalities

$$\Gamma(A_j,P) = \begin{bmatrix} -P+\alpha_1 I & * & * \\ 0 & -\beta_1 I & * \\ \tilde{A}+\tilde{B}K_j\bar{I}_j+\tilde{I}L\tilde{C} & \tilde{E}_1+\hat{I}L\tilde{E}_2 & -P \end{bmatrix} < 0, \quad j \in \bar{N} \tag{18}$$

hold. Then, the system described by Equs. (13) and (14) with the controllers described by Equ. (9) is asymptotically stable.

Proof. Following the result obtained from Theorem 1, $\Omega(A_j,P)$ can be written as

$$\begin{bmatrix} \bar{A}_j^T P\bar{A}_j - P + \beta_1 I & \bar{A}_j^T P\bar{E}_1 \\ * & \bar{E}_1^T P\bar{E}_1 - \alpha_1 I \end{bmatrix} =$$

$$\begin{bmatrix} -P+\beta_1 I & 0 \\ * & -\alpha_1 I \end{bmatrix} + \begin{bmatrix} \bar{A}_j^T P \\ \bar{E}_1^T P \end{bmatrix} P^{-1}\begin{bmatrix} P\bar{A}_j & P\bar{E}_1 \end{bmatrix}.$$

Based on Lemma 1 and Equs. (13) and (14),

$$\begin{bmatrix} -P+\beta_1 I & 0 \\ * & -\alpha_1 I \end{bmatrix} + \begin{bmatrix} \bar{A}_j^T P \\ \bar{E}_1^T P \end{bmatrix} P^{-1}\begin{bmatrix} P\bar{A}_j & P\bar{E}_1 \end{bmatrix} =$$

$$\begin{bmatrix} -P+\alpha_1 I & * & * \\ 0 & -\beta_1 I & * \\ \bar{A}_j & \bar{E}_1 & -P \end{bmatrix} =$$

$$\begin{bmatrix} -P+\alpha_1 I & * & * \\ 0 & -\beta_1 I & * \\ \tilde{A}+\tilde{B}K_j\bar{I}_j+\tilde{I}L\tilde{C} & \tilde{E}_1+\hat{I}L\tilde{E}_2 & -P \end{bmatrix} \tag{19}$$

Since in Theorem 1 the sufficient condition for the asymptotic stability of the system is $\Omega(A_j,P) < 0$;

based on Equ. (19) and Lemma 1; it is equivalent to $\Gamma(A_j,P) < 0$.

IV. Simulation

In this section, the effectiveness of the proposed algorithm in this paper is demonstrated via two examples. Both examples are chosen from the literature and both systems are affected by delay, packet disorder, packet dropout, and input and output disturbances.

Example 1. In this example the plant studied in [10] is considered, and the stability of the system under network imperfections and disturbances is investigated. The ETPC scheme proposed here and the algorithm proposed in [10] are both applied to the system and the results are compared with each other from the stability point of view.

The state space equations of the system are

$$x(k+1) = Ax(k) + Bu(k) + E_1w_1(k)$$

$$y(k) = Cx(k) + E_2w_2(k)$$

in which

$$A = \begin{bmatrix} -0.85 & 0.271 & 0.488 \\ 0.482 & 0.1 & 0.24 \\ 0.002 & 0.3681 & 0.707 \end{bmatrix}, B = \begin{bmatrix} 0.5 & 0.1 \\ 0.3 & -0.4 \\ 0.2 & 0.5 \end{bmatrix},$$

$$C = \begin{bmatrix} 0.1 & 0.2 & 1 \\ 0.4 & 0.3 & 0.1 \end{bmatrix}, \quad E_1 = I_{3\times3}, E_2 = 0.1I_{2\times2}.$$

The constants in Assumption 2 are selected as $\alpha_1 = 1$, $\beta_1 = 0.01$, $\alpha_2 = 1$ and $\beta_2 = 0.01$. The sampling period is set as $T = 0.01$. The upper bounds of random transmission delays and consecutive packet loss in feedback and feedforward channels are set as $D_1 = 2T, D_2 = T, L_1 = 1$ and $L_2 = 1$. The initial states of the plant and observer are $x(0) = [0.98, 0.8, -1.5]^T$ and $\hat{x}(0) = [0.8, 0.9, -1.35]$, respectively, and the upper bound of non-triggering is set as $R = 3T$.

First, the stability of the system under the proposed algorithm in [10] is investigated. Figs. 4 and 5 present the instability of the system states and system output, respectively, in the presence of delay and packet loss without compensation. In Figs. 6 and 7, the system states and system outputs using the proposed ETPC method in this paper are illustrated, respectively. Time diagrams in these two Figs. 6 and 7 show the effectiveness of the proposed method in this paper in compensation of both delay and packet loss and also demonstrate the rapid convergence of the system states towards stability.

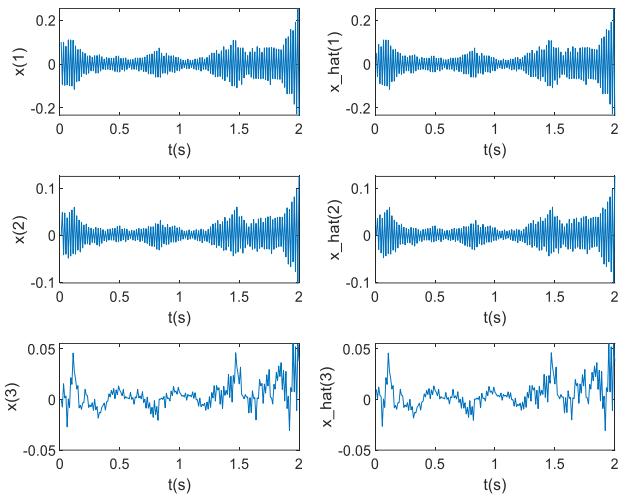

Fig. 4. System states under the algorithm proposed in [10] for Example 1.

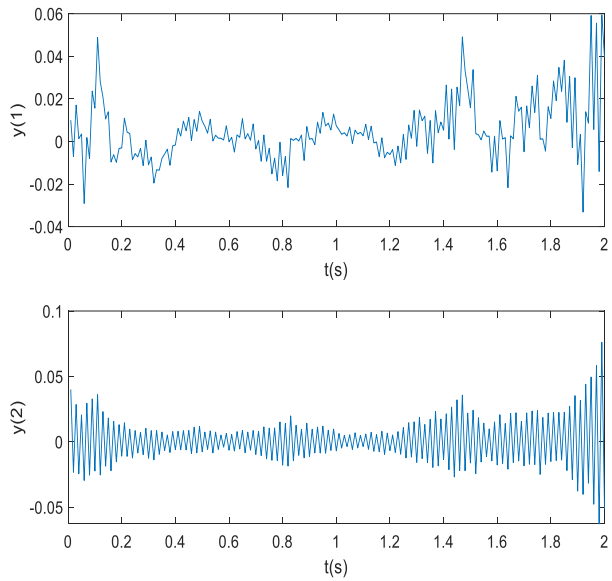

Fig. 5. System outputs under the algorithm proposed in [10] for Example 1.

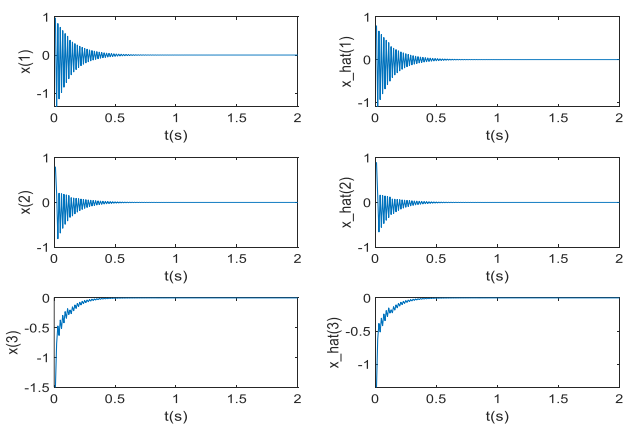

Fig. 6. System states and estimation of system states by the observer under the algorithm proposed in this paper for Example 1.

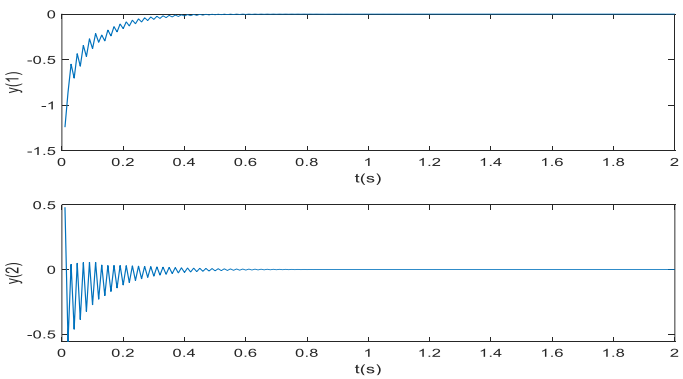

Fig. 7. System outputs under the algorithm proposed in this paper for Example 1.

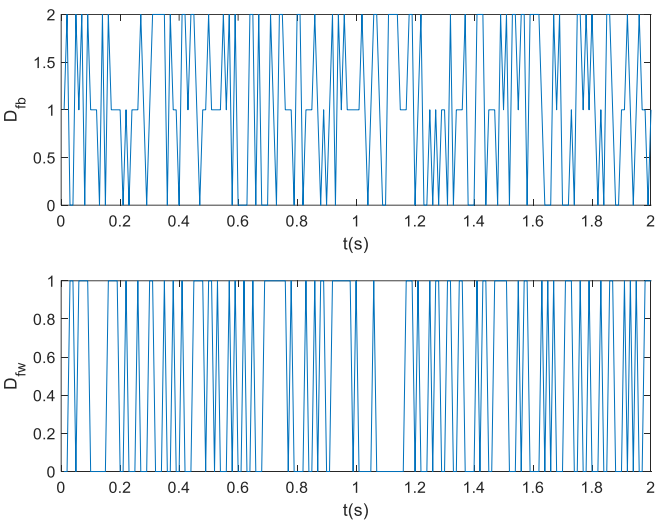

Fig. 8. Random delay in the feedback and feedforward channel of the communication network for Example 1.

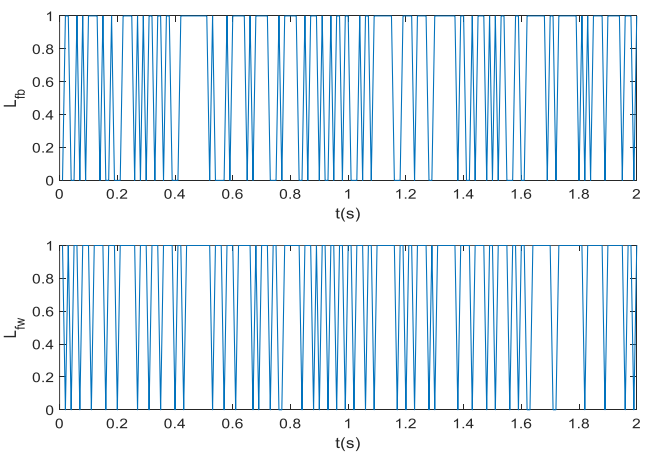

Fig. 9. Random packet loss in the feedback and feedforward channel of the communication network for Example 1.

Comparing the real system states and estimated system states in Fig. 6 represents the precision of the observer's estimations, which confirms the choice of the observer and the precision of

the observer gain calculation via the proposed LMIs. The number of triggering instants shows that the event detector triggers 49 times among 200 sampling instants, which means more than 75% reduction in the number of sent packets by using the proposed control scheme in this paper.

Figs. 7 and 8 display the randomness of the occurrence of delay and packet loss, respectively, in both feedback and feedforward channels. They show that the simulated system has been considered in one of the worst cases in which almost every packet is exposed to both delay and packet loss in both feedback and feedforward channels.

Example 2. In this example the effectiveness of the algorithm is checked on the system studied in [23]. The studied system is similar to the one investigated in [10] but the method is different. The state space equations of the system are

$$x(k+1) = Ax(k) + Bu(k) + E_1 w_1(k)$$

$$y(k) = Cx(k) + E_2 w_2(k)$$

in which matrices are set as

$$A = \begin{bmatrix} -0.85 & 0.271 & -0.488 \\ 0.482 & 0.1 & 0.24 \\ 0.002 & 0.3681 & 0.707 \end{bmatrix}, \quad B = \begin{bmatrix} 0.5 & 0.1 \\ 0.3 & -0.4 \\ 0.2 & 0.5 \end{bmatrix},$$

$$C = \begin{bmatrix} 0.1 & 0.2 & 1 \\ 0.4 & 0.3 & 0.1 \end{bmatrix}$$

$$E_1 = \begin{bmatrix} 1 & 0 \\ 1 & 1 \\ 0 & 1 \end{bmatrix}, \quad E_2 = I_{2\times 2}.$$

The constants considered in Assumption 2 are selected similar to Example 1, as $\alpha_1 = 1$, $\beta_1 = 0.01$, $\alpha_2 = 1$ and $\beta_2 = 0.01$. The sampling period is set as $T = 0.01$. The upper bounds of random transmission delays and consecutive packet loss in feedback and feedforward channels are set as $D_1 = 2T, D_2 = T, L_1 = 1$ and $L_2 = 1$. The initial states of the plant and observer are $x(0) = [-0.4, 0.1, 0.2]^T$ and $\hat{x}(0) = [0.38, 0.08, 0.16]$, respectively, and the upper bound of non-triggering is set as $R = 3T$.

Figs. 10 and 11 investigate the stability of the system in the presence of network imperfections and disturbances, while the ETPC algorithm in [23] is applied to the system. Both Figs. 10 and 11 show that the system cannot tolerate the network imperfections, and system states and system output diverge.

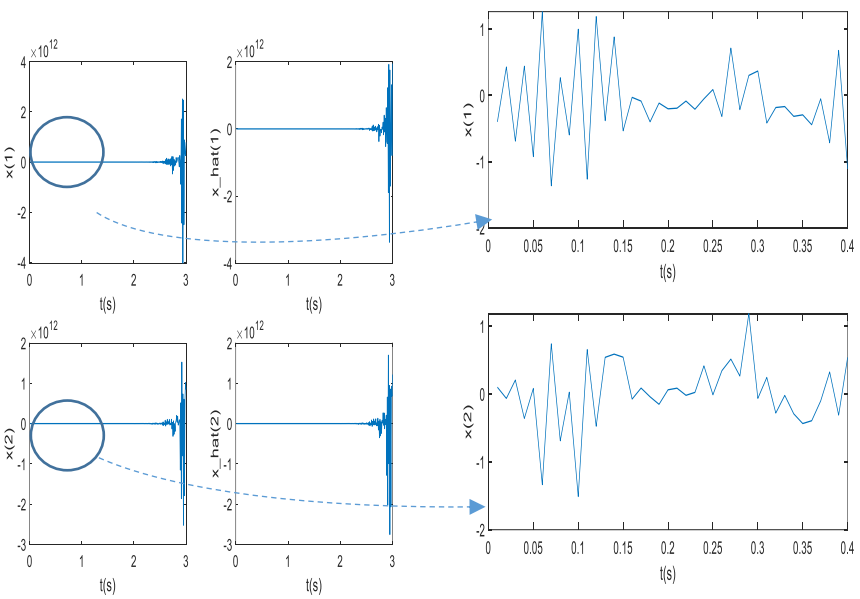

Fig. 10. System states under the algorithm proposed in [23] for Example 2.

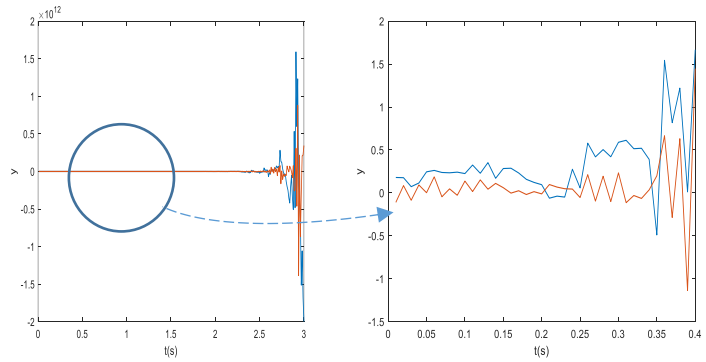

Fig. 11. System outputs under the algorithm proposed in [23] for Example 2.

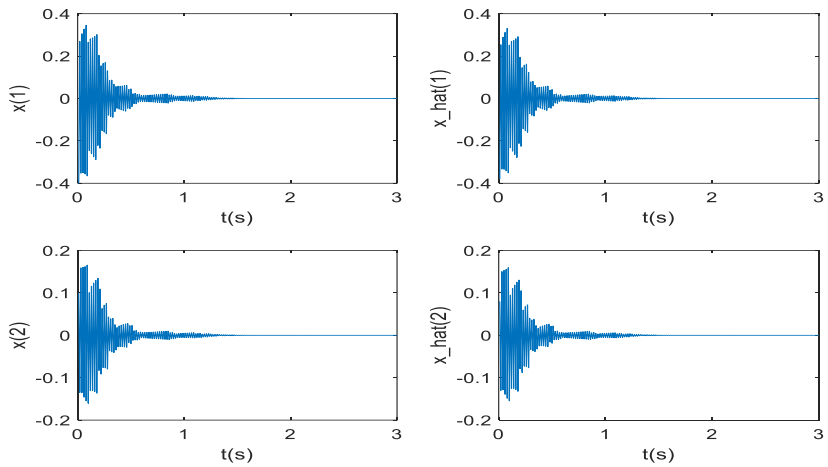

Fig. 12. System states and estimation of system states by the observer under the algorithm proposed in this paper for Example 2.

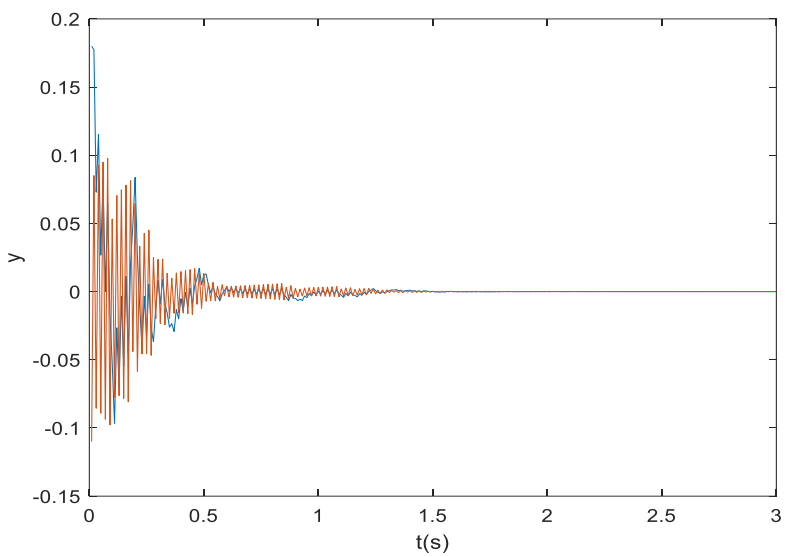

Fig. 13. System outputs under the algorithm proposed in this paper for Example 1.

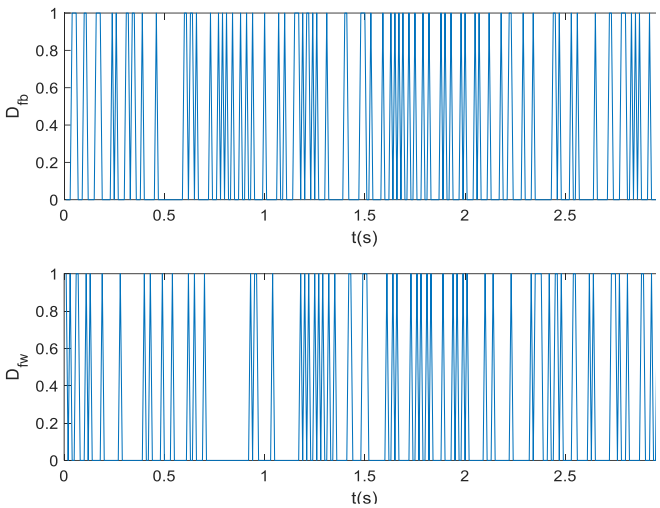

Fig. 14. Random delay in the feedback and feedforward channel of the communication network for Example 2.

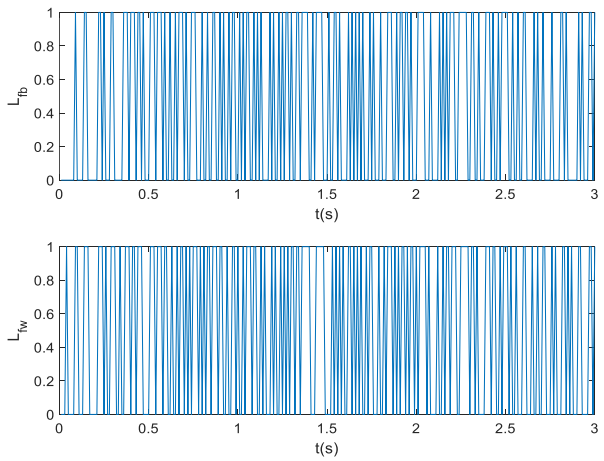

Fig. 15. Random packet loss in the feedback and feedforward channel of the communication network for Example 2.

Figs. 12 and 13 depict the effectiveness of the proposed algorithm in this paper for stabilizing the system exposed to the network imperfections and disturbances. Figs. 12 and 13 show the rapid convergence of system states and system output, respectively, clarifying that network imperfections are highly compensated by the proposed algorithm in this paper. Based on Fig. 12, since the trajectories of the estimation of system states follow the trajectories of the system states, the appropriate choice of the observer and the precision of the observer gain calculated are confirmed.

The number of triggering instants shows that the event detector triggers 246 times among 500 sampling instants. More than 50% reduction in the number of sent packets using the control scheme proposed in this paper, indicates the great effectiveness of the control scheme in saving network bandwidth and resources.

Figs. 14 and 15 display the randomness of the occurrence of delay and packet loss, respectively, in both feedback and feedforward channels. They show that; similar to example 1; the simulated system has been considered in one of the worst cases in which almost every packet is exposed to both delay and packet loss in both feedback and feedforward channels.

V. Conclusion

In this paper, the problem of designing an asymptotically stable ETPC for an output-feedback networked control system was investigated. The considered NCS structure was assumed to be exposed to external input and output disturbances and network imperfections, including delay, packet dropout, packet disorder, and limitation of network bandwidth and resources. An observer-based event-detector was exerted to confine the sent data packets to those which were critically necessary for the stabilization of the system. Thus, network resources and bandwidth were saved, and the effect of network transmission on the entire process was noticeably limited.

Using a switched predictive controller with multiple gains led to a more flexible controller than conventional controllers with one fixed gain. By deriving a new augmented representation of state-space equations of the system, observer gain and controller gains were calculated through solving LMIs. Thus, the asymptotic stability of the system was guaranteed based on the Lyapunov function theorem. Two selectors were also employed on the controller side and the actuator side of the network to deal with packet disorder. To demonstrate the effectiveness of the proposed ETPC method, two examples were presented. Both simulated systems were considered in one of their worst cases in which almost every packet was exposed to random delay and random packet loss in the communication network. Simulation results depicted the rapid convergence of the system states and outputs in both examples under the algorithm proposed in this paper, while system states and system outputs diverged under the algorithms proposed in papers [10] and [22]. The number of packets sent through the network showed more than 75% reduction in the first example and more than 50% reduction in the second example, in comparison with the conventional time-triggered controllers. This reduction has led to saving network bandwidth and network resources noticeably.

References

[1] J. P. Hespanha, P. Naghshtabrizi, and Y. Xu, “A survey of recent results in networked control systems,” *Proceedings of IEEE*, Vol. 95, No. 1, pp. 138-162, Jan. 2007.

[2] R. Aragues, J. Cortes, and C. Sagues, “Distributed consensus on robot networks for dynamically merging feature-based maps,” *IEEE Transactions on Robotics*, Vol. 28, No. 4, pp. 840-854, Aug. 2012.

[3] F. Y. Wang, "Parallel control and management for intelligent transportation systems: Concepts, architectures, applications," *IEEE Transactions on Intelligent Transportation Systems*, Vol. 11, No. 3, pp. 630-638, Sep. 2010.

[4] C. A. Castro, A. Alqassis, S. Smith, T. Ketterl, Y. Sun, S. Ross, A. Rosemurgy, P. P. Savage, and R. D. Gitlin, "A wireless robot for networked laparoscopy," *IEEE Transactions on Biomedical Engineering*, Vol. 60, No. 4, pp. 930-936, Apr. 2013.

[5] D. Ding, Q. -L. Han, Z. Wang, and X. Ge, "A Survey on Model-Based Distributed Control and Filtering for Industrial Cyber-Physical Systems," *IEEE Transactions on Industrial Informatics*, Vol. 15, No. 5, pp. 2483-2499, May 2019.

[6] X. -M. Zhang, Q. -L. Han, and X. Yu, "Survey on recent advances in networked control systems," *IEEE Transactions on Industrial Informatics*, Vol. 12, No. 5, pp. 1740-1752, Oct. 2016.

[7] X. -M. Zhang, Q. -L. Han, X. Ge, D. Ding, L. Ding, D. Yue, and C. Peng, "Networked control systems: a survey of trends and techniques," *IEEE/CAA Journal of Automatica Sinica*, Vol. 7, No. 1, pp. 1-17, Jan. 2020.

[8] M. S. Mahmoud, and M. Hamadan, "Fundamental issues in networked control systems," *IEEE/CAA Journal of Automatica Sinica*, Vol. 5, No. 5, pp. 902-922, July 2018.

[9] S. Rahmati, and H. Eliasi, "Robust decentralized model predictive control for a class of interconnected systems," *International Journal of Industrial Electronics, Control and Optimization*, Vol. 3, No. 3, pp. 327-336, July 2020.

[10] R. Wang, G. -P. Liu, W. Wang, D. Rees, and Y. -B. Zhao, "H_∞ control for networked predictive control systems based on the switched lyapunov function method", *IEEE Transactions on Industrial Electronics*, Vol. 57, No. 10, pp. 3565-3571, Oct. 2010.

[11] H. Fasih, S. Tavakoli, J. Sadeghi, and H. Torabi, "Kalman filter-smoothed random walk based centralized controller for multi-input multi-output processes," *International Journal of Industrial Electronics, Control and Optimization*, Vol. 2, No. 2, pp. 155-166, Apr. 2019.

[12] Z. Heng, P. Chen, Z. Jin, and Z. Chu, "Event-triggered control in networked control systems: a survey," in *The 27th Chinese Control and Decision Conference (2015 CCDC)*, pp. 3092-3097, Qingdao, 2015.

[13] J. Sanchez, C. Louembet, F. Gavilan, and R. Vazquez, "An event-triggered predictive controller for spacecraft rendezvous hovering phases", in *21st IFAC Symposium on Automatic Control in Aerospace*, United Kingdom, hal-02053115v2, Aug. 2019.

[14] A. Ferrara, S. Sacone, and S. Siri, "Event-triggered model predictive schemes for freeway traffic control", *Transportation Research Part C: Emerging Technologies*, Vol. 58, Part C, pp. 554-567, Sept. 2015.

[15] A. Chakrabarty, S. Zavitsanou, F. J. Doyle, E. Dassau, "Event-triggered model predictive control for embedded artificial pancreas systems", *IEEE Transactions on Biomedical Engineering*, Vol. 65, No. 3, pp. 575-586, Mar. 2018.

[16] D. Lehmann, E. Henriksson and K. H. Johansson, "Event-triggered model predictive control of discrete-time linear systems subject to disturbances", in *2013 European Control Conference (ECC)*, Switzerland, pp. 1156-1161, 2013.

[17] H. Yang, X. Guo, L. Dai, and Y. Xia, "Event-triggered predictive control for networked control systems with network-induced delays and packet dropouts", *International Journal of Nonlinear Control*, Vol. 28, No. 4, pp. 1350-1365, Mar. 2018.

[18] X. Yin, and D. Yue, "Model-based event-triggered predictive control for networked systems with communication delays compensation", *International Journal of Robust and Nonlinear Control*, Vol. 25, No. 18, pp. 3572-3595, Dec. 2015.

[19] C. Peng, M. Wu, X. Xie, and Y. -L. Wang, "Event-triggered predictive control for networked nonlinear systems with imperfect premise matching", *IEEE Transactions on Fuzzy Systems*, Vol. 26, No. 5, pp. 2797-2806, Jan. 2018.

[20] V. Lechappe, E. Moulay, F. Plestan and Q. -L. Han, "Discrete predictor-based event-triggered control of networked control systems", *Automatica*, Vol. 107, pp. 281-288, Sept., 2019.

[21] D. Wu, X. -M. Sun, C. Wen, and W. Wang, "Redesigned predictive event-triggered controller for networked control system with delays," *IEEE Transactions on Cybernetics*, Vol. 46, No. 10, pp. 2195-2206, July 2016.

[22] R. Yang and W. X. Zheng, "Output-based event-triggered predictive control for networked control systems," *IEEE Transactions on Industrial Electronics*, Vol. 67, No. 12, pp. 10631-10640, Dec. 2020.

[23] W. Fu, S. X. Yang, C. Huang, and G. Liu, "Predictive triggered control for networked control systems with event-triggered mechanism," *Cluster Computing*, Vol. 22, pp. 10185-10195, Sept. 2019.

[24] A. Gonzalez, A. Cuenca, V. Balaguer, and P. Garcia, "Event-triggered predictor-based control with gain-scheduling and extended state observer for networked control systems," *Information Sciences*, Vol. 491, pp. 90-108, July 2019.

Beheshte Sadeghi Sabzevari received her B.Sc degree in control engineering from Sharif University of Technology, Tehran, Iran in 2010 and M.Sc degree in control engineering from Ferdowsi University of Mashhad, Mashhad, Iran in 2012. She is currently a Ph.D candidate at Shahrood University of Technology. Her research interests include Optimization control, Model Predictive control and Adaptive control.

Mohammad Haddad Zarif received his PhD degree in Electrical Engineering from CITY University of London, England in 1992. He joined Department of Electrical Engineering in Shahrood University of Technology, Iran in 1994. He is now an associate professor. His research interests include classic control and optimization control.

Seyed Kamal Hosseini Sani received his B.Sc. degree in electrical engineering from Ferdowsi university of Mashhad, Mashhad, Iran, in 1995 and M.Sc. degree in control engineering from K.N.T. University of technology, Tehran, Iran, in 1998 and Ph.D. degree in control engineering from Tarbiat Modares university, Tehran, Iran, in 2006. Presently his is an associate professor of control engineering department of Ferdowsi university of Mashhad, Mashhad, Iran. His research interests are in Digital and Adaptive control, Model predictive control, Applied control, Wind turbine and Power converter systems.

International Journal of Industrial Electronics, Control and Optimization © 2022 IECO
Vol. 5, No. 1, pp. 23-30 , Jan (2022)

Identification of Switched ARX Systems Using an Iterative Weighted Least Squares Algorithm

Hamed Torabi[1, †], and Hadi Keshvri-Khor[2]

[1] Faculty of Electrical and Computer Engineering, University of Sistan and Baluchestan, Zahedan, Iran
[2] Khorasan Institute of Higher Education, Mashhad, Iran

ABSTRACT

This paper presents a new algorithm for the identification of a specific class of hybrid systems. Hybrid system identification is a challenging problem since it involves the estimation of discrete and continuous states simultaneously. Using the method known as the product of errors, this problem can be formulated such that the identification of continuous state is independent of discrete state estimation. We propose a new iterative weighted least squares algorithm (IWLS) for the identification of switched autoregressive exogenous systems (SARX). In the method, the parameters of only one subsystem are updated at each iteration while the parameters of the other subsystems are assumed known. The proposed method estimates, all four main parameters of hybrid systems, namely subsystem degrees, number of subsystems, unknown parameters vector, and the switching signal. The simulation results show that our proposed method has a good performance in identifying the parameters of the subsystems and the switching signal. Also, the superiority of our algorithm is demonstrated by modeling two SARX systems.

Article Info

Keywords:

Iterative weighted least squares, Product of error, Switched auto regressive exogenous, Switched linear systems, System identification

Article History:

Received 2021-04-06
Accepted 2021-07-29

I. INTRODUCTION

Hybrid systems are dynamic models that consist of discrete and continuous states. These systems are used when there is an interaction between physical systems and logic devices such as digital computers and can model physical phenomena that exhibit discontinuous behaviors. A hybrid system is a combination of several continuous subsystems, only one of which is active at any time instance. Continuous subsystems are connected through a discrete state variable called switching signal or discrete state. When the switching signal changes, switching occurs between the subsystems.

Since the problem of hybrid system identification involves estimating sub-model parameters and how these sub-models relate to each other with respect to the switching signal, it cannot be solved by classical identification methods, so solving this problem has gained much attention among researchers. Due to the development of applications of hybrid systems, much research has been done in the field of hybrid system identiification. The proposed methods have mostly been developed around piecewise affine (PWA) and affine switched (SA) systems. Roll et al. [1] used mixed integer linear or quadratic programming for the identification of PWA autoregressive exogenous (PWARX) systems by focusing on hinging hyperplanes in

† **Corresponding Author**: Hamed.torabi@ece.usb.ac.ir
Tel: +98-54- 31136556, Faculty of Electrical and Computer Engineering, University of Sistan and Baluchestan, Zahedan, Iran.

which the convergence to a global optimum was guaranteed. Vidal et al. [2] proposed an algebraic method for the problem of switched linear system (SLS) identification using a new error function, which is called product of errors. The identification problem of hybrid systems was simplified in a way that the estimation of sub-model parameters became independent of the discrete state estimation. Then, by applying a technique known as algebraic method, the parameters of sub-models were estimated. Juloski et al. [3] used a probabilistic method for linear hybrid system identification. In this probabilistic method, at each iteration, using prior probability distribution of the parameters and the Bayesian rule, the posterior probability distribution of the system parameters is calculated.

A bounded-error approach for PWARX system identification is discuused in [4]. Minimality and also identifiability of SARX systems are presented in [5]. The problem of identifying SARX systems when measurement data is impregnated with large amounts of noise is discussed in [6]. The problem of identifying SARX models based on assigning measurement data to a suitable subsystem based on a new robust criterion is presented in [7]. Using the Bayesian system identification method, not only does it calculate a posterior distribution on the model parameters to indicate the level of uncertainty of the estimated values, but it also automatically determines the desired number of local models [8]. An algebraic geometric method (AG) is proposed in [9] to identify ARX systems when both process and measurement are noisy. A recursive identification method is proposed in [10] for piecewise ARX models, which uses a likelihood function that adaptively fines the complexity of the model. A novel incremental algorithm has been suggested, which is based on the genetic and LOLIMOT algorithms for identification and fault detection and is of high dimension systems [11].

In this paper, we propose a new IWLS algorithm for the identification problem of switched ARX (SARX) systems using the so-called hybrid decoupling constraint method and defining the error function as the error product. Identification of SARX systems is calculated so that the subsystem parameters are estimated independent of the switch signal so that the parameters of only one subsystem are updated at each iteration while the parameters of the other subsystems are assumed to be known.

The paper is organized as follows. Section II introduces different types of linear hybrid systems. Section III explains the identification problem of hybrid systems while, in Section IV, we reformulate this problem such that the identification of continuous state becomes independent of the estimation of discrete state. Section V suggests a new method based on iterative weighted least squares for the identification of hybrid systems. The validity and superiority of the proposed method is shown in Section VI through numerical examples and simulations.

II. LINEAR HYBRID SYSTEMS

In this paper, we deal with the problem of identifying a particular class of hybrid systems. Piecewise affine systems (PWA) are a special class of hybrid systems that combine a number of affine subsystems in such a way that only one subsystem is active at a time. A discrete-time PWA system with s subsystems can be represented in the form of state space as follow:

$$\begin{aligned} x(t+1) &= A_{\sigma(t)}x(t) + B_{\sigma(t)}u(t) + b_{\sigma(t)} \\ y(t) &= C_{\sigma(t)}x(t) \end{aligned} \tag{1}$$

where $x(t) \in R^n$ is the continuous-state trajectory, $\sigma(t) \in \{1,2,...,s\}$ is a piecewise constant function called switching signal, $A_i \in R^{n\times n}$, $B_i \in R^{n\times p}$, $b_i \in R^{n\times 1}$ are the affine section of PWA system, and $C_i \in R^{q\times n}$ is the state-space matrices corresponding to the i[th] subsystem. Switching among subsystems occurs when the switching signal changes. When the switching signal changes, switching occurs between the subsystems. Switching signal changes can be determined in different ways. If the switching signal is deterministic and independent of continuous states, the system is called switched affine (SA). While in piecewise affine (PWA) systems, the discrete state is determined according to the continuous states and input variable as follows:

$$\sigma(t) = \mathrm{i} \quad \text{iff} \quad \begin{bmatrix} x(t) \\ \mathrm{u}(t) \end{bmatrix} \in \Omega_i \qquad i = 1,2,...,s \tag{2}$$

where $\{\Omega_i\}_{i=1}^{s}$ is complete partitioning of state-input space. PWA and SA systems can also be shown in the input-output form with autoregressive exogenous input (ARX) models:

$$y(t) = \sum_{j=1}^{n_a} a_j(\sigma) y(t-j) + \sum_{j=1}^{n_b} b_j(\sigma) u(t-j) + c(\sigma) \tag{3}$$

where n_a is the system degree, n_b is the input, and c is affine part in the ARX model. When the switching signal is deterministic and independent of continuous states, system (3) is called switched ARX (SARX) and if the switching signal is

determined according to the continuous states and input variable, the system is called piecewise ARX (PWARX). Eq. (3) can also be presented in the form of linear regression:

$$y(t)=\varphi^T(t)\theta_{\sigma(t)} \tag{4}$$

where $\varphi(t)$ is the extended regression vector and is defined as below:

$$\varphi(t)=\left[y(t-1)\ \cdots\ y(t-n_a)\ u(t-1)\ \cdots\ u(t-n_b)\ 1\right]^T \tag{5}$$

and θ_i is the vector of parameters for the i[th] subsystem.

III. HYBRID SYSTEM IDENTIFICATION PROBLEM

In the previous sections, different linear hybrid systems were introduced. Since SARX systems are more common than other linear hybrid systems, we focus on identifying SARX systems. The general problem of identifying SARX systems can be summarized as follows [2], [6].

Given the input-output data pairs, $\{(u(t),y(t))\}_{t=1}^{N}$ estimates:

1. Subsystem degrees, n_a and n_b
2. Number of subsystems s.
3. Unknown parameters vector, θ_i for each subsystem $i=1,2,\ldots,s$.
4. Discrete state or switching signal $\sigma(t)$ for $t>\max\{n_a,n_b\}$.

IV. ERROR PRODUCT METHOD

As mentioned, in the problem of identifying hybrid systems, not only the number of subsystems and the degree of the subsystems but also the switching signal and subsystem parameters must be estimated. As a result, it must be determined that each input/output data pair belongs to which subsystem and the system parameters are changed to approximate the data behavior. Conventional methods start using the clustering algorithm in all regression vector columns, and a linear model is embedded for each data cluster. The identification error in SARX systems is as follows:

$$\varepsilon(t)=\min_i\left\{\left|y(t)-\varphi^T(t)\theta_i\right|\right\}\quad i=1,2,3,\ldots,s \tag{6}$$

The cost function could be presented as the sum of errors as follows:

$$\begin{aligned}V_N(\theta,Z^N)&=\sum_{t=1}^{N}\ell(\varepsilon(t))\\&=\sum_{t=1}^{N}\ell\left(\min_i\left\{\left|y(t)-\varphi^T(t)\theta_i\right|\right\}\right)\end{aligned} \tag{7}$$

where $\ell(\cdot)$ is a real positive function. For example, $\ell(\cdot)$ could be a quadratic or absolute value function. In order to minimize the cost function (7), the parameters of s hyperplanes should be determined such that each data pair is near to, at least, one hyperplane. We define the error function for all sub-models as (8).

$$\varepsilon_i(t)=y(t)-\varphi^T(t)\theta_i\quad i=1,2,\ldots,s \tag{8}$$

where $\varepsilon_i(t)$ shows the prediction error of the t[th] data pair with the i[th] sub-model. If the output prediction errors defined in (8) are multiplied by each other, an error function called the error product is obtained as (9).

$$\begin{aligned}\varepsilon(t)&=\prod_{i=1}^{s}\ell_i(\varepsilon_i(t))\\&=\prod_{i=1}^{s}\ell_i\left(y(t)-\varphi^T(t)\theta_i\right)\end{aligned} \tag{9}$$

where $\ell_i(\cdot)$ is a norm function related to the i[th] subsystem [2],[6]. According to (9), different norms can be defined for the error of each subsystem. When describing the identification method, the advantage of being able to choose different norms will be discussed in Section V. The most important result of the error function (9) is that the cost function for the problem of identifying SARX systems can be defined as follows:

$$V_N(\theta,Z^N)=\frac{1}{N}\sum_{t=1}^{N}\prod_{i=1}^{s}\ell_i\left(y(t)-\varphi^T(t)\theta_i\right) \tag{10}$$

According to (10), it can be concluded that the identification of SARX systems is equivalent to the determination of s hyperplanes where each hyperplane represents a subsystem. To minimize the cost function (10), the output $y(t)$ should only be close to one of the hyperplanes. In this case, the distance between $y(t)$ and the hyperplane is zero (or a small amount), and multiplying it by other distances reduces the error e(t). The most important advantage of the cost function (10) rather than (7) is that there is no need to cluster the data and determine which subsystem is responsible for

producing the t[th] data while by minimizing cost function (10), unknown parameters θ_i can be estimated independently of the switching signal.

V. Proposed Method for PWARX Identification

In this section, a new method is proposed for identifying SARX systems. The advantage of this method over other methods is its simplicity in solving and low volume of calculations. We rewrite the cost function as follows:

$$V_N\left(\theta,Z^N\right)= \left\| \begin{matrix} \ell_1\left(y(1)-\varphi^T(1)\theta_1\right)\times \ell_2\left(y(1)-\varphi^T(1)\theta_2\right)\times\cdots\times \ell_s\left(y(1)-\varphi^T(1)\theta_s\right) \\ \ell_1\left(y(2)-\varphi^T(2)\theta_1\right)\times \ell_2\left(y(2)-\varphi^T(2)\theta_2\right)\times\cdots\times \ell_s\left(y(2)-\varphi^T(2)\theta_s\right) \\ \vdots \\ \ell_1\left(y(N)-\varphi^T(N)\theta_1\right)\times \ell_2\left(y(N)-\varphi^T(N)\theta_2\right)\times\cdots\times \ell_s\left(y(N)-\varphi^T(N)\theta_s\right) \end{matrix} \right\| \quad (11)$$

Minimizing the cost function (10) is an easy problem, assuming that only the i[th] hyperplane is unknown. The above cost function with the vector of parameters θ_j for $j\neq i$ is as follows:

$$V_N^i\left(\theta,Z^N\right)= \left\| \begin{matrix} W_i(1)\times \ell_i\left(y(1)-\varphi^T(1)\theta_i\right) \\ W_i(2)\times \ell_i\left(y(2)-\varphi^T(2)\theta_i\right) \\ \vdots \\ W_i(N)\times \ell_i\left(y(N)-\varphi^T(N)\theta_i\right) \end{matrix} \right\| \quad (12)$$

where $V_N^i\left(\theta,Z^N\right)$ is the cost function that specifies only unknown parameters when other parameters are known, and $W_i(t)$ determines the weight of the t[th] data and is defined as:

$$W_i(t)=\prod_{\substack{j=1\\ j\neq i}}^{N}\ell_j\left(e_j(t)\right)=\prod_{\substack{j=1\\ j\neq i}}^{N}\ell_j\left(y(t)-\varphi^T(t)\theta_j\right) \quad (13)$$

What is interesting about cost function (12) is that if all weight values $W_i(t)$ are equal, the identification problem will be a prediction error method (PEM) in which case $W_i(t)$ weights will not be equal and the problem is converted to weighted PEM (WPEM). In fact, while only one sub-model is unknown and the other is known, the product of the errors is small and the corresponding weights are small for those data determined by known sub-models, so it has little effect on unknown parameters estimation. On the other hand, data not generated by known sub-models have the greatest impact on the optimization problem because the corresponding weights have significant values. The advantage of being able to choose different norms $\ell_i(\cdot)$ is that by choosing 2-norm, the problem becomes the problem of weighted least squares (WLS), so it can be easily solved by conventional analytical methods. The analytical solution of the cost function (12) is obtained as:

$$\hat{\theta}_i=\left[R(N)\right]^{-1}f(N) \quad (14)$$

$$R(N)=\frac{1}{N}\sum_{t=1}^{N}W_i(t)\varphi(t)\varphi^T(t) \quad (15)$$

$$f(N)=\frac{1}{N}\sum_{t=1}^{N}W_i(t)\varphi(t)y(t) \quad (16)$$

In this condition, other norms $\ell_j(\cdot)$ for $j\neq i$ can have different choices depending on the type of problem. The suitable choice of norms $\ell_j(\cdot)$ for $j\neq i$ can affect the rate of algorithm convergence and stability of system [6].

VI. Suggested Algorithm

By choosing an appropriate norm $\ell_i(\cdot)$ for $j\neq i$ and acceptable value for prediction error ε and by assuming that the number of subsystems and their degrees are known, the following algorithm is proposed for SARX system identification. The degrees of all subsystems are assumed equal.

1- Let

$t=1:N$ and $i=1:s$, $\varepsilon_i(t)=1$ and $k=0$

2- Let

$k=k+1$ and i is the reminder of k divided by s

3- Update $W_i(t)$ using Eq. (13).

4- Update θ_i according to Eq. (14-16).

5- Update error vector $\varepsilon_i(t)$ by Eq. (8).

6- Repeat steps 2-5 until condition (17) is met:

$$\frac{1}{N}\sum_{t=1}^{N}\left\|\min_i\left\{y(t)-\varphi^T(t)\theta_i\right\}\right\|\leq\lambda \quad (17)$$

$\lambda=0.01$, After determining the sub-model parameters, the switching signal is calculated by solving the following equation.

$$\sigma(t)=\arg\min_i\left\{\left|y(t)-\varphi^T(t)\theta_i\right|\right\}\quad i=1,2,...,s \quad (18)$$

VII. Numerical Examples and Simulations

Two different systems have been used to evaluate the accuracy and efficiency of the proposed method.

A. *Example* 1

Assume that the input-output data pair $\{(x(t), y(t))\}_{t=1}^{71}$ is generated by the system [4,8].

$$y(t)=\begin{cases}\begin{bmatrix}1 & 0.5\end{bmatrix}\begin{bmatrix}x(t)\\ 1\end{bmatrix}+\upsilon_1, & \text{if } x\in[-5,-2)\\ \begin{bmatrix}-0.5 & 0\end{bmatrix}\begin{bmatrix}x(t)\\ 1\end{bmatrix}+\upsilon_2, & \text{if } x\in[-2,2)\end{cases} \quad (19)$$

in which 30 points on the interval $[-5,-2)$ and 41 points on the interval $[-2,2)$ with uniform distribution are generated. The outputs are computed using model (19) and υ_1 and υ_2 indicate noise with the zero mean and uniform distribution on intervals $[-0.8,0.8]$ and z, respectively. The generated data from system (19) is illustrated in Fig. 1.

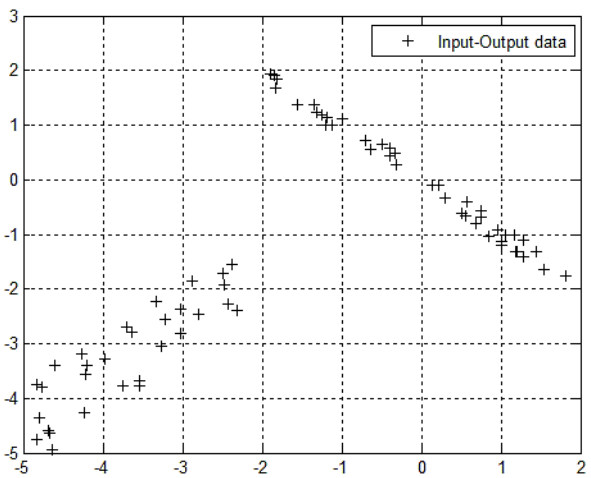

Fig. 1. Input/output data.

The sub-models obtained in the first iteration after applying the proposed algorithm to the data are shown in Fig. 2, which uses the Euclidean norm as the selected norm.

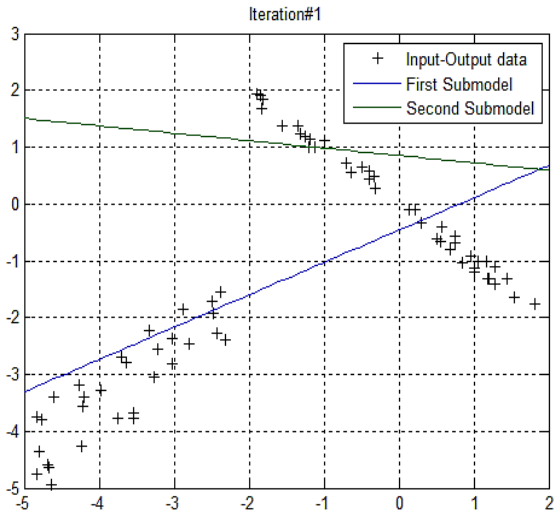

Fig. 2. The models obtained after the first iteration

Because of the weighting, the values are initially equal to one, the first sub-model tries to model all the data as shown in Fig. 2. After the first model is determined, the parameters of the second model are determined. Since the weight values have changed, the data that are far from the first model have a higher weight and more importance. Figs. 3 and 4 show how these sub-models have changed in the second and third iterations of the algorithm, and only after three iterations, the values of the parameters tend to their actual values. The model can predict the output as shown in Fig. 4. The values estimated for the switching signal are shown in Fig. 5.

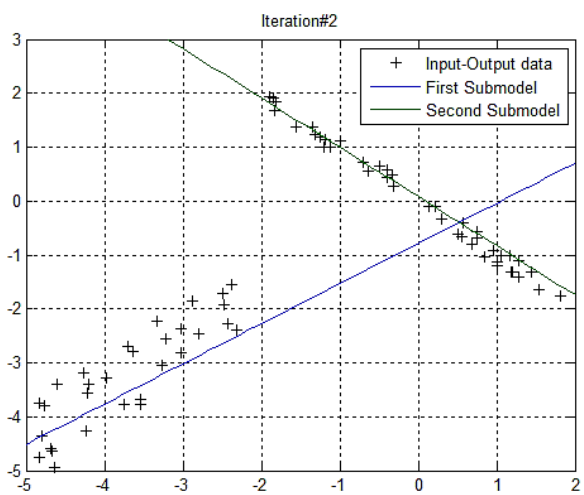

Fig. 3. Subsystem models after the second iteration.

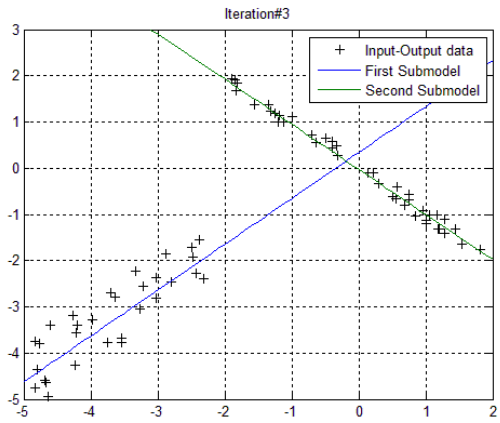

Fig. 4. Subsystem models after the third iteration.

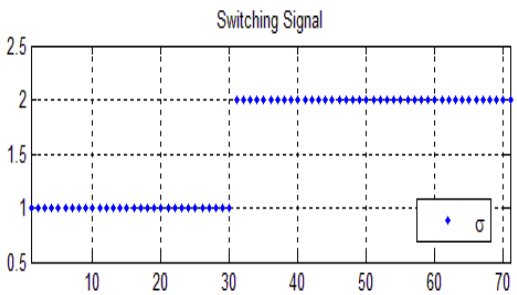

Fig. 5. The values estimated for the discrete signal.

B. Example 2

To compare the method proposed in this paper with other methods in identifying the hybrid system, the simulation results are compared with the method presented in [2]. The reason for choosing a reference [2] for comparison is that the method used in this reference is based on the product of errors and polynomial factors. Proposing a simple iterative least-squares weight algorithm to estimate the parameter of SARX systems is a novelty of our method in this paper compared to the reference method [2]. In addition, the cost function used in [2] is the same as Eq. (10) with the choice of 1-norm ($\ell_i(\varepsilon)=|\varepsilon|$) as the selective norm, while in the method proposed in this paper, the selective norm can be adjusted according to different conditions. Proper selection of the selected norm leads to a robust algorithm against outliers. Each linear system is defined as follows:

$$y(t)=a_1(\sigma(t-1))y(t-1)+a_2(\sigma(t-1))y(t-2)+c_1(\sigma(t-1))u(t-1)+e(t) \quad (20)$$

where $\sigma(t)\in\{1,2,3\}$ is the switching signal and is determined after 1000 iterations as below:

$$\sigma(t)=\begin{cases}1 & 1\le t\le 30\\ 2 & 31\le t\le 60\\ 3 & 61\le t\le 100\end{cases} \quad (21)$$

Parameters were randomly selected and simulations were performed on 1000 SARX systems. The parameters a_1 and a_2 are selected in each experiment for each of the three sub-models such that the complex digital poles are evenly distributed on the wall $0.8\le\|z\|\le 1$. Fig. 6 shows the location of complex poles in the ring.

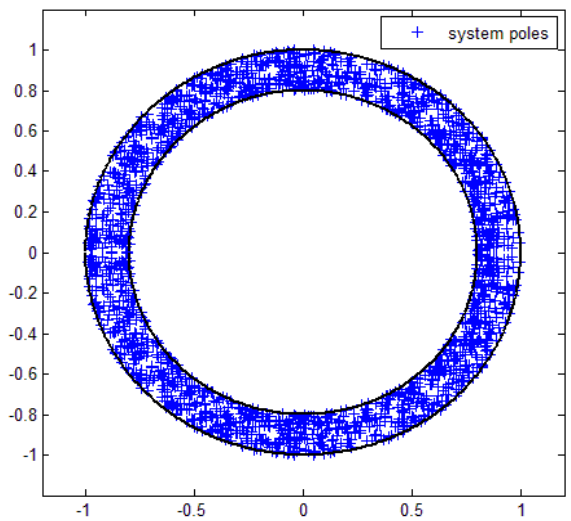

Fig. 6. The location of the system poles.

Parameter c_1 is also determined randomly in each trial and for each of the three linear sub-models with zero mean, unit variance, Gaussian distribution. The initial values of the continuous states are randomly chosen with zero mean Gaussian distribution and variance $\sum=I_2$ for each trial. The measurement noise $e(t)$ is a white noise with zero mean and variance σ_e. To investigate the effect of noise on the identification method, the problem is repeated five times with different values of σ_e. The results of the comparison between the method presented in this paper (IWLS) with the method presented in [2], which is a polynomial factorization algorithm (PFA) and a polynomial differentiation algorithm (PDA), are shown in Fig. 7-9. At each trial, and for each sub system, the error between real parameters of the system (a_1,a_2,c_1) and estimated parameters $(\hat{a}_1,\hat{a}_2,\hat{c}_1)$ is determined as $\|(a_1,a_2,c_1)-(\hat{a}_1,\hat{a}_2,\hat{c}_1)\|_2$, and the mean error is

obtained with averaging on 1000 trials and 3 sub-systems. Fig. 7 illustrates the mean error of sub model parameters. In each experiment and for each subsystem, the error between the actual system parameters (a_1, a_2, c_1) and the estimated parameters $(\hat{a}_1, \hat{a}_2, \hat{c}_1)$ is determined as $\|(a_1, a_2, c_1) - (\hat{a}_1, \hat{a}_2, \hat{c}_1)\|_2$ and the mean of the error is obtained by averaging over 1000 experiments and three subsystems. Fig. 7 shows the mean error of the submodel parameters.

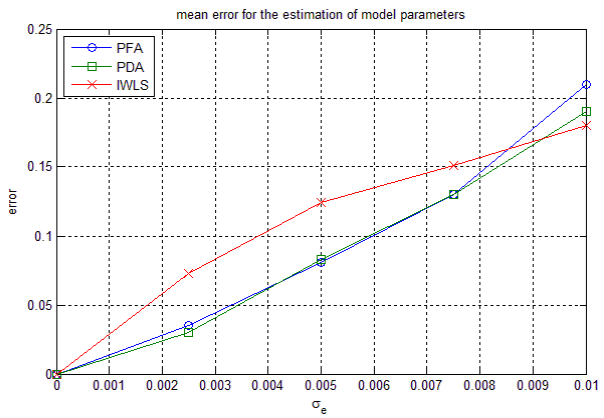

Fig. 7. The mean error of the estimated parameters.

Fig. 8 demonstrates the mean error of output prediction. At each trial, the output prediction error is determined as $\sum_{t=1}^{100} |y(t) - \hat{y}(t)|$, and the mean error is obtained by averaging on 1000 trials.

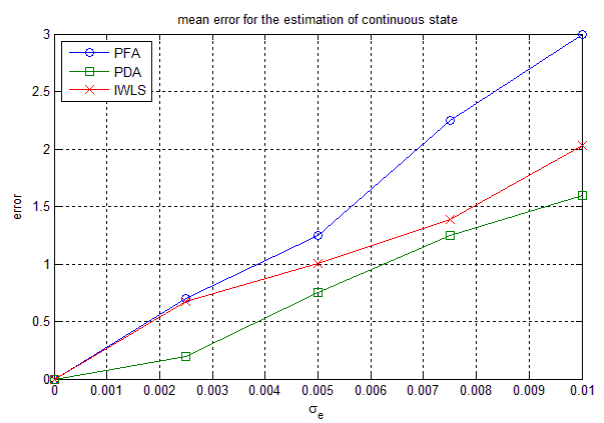

Fig. 8. The mean error for the output prediction.

The mean error of switching signal estimation is shown in Fig. 9. The mean error of switching signal estimation is calculated by dividing the number of cases in which the switching signal is incorrectly estimated in all cases. As shown in Fig. 7, the method proposed in this paper shows a little more error in estimating the subsystem parameters but has less error in output prediction compared to PDA and more than PFA as shown in Fig. 8. Finally as shown in Fig. 9, the error of the proposed method in estimating the switching signal is much less than PDA and PFA methods.

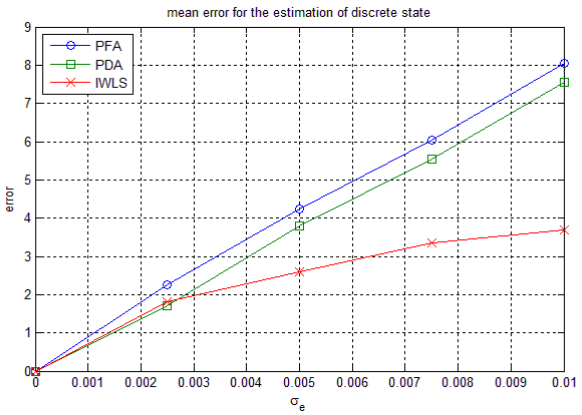

Fig. 9. The mean error of the estimation of switching signal.

CONCLUSION

This paper presented a new method for identifying SARX systems. Using a method called the product of errors, the cost function for identifying SARX systems is defined in such a way that the continuous state estimation is independent of the discrete state estimation. An iterative least squares weight method is also proposed to estimate the sub-model parameters, in which only one sub-model is unknown and the other models are assumed known in each iteration, so the cost function can be easily solved analytically. To show the effectiveness and superiority of the proposed method in identifying SARX systems, simulations and numerical examples were given.

REFERENCES

[1] J. Roll, A. Bemporad, and L. Ljung, "*Identification of piecewise affine systems via mixed-integer programming*," *Automatica*, vol. 40, no. 1, pp. 37-50, 2004.

[2] R. Vidal, S. Soatto, Y. Ma, and S. Sastry, "*An algebraic geometric approach to the identification of a class of linear hybrid systems*," in *42nd IEEE International Conference on Decision and Control (IEEE Cat. No. 03CH37475)*, vol. 1: IEEE, pp. 167-172, 2003.

[3] A. L. Juloski, S. Weiland, and W. Heemels, "*A Bayesian approach to identification of hybrid systems*," *IEEE Transactions on Automatic Control*, vol. 50, no. 10, pp. 1520-1533, 2005.

[4] A. Bemporad, A. Garulli, S. Paoletti, and A. Vicino, "*A bounded-error approach to piecewise affine system*

identification," *IEEE Transactions on Automatic Control*, vol. 50, no. 10, pp. 1567-1580, 2005.

[5] M. Petreczky, L. Bako, S. Lecoeuche, and K. Motchon, *"Minimality and identifiability of discrete-time SARX systems*," *arXiv preprint arXiv:2002.01818*, 2020.

[6] S. Hojjatinia, C. M. Lagoa, "*Identification of switched autoregressive exogenous systems from large noisy datasets*," *International Journal of Robust and Nonlinear Control*, vol. 30, no. 15, pp. 5777-5801, 2020.

[7] Z. Du, L. Balzano, and N. Ozay, "*A robust algorithm for online switched system identification*," *IFAC-PapersOnLine*, vol. 51, no. 15, pp. 293-298, 2018.

[8] Y. Lu, S. Khatibisepehr, and B. Huang, "*A variational Bayesian approach to identification of switched ARX models*," in *53rd IEEE Conference on Decision and Control*,: IEEE, pp. 2542-2547, 2014.

[9] S. Nazari, B. Rashidi, Q. Zhao, and B. Huang, "*An iterative algebraic geometric approach for identification of switched arx models with noise*," *Asian Journal of Control*, vol. 18, no. 5, pp. 1655-1667, 2016.

[10] P. Mattsson, D. Zachariah, and P. Stoica, "*Recursive identification method for piecewise ARX models: A sparse estimation approach*," *IEEE Transactions on Signal Processing*, vol. 64, no. 19, pp. 5082-5093, 2016.

[11] M. Teshnehlab and M. Aliyari-shore-deli, "*Fault detection and identification of high dimensionsystem by GLOLIMOT*," International journal of Industrial Electronics, Control and Optimization, vol. 2, no. 4, pp.331 -342, 2019.

Hamed Torabi received the B.S degree from Sistan and Baluchestan University, Iran, the MSc from the University of Science and Technology of Iran and the Ph.D. from Ferdowsi University of Mashhad, Iran in Electrical and Control Engineering. He is currently an Assistant Professor with University of Sistan and Baluchestan, Zahedan, Iran. His research interests cover the estimation and Kalman filter, system identification and control.

Hadi keshvari-khor was born in Mashhad, Iran, in 1983. He received the B.S., M.Sc. and Ph.D. degrees in Electrical and control Engineering from Ferdowsi University of Mashhad, Iran, in 2007, 2010 and 2017 respectively. In 2010, he joined Khorasan Institute of Higher Education, Mashhad, Iran, where he is currently an Assistant Professor. Currently he is the Chairman of the Board of Directors of the Abzarazma instruments Co, Mashhad, Iran. His research interests include the hybrid and switched systems, system identification, and process automation.

International Journal of Industrial Electronics, Control and Optimization © 2022 IECO
Vol. 5, No. 1, pp. 31-42 , Jan (2022)

3LEE: A 3-Layer Effort Estimator for Software Projects

Amin Moradbeiky [1], Vahid Khatibi Bardsiri [2,†], and Mehdi Jafari [3]

[1,2] Department of Computer Engineering, Faculty of Science, Kerman Branch, Islamic Azad University, Kerman, Iran
[3] Department of Electrical Engineering, Faculty of Engineering, Kerman Branch, Islamic Azad University, Kerman, Iran

ABSTRACT

Managing software projects due to its intangible nature is full of challenges when predicting the effort needed for development. Accordingly, there exist many studies with the attempt to devise models to estimate efforts necessary in developing software. According to the literature, the accuracy of estimator models or methods can be improved by correct application of data filtering or feature weighting techniques. Numerous models have also been proposed based on machine learning methods for data modeling. This study proposes a new model consisted of data filtering and feature weighting techniques to improve the estimation accuracy in the final step of data modeling. The model proposed in this study consists of three layers. Tools and techniques in the first and second layers of the proposed model select the most effective features and weight features with the help of LSA (Lightning Search Algorithm). By combining LSA and an artificial neural network in the third layer of the model, an estimator model is developed from the first and second layers, significantly improving the final estimation accuracy. The upper layers of this model filter out and analyze data of lower layers. This arrangement significantly increased the accuracy of final estimation. Three datasets of real projects were used to evaluate the accuracy of proposed model, and the results were compared with those obtained from different methods. The results were compared based on performance criteria, indicating that the proposed model effectively improved the estimation accuracy.

Article Info

Keywords:
Development Effort Estimation, Lightning Search Algorithm, Neural Networks, Software Project

Article History:
Received 2021-09-14
Accepted 2021-12-30

I. INTRODUCTION

Software effort estimation is directly related to the development and success of software project, consequently, this estimation is considered as a major challenge for researchers and the practitioners in software industry. Estimation methods are divided of algorithmic and non-algorithmic categories [1], the first is based on mathematical and the second on heuristic and metaheuristic methods.

In both methods, usually a model is devised a number of tools and algorithms proposed to estimate of the software development effort. In each one of these models, tools and algorithms are combined in their unique sense to provide a precise estimate of the software development effort. Some of these tools or algorithms are applied as an intermediate tool to increase the accuracy of the method. The following studies support this claim in increasing the accuracy of the neural network:

- Neural networks are one of the most commonly adopted methods in AI; Elman's neural network is applied in [2] for software development effort estimation.
- Rankovic and et al. [3] proposed four new models based on artificial neural network and they utilized five datasets to test them.
- Kumar and et al. [4] used neural networks to deep learning in software effort estimation.
- The dilation-erosion-linear perceptron was introduced in 2012,and is applied in many articles for prediction, but if there exists complexity of input/output then, it will not be sufficient. Araujo et al.[5] optimized the structure of this

[†]**Corresponding Author**: ampayam@yahoo.com
Tel: +98-9153432720, Department of Computer Engineering, Faculty of Science, Kerman Branch, Islamic Azad University, Kerman, Iran

perceptron, using the descending gradient in the learning process, and used it in software effort estimation.
- A combination of satin bowerbird optimization algorithm (SBO) and the Neuro-fuzzy (ANFIS) is applied to increase the accuracy in predicting software error [6].

A number of researchers seek to increase the accuracy of the Analogy Based Estimation (ABE) method through different tools, or use ABE as a tool to increase the accuracy of the other tools:
- ABE method has been commonly used for software effort estimation by researchers. The differential equation (DE) algorithm is applied in similarity function to weight the features, named Differential evolution in Analogy-Based Estimation (DABE) [7], to improve the efficiency of this method.
- There exists no exact definition on projects similarity. A similarity region is identified by [8] for feature selection in similar projects through Case-Based Reasoning (CBR) concept.
- One of the algorithms combined through ABE methods is genetic algorithm [9].
- Application of Particle swarm optimization (PSO) algorithm to increase ABE precision [10] and a hybrid model from PSO and simulated annealing algorithm to improve ABE performance [11] is proposed.

Fuzzy logic-based tools and technique combination with other methods are used in some studies for performance and accuracy improvement:
- The estimation model (EM) proposed by [12] is to divide the projects into categories with similar distribution parameters, followed by adopting the fuzzy method are used in estimation and is applied from the firefly algorithm in the rule-base system for selection.
- effective parameters on the estimation are proposed by [13], where attempt is made to increase precision through the fuzzy method.
- A combination of two algorithmic and non-algorithmic methods COCOMO and NEURO-Fuzzy is applied in [14], where the accuracy of the estimation increased by sending the outputs of NEURO-Fuzzy to the COCOMOII.
- Idri and et al. assessed the effect of missing data (MD) techniques on ABE and fuzzy-analogy. [15].
- Usually the fuzzy logic is applied in solving error prediction problem because it can perform with incomplete data, while the main problem is the great volume of rules which slowed the decision making process. Attempt is made by [16] reduce this volume by applying fuzzy controllers instead of fuzzy logic.
- Karimi and Gandomani used a combination of differential evolution algorithm and fuzzy-neural network for Software development effort estimation modeling [17].
- Chhabra and Singh used optimizing design of fuzzy model for software effort estimation using particle swarm optimization algorithm [18].

Some researchers only use tools based on algorithmic methods:
- The COCOMO, proposed by [19], the COCOMOII, proposed by [20], SLIM, proposed by [21], Function Point Analysis, proposed by[22] and Dotti model proposed by [23].
- The regression-based methods like: linear regression methods [24, 25], non-linear regression methods [25], tree regression methods [26, 27].

Artificial intelligence algorithms can improve the efficiency of formulated methods by searching for the appropriate configuration for these methods [28]. This approach has been followed in some articles:
- Updated K-modes clustering basic algorithms are applied in effort prediction. in the proposal model by [29] the Beysian belief network is constructed from of the COCOMO model, where the intervals are of fuzzy numbers, then, the PSO algorithm and Genetic algorithm (GA) are combined to improve the software effort estimation.
- Machine learning algorithms are commonly applied in problem estimation Two different types of Support Vector Machine (SVM) are applied by [30] to predict effort and compare with the other methods like neural networks, decision tree etc. Various feature selection methods have also been used to performance optimization of machine learning based methods [31].
- Meta-heuristic algorithms are commonly applied by researchers in many cases. A hybrid Meta-heuristic algorithm, consisting of Cuckoo Optimization Algorithm (COA), Harmonic Search [32], and DE algorithm is applied to optimizing COCOMO parameters [33], and to improve software effort estimation.

Some studies emphasize identifying key project features and their relationship with the software development effort. There has been an emphasis on identifying interrelated features influencing the software development effort [34]. Features influencing effort has been identified by a neural network [35]. The PSO algorithm [36] and the Bayesian technique [37] have been used to identify features influencing the software development effort.

A novel model is proposed in this study by analyzing models previously presented in the literature. Data preparation tools have been proposed in some studies to improve the estimation accuracy. Some studies have emphasized the different effectiveness of various project features on the software development effort, and attempts have made to propose a model to exactly estimate the effort considering project features and effectiveness of different features. The effectiveness has been defined as a coefficient in the literature. Data modeling by machine learning methods has also been performed in some studies. Accordingly, in the

proposed model, various separately used techniques and tools in the literature for improving the estimation accuracy were adopted in a model with separate layers. Each layer in this model increases the accuracy of the next layer. Simply speaking, the output of each layer in this model is input to the next layer, improving the final performance of the proposed model.

Table I
Various methods in software effort estimation

Study	Year	Dataset	Evaluation Method	Method	Ref No.
1	2019	21 Project(1 Dataset)	MMRE, Pred, MSE	ANN	[2]
2	2021	COCOMO, NASA, Kemerer	MAE, Pred, MMRE	ANN	[3]
3	2017	ISBSG, Albrecht, Kemerer	MMRE, Pred	ANFIS	[6]
4	2007	CF, DPS	MMRE, Pred, MdMRE	ABE	[9]
5	2012	CF, DPS, ISBSG	MMRE, Pred	PSO, ABE	[10]
6	2019	Desharnais, COCOMO	MMRE, Pred	Firefly algorithm	[12]
7	2019	4 Project(1 Dataset)	MMRE, VAF	Fuzzy	[13]
8	2018	COCOMO	MMRE	Neuro fuzzy	[14]
9	2021	Kemerer, Albrecht	MMRE, Pred	ANFIS	[17]
10	2020	COCOMO	MMRE, Pred	PSO, Fuzzy	[18]
11	2016	COCOMO	MMRE	Bayesian network	[29]
12	2018	ISBSG	MAE	SVR	[30]
13	2017	COCOMO	MMRE	Cuckoo Search	[32]
14	2018	COCOMO	MMRE, Pred, MAE	DE	[33]
15	2020	ISBSG, Desharnais	MMRE, Pred	ACO, ABE	[38]

Section II discusses the ABE method used for estimating the software development effort. Section III introduces criteria for calculating the accuracy of the proposed model. Section IV introduces the proposed model. Section V discusses a cross validation method for evaluating the stability of the proposed model results. Section VI introduces three datasets of real projects used for testing the proposed model. Section VII introduces techniques compared with the proposed model. Section VIII presents the test results of the proposed model. The model results are analyzed in Section IX.

II. ANALOGY-BASED ESTIMATION METHOD (ABE)

Estimation methods are of the two algorithm and non-algorithm. Because the first methods are not appropriate to be adopted in dynamic environment of software projects, the second methods are applied in this context, making ABE one of the most applicable methods. ABE method is adopted in the unspecified value estimation of single feature (i.e. effort or cost) of one project. The steps of this method are described in the following sub-sections.

A. Similarity Function

The similarity of projects through studying features with certain value(s) is determined through this function. For this purpose, the following Euclidean, Eq. 3 and Manhattan Eq. 4 similarity determination methods are applied. The project features include both the digit and non-digit groups. With respect to the digit features, in both the methods, the space of digit features is estimated for the project's difference estimation. With respect to the non-digit features, the level of difference is set at 0 or 1. These methods differ in the digit feature value space estimation context, where, the P and P' statements constitute the study projects and f_i and f'_i constitute the i^{th} feature of P and P' projects, respectively. The result reveals the similarity level between the two projects.

$$\delta = 0.0001$$

$$sim(p,p') = \frac{1}{\left[\sqrt{\sum_{i=1}^{n} w_i Dis(f_i,f_i')} + \delta\right]}$$

$$Dis(f_i,f_i') = \begin{cases} (f_i - f_i')^2 & \text{if } f_i \text{ and } f_i' \text{ are numerical or ordinal} \\ 0 & \text{if } f_i \text{ and } f_i' \text{ are nominal and } f_i = f_i' \\ 1 & \text{if } f_i \text{ and } f_i' \text{ are nominal and } f_i \neq f_i' \end{cases} \quad (1)$$

$$\delta = 0.0001$$

$$sim(p,p') = \frac{1}{\left[\sum_{i=1}^{n} w_i Dis(f_i,f_i') + \delta\right]}$$

$$Dis(f_i,f_i') = \begin{cases} |f_i - f_i'| & \text{if } f_i \text{ and } f_i' \text{ are numerical or ordinal} \\ 0 & \text{if } f_i \text{ and } f_i' \text{ are nominal and } f_i = f_i' \\ 1 & \text{if } f_i \text{ and } f_i' \text{ are nominal and } f_i \neq f_i' \end{cases} \quad (2)$$

B. Solution Function

This function is applied in the effort estimation of one project according to the effort of k projects with more similarities.

$$C_p = \sum_{k=1}^{K} \frac{Sim(p,p_k)}{\sum_{i=1}^{K} Sim(p,p_i)} C_{p_k} \quad (3)$$

Where, P is the project, the effort value of which is

intended to be estimated. Symbol P_i is the i^{th} project of K more similar project. Symbol C_{Pi} is a certain value to be estimated from the j^{th} more similar project.

C. The best value of K

The K value is applied in effort estimations with a high accuracy. An appropriate K value mostly depends on the study projects. If the difference in study projects is slightly high, the K value accuracy reduces, because the effective projects manifest more differences at the final stage of estimation. If the study projects are too close to one another, the low value of K results prevents the study of similar projects. The existence of these projects in the final stage is of a positive influence on the results' accuracy. This accuracy is due to a reduction in the noise rate during estimation process. Consequently, no constant value of K can be considered, thus, it is better for K to be determined in its dynamic sense.

According to the above-mentioned points, no constant value of K can be considered. Therefore, it is better for K to be determined in its dynamic sense.

III. EQUATIONS FOR ESTIMATION ERROR CALCULATION

In this section, utilized equations to evaluate the accuracy of the proposed model and compare it with other methods are introduced. These equations are commonly used for accuracy evaluation by researchers in the field. The results of equations are displayed as diagrams for better accuracy evaluation and comparison. utilized equations are presented in Equ (4 to 8), relative error (RE), magnitude of relative error (MRE), median magnitude of relative error (MdMRE), prediction percentage (PRED) and Mean of absolute error(MAE):

$$RE = \frac{Estimate - Actual}{Actual} \quad (4)$$

$$MRE = \frac{|Estimate - Actual|}{Actual} \quad (5)$$

$$MdMRE = Median(MRE) \quad (6)$$

$$PRED(X) = \frac{A}{N} \quad (7)$$

$$MAE = \frac{1}{N}\sum_{1}^{n} |Estimate - Actual| \quad (8)$$

IV. THE PROPOSED MODEL

This paper presents a new model called 3 Layer Effort Estimator (3LEE). 3LEE is composed of two sections: training and test. The training section of this model is consists of three layers, each responsible refine the data and enhance the precision of estimation. The model of layer 1 is shown in Fig (1), where, the best features are selected based on the feature selection and ABE method with several iteration. At every one of iterations, a subset of features is selected and the MdMRE error value is calculated for that set of feature. The iteration continues until the whole set of selected features end. What is obtained here a set of the best features with the highest effect on software development effort estimation, which is applied to send as an input to the next layer.

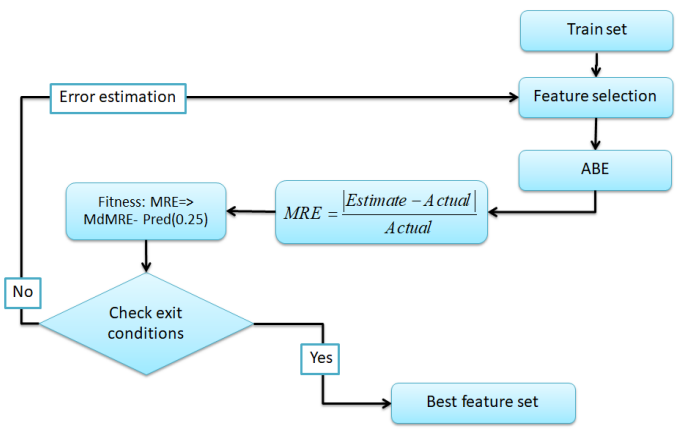

Fig. 1. The flowchart of training section model, layer 1

The layer 2 model is shown in Fig. (2). which undergoes training through the selected features as its input. This model is iterated for many times through LSA algorithm, and at each iteration the LSA algorithm suggests an appropriate setting for ABE. The ABE method processes projects and estimates them based on settings suggested by the LSA algorithm. This process runs until the estimation error reaches a specific threshold or the iterations are ended. Finally, the best setting for ABE is the result obtained through implementing the model of this layer. The obtained

settings are applied as the input for layer 3.

The second layer of the proposed model includes a hybrid model of the ABE and LSA method. The ABE method searches for the most similar projects with the target project to estimate software development effort based on features adaptation. The ABE method uses the LSA algorithm to increase estimation accuracy. The LSA algorithm tries to propose the most appropriate configuration for ABE method and helps it to provide a more accurate estimation. The configuration proposed by the LSA algorithm differs based on project conditions and its features. On the other hand, the first layer helps increase the second layer's accuracy by processing input data to the first layer. Simply speaking, higher quality data enters the second layer with the help of the first layer. The estimate obtained from the second layer is not the final estimation. In the third layer, a model is developed of the estimator of first and second layers and based on their input and output. This layer leads to improved final estimated accuracy.

The layer 3 model is shown in Fig. (3) which undergoes predicting proper estimation error based on a project's data. To estimate the prediction error, Artificial Neural Network (ANN) is applied. The proper configuration of ABE obtained in layer 2 is received as its input and best features obtained in layer 1. This layer's model is iterated through the LSA algorithm, where at each iteration, the LSA algorithm proposes proper values for b and w of ANN. Here, ANN predicts estimation error for each project and ABE estimates the effort. The resulting values are applied in Eq. 9 for estimation:

$$E_{Final}[i]=\left|E_{ABE}[i]-(Error[i]\times Th)\right| \quad (9)$$

Where, i is the number of projects, E_{ABE} is the estimation from the ABE method and Error is the error proposed by the ANN, and the *Th* coefficient is the percentage of effect of suggested error on the value of estimation. The result of this equation is the value of final estimation. In the proposed model, the third layer has very important role. This layer tries to provide a more accurate estimate of the project through building a model. The built model receives the project characteristics and the estimated amount of effort to make the estimation by using equation 9. In other words, this layer tries to get a more accurate perspective of the project status. On the other hand, the sub layers of this layer have also strengthened its accuracy by refining and providing data.

After final estimation of each project is run, the resulting value is applied in Eqs. (5, 6, 7 and 8). Consequently, the estimation error is calculated based on settings suggested by LSA algorithm. The obtained estimation error is returned to the LSA algorithm as a feedback and this process goes on until the error resulting from estimation does not reach a specific threshold or iteration of the LSA algorithm ends. This layer will provide the best settings for estimation of prediction error Through ANN. These proposed settings reduce final estimation error.

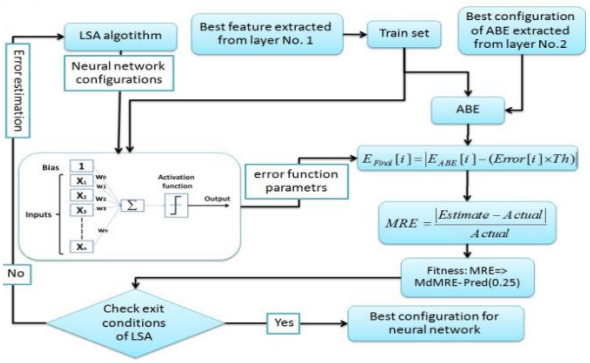

Fig. 2. The flowchart of training section model, layer 2

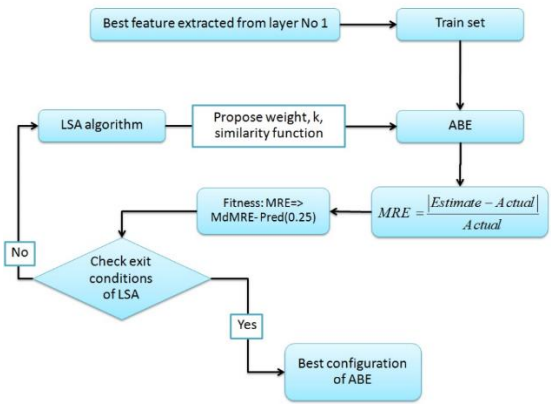

Fig. 3. The flowchart of training section model, layer 3

The test section flowchart is shown in Fig. (4), where, the set of test projects is estimated through settings proposed in layer 2 for ABE and the features specified in layer 1 based on estimation error predicted by layer 3. The MdMRE and PRED values resulting from running of this stage are considered as the estimation errors.

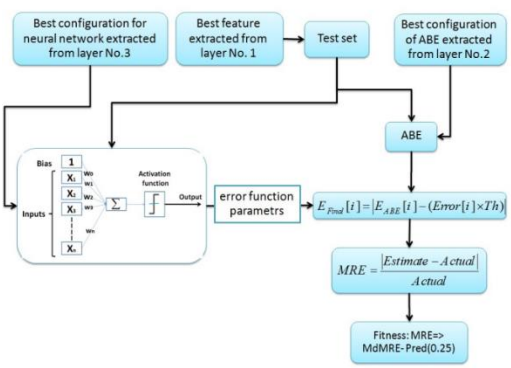

Fig. 4. The test section model flowchart

V. CROSS VALIDATION METHOD

Based on the proposed model, projects must be divided into two groups of training and test. The arrangement of projects in dividing process effects on the accuracy of the

proposed model *[39]*. For sustainability provement of the models, different cross validation methods including 3 fold, 10 fold, etc. can be used. Each one of these methods provides a specific arrangement for projects. Based on the performed study *[39]*, leave-one-out (LOO) is the best method for evaluation and its achieved accuracy is independent from arrangement of projects. In this paper, LOO method is adopted.

VI. INTRODUCING DATASETS

In testing stage of proposed model, dataset of real projects are utilized. These datasets are applied by many researchers. The details of the data analyzes of this datasets are tabulated in Table II. The desharnais dataset consists of 81 real software projects. This dataset is collected in canadian software houses. The projects in desharnais dataset are described by 11 features. In this dataset, one of the features named 'Cost' is dependent and ten other features named 'TeamExp', 'ManagerExp', 'YearEnd', 'Duration', 'Transactions', 'Entities', 'AdjFP', 'AdjFactor', 'RawFP', and 'Dev.Env' are independent. In this paper, only 77 projects of this dataset are used for tests because the other 4 projects have defective data.

The maxwell dataset contains data on 62 real software projects. There is one dependent feature called 'effort' and 25 independent features indexed from 1 to 25 in this dataset.

The cocomo dataset contains data on 63 real software projects. The independent features are 'rely', 'data', 'cplx', 'time', 'stor', 'virt', 'turn', 'acap', 'aexp', 'pcap', 'vexp', 'lexp', 'modp', 'tool', 'sced', and 'loc', also 'actual' is the only dependent feature in this dataset.

Table II
Datasets

Name	Number of sample	Number of features	Mean(effort)
COCOMO	63	17	683
Desharnais	77	10	4795
Maxwell	62	26	8223

VII. TECHNIQUES

This proposed model is compared with the following methods for evaluating accuracy:

- Ordinary Least Squares (OLS): this method is based on the regression and the best line of regression.
- Robust Regression (ROR): ROR uses regression for estimation. This method utilizes weighting to increase estimation accuracy in unusual data [40].
- Multivariate Adaptive Regression Splines (MARS): is a non-linear and non-parametric regression method indicative of some interesting features like ease in interpretation, the ability to model complex non-linear correlation, with a rapid output [41].
- Classification and Regression Tree (CART): One of the commonly used methods for data classification is the CART method. The CART method adopts decision tree for data classification [42].
- M5: The M5 method utilizes modeling technique for data estimation and the developed model has a tree structure. This method separately computes a linear regression for each leaf in the developed tree model. [43].
- Multi Layered Perceptron (MLP): Neural network is a non-linear modeling technique. Multi Layered Perceptron-based neural network is applied by many researches. This method is based on a network of neurons in an input layer, one or more hidden layers and an output layer [44].
- Case based learning reasoning (CBR): The CBR operator search for the most similar sample to the sample we intend to estimate. The similarity of samples is calculated through this method. In this method, the K determines the number of most similar samples that must be used for data estimation [45].

VIII. TESTING DATASETS

The objective of testing this model is to evaluate the degree of its precision. The tests are run on the introduced datasets. The results here are displayed and analyzed through separate dataset. Precision of this model in these tests is calculated and displayed through the criteria and equations introduced in section III. In this paper, MATLAB software has been used for modeling. The tests of the proposed model and all compared models in this paper are performed on a computer with 4th generation i5 CPU and 4GB RAM. In the configuration of LSA algorithm, the size of initial population factor and the maximum numbers of iterations are considered 50 and 150 times respectively. The adopted neural network in this study is Feedforward network. The network settings are suggested by the LSA algorithm. Determining the vector of bias values, weight, and the best number of hidden layers for neural network are the suggested configuration by the LSA algorithm. These settings have been selected based on the results of multiple experiments.

A. Desharnais dataset test

Desharnais dataset test is selected as the first, the specifications of which are presented in section VI. The MRE value obtained from implementing this proposed model is expressed in Fig. (5). The MdMRE value for this test is 0.22 and the PRED value is 0.51.

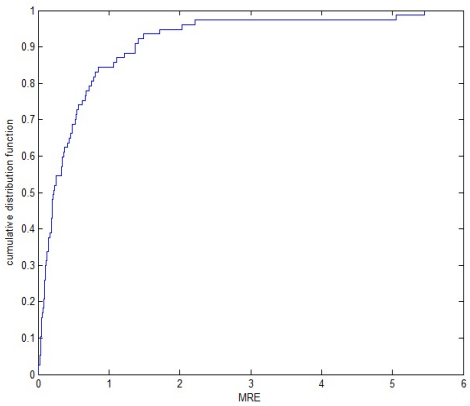

Fig. 5. MRE error frequency distribution with 3LEE model for desharnais dataset

The frequency distribution diagram of MRE error is graphed in Fig. (5), where the percentage of distribution of different values of MRE error are exposed. The horizontal axis of this graph indicates the MRE quantity. The vertical axis of this graph represents the percentage of projects with a specific MRE quantity. As observed in Fig. (5), a high percentage of errors fall within a range less than 0.5. The higher slope of this diagram in one area signifies higher percentage of error distribution within that specified range. As the graph moves toward bigger errors, its slope becomes less, even reaches zero, indicating fewer projects with low estimation accuracy.

B. COCOMO dataset test

Specifications of this dataset are presented in section VI. The MRE value obtained from implementing this proposed model is expressed in Fig. (6). The MdMRE value for this test is 0.53 and the PRED value is 0.19.

TABLE III

Comparison of MdMRE criterion in datasets

method	desharnais	maxwell	COCOMO
CART	0.35	0.45	0.77
CBR K=1	0.45	0.59	0.85
CBR K=2	0.42	0.55	0.76
CBR K=3	0.42	0.44	0.78
CBR K=4	0.38	0.52	0.78
LSSVM	0.41	0.45	1.33
M5'	0.39	0.49	0.71
MARS	0.57	0.48	3.70
MLP	0.54	0.56	0.87
OLS	0.53	0.48	4.06
ROR	0.49	0.59	0.98
PSO+ABE [10]	0.40	0.47	0.75
ACO+ABE [38]	0.36	0.48	0.75
RF [46]	0.39	0.32	1.86
3LEE	0.22	0.24	0.53

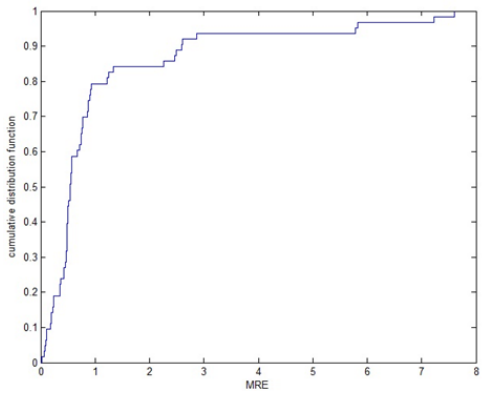

Fig. 6. MRE error frequency distribution with the 3LEE model for the COCOMO dataset

The frequency distribution diagram of MRE error for the COCOMO dataset is shown in Fig. (6), where the horizontal axis, represent the MRE quantity and the vertical axis represent the percentage of projects with a specific MRE quantity. As observed here, a high percentage of errors fall within a range of less than 1. This is obvious from figure 6. The higher slope areas of the diagram contain small errors and as the diagram moves towards bigger errors, its slope becomes less, and even reaches zero, indicating fewer projects with low estimation accuracy.

C. Maxwell dataset test

The next test is run on the maxwell dataset, specifications of which are given in section VI. The MRE value obtained from implementing this proposed model is expressed in Fig. (7). The MdMRE value for this test is 0.24 and the PRED value is 0.5.

Table IV

Comparison of Pred(0.25) criterion in datasets

method	desharnais	maxwell	COCOMO
CART	0.27	0.32	0.12
CBR K=1	0.25	0.25	0.07
CBR K=2	0.29	0.22	0.17
CBR K=3	0.29	0.29	0.07
CBR K=4	0.31	0.24	0.06
LSSVM	0.24	0.29	0.09
M5'	0.29	0.22	0.17
MARS	0.23	0.29	0.07
MLP	0.24	0.20	0.19
OLS	0.27	0.24	0.12
ROR	0.36	0.29	0.19
PSO+ABE [10]	0.40	0.29	0.09
ACO+ABE [38]	0.36	0.32	0.09
RF [46]	0.36	0.40	0.12
3LEE	0.51	0.5	0.19

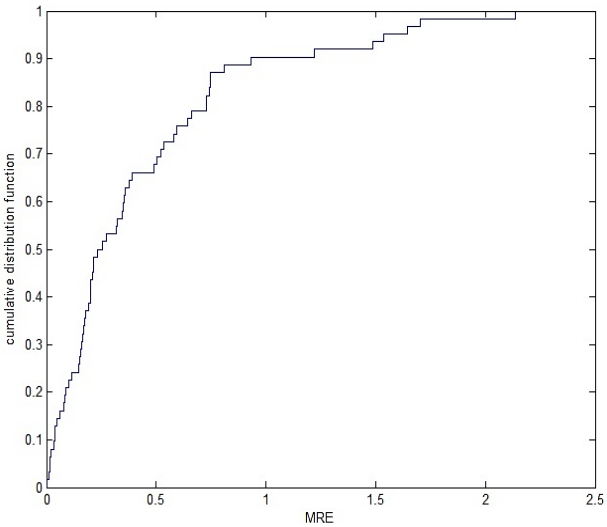

Fig. 7. MRE error frequency distribution with the 3LEE model for the maxwell dataset

The frequency distribution diagram of MRE error for the Maxwell dataset is drawn in Fig. (7), where, the horizontal axis, represent the MRE quantity and the vertical axis represent the percentage of projects with a specific MRE quantity. As observed here, about 70% of the projects are estimated with less than 0.5 error and big errors are of a small distribution.

IX. ANALYSIS AND COMPARISON OF THE RESULTS

For accuracy comparison of the proposed model with other methods, numerous tests are performed. These tests are performed on the same test conditions with the proposed model. The results of tests for comparison are shown in table III and IV. In these tables, the results of the tests are comparable with each other. The obtained results indicate the high precision of the 3LEE model. Moreover, the PRED value of the 3LEE model reveals a high precision estimations rate in this model.

This precision is due to fact that refining filters are separated which in turn increase data precision. In estimation research, in cases where data refining methods are applied, they join estimation process which leads to many problems. Combining the refinement and estimation processes lead to problems for the model leading to less precision in the results. In the early tests run, here refinement and estimation are run in a simultaneous manner making the results hardly precise. However, when the stages are defined and implemented in separate layers, the precision of the results face drastic changes.

Another reason for high precision of the results here is the predictive contribution of the estimation error obtained through Eq. (9). This method is very effective in normalizing and reducing MRE for projects with a high estimation error percentage. Applying, Eq. (9) and layer 3 lead to a considerable decline in upper limit of MRE With a drastic decline in an acceptable range.

In running tests on the 3LEE model, identifying the proper sequence of layer placement is one of the most important items to be tested. The proposed sequence of layers is obtained as a result of running different tests and the layers' movement. The results of various tests confirm the sequence of layers.

The MdMRE and PRED criteria of the proposed model are compared with other methods as shown in Fig. (8, 9 and 10), respectively. The results of this comparison for the COCOMO Dataset are shown in Fig. (8), where, the MdMRE value of this proposed model is lower than that of the MdMRE value of all methods. The PRED value of this proposed model is greater than that of the PRED values of all methods. The Desharnais dataset is assessed in Fig. (9), where the PRED value of this proposed model is greater than that of its MdMRE value. This difference reflects the high accuracy of the estimates provided by this model. The results of this comparison are shown for the maxwell Dataset, Fig. (10), where, PRED value of this proposed model is greater than its MdMRE value. This difference reflects the high accuracy of the estimates provided by this model. The difference in accuracy here model with other methods is based on the PRED and MdMRE criteria, Fig. (10).

Another comparison is made based on MAE benchmark to better assess the accuracy of this proposed model. This criterion represents the mean error of estimation in the projects, Fig. (11), whereas observed the 3LEE model is more accurate than all its counterparts. The accuracy of this model, according to the MAE criteria, is about 70% higher than its counterparts. The other methods, even close to this model, in one of the datasets, are not able to repeat their own estimation accuracy in other data sets. This point reflects the ability of this model to be adaptive in project conditions.

To determine 3lee overall performance, Wilcoxon, a statistical test, is executed which would confirm the superiority of this model. Wilcoxon test specifies the difference between two data samples that the difference is determined by P-value parameter. Based on this method two samples of data statistically different when p-value quantity is less than 0.05. In this article, the P-value quantity of different methods is compared with the 3LEE method. The P-value of each one of the assessed methods in comparison to the 3LEE model is tabulated in Table V. The P-value quantity of Wilcoxon test in all methods and all dataset is less than 0.05. The results of this test confirm the statistical significance of this model.

TABLE V

P-Values obtained from wilcoxon test

method	desharnais	maxwell	COCOMO
CART	0.0381	0.0347	0.0356
CBR K=1	0.0215	0.0012	0.0015
CBR K=2	0.0461	0.0119	0.0473
CBR K=3	0.0283	0.0303	0.0125
CBR K=4	0.0493	0.0071	0.0088
LS-SVM	0.0434	0.0138	0.00076
M5'	0.026	0.01	0.0338
MARS	0.0039	4.80E-05	4.38E-08
MLP	0.00078	0.00037	0.0342
OLS	0.0017	0.0219	3,51E-04
ROR	0.0313	0.000964	0.0166
PSO+ABE [10]	0.0391	0.0383	0.0368
ACO+ABE [38]	0.041	0.0389	0.037
RF [46]	0.048	0.05	2.3853e-005

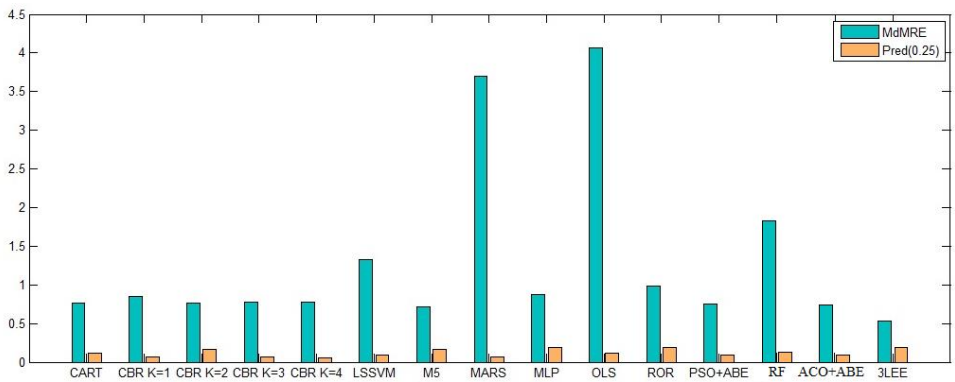

Fig. 8. Comparing methods on cocomo dataset

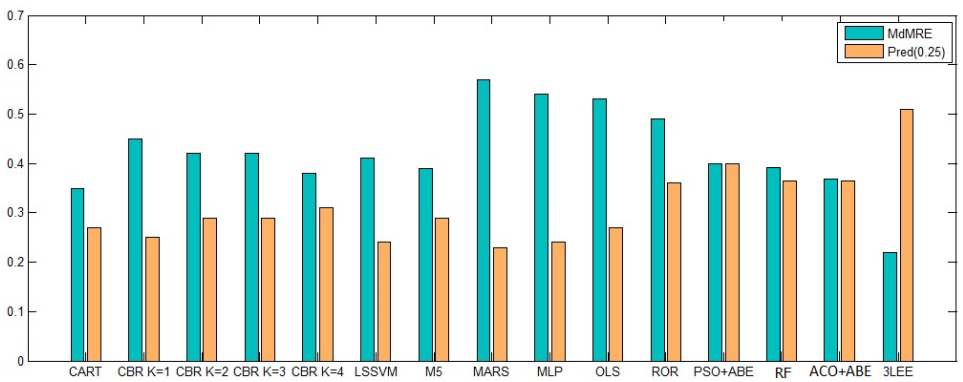

Fig. 9. Comparing methods on desharnise dataset

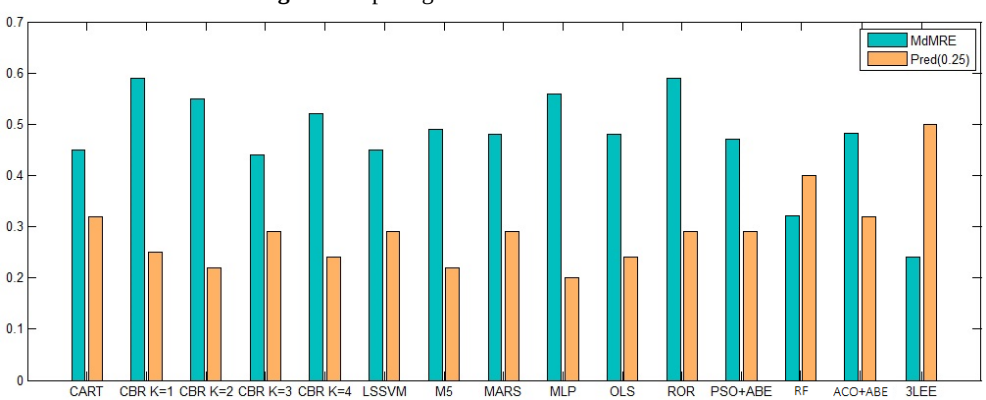

Fig. 10. Comparing methods on maxwell dataset

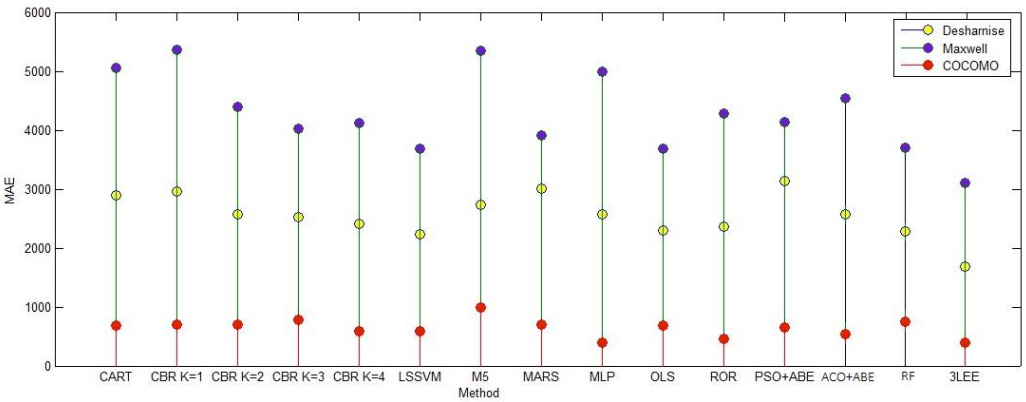

Fig. 11. Comparison of MAE criterion in datasets

X. CONCLUSION

According to the literature, the use of data processing methods, identification methods of effective features, and identification of types of relationships between project features on software project effort, or data modeling increase the estimation accuracy. Moreover, the correct application of heuristic algorithms for configuring methods and tools plays a key role in increased efficiency. A novelty of this study is to present sub-models with the above objectives for identifying features and their effective relationships, exactly configuring data modeling techniques, and estimating by the LSA algorithm based on feature similarity. The other novelty is to propose a model consisting of three layers in which sub-models are organized in their layers to improve their accuracy. The first layer of the proposed model acts on project features. In the second layer, the ABE method, an estimation method based on feature similarity, is configured using the LSA algorithm. The accuracy of the second layer is increased by using the analysis results of the first layer on project features. Combining the neural network and LSA, an estimator model of the first and second layers is developed in the third layer based on its outputs and inputs to increase the final estimation accuracy. Testing each layer slightly increased the estimation accuracy, but properly organizing all these layers significantly increased the final estimation accuracy. Using the heuristic algorithm in this model improved the flexibility of layers and their consistency with project conditions. This model is tested and its precise results were displayed. Precision of the results here suggests that many models presented by researchers so far can become more precise if redesigned based on the procedures presented here. Here, a new method is applied to increase the accuracy of the estimation model. In addition to data modeling to estimate the effort, a separate modeling is performed to estimate the model error. The error modeling is made in Layer 3. The result of this model indicates the final value of the estimation. Separate error modeling is contributive in reducing error estimation.

References

[1] A. K. Bardsiri and S. M. Hashemi, "Software effort estimation: a survey of well-known approaches," *International Journal of Computer Science Engineering (IJCSE)*, vol. 3, pp. 46-50, 2014.

[2] S. Bilgaiyan, S. Mishra, and M. Das, "Effort estimation in agile software development using experimental validation of neural network models," *International Journal of Information Technology*, vol. 11, pp. 569-573, 2019.

[3] D. Rankovic, N. Rankovic, M. Ivanovic, and L. Lazic, "Convergence rate of Artificial Neural Networks for estimation in software development projects," *Information and Software Technology*, p. 106627, 2021.

[4] P. S. Kumar, H. S. Behera, A. Kumari, J. Nayak, and B. Naik, "Advancement from neural networks to deep learning in software effort estimation: Perspective of two decades," *Computer Science Review*, vol. 38, p. 100288, 2020.

[5] R. d. A. Araujo, A. L. Oliveira, and S. Meira, "A class of hybrid multilayer perceptrons for software development effort estimation problems," *Expert Systems with Applications*, vol. 90, pp. 1-12, 2017.

[6] S. H. S. Moosavi and V. K. Bardsiri, "Satin bowerbird optimizer: A new optimization algorithm to optimize ANFIS for software development effort estimation," *Engineering Applications of Artificial Intelligence*, vol. 60, pp. 1-15, 2017.

[7] T. R. Benala and R. Mall, "DABE: differential evolution in analogy-based software development effort estimation," *Swarm and Evolutionary Computation*, vol. 38, pp. 158-172, 2018.

[8] Q. Liu, J. Xiao, and H. Zhu, "Feature selection for software effort estimation with localized neighborhood mutual information," *Cluster computing*, vol. 22, pp. 6953-6961, 2019.

[9] N.-H. Chiu and S.-J. Huang, "The adjusted analogy-based software effort estimation based on similarity distances," *Journal of Systems and Software*, vol. 80, pp. 628-640, 2007.

[10] V. K. Bardsiri, D. N. A. Jawawi, S. Z. M. Hashim, and E. Khatibi, "A PSO-based model to increase the accuracy of software development effort estimation," *Software Quality Journal*, vol. 21, pp. 501-526, 2013.

[11] Z. Shahpar, V. Khatibi, and A. Khatibi Bardsiri, "Hybrid PSO-SA approach for feature weighting in analogy-based software project effort estimation," *Journal of AI and Data Mining*, 2021.

[12] V. Resmi, S. Vijayalakshmi, and R. S. Chandrabose, "An effective software project effort estimation system using optimal firefly algorithm," *Cluster Computing*, vol. 22, pp. 11329-11338, 2019.

[13] J. F. Vijay, "Enrichment of accurate software effort estimation using fuzzy-based function point analysis in business data analytics," *Neural Computing and Applications*, vol. 31, pp. 1633-1639, 2019.

[14] I. Kaur, G. S. Narula, R. Wason, V. Jain, and A. Baliyan, "Neuro fuzzy—COCOMO II model for software cost estimation," *International Journal of Information Technology*, vol. 10, pp. 181-187, 2018.

[15] A. Idri, I. Abnane, and A. Abran, "Missing data techniques in analogy-based software development effort estimation," *Journal of Systems and Software*, vol. 117, pp. 595-611, 2016.

[16] P. R. Sree and R. SNSVSC, "Improving efficiency of fuzzy models for effort estimation by cascading & clustering techniques," *Procedia Computer Science*, vol. 85, pp. 278-285, 2016.

[17] A. Karimi and T. J. Gandomani, "Software development effort estimation modeling using a combination of fuzzy-neural network and differential evolution algorithm," *International Journal of Electrical & Computer Engineering (2088-8708)*, vol. 11, 2021.

[18] S. Chhabra and H. Singh, "Optimizing design of fuzzy model for software cost estimation using particle swarm optimization algorithm," *International Journal of Computational Intelligence and Applications*, vol. 19, p. 2050005, 2020.

[19] B. Barry, "Software engineering economics," *New York*, vol. 197, 1981.

[20] B. Boehm, C. Abts, A. Brown, S. Chulani, B. Clark, E. Horowitz, *et al.*, "Software cost estimation with COCOMO II. Prentice Hall PTR," *Upper Saddle River, NJ*, 2000.

[21] L. H. Putnam, "A general empirical solution to the macro software sizing and estimating problem," *IEEE transactions on Software Engineering*, pp. 345-361, 1978.

[22] A. J. Albrecht and J. E. Gaffney, "Software function, source lines of code, and development effort prediction: a software science validation," *IEEE transactions on software engineering*, pp. 639-648, 1983.

[23] S. A. Abbas, X. Liao, A. U. Rehman, A. Azam, and M. Abdullah, "Cost estimation: A survey of well-known historic cost estimation techniques," *Journal of Emerging Trends in Computing and Information Sciences*, vol. 3, pp. 612-636, 2012.

[24] G. R. Finnie, G. E. Wittig, and J.-M. Desharnais, "A comparison of software effort estimation techniques: Using function points with neural networks, case-based reasoning and regression models," *Journal of systems and software*, vol. 39, pp. 281-289, 1997.

[25] P. Sentas, L. Angelis, I. Stamelos, and G. Bleris, "Software productivity and effort prediction with ordinal regression," *Information and software technology*, vol. 47, pp. 17-29, 2005.

[26] L. C. Briand, K. El Emam, D. Surmann, I. Wieczorek, and K. D. Maxwell, "An assessment and comparison of common software cost estimation modeling techniques," in *Proceedings of the 1999 International Conference on Software Engineering (IEEE Cat. No. 99CB37002)*, 1999, pp. 313-323.

[27] L. C. Briand, T. Langley, and I. Wieczorek, "A replicated assessment and comparison of common software cost modeling techniques," in *Proceedings of the 22nd international conference on Software engineering*, 2000, pp. 377-386.

[28] M. Dehghani, Z. Montazeri, O. P. Malik, A. Ehsanifar, and A. Dehghani, "OSA: Orientation Search Algorithm," *International Journal of Industrial Electronics Control and Optimization*, vol. 2, pp. 99-112, 2019.

[29] F. Zare, H. K. Zare, and M. S. Fallahnezhad, "Software effort estimation based on the optimal Bayesian belief network," *Applied Soft Computing*, vol. 49, pp. 968-980, 2016.

[30] A. García-Floriano, C. López-Martín, C. Yáñez-Márquez, and A. Abran, "Support vector regression for predicting software enhancement effort," *Information and Software Technology*, vol. 97, pp. 99-109, 2018.

[31] S. Beiranvand and Z. Chahooki, "Bridging the semantic gap for software effort estimation by hierarchical feature selection techniques," *Journal of AI and Data Mining*, vol. 4, pp. 157-168, 2016.

[32] A. Puspaningrum and R. Sarno, "A hybrid cuckoo optimization and harmony search algorithm for software cost estimation," *Procedia Computer Science*, vol. 124, pp. 461-469, 2017.

[33] S. P. Singh, V. P. Singh, and A. K. Mehta, "Differential evolution using homeostasis adaption based mutation operator and its application for software cost estimation," *Journal of King Saud University-Computer and Information Sciences*, 2018.

[34] A. Ali and C. Gravino, "Improving software effort estimation using bio-inspired algorithms to select relevant features: An empirical study," *Science of Computer Programming*, vol. 205, p. 102621, 2021.

[35] S. Goyal and P. K. Bhatia, "Feature selection technique for effective software effort estimation using multi-layer perceptrons," in *Proceedings of ICETIT 2019*, ed: Springer, 2020, pp. 183-194.

[36] A. Setiadi, W. F. Hidayat, A. Sinnun, A. Setiawan, M. Faisal, and D. P. Alamsyah, "Analyze the Datasets of Software Effort Estimation With Particle Swarm Optimization," in *2021 International Seminar on Intelligent Technology and Its Applications (ISITIA)*, 2021, pp. 197-201.

[37] P. Phannachitta, "On an optimal analogy-based software effort estimation," *Information and Software Technology*, vol. 125, p. 106330, 2020.

[38] S. Ranichandra, "Optimizing non-orthogonal space distance using ACO in software cost estimation," *Mukt Shabd J*, vol. 9, pp. 1592-1604, 2020.

[39] E. Kocaguneli and T. Menzies, "Software effort models should be assessed via leave-one-out validation," *Journal of Systems and Software*, vol. 86, pp. 1879-1890, 2013.

[40] P. W. Holland and R. E. Welsch, "Robust regression using iteratively reweighted least-squares," *Communications in Statistics-theory and Methods*, vol. 6, pp. 813-827, 1977.

[41] J. H. Friedman, "Multivariate adaptive regression splines," *The annals of statistics*, pp. 1-67, 1991.

[42] J. R. Quinlan, *C4. 5: programs for machine learning*: Elsevier, 2014.
[43] Y. Wang and I. H. Witten, "Induction of model trees for predicting continuous classes," 1996.
[44] K. Hornik, M. Stinchcombe, and H. White, "Multilayer feedforward networks are universal approximators," *Neural networks*, vol. 2, pp. 359-366, 1989.
[45] J. Li, G. Ruhe, A. Al-Emran, and M. M. Richter, "A flexible method for software effort estimation by analogy," *Empirical Software Engineering*, vol. 12, pp. 65-106, 2007.
[46] H. Mustapha and N. Abdelwahed, "Investigating the use of random forest in software effort estimation," *Procedia computer science*, vol. 148, pp. 343-352, 2019.

Amin Moradbeiky received his B.Sc. from University of Sistan and Baluchestan, Iran in 2009 and M.Sc. from Islamic Azad University, Kerman Branch, Iran in 2014, both in engineering of information technology. He is currently Ph.D. student of software engineering in Islamic Azad University, Kerman Branch, Iran. His research interests are soft computing techniques, software test and software measurement.

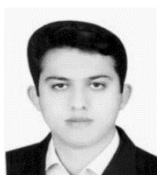

Vahid Khatibi Bardsiri, he is a lecturer at the Department of Computer Science, Islamic Azad University, Bardsir Branch, Iran. He holds B.Sc. and M.Sc. Degrees in software engineering from Ferdowsi University of Mashhad, Iran (2002) and Science and Research Branch of Islamic Azad University, Iran (2004), respectively. He received his Ph.D. in the area of software development effort estimation at Universiti Teknologi Malaysia (UTM), 2013. He is a senior member of International Association of Computer Science and Information Technology (IACSIT). His research interests are agile software development methods, soft computing techniques and software measurement.

Mehdi Jafari, received the B.S. in electronic engineering and M.S. degrees in communication systems from Shiraz University of technology in 1992 and 1996, respectively. During 1992-1998 he stayed in signal processing research laboratory, ministry of telecommunications of Iran. He received Ph. D degree in communication systems in science and research branch of Islamic Azad University in January 2008. He is currently head of electrical engineering department of Islamic Azad University, Kerman Branch. His main research interests are artificial intelligence, image and video processing, pattern recognition and prediction.

International Journal of Industrial Electronics, Control and Optimization © 2022 IECO
Vol. 5, No. 1, pp. 43-50 , Jan (2022)

A Comprehensive Learning Polynomial Auto-Regressive Model based on Optimization with the Application of Time Series Forecasting

Nastaran Darjani[1], and Hesam Omranpour[2, †]

[1,2]Department of Electrical and Computer Engineering, Babol Noshirvani University of Technology, Babol, Iran

ABSTRACT

Nowadays, time series analysis is an important challenge in engineering problems. This paper proposes a Comprehensive Learning Polynomial Autoregressive Model for predicting linear and nonlinear time series. The model is based on the autoregressive model but developed in a polynomial aspect to make it more robust and accurate. The model predicts future values by learning the weights of the weighted sum of the polynomial combination of previous data. The learning process for the hyperparameters and properties of the model in the training phase is performed by the metaheuristic optimization method. Using this model, we can predict nonlinear time series, as well as linear time series. The proposed method was implemented on eight standard stationary and non-stationary large-scale real-world datasets. It outperformed the state-of-the-art methods that use deep learning in seven time series and has better results compared to all other methods in six datasets. Experimental results show the advantage of the model's accuracy over other compared methods on various prediction tasks based on the root-mean-square error.

Article Info

Keywords:
Autoregressive, Forecasting, Machine learning, Optimization, Time series prediction

Article History:
Received 2021-08-17
Accepted 2021-12-18

I. INTRODUCTION

Nowadays, time series prediction is used in a wide range of areas including energy [1], traffic [2],[3], economy tourism [4], and health [5]. The methods defined for time series prediction are divided into statistical and non-statistical sections. The autoregressive (AR) and Autoregressive Integrated Moving Average (ARIMA) models are two examples of statistical methods [6]. Models for forecasting commodity prices, including oil or natural gas are already in application with ARIMA [7]–[9]. Also, these methods are used for load forecasting in power systems with acceptable results [10]. These methods are linear models for accurate prediction of time series; however, these are only satisfactory for linear time series and unsuitable for nonlinear time series [11]. Multiple methods have been extended from classic methods to satisfy this limitation. Multiresolution autoregressive model (MAR) is a wavelet-based AR model presented in [12]. Due to Kalman filter-inspired recurrence scheme, which allows not recomputing all estimations for each new value, this method is a faster and more flexible algorithm than the basic AR model.

Neural networks [13]–[16],[17] and Fuzzy methods [18]–[21] are known as non-statistical and soft computing methods. The advantages of artificial neural networks are their flexible nonlinear modeling capability, strong adaptability, and their learning and extensive parallel computing abilities [22],[23], but the neural network is inadequate in predicting linear time series and also requires a lot of training data to accurately predict future data [24]. In [25], time series is decomposed using multiscale fast wavelet transform, and each scale's wavelet coefficients are learned with a multilayer perceptron to predict the next sample of time series. More recently, more deep learning-based methods have been developed but

†**Corresponding Author:** H.Omranpour@nit.ac.ir
Tel: 01135501467, Department of Electrical and Computer Engineering, Babol Noshirvani University of Technology, Babol, Iran

Algorithm I. Fitness Function

Input: *particles*
Output: *RMSE*
/ decoding particles to matrix of weight matrix and bias */*
1: ***for*** *each number j of time series window* ***do***
2: ***for*** *each power i of CLPAR model* ***do***
3: *set i-th particle from j-th part with n size particles to w(i, j)*
4: ***end for***
5: ***end for***
6: set last particle to bias
/ predict last data of windows with weight and bias based on Equ. 3 */*
7: ***for*** *each position i in time series window* ***do***
8: *set 0 to p*
9: ***for*** *each number j of time series window* ***do***
10: ***for*** *each power k of CLPAR model* ***do***
11: *set power k of i-th data in j-th window multiplied by w(j, k) to p*
12: ***end for***
13: ***end for***
14: *set p + bias to ypredict(i)*
15: ***end for***
/ calculate RMSE by applying Equ. 5 */*
16: set square sum of (y – ypredict)^2 divided by size of y to RMSE

these methods also have the same advantages and disadvantages. High-order Fuzzy Cognitive Maps (HFCMs) are learned via Convolutional Neural Network (CNN) deep learning networks in [26].

Fuzzy methods predict the time series using a function-estimation approach by one or more fuzzy rules [27]. In these methods, every sample of time series is used to evaluate parameters of the fuzzy model and then the error of test data reported [28],[29]. In [30], the Adaptive-Network-Based Fuzzy Inference System (ANFIS) is employed by using a hybrid learning procedure. In [27], sparse autoencoder (SAE) extracts features from the original time series and feeds them to an HFCM predictor. A combination of HFCMs with SAE output is used to calculate the predicted time series. Another FCM-based method is mentioned in [31], where HFCMs are combined with Haar wavelet transform to manage nonstationary time series.

In the real world, time series are composed of linear and non-linear parts. The abovementioned methods are only appropriate for either linear or non-linear time series. As the nonlinear part of the time series dominates the linear part, the nonlinear models produce a satisfactory result. The same outcome is achieved when the linear part of the time series is greater than the nonlinear part. In either case, one part of the time series is ignored, which reduces the prediction accuracy [32].

II. Proposed Model

This paper introduces a polynomial model generalized from the classic AR model in which nonlinear properties, besides linear ones, are considered. The method provides nonlinearity with the possibility of having different powers of previous data points. Section II introduces the proposed model with two phases of training and testing algorithms. In section III, the RMSE value of the proposed method is compared with the other methods

TABLE I

RMSE IN TESTING AND TRAINING DATA REPRESENTED BY THE BEST POLYNOMIAL DEGREE AND WINDOW SIZE

Dataset	R-squared	Testing RMSE	Training RMSE	Optimal polynomial degree	Optimal window size
Sunspot	0.839	16.947	13.06	1	13
Mackey-Glass	0.996	0.007	0.0077	2	6
S&P 500 stock index	0.988	10.247	10.69	1	9
Monthly milk production	0.992	6.839	5.91	1	14
Monthly closings of the Dow-Jones	0.993	22.549	21.46	2	37
Monthly critical radio frequencies	0.945	0.320	0.32	3	49
CO2 (ppm)	0.996	0.357	0.37	1	17
Monthly Lake Erie levels	0.913	0.336	0.24	3	28

. Section IV presents the concluding points. AR-based methods make accurate predictions of linear time series but they are unable to predict nonlinear real-world problems [12]. The proposed model can be considered an extension of the AR model. Equ. (1) is used in AR-based models from a prediction that is the linear sum of the previous amounts [33].

$$Y_t = \sum_{i=1}^{p} \varphi_i Y_{t-i} + \varepsilon_t \quad (1)$$

But, the behavioral pattern of the series might not be entirely linear, so this paper presents an equation that does not have this limitation. A separate coefficient is assigned for each power of $y_{(t-i)}$ data. An ε_t bias value is also considered. Equ. (2) is achieved by simplifying Equ. (1). The sum of ε_i is replaced by ε in Equ. (2).

$$Y_t = \varepsilon + \sum_{i=1}^{p} \varphi_i Y_{t-i} \quad (2)$$

On the other hand, if the different powers of the y_{t-i} data are used to predict y_t, this sum will reach a large amount, so in addition to inserting the coefficient, data is also normalized. We consider an equation consisting of two sigmas. One is on the powers of y_{t-i} and the other on the sum of these values on the preceding p data. The sum of the two sigmas, which were mentioned above, is considered for every number in the time series. Finally, this equation is presented for modeling in this paper. Equ. (3)(6) need to learn the coefficients. The extended polynomial capability enables the method to satisfy nonlinear time series prediction although, with a much bigger search space, it can be challenging to estimate the parameters. Given that a window with the length p is used for prediction and also the upper limit of polynomial degree is n, learning is done in a space

TABLE II

COMPARISON WITH OTHER PREDICTION MODELS IN TERMS OF RMSE

Dataset	CLPAR	CNN-FCM [25] (2020)	RNN [25] (2020)	SAE-FCM [26] (2019)	Wavelet-HFCM [30] (2018)	ANFIS [29] (classic)	AR Model [6] (classic)	Multiresolution AR model [12] (2005)	ScaleNet-Multiscale Neural Network [24] (classic)
Sunspot time series	16.947	17.949	19.292	17.390	18.916	22.753	35.262	19.186	19.901
Mackey-Glass time series	0.007	0.0013	0.0005	0.0009	0.004	0.001	0.035	0.002	0.005
S&P 500 stock index	10.247	20.816	27.896	11.893	16.105	14.935	17.897	16.041	17.696
Monthly milk production per cow	6.839	30.474	29.253	7.931	8.258	9.578	57.717	37838	27.113
Monthly closings of the Dow-Jones industrial index	22.549	25.190	26.232	21.335	23.159	57.526	29.822	26.733	28.532
Monthly critical radio frequencies	0.320	0.567	0.613	0.490	0.547	0.651	0.902	0.662	0.652
CO2 (ppm) at Mauna Loa	0.357	0.731	1.420	0.366	0.56	0.91	1.35	0.812	1.695
Monthly Lake Erie levels	0.336	0.391	0.374	0.359	0.377	0.458	0.638	0.39	0.402

with the size $p \times n$. This space reaches $(p \times n) + 1$ by inserting the epsilon bias value. This search space is bigger than that of the classic method with $n + 1$ estimation. These coefficients are learned from an optimization perspective. GWO is used to find the best values for these coefficients and epsilon [34].

$$Y_t = \varepsilon + \sum_{j=1}^{n} \sum_{i=1}^{p} \varphi_{ij} Y_{t-i}^{j} \tag{3}$$

A. Model Training Level

The training algorithm is as follows:

- Normalizing the data
- Windowing the data: Segmentation into p-size data per y_t
- Learning the coefficients with GWO: Calculating the output for each window using Equ. (3) and obtaining RMSE as fitness

where the algorithm input is time series and outputs are the best φ and ε.

1) Normalization Phase: In this phase, all the data is placed in the range [0, 1] as follows,

$$d_i = \left(\frac{d_i - min}{max - min} \right) \tag{4}$$

where *min* and *max* stands for minimum and maximum data, respectively and d_i is the *i*-th data in time series.

2) Windowing Phase: In this section, data is prepared and resized to p to fit in Equ. (3). For example, for time series with the length L and window of 3, windowing consists of each data with its previous two data, and the number of rows is $t = L - p + 1$.

3) Learning the Coefficients: We must obtain the weights for Equ. (3) according to the windowing phase. In the windowing phase, there are $Tlength - p + 1$ equations with $(p \times n) - 1$ unknowns (weights) where *Tlength* is the time series size. Weights of these equations are achieved by using an optimizer. The optimizer used here is grey wolf optimization [34].

To code the particles existing in optimization search space (wolves in GWO), an $n \times p$ matrix and an epsilon variable are used. The $n \times p$ matrix shows the weights of particles (wolves) in Equ. (3).

Inputs of the fitness function are trained windowed data and a particle (wolf). By using the coefficients and inserting them in Equ. (3)(6), the RMSE of the trained window is returned as output. RMSE, which calculates the difference between the original time series and the predicted one, is obtained using Equ. (5) where L is the length of time series and x_i and y_i stand for the predicted time series and the normalized original time series, respectively [30]. Algorithm I shows the pseudo-code of the fitness function.

$$RMSE = \sqrt{\frac{\sum_{i=1}^{L} (x_i - y_i)^2}{L}} \tag{5}$$

B. Model Testing

In this section, outputs of the training data that include best weights and epsilon are used in Equ. (3) to predict the testing data.

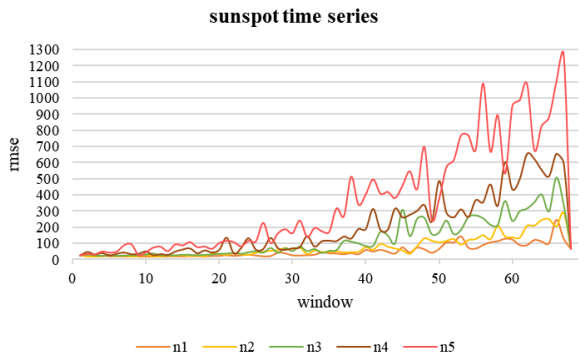

Fig. 1. RMSE in different window sizes and polynomial degrees. The horizontal axis is window size and different colors of the line represent the maximum polynomial degree in Equ. (3).

III. Experimental Result

This section presents the results of the implemented experiments on real data. First, we introduce the datasets. The results of the implementation are then presented along with analysis and comparison with other methods.

A. Datasets

To show the efficiency of the suggested model, we use eight benchmark time series with distinct characteristics. The first one is the sunspot time series that has recorded the annual amount of sunspots from 1700 to 1987, which includes a total of 289 observations and has often been used by other researchers [31],[35]–[40]. The second dataset contains a total of 251 recorded observations, used in associated publications [31],[41]–[46] and accessible from the Yahoo finance website [47]. It concerns the day-to-day price of the S&P 500 stock index from 1 June 2016 to 1 June 2017. The third dataset records a total of 168 observations in the monthly manufacturing of milk in pounds from January 1962 to December 1975 [48]. In the fourth dataset, the index of Dow-Jones Industrial monthly closing has recorded a total of 291 observations from August 1968 until August 1981 [49]. The fifth dataset includes 240 observations that reflect the highest radio frequency used in Washington, D.C. between May 1934 and April 1954 in [50]. The sixth dataset relates to 192 observations [51] recording CO_2 (ppm) at Mauna Loa from 1965 to 1980 and the seventh dataset, including 600 observations [52], contains the monthly Lake Erie level from 1921 to 1970. A first-order nonlinear differential delay equation is described by Equ. (6). The last dataset, the chaotic Mackey-Glass time series [53], is derived from that. This time series validates the effectiveness of prediction models in [31],[35],[36],[54]–[57]. The dataset of the Mackey-Glass time series was acquired by solving the fourth-order Runge-Kutta algorithm with 1000 points from t = 124 to t = 1123 by solving Equ. (6). In addition, the initial conditions $\boldsymbol{x}(\mathbf{0})$ and τ are set to 1.2 and 17, respectively [31].

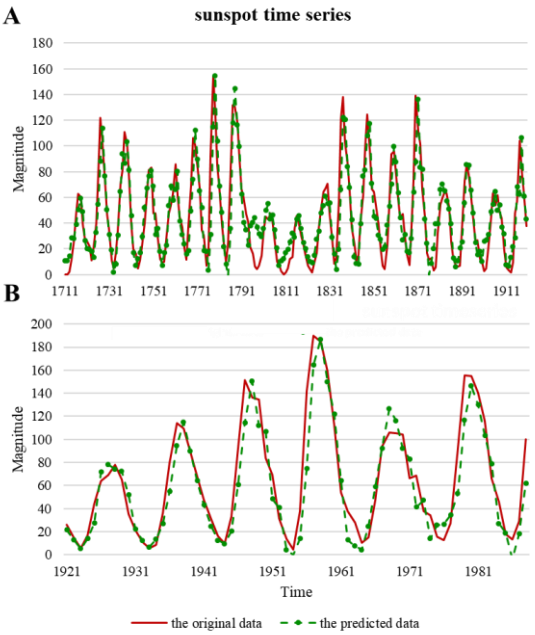

Fig. 2. Original time series and predicted time series in (A) training data, (B) testing data.

$$\dot{x} = \frac{0.2x(t-\tau)}{1+x^{10}(t-\tau)} - 0.1x(t) \tag{6}$$

Each dataset is divided into testing and training. Given that the time series prediction is applied to forecast future data, the time series in the experiments in this paper is broken into two parts of testing and training at one point. This segmentation causes the next *k*-th data to be predicted as well as the next data.

B. Survey of the Effect of Window Size and Polynomial Degree

This section presents the results of the implementation of the proposed method on the eight databases introduced in the previous section with different window sizes and polynomial degrees. Fig. 1 shows the RMSE levels of the testing data for the sunspot time series. Graph row represents the size of the window and each curve represents a polynomial degree. As the window size and polynomial degree increase, the complexity of the model increases. On the other hand, the search space for learning weights also increases so the optimizer may not be able to produce the optimized results in a limited time. Therefore, test errors are more likely to occur for large n and p values with the same number of iterations. Table I presents the best values for polynomial degree and window length for each dataset. Due to the unlimited statistics range of RMSE ($[0, +\infty)$), which is not

informative about the quality of regression performance individually,

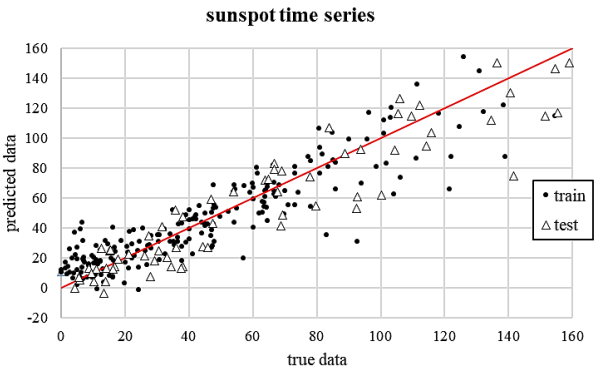

Fig. 3. The original and predicted data in the testing and training datasets.

R-squared values are shown in Table I. It can be determined how well the independent variables can account for the variance of the dependent variables, which is defined as follows [58]:

$$R^2 = 1 - \frac{\sum_{i=1}^{L}(x_i - y_i)^2}{\sum_{i=1}^{L}(\bar{y} - y_i)^2} \quad (7)$$

where x_i is the predicted i-th value and y_i and $\bar{y}$ are the original corresponding time series and their means, respectively.

C. Implementation Results After Parameter Tuning

In this section, charts are provided using the best values obtained based on Table I. Fig. 2 shows the original data and also the data that has been predicted by the proposed model over time on the sunspot time series. Fig. 2 contains the predicted training (A) and predicted testing (B) data. Also, to determine the deviation rate of the data predicted from the actual data, scatter plots of the sunspot dataset are shown in Fig. 3.

One of the challenges in nonstationary time series is to obtain periodicity. The periodicity presented in Fig. 2 is obtained by averaging the distance between adjacent peaks (valleys). This frequency (periodicity) is not necessarily nonstationary (periodicity). Therefore, the frequency in the time series might be obtained by multiplying the frequency existing in Fig. 3 to a natural number. By comparing the columns of the periodicity table and the window size in Table I, it can be observed that the defined periodicity is a numerical coefficient of the optimal window size. This coefficient in the Mackey-Glass time series, milk production per cow, monthly critical Mauna Loa, and the model can predict these data as a sum of linear coefficients of the pre-data. But, this value is greater than 1 for datasets of Mackey-Glass time series, monthly closings of the Dow-Jones industrial index, monthly critical radio frequencies, and monthly Lake Erie levels, which means the pattern in the data from the previous window is polynomial.

D. Comparison against other methods

This section compares the proposed method with other state-of-the-art and classical prediction methods in terms of RMSE value. Table II shows the results of this comparison. The classic statistical AR model [6] is suitable for linear time series. However, this method cannot satisfy nonlinear and nonstationary time series, which are more likely to exist in the real world. Therefore, the RMSE results of more complex time series for this method are not as good as those of the other methods. This method has the worst RMSE value in half of the tested time series against other ones. Multiresolution AR model [12] is an extended method of AR model, which uses wavelet theory to break complex time series into multiple linear time series and AR model to them. This method is slightly better than the AR model. Moreover, it is faster than the classic method because of the recurrence scheme, which removes some recomputing stages of estimations. Artificial neural networks and deep learning methods [25],[26] are functional and flexible for the nonstationary time series. But, these methods need a huge amount of data to train in order to make a reliable prediction and be robust. In Tabel II, RMSE values for these methods have mixed results. The RNN method [26] has the worst accuracy in the S&P stock index time series and is the second-worst method in the CO2 time series. In contrast, it has the best RMSE for the Mackey-Glass time series against other methods. Moreover, ScaleNet-Multiscale Neural Network [25] has average results compared to other methods except for the CO2 Mauna Loa time series, which has the highest error against other ones. The weak results in these methods are caused by not having enough training data in comparison to lots of estimation parameters. Fuzzy methods [27], [30], [31] use fuzzy rules to estimate the parameters of the given function. Although these methods have the closest results to the proposed method, the function-estimation approach in these models can be complicated and does not have robustness and flexibility for many time series. In [26], HFCMs learn via deep learning networks to have the flexibility of the neural networks in addition to the simplicity of the fuzzy methods. For most time series, the suggested modeling technique can provide maximum accuracy and still obtain remarkable predictions for a further time series. In Dow-Jones industrial index time series, the SAE-FCM method has slightly higher RMSE than the proposed method. All other methods have lower RMSE than CLPAR in the Mackey-Glass time series except for the classic AR model. In fact, in all datasets, the proposed method outperforms the classic AR model, which is the model that CLPAR derives from it. Regardless of the Mackey-Glass time series, CLPAR entirely outperforms ANN-based methods and has lower error against fuzzy methods in six out of the seven

benchmarks.

IV. Conclusions

In this paper, we proposed a model for predicting time series. One of the classic models for this purpose is the AR model, which is developed to predict linear time series. The described model is based on the AR model generalized to include nonlinear properties besides linear ones. The classic autoregressive model has a coefficient of previous data. The proposed model also uses the same idea to consider the linear property, and to satisfy the nonlinearity property, we considered coefficients of powers of pre-data. These coefficients learn from training data with a grey wolf optimizer.

The proposed prediction modeling method was applied to several datasets, which yielded satisfactory results. In six out of eight datasets, this model achieved the highest accuracy against other methods. In the remaining dataset, the Mackey-Glass time series, an acceptable error value was achieved in terms of RMSE. It is suggested that other optimizations and learning methods can be used to improve the accuracy of the CLPAR method until better accuracy is achieved in the Mackey-Glass dataset.

Acknowledgment

The authors gratefully acknowledge the Babol Noshirvani University of Technology for the financial support for the present research through a research grant.

References

[1] V. Ediger, S. Akar, *ARIMA forecasting of primary energy demand by fuel in Turkey*, Energy Policy. 35 (2007) 1701–1708.

[2] M. Khashei, F.M. Rafiei, M. Bijari, Hybrid fuzzy auto-regressive integrated moving average (FARIMAH) model for forecasting the foreign exchange markets, *Int. J. Comput. Intell. Syst.* 6 (2013) 954–968.

[3] K. Kumar, V.K. Jain, *Autoregressive integrated moving averages (ARIMA) modelling of a traffic noise time series*, Appl. Acoust. 58 (1999) 283–294.

[4] F.-L. Chu, A fractionally integrated autoregressive moving average approach to forecasting tourism demand, *Tour. Manag.* 29 (2008) 79–88.

[5] H.-K. Yu, N.-Y. Kim, S.S. Kim, C. Chu, M.-K. Kee, Forecasting the number of human immunodeficiency virus infections in the Korean population using the autoregressive integrated moving average model, Osong Public Heal. Res. Perspect. 4 (2013) 358–362.

[6] G. Zheng, J.L. Starck, J.G. Campbell, F. Murtagh, Multiscale transforms for filtering financial data streams, J. Comput. Intell. Financ. 7 (1999).

[7] M.D. Chinn, M. LeBlanc, O. Coibion, The predictive characteristics of energy futures: Recent evidence for crude oil, natural gas, gasoline and heating oil, Nat. Gas, Gasol. Heat. Oil (October 2001). UCSC Econ. Work. Pap. (2001).

[8] C. Morana, A semiparametric approach to short-term oil price forecasting, Energy Econ. 23 (2001) 325–338.

[9] W.K. Buchanan, P. Hodges, J. Theis, Which way the natural gas price: an attempt to predict the direction of natural gas spot price movements using trader positions, Energy Econ. 23 (2001) 279–293.

[10] M.T. Hagan, S.M. Behr, *The time series approach to short term load forecasting, IEEE Trans*. Power Syst. 2 (1987) 785–791.

[11] G.E.P. Box, G.M. Jenkins, Time series analysis: forecasting and control, Holden-Day, 1976. https://books.google.com/books?id=1WVHAAAAMAAJ.

[12] O. Renaud, J.-L. Starck, F. Murtagh, Wavelet-based combined signal filtering and prediction, IEEE Trans. Syst. Man, Cybern. Part B. 35 (2005) 1241–1251.

[13] G. Zhang, B.E. Patuwo, M.Y. Hu, Forecasting with artificial neural networks: *The state of the art, Int. J. Forecast*. 14 (1998) 35–62.

[14] T.-S. Quah, B. Srinivasan, Improving returns on stock investment through neural network selection, *Expert Syst. Appl.* 17 (1999) 295–301.

[15] L.R. Rabiner, A tutorial on hidden Markov models and selected applications in speech recognition, Proc. IEEE. 77 (1989) 257–286.

[16] J. Roman, A. Jameel, Backpropagation and recurrent neural networks in financial analysis of multiple stock market returns, in: Proc. HICSS-29 29th Hawaii Int. Conf. Syst. Sci., 1996: pp. 454–460.

[17] S. A. Ghoreishi, and H. Khaloozadeh, "Application of Covariance Matrix Adaptation-Evolution Strategy to Optimal Portfolio," *International Journal of Industrial Electronics, Control and Optimization*, Vol. 2, No. 2, pp. 81-90, 2019.

[18] A. Setare, O. Hesam, M. Homayun, Application of a fuzzy method for predicting based on high-order time series, in: 2014 Iran. Conf. Intell. Syst., 2014: pp. 1–6.

[19] H.-K. Yu, Weighted fuzzy time series models for TAIEX forecasting, *Phys. A Stat. Mech. Its Appl.* 349 (2005) 609–624.

[20] S.-M. Chen, Forecasting enrollments based on fuzzy time series, Fuzzy Sets Syst. 81 (1996) 311–319.

[21] K. Huarng, Heuristic models of fuzzy time series for forecasting, *Fuzzy Sets Syst*. 123 (2001) 369–386.

[22] J.L. Ticknor, A Bayesian regularized artificial neural network for stock market forecasting, Expert Syst. Appl. 40 (2013) 5501–5506.

[23] L. Wang, Y. Zeng, T. Chen, Back propagation neural network with adaptive differential evolution algorithm for time series forecasting, Expert Syst. Appl. 42 (2015) 855–863.

[24] T.C. Jo, The effect of virtual term generation on the neural-based approaches to time series prediction, in: 2003 4th Int. Conf. Control Autom. Proc., 2003: pp. 516–520.

[25] A.B. Geva, ScaleNet-multiscale neural-network architecture

for time series prediction, IEEE Trans. Neural Networks. 9 (1998) 1471–1482.

[26] P. Liu, J. Liu, K. Wu, CNN-FCM: System modeling promotes stability of deep learning in time series prediction, Knowledge-Based Syst. 203 (2020) 106081. doi:10.1016/j.knosys.2020.106081.

[27] K. Wu, J. Liu, P. Liu, S. Yang, Time Series Prediction Using Sparse Autoencoder and High-order Fuzzy Cognitive Maps, IEEE Trans. Fuzzy Syst. (2019). doi:10.1109/TFUZZ.2019.2956904.

[28] J.G. Carvalho Jr, C.T. Costa Jr, Identification method for fuzzy forecasting models of time series, Appl. Soft Comput. 50 (2017) 166–182.

[29] O.C. Yolcu, F. Alpaslan, Prediction of TAIEX based on hybrid fuzzy time series model with single optimization process, Appl. Soft Comput. 66 (2018) 18–33.

[30] J.-S. Jang, ANFIS: adaptive-network-based fuzzy inference system, IEEE Trans. Syst. Man. Cybern. 23 (1993) 665–685.

[31] S. Yang, J. Liu, Time-series forecasting based on high-order fuzzy cognitive maps and wavelet transform, IEEE Trans. Fuzzy Syst. 26 (2018) 3391–3402.

[32] E. Bas, E. Egrioglu, C.H. Aladag, U. Yolcu, Fuzzy-time-series network used to forecast linear and nonlinear time series, Appl. Intell. 43 (2015) 343–355.

[33] H. Akaike, Fitting autoregressive models for prediction, Ann. Inst. Stat. Math. 21 (1969) 243–247.

[34] S. Mirjalili, S.M. Mirjalili, A. Lewis, Grey Wolf Optimizer, Adv. Eng. Softw. 69 (2014) 46–61. doi:10.1016/j.advengsoft.2013.12.007.

[35] W. Lu, J. Yang, X. Liu, W. Pedrycz, The modeling and prediction of time series based on synergy of high-order fuzzy cognitive map and fuzzy c-means clustering, Knowledge-Based Syst. 70 (2014) 242–255.

[36] S. Soltani, On the use of the wavelet decomposition for time series prediction, Neurocomputing. 48 (2002) 267–277.

[37] H.S. Lopes, W.R. Weinert, EGIPSYS: an enhanced gene expression programming approach for symbolic regression problems, Int. J. Appl. Math. Comput. Sci. 14 (2004) 375–384.

[38] C. Ferreira, Gene expression programming: mathematical modeling by an artificial intelligence, Springer, 2006.

[39] H. Cao, L. Kang, Y. Chen, J. Yu, Evolutionary modeling of systems of ordinary differential equations with genetic programming, Genet. Program. Evolvable Mach. 1 (2000) 309–337.

[40] Y. Peng, C. Yuan, X. Qin, J. Huang, Y. Shi, An improved gene expression programming approach for symbolic regression problems, Neurocomputing. 137 (2014) 293–301.

[41] S.T.A. Niaki, S. Hoseinzade, Forecasting S&P 500 index using artificial neural networks and design of experiments, J. Ind. Eng. Int. 9 (2013) 1.

[42] R. Majhi, G. Panda, G. Sahoo, A. Panda, A. Choubey, Prediction of S&P 500 and DJIA stock indices using particle swarm optimization technique, in: 2008 IEEE Congr. Evol. Comput. (IEEE World Congr. Comput. Intell., 2008: pp. 1276–1282.

[43] R. Tsaih, Y. Hsu, C.C. Lai, Forecasting S&P 500 stock index futures with a hybrid AI system, Decis. Support Syst. 23 (1998) 161–174.

[44] M. Martens, Measuring and forecasting S&P 500 index-futures volatility using high-frequency data, J. Futur. Mark. Futur. Options, Other Deriv. Prod. 22 (2002) 497–518.

[45] E. Hajizadeh, A. Seifi, M.H.F. Zarandi, I.B. Turksen, A hybrid modeling approach for forecasting the volatility of S&P 500 index return, Expert Syst. Appl. 39 (2012) 431–436.

[46] S.A. Hamid, Z. Iqbal, Using neural networks for forecasting volatility of S&P 500 Index futures prices, J. Bus. Res. 57 (2004) 1116–1125.

[47] Yahoo, GSPC historical prices j S&P 500 stock, (n.d.). https://finance.yahoo.com/quote/%5EGSPC/history?p=%5EGSPC (accessed August 16, 2019).

[48] Monthly milk production: pounds per cow. Jan 62 - Dec 75, (n.d.). https://datamarket.com/data/set/22ox/monthly-milk-production-poundsper-cow-jan-62-dec-75#!ds=22ox&display=line (accessed August 16, 2019).

[49] Monthly closings of the Dow-Jones industrial index, Aug. 1968 - Aug. 1981, (n.d.). https://datamarket.com/data/set/22v9/monthlyclosings-of-the-dow-jones-industrial-index-aug-1968-aug-%0A1981#!ds=22v9&display=line (accessed August 16, 2019).

[50] Monthly critical radio frequencies in Washington, D.C., May 1934 - April 1954, (n.d.). https://datamarket.com/data/set/22u2/monthlycritical-radio-frequencies-in-washington-dc-may-1934-april-1954-these frequencies-reflect-the-highest-radio-frequency-that-can-be-used-forbroadcasting#!ds=22u2&display=line.

[51] Co2 (ppm) mauna loa, 1965-1980, (n.d.). https://datamarket.com/data/set/22v1/co2-ppm-mauna-loa-1965-%0A1980#!ds=22v1&display=line (accessed August 16, 2019).

[52] Monthly Lake Erie levels 1921 - 1970, (n.d.). https://datamarket.com/data/set/22pw/monthly-lake-erie-levels-1921-%0A1970#!ds=22pw&display=line (accessed August 16, 2019).

[53] M.C. Mackey, L. Glass, Oscillation and chaos in physiological control systems, Science (80-.). 197 (1977) 287–289.

[54] H.J. Song, C.Y. Miao, Z.Q. Shen, W. Roel, D.H. Maja, C. Francky, Design of fuzzy cognitive maps using neural networks for predicting chaotic time series, Neural Networks. 23 (2010) 1264–1275.

[55] C.-F. Juang, Y.-W. Tsao, A self-evolving interval type-2 fuzzy neural network with online structure and parameter learning, IEEE Trans. Fuzzy Syst. 16 (2008) 1411–1424.

[56] B.-T. Zhang, P. Ohm, H. Mühlenbein, Evolutionary induction of sparse neural trees, Evol. Comput. 5 (1997) 213–236.

[57] T. Hastie, R. Tibshirani, J. Friedman, Model assessment and selection, in: Elem. Stat. Learn., Springer, 2009: pp. 219–259.

[58] Chicco, Davide, Matthijs J. Warrens, and Giuseppe Jurman. "The coefficient of determination R-squared is more informative than SMAPE, MAE, MAPE, MSE and RMSE in regression analysis evaluation." PeerJ Computer Science 7 (2021): e623.

Nastaran Darjani received her B.Sc. degree in Computer Science from the Babol University of Technology, Babol, Iran. Her areas of interest are visual perception in the human brain and human vision-inspired neural networks.

Hesam Omranpur received his B.Sc. degree in Computer Engineering-Software Engineering from the Iran University of Science and Technology, and his M.S. and Ph.D. degrees in Artificial Intelligence from the Amir Kabir University of Technology, Tehran, Iran in 2006, 2009, and 2016 respectively. He is currently an assistant professor with the Department of Electrical and Computer Engineering, the Babol Noshirvani University of Technology, Iran. His current research interests include optimization, machine learning, pattern recognition, and brain-computer interface.

International Journal of Industrial Electronics, Control and Optimization © 2022 IECO
Vol. 5, No. 1, pp. 51-62 , Jan (2022)

Development of Quasi Z-Source Inverters Based on Diode-Cells: Analysis and Implementation

Sara Laali[1,†], and Ebrahim Babaei[2]

[1]Department of Electrical Engineering, North Tehran Branch, Islamic Azad University, Tehran, Iran
[2] Faculty of Electrical and Computer Engineering, University of Tabriz, Tabriz, Iran

ABSTRACT

This paper proposes two newly developed quasi Z-source inverters (QZSI) based on two new diode-cells. The proposed inverters are called continuous diode assisted quasi Z-source inverter (CDQAZSI) and discontinuous diode assisted quasi Z-source inverter (DDQAZSI). These inverters are thoroughly examined in three modes: two-cell QZSI, three-cell QZSI, and n-cell QZSI that is called developed QZSI. Additionally, the equations of the diodes' voltage and current, capacitors' voltage stress, boost factor, inductor currents, and dc-link current are computed. All equations are given for the proposed generalized topologies. The major advantage of these inverters is the potential of deriving desired boost factor value devoid of extra elements. Furthermore, increasing the number of the diode-cells used in the proposed QZSI reduces the values of dc-link current, inductor current, and diode current. Lastly, to verify the performance of the proposed topologies, the practicality of the proposed QZSI is authenticated by experimental results through a laboratory prototype.

Article Info

Keywords:
Boost factor, Continuous current; Diode-cell, Discontinuous current, Shoot-through state (ST), Z-source inverters.
Article History:
Received 2020-12-8
Accepted 2021-8-12

I. INTRODUCTION

Two types of conventional inverters are voltage and current source inverters. The magnitude of input dc voltage in voltage source inverters is less than the magnitude of the effective output voltage, so these inverters function as buck inverters. However, current source inverters function as boost inverters. Individually, these inverters do not function in the buck-boast mode. Furthermore, in voltage source inverters, electromagnetic interference or error gating of power switches will short-circuit the switches of the inverters while an open circuit of the switches will occur when similar conditions occur for current source inverters. These phenomena destroy the inverter [1-4]. Consequently, Z-source inverters (ZSIs) were presented in 2003 by Peng to resolve these limitations [1]. ZSIs are composed of an X-shaped connection of two capacitors and two inductors. ZSIs function in two modes of operation, the shoot-through (ST) and non-shoot-through (non-ST) states. The output voltage magnitude can be controlled, i.e., increased or reduced in the ST state. Therefore, ZSIs have buck-boost functionality. The buck-boost functionality is a major advantage of ZSIs when compared to traditional voltage and current source inverters. Other merits of ZSIs are less distorted output waveform and high reliability [5-6]. Applications of ZSIs are hybrid electric drives, PV systems, motor drives, wind power, distributed generations, and solar cell systems [6-9].

There are different control methods for ZSIs, among which the major ones include the maximum constant boost control method, the maximum boost control method, the simple boost control method, and the maximum boost control method with third-harmonic injection [10-12]. These control methods have their own advantages and disadvantages. This paper focuses on the simple boost control method.

Since the introduction of conventional ZIS topology, various ZSI topologies have been published. Extended boost switched-

[†]**Corresponding Author**: s.laali@iau-tnb.ac.ir
Tel: +98-2177009801, Fax: +98-2177009848, North Tehran Branch, Islamic Azad University
Department of Electrical Engineering, North Tehran Branch, Islamic Azad University, Tehran, Iran

inductor/active-switched-capacitor quasi-Z-source inverters [13], L-Z-source inverters [14], half-bridge Z-source converters [6], gain half-bridge switched-boost inverters [7], switched-coupled-inductor quasi-Z-source inverters [15], quasi-switched boost inverters [16], quasi-Z-source cascaded hybrid five-level inverters [17], and a group of single-phase Z-source AC-AC converters with magnetic coupling and safe-commutation strategy [18], switched boost inverter using a transformer [19], extended switched-inductor quasi-Z-source inverters [20], and new switched-inductor quasi-Z-source inverters [21] are some of the ZSIs presented. Moreover, other quasi-Z-source inverters were presented in [22-24].

The low boost factor is the major disadvantage of these topologies. The boost factor value is increased by increasing the duty cycle of the ST state. Nevertheless, a new drawback of low value for modulation technique is introduced. Applying a dc-dc converter is another strategy for increasing the boost factor value, which also results in increased cost and weight of the inverter.

Two newly developed QZSIs are proposed to solve the disadvantage of the low boost factor and the other disadvantages. These inverters are based on two new diode-cells as basic units. Additionally, the proposed topologies are thoroughly analyzed and the equations of the diode voltage-current stress, capacitor voltage stress, boost factor, inductor currents, and dc-link current are computed in these inverters. The boost factor value is increased when more of the proposed basic units are used, which in turn decreases the diode and inductor current values. These are some merits of the proposed inverter. Lastly, the accurate operation of the proposed QZSI is proven by means of experimental results.

II. PROPOSED TOPOLOGY

The power circuits of the diode-assisted quasi Z-source inverters (DAQZSIs) are illustrated in Figs. 1(a) and (b), respectively [22]. Each inverter is made-up of one diode-cell and one conventional Z-source inverter. Individual diode cells as a new basic unit comprise of two diodes, one inductor, and one capacitor. As shown in Fig. 1, based on the connection of the elements used, there are two different states for the DAQZSI. The current of the input dc source will be continuous if the inductance of the basic unit is series-connected to the input dc source. This inverter is called a continuous diode-assisted quasi Z-source inverter (CDAQZSI) and is shown in Fig. 1(a). Otherwise, the current of the input dc source is discontinuous if the last inductance is not connected series. This inverter is shown in Fig. 1(b) and is called a discontinuous diode-assisted quasi Z-source inverter (DDQAZSI). The modulation strategies of the proposed QZSIs are as same as conventional ZSIs.

This proposes two newly developed DAQZSIs that are thoroughly analyzed. In these inverters, the capacitor and inductor values are deemed equal. The various stages of analysis use a current source and a power switch S to model the single-phase inverter. Additionally, the general equations are calculated for the voltage and current of all elements used, so the boost factor equation is calculated.

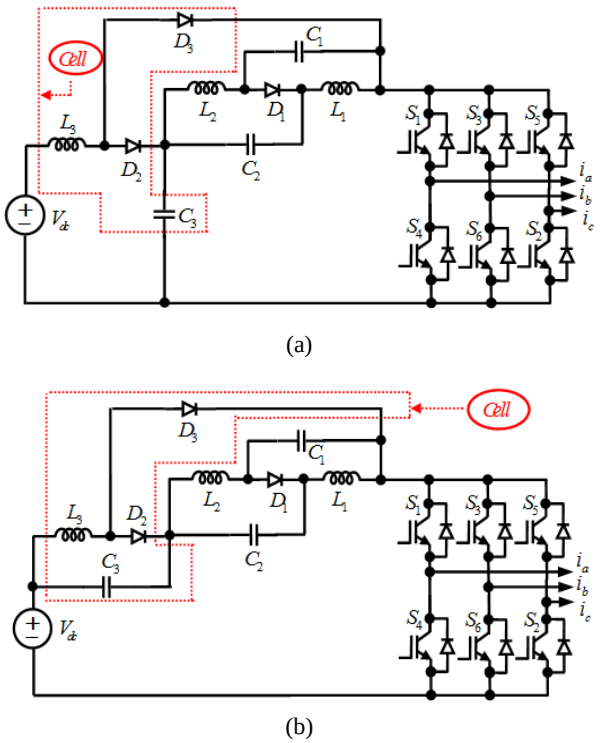

Fig. 1. The power circuit of DAQZSI topologies based on one diode-cell; (a) continuous state; (b) discontinuous state

A. Proposed CDAQZSI

This sub-section proposes the new topology for the QZSI based on a diode-assisted basic unit and in the continuous current state. The new topology is analyzed with respect to the use of two basic units, the use of three basic units, and finally, its developed topology. Moreover, the voltage equations of capacitors and diodes and the current equations of inductors, diodes, and dc-link are calculated in addition to the equation of the boost factors for all states.

B. Proposed CDAQZSI Based on Two Diode-cells

Fig. 2 illustrates the proposed CDAQZSI power circuit. The proposed topology is derived from incorporating two diode-cells into the traditional ZSI. The proposed topology is composed of four inductors, four capacitors, and five diodes. Two states of operation are possible in the proposed topology, shoot-though and non-shoot-through states. Switch S and diodes D_3 and D_5 conduct while diodes D_1, D_2, and D_4 are turned off during the ST state. During this mode, the input voltage and capacitors charge the inductors. During non-ST state, diodes D_1, D_2, and D_4 conduct while switch S and diodes D_3 and D_5 are turned-off. Therefore, inductors discharge the

stored energy to charge the capacitors.

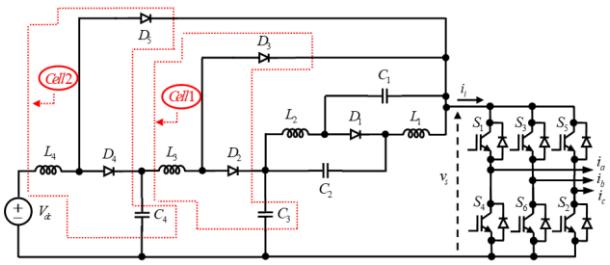

Fig. 2. Two-diode-cell QZSI with continuous current

C. Computation of Boost Factor and Capacitor Voltage Stress

By applying KVL for the ST power circuit, we have:

$$v_{L2}+V_{C1}=v_{L1}+V_{C2} \quad (1)$$

$$V_{C4}+v_{L3}=0 \quad (2)$$

$$v_{L4}-V_{dc}=0 \quad (3)$$

$$V_{C3}+V_{C1}+v_{L2}=0 \quad (4)$$

$$V_{C3}+V_{C2}+v_{L1}=0 \quad (5)$$

Applying KVL to the non-ST power circuit will produce the following equations:

$$V_{C2}=v_{L2} \quad (6)$$

$$V_{C1}=v_{L1} \quad (7)$$

$$v_{L4}-V_{dc}-V_{C4}=0 \quad (8)$$

$$v_{L3}-V_{C3}+V_{C4}=0 \quad (9)$$

where V_{C1} to V_{C4} are the capacitor voltage of C_1 to C_4, respectively, V_{L1} to V_{L4} are the inductor voltage of L_1 to L_4, respectively, and V_{dc} is the dc voltage source.

According to the above equations and based on the point that the average voltage of the inductor is equal to zero, the following expressions are developed:

$$V_{C1}=V_{C2}=\frac{-D_{sh}}{(1-2D_{sh})(1-D_{sh})^2}V_{dc} \quad (10)$$

$$V_{C3}=\frac{-1}{(1-D_{sh})^2}V_{dc} \quad (11)$$

$$V_{C4}=\frac{-1}{1-D_{sh}}V_{dc} \quad (12)$$

Boost factor of the proposed QZSI is computed as:

$$v_{s,\max}=-(V_{C1}+V_{C2}+V_{C3})=\frac{1}{(1-2D_{sh})(1-D_{sh})^2}V_{dc} \quad (13)$$

$$B=\frac{v_{s,\max}}{V_{dc}} \quad (14)$$

where the voltage across switch S is v_S. From the equations above, putting (10) to (12) into (14), the boost factor value is computed as:

$$B=\frac{1}{(1-2D_{sh})(1-D_{sh})^2} \quad (15)$$

By comparing (15) with the traditional ZSI boost factor value, which is equal to $B=1/(1-2D_{sh})$, it is evident that this new topology increases boost factor value. Additionally, by comparing this structure with the one-diode cell QZSI, which is equal to $B=1/(1-2D_{sh})(1-D_{sh})$, it is obvious that the boost factor is increased when one basic unit is added.

D. Computation of Diodes Voltage Stress

Implementing the KVL analysis of Fig. 2 and also factoring capacitors voltage stress value based on (10) to (12) will yield:

$$V_{D1}=V_{C1}+V_{C2}+V_{C3}=\frac{-1}{(1-2D_{sh})(1-D_{sh})^2}V_{dc} \quad (16)$$

$$V_{D2}=V_{C3}=\frac{-1}{(1-D_{sh})^2}V_{dc} \quad (17)$$

$$V_{D3}=V_{C1}+V_{C2}=\frac{-2D_{Sh}}{(1-2D_{Sh})(1-D_{Sh})^2}V_{dc} \quad (18)$$

$$V_{D4}=V_{C4}=\frac{-1}{1-D_{sh}}V_{dc} \quad (19)$$

$$V_{D5}=-V_{C4}+V_{C3}+V_{C1}+V_{C2}=\frac{2D_{sh}^2-3D_{sh}}{(1-2D_{sh})(1-D_{sh})^2}V_{dc} \quad (20)$$

E. Computation of Diodes, Inductors and DC-Link current values

By implementing the KCL analysis of Fig. 2 and given that the average capacitor current value for a period is zero, the following are derived:

$$i_i=(1-D_{sh})(1-2D_{sh})I_{dc} \quad (21)$$

$$I_{L1}=I_{L2}=(1-D_{sh})^2I_{dc} \quad (22)$$

$$I_{L3}=(1-D_{sh})I_{dc} \quad (23)$$

$$I_{L4}=I_{dc} \quad (24)$$

in which I_{dc} and I_{L1} to I_{L4} are the input dc current and current of inductors L_1 to L_4. In addition, i_i is the dc-link current.

By implementing the KCL analysis of Fig. 2 and putting (21) to (24), we derive:

$$I_{D1}=I_{L1}+I_{L2}-i_i=(1-D_{sh})I_{dc} \quad (25)$$

$$I_{D2}=I_{L3}=(1-D_{sh})I_{dc} \quad (26)$$

$$I_{D3}=I_{L3}=(1-D_{sh})I_{dc} \quad (27)$$

$$I_{D4}=I_{L4}=I_{dc} \quad (28)$$

$$I_{D5}=I_{L4}=I_{dc} \quad (29)$$

Contrasting the equations above, it is conspicuous that the added diode current values are equivalent. That is, diodes D_2 and D_3 of the first diode-cell have equivalent current values and the diodes of the second diode-cell D_4 and D_5 also have

equivalent current values. Additionally, by comparing to the traditional ZSI, increasing the quantity of the utilized proposed basic unit while decreasing the diode, inductor and dc-link current values are obtained.

F. Proposed CDAQZSI based on Three Diode-cells

Three diode-cells based on QZSI are proposed in this section. By adding two diodes, one inductor, and one capacitor to the two diode-cells, a three-diode-cell QZSI topology will be produced whose power circuit is illustrated by Fig. 3.

In the ST state, diodes D_3, D_5 and D_7 are turned on and diodes D_1, D_2, D_4 and D_6 are turned off. Therefore, the inductors and capacitors will be charged and discharged, respectively. During the non-ST state, diodes D_1, D_2, D_4 and D_6 are turned on and diodes D_3, D_5 and D_7 are turned off. Therefore, the inductors and capacitors will be discharged and charged, respectively. In this topology, equations of dc-link current, inductor current, capacitor voltage stress, diode voltage stress, and diode current are summarized in Table I.

By implementing the KVL analysis of Fig. 3 at the non-ST state, we derive:

$$v_{s,\max} = -(V_{C1} + V_{C2} + V_{C3}) \tag{30}$$

The boost factor is derived by substituting the capacitors voltage stress from Table I into (30) and changing this equation into (14):

$$B = \frac{v_{s,\max}}{V_{dc}} = \frac{1}{(1-2D_{sh})(1-D_{sh})^3} \tag{31}$$

By comparing (31) with the obtained boost factor in the conventional Z-source inverter that is equal to $B = 1/(1-2D_{sh})$, it results that this new topology increases the value of the boost factor. In addition, by contrasting the equation of the diode current in Table I, the results show that the diode currents of D_1, D_2, D_3 are equivalent. Similarly, the results show that the equation of diodes current of D_4 and D_5 are equivalent. Furthermore, the input dc current value and diodes D_6 and D_7 current values are equivalent. Additionally, the diode current values can be minimized by a factor of (1-D_{sh}) when D_{sh} value is increased. In addition, by increasing the value of D_{sh}, the diodes' current values are decreased by a factor of (1-D_{sh}). This is the same explanation about the inductors' current. When more basic units are used, their values are reduced by a factor of (1-D_{sh}).

G. Proposed Developed CDAQZSI

So, to derive the required boost factor, it is feasible to develop the proposed QZSI with the same number of active elements by adding n diode-cells in a back-to-back state at the end of the inverter. This characteristic, when compared to the traditional ZSI, is the major advantage of the proposed inverter. Fig. 4 shows the power circuit of the proposed inverter. Individual cells of the proposed inverter are composed of two diodes, one inductor, and one capacitor, respectively. The numbers of the power electronic elements in the proposed CDAQZSI are derived from

$$N_L = n + 2 \tag{32}$$

$$N_C = n + 2 \tag{33}$$

$$N_D = 2n + 1 \tag{34}$$

in which n is the number of the diode-cells used.

H. Computation of Boost Factor and Capacitor Voltage Stress

By contrasting the capacitor voltage stress of two and three diode-cells of C_1 and C_2 by (10) and Table 1 equations, it is evident that the capacitor voltage stress is affected by a factor of $1/1-D_{sh}$ when the number of the basic units is increased. The same explanation about the capacitor voltage stress is valid. Furthermore, the voltage stress of the individual diode-cells is affected by the same factor of $1/1-D_{sh}$ when the number of the basic units is increased, i.e. the new capacitor in the existing topology and the capacitor in this new topology are affected by the same factor. For example, the voltage stress of C_3 in the two-diode-cell QZSI is equivalent to the voltage stress of C_4 in the three-diode-cell QZSI.

Moreover, as it is clear from the diode basic unit's topology, by utilizing individual diode-cell, two diodes are included in the proposed ZSI. Additionally, by contrasting (16) and (17) with the same equations in Table I, it is apparent that the voltage stress of the diodes is affected by a factor of $1/1-D_{sh}$ when the number of diode-cells utilized is increased.

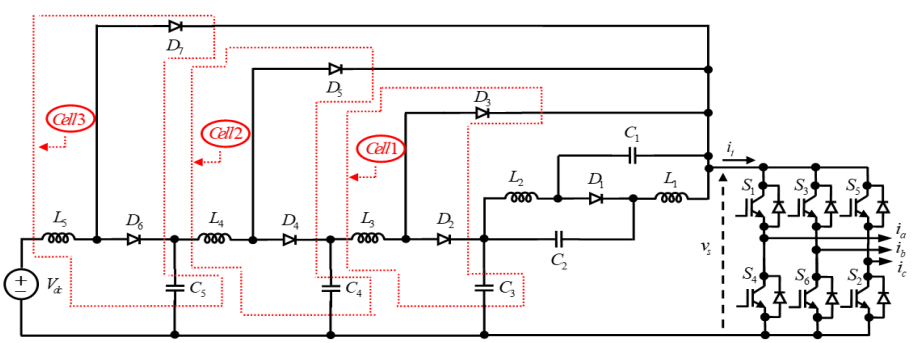

Fig. 3. A three-diode-cell QZSI with the continuous current.

TABLE I

VOLTAGE AND CURRENT EQUATIONS OF ALL ELEMENTS IN THE THREE-CELL CDAQZSI

Capacitors' Voltage Equations	Inductors' Current Equations	Diodes' Voltage Equations	Diodes' Current Equations
$V_{C1}=V_{C2}=\frac{-D_{sh}}{(1-2D_{sh})(1-D_{sh})^3}V_{dc}$	$I_{L1}=I_{L2}=(1-D_{sh})^3 I_{dc}$	$V_{D1}=\frac{-1}{(1-2D_{sh})(1-D_{sh})^3}V_{dc}$	$i_i=(1-D_{sh})^2(1-2D_{sh})I_{dc}$
$V_{C3}=\frac{-1}{(1-D_{sh})^3}V_{dc}$	$I_{L3}=(1-D_{sh})^2 I_{dc}$	$V_{D2}=\frac{-1}{(1-D_{sh})^3}V_{dc}$	$I_{D1}=I_{D2}=I_{D3}=(1-D_{sh})^2 I_{dc}$
$V_{C4}=\frac{-1}{(1-D_{sh})^2}V_{dc}$	$I_{L4}=(1-D_{sh})I_{dc}$	$V_{D3}=\frac{-2D_{Sh}}{(1-2D_{Sh})(1-D_{Sh})^3}V_{dc}$	$I_{D4}=I_{D5}=(1-D_{sh})I_{dc}$
$V_{C5}=\frac{-1}{1-D_{sh}}V_{dc}$	$I_{L5}=I_{dc}$	$V_{D4}=\frac{-1}{(1-D_{sh})^2}V_{dc}$	$I_{D6}=I_{D7}=I_{dc}$
-	-	$V_{D5}=\frac{2D_{sh}^2-3D_{sh}}{(1-2D_{sh})(1-D_{sh})^3}V_{dc}$ $V_{D6}=\frac{-1}{1-D_{sh}}V_{dc}$ $V_{D7}=\frac{-2D_{sh}^3+5D_{sh}^2-4D_{sh}}{(1-2D_{sh})(1-D_{sh})^3}V_{dc}$	-

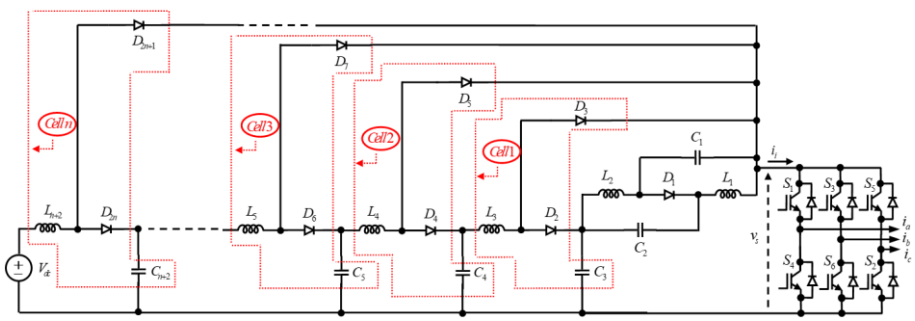

Fig. 4. The proposed developed QZSI topology with the continuous current

This characteristic is applied for series connection of inductor and diodes in individual cells. In addition, by comparing (16), (17), and (19) with the same equation in Table I, it is apparent that in the same diode-cell, the voltage stress of capacitors and series-connected diodes are equivalent. This means that in the same diode-cell, the voltage stress of capacitor C_3 is equivalent to the voltage stress of diode D_2. Moreover, contrasting equations of the inductor current of two-diode-cell-based QZSI (22) to (24) with the same equations in the three-diode-cell QZSI in Table I, it is apparent that the inductor current value is reduced by a factor of (1-D_{sh}) when the number of the diode-cells used is increased. Furthermore, the dc source current value is equivalent to the inductor current value because they are series-connected. In addition, by considering the diodes' current equations from (25) to (29) and the same equations in Table I, it is observed that the diode current value is reduced by a factor of (1-D_{sh}) when more diode-cells are applied. Additionally, the current values of the inductors and diodes in the same cell are equivalent. For example, the current values of inductors L_4 and diodes D_4 and D_5 are equivalent (I_{D4}=I_{D5}=I_{L4}). Therefore, it is feasible to derive current and voltage equations for n-cell CDAQZSI with various utilized elements as indicated in Table II.

The peak input voltage for this topology is expressed by:

$$v_{s,\max}=-(V_{C1}+V_{C2}+V_{C3}) \tag{35}$$

In addition, by substituting the value of voltage capacitors from Table II into (14), the boost factor value is derived by:

$$B=\frac{1}{(1-2D_{Sh})(1-D_{Sh})^n} \tag{36}$$

As it is clear from (36), the value of the boost factor is increased with a factor of $1/1-D_{sh}$ by adding the number of utilized new diode-assisted basic units. This result is also derived without using extra active elements. In addition, the current values of dc-link, diodes, and inductors are also decreased by increasing the number of the basic units.

TABLE II

VOLTAGE AND CURRENT EQUATIONS OF ALL ELEMENTS IN n-CELL CDAQZSI

Capacitors' Voltage Equations	Inductors' Current Equations	Diodes' Voltage Equations	Diodes' Current Equations
$V_{C1}=V_{C2}=\frac{-D_{sh}}{(1-2D_{sh})(1-D_{sh})^{n}}V_{dc}$	$I_{L1}=I_{L2}=\frac{(1-D_{sh})}{(1-2D_{sh})}\mathrm{i}_{i}=(1-D_{sh})^{n}I_{dc}$	$V_{D1}=\frac{-1}{(1-2D_{sh})(1-D_{sh})^{n}}V_{dc}$	$\mathrm{i}_{i}=(1-2D_{sh})(1-D_{sh})^{n-1}I_{dc}$
$V_{C3}=\frac{-1}{(1-D_{sh})^{n}}V_{dc}$	$I_{L\,j+1}=\frac{1}{(1-D_{sh})}I_{L\,j}$ for $j=2,3,4,\cdots,n$	$V_{D2}=\frac{-1}{(1-D_{sh})^{n}}V_{dc}$	$I_{D1}=I_{D2}=I_{D3}=(1-D_{sh})^{n-1}I_{dc}$
$V_{C\,j+2}=(1-D_{sh})^{j-1}V_{C3}$ for $j=1,2,3,\cdots,n$	$I_{L\,n+2}=I_{dc}$	$V_{D3}=\frac{-2D_{sh}}{(1-2D_{sh})(1-D_{sh})^{n}}V_{dc}$	$I_{D\,2j}=I_{D\,2j+1}=\frac{1}{1-D_{sh}}I_{D\,2j-1}$ for $j=2,3,4,\cdots,n$
-	-	$V_{D\,2j+1}=\frac{1}{(1-D_{sh})}-\frac{1}{(1-2D_{sh})(1-D_{sh})^{j}}V_{dc}$ $j=2,3,\cdots,n$ $V_{D2j}=(1-D_{sh})^{j-1}V_{D2}$ for $j=1,2,3,\cdots,n$	-

I. Proposed DDAQZSI

In this sub-section, another new topology is proposed for QZSI based on the diode-assisted basic unit and in the discontinuous current state. This new topology is analyzed based on using two basic units, three basic units, and finally its developed topology. In addition, the related equations for all states of all used elements are calculated, and then the general equation for the boost factor, voltage, and current of the used power electronic devices are proposed.

J. Proposed DDAQZSI Based on Two Diode-cells

The power circuit of the proposed two-cell DDAQZSI is shown in Fig. 5. As illustrated by this figure, one basic unit is composed of two diodes, one inductor, and one diode, which are added to the one-cell DAQZSI. The operating modes of this inverter are segmented into ST and non-ST states. During the ST state, diodes D_1, D_2, D_4 are turned off whiles switch S and diodes D_3 and D_5 are turned on. Therefore, the capacitors and inductors will be discharged and charged accordingly. During the non-ST state, diodes D_1, D_2, D_4 are turned on while switch S and diodes D_3 and D_5 are turned off. Therefore, the capacitors and inductors will be charged and discharged accordingly.

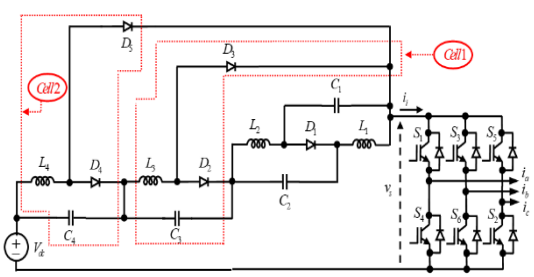

Fig. 5. The two-cell DAQZSI with the discontinuous current.

K. Computation of Boost Factor and Capacitor Voltage Stress

By applying KVL in Fig. 5, we have:

$$v_{L4}-V_{dc}=0 \tag{37}$$

$$v_{L2}+V_{C1}=v_{L1}+V_{C2} \tag{38}$$

$$-V_{dc}+V_{C4}+v_{L3}=0 \tag{39}$$

$$-V_{dc}+V_{C3}+V_{C4}+V_{C1}+v_{L2}=0 \tag{40}$$

$$-V_{dc}+V_{C3}+V_{C4}+V_{C2}+v_{L1}=0 \tag{41}$$

$$V_{C4}=v_{L4} \tag{42}$$

$$v_{L3}=V_{C3} \tag{43}$$

$$V_{C2}=v_{L2} \tag{44}$$

$$V_{C1}=v_{L1} \tag{45}$$

$$v_{L1}=v_{L2} \tag{46}$$

$$V_{C1}=V_{C2} \tag{47}$$

Given that the inductor average voltage is zero, the following results are derived:

$$V_{C1}=V_{C2}=\frac{-D_{sh}}{(1-2D_{sh})(1-D_{sh})^{2}}V_{dc} \tag{48}$$

$$V_{C3}=\frac{-D_{sh}}{(1-D_{sh})^{2}}V_{dc} \tag{49}$$

$$V_{C4}=\frac{-D_{sh}}{1-D_{sh}}V_{dc} \tag{50}$$

In addition, implementing the KVL analysis of Fig. 5 will yield the following:

$$v_{s,\max}=V_{dc}-(V_{C4}+V_{C3}+V_{C2}+V_{C1}) \tag{51}$$

Substituting the values of V_{C1} to V_{C4} from (48) to (50) into

(51), the peak inverter input dc voltage is equivalent to:

$$v_{s,\max} = \frac{1}{(1-2D_{sh})(1-D_{sh})^2} V_{dc} \quad (52)$$

In DDAQZSI, the boost factor is computed by:

$$B = \frac{v_{s,\max}}{V_{dc}} = \frac{1}{(1-2D_{sh})(1-D_{sh})^2} \quad (53)$$

By comparing (53) with the obtained boost factor in the conventional Z-source inverter, which is equal to $B = 1/(1-2D_{sh})$, it results that this new topology increases the value of the boost factor.

L. Computation of Diodes Voltage Stress

Implementing the KVL analysis of Fig. 5 and substituting the voltage values of capacitors C_1 to C_4 from (48) to (50) into the equations of diodes voltage is derived by:

$$V_{D1} = \frac{-1}{(1-2D_{sh})(1-D_{sh})^2} V_{dc} \quad (54)$$

$$V_{D2} = -V_{dc} + V_{C3} + V_{C4} = \frac{-1}{(1-D_{sh})^2} V_{dc} \quad (55)$$

$$V_{D3} = V_{C1} + V_{C2} = \frac{-2D_{Sh}}{(1-2D_{Sh})(1-D_{Sh})^2} V_{dc} \quad (56)$$

$$V_{D4} = V_{C4} - V_{dc} = \frac{-1}{1-D_{sh}} V_{dc} \quad (57)$$

$$V_{D5} = V_{C3} + V_{C1} + V_{C2} = \frac{2D_{sh}^2 - 3D_{sh}}{(1-2D_{sh})(1-D_{sh})^2} V_{dc} \quad (58)$$

M. Computation of Diodes, Inductors, and DC-Link Current Values

By implementing the KCL analysis of Fig. 5 and given that the average capacitor current value for a period is zero, the following are derived:

$$i_i = I_{dc} \quad (59)$$

$$I_{L1} = I_{L2} = \frac{(1-D_{sh})}{(1-2D_{sh})} I_{dc} \quad (60)$$

$$I_{L3} = \frac{1}{1-2D_{sh}} I_{dc} \quad (61)$$

$$I_{L4} = \frac{1}{(1-D_{sh})(1-2D_{sh})} I_{dc} \quad (62)$$

By implementing the KCL analysis of Fig. 5 and putting (59) to (62), we derive

$$I_{D1} = I_{L1} + I_{L2} - i_i = \frac{1}{1-2D_{sh}} I_{dc} \quad (63)$$

$$I_{D2} = I_{D3} = I_{L3} = \frac{1}{1-2D_{sh}} I_{dc} \quad (64)$$

$$I_{D4} = I_{D5} = I_{L4} = \frac{1}{(1-D_{sh})(1-2D_{sh})} I_{dc} \quad (65)$$

N. Proposed Three-cell DDAQZSI

The analysis of the proposed three-cell DDAQZSI is investigated in this section. It is derived by adding two diodes, one inductor, and one capacitor to the two-cell DDAQZSI. Fig. 6 illustrates the three-cell DDAQZSI power circuit. Two states of operation are possible in the proposed topology, shoot-though and non-shoot-through states. Diodes D_3, D_5, and D_7 conducts whiles diodes D_1, D_2, D_4, and D_6 are turned off during the ST state. Therefore, the capacitors and inductors will be discharged and charged accordingly. During the non-ST state, diodes D_1, D_2, D_4, and D_6 are turned on whiles diodes D_3 and D_5 are turned off. Therefore, the capacitors and inductors will be charged and discharged accordingly. Table III shows the equations obtained for all elements in the topology.

The implementation of the KVL analysis of Fig. 6 will yield the following results:

$$v_{s,\max} = V_{dc} - (V_{C5} + V_{C4} + V_{C3} + V_{C2} + V_{C1}) \quad (66)$$

By substituting capacitors voltage stress from Table III into (66) and putting this equation into (53), the boost factor value is derived from:

$$B = \frac{v_{s,\max}}{V_{dc}} = \frac{1}{(1-2D_{sh})(1-D_{sh})^3} \quad (67)$$

By considering (53) and (67), it is evident that the boost factor value is increased by a factor of $1/1-D_{sh}$ when one basic unit is added. Contrasting equations of diodes' current from Table III, it is evident that diodes D_1, D_2, and D_3 have equivalent current values. Likewise, diodes D_4 and D_5 have equivalent current equations. This analysis is valid for diodes D_6 and D_7. Simply put, the diode current equations for individual cells are equivalent when each cell is added.

O. Proposed Developed DDAQZSI

So, to derive the required boost factor, it is feasible to develop the proposed DDAQZSI with the same number of active elements by increasing the number of the basic unit used in a back-to-back state at the end of the inverter. This characteristic, when compared to the traditional ZSI, is the major advantage of the proposed inverter. Fig. 7 shows the power circuit of the proposed inverter. Individual cells of the proposed inverter are composed of two diodes, one inductor, and one capacitor. The number of the power electronic elements used in the proposed DDAQZSI is derived by:

$$N_L = n + 2 \quad (68)$$

$$N_C = n + 2 \quad (69)$$

$$N_D = 2n + 1 \quad (70)$$

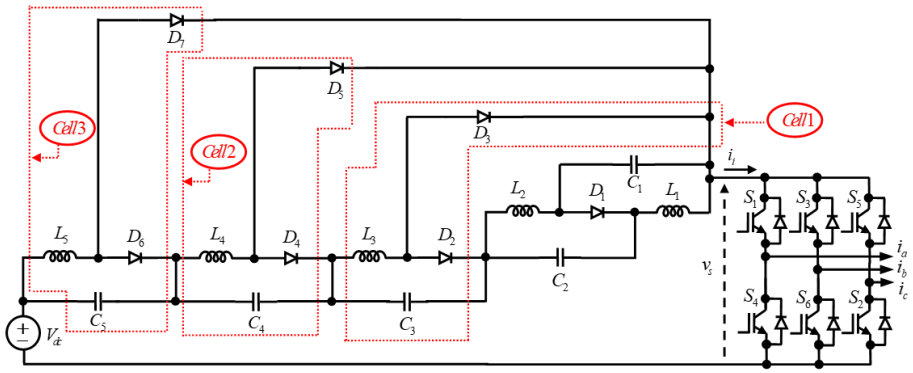

Fig. 6. The three-cell DDAQZSI power circuit with discontinuous current

TABLE III

VOLTAGE AND CURRENT EQUATIONS OF THREE-CELL DDAQZSI

Capacitors' Voltage Equations	Inductors' Current Equations	Diodes' Voltage Equations	Diodes' Current Equations
$V_{C1}=V_{C2}=\frac{-D_{sh}}{(1-2D_{sh})(1-D_{sh})^3}V_{dc}$	$I_{L1}=I_{L2}=\frac{1-D_{sh}}{1-2D_{sh}}I_{dc}$	$V_{D1}=\frac{-1}{(1-2D_{sh})(1-D_{sh})^3}V_{dc}$	$i_i=I_{dc}$
$V_{C3}=\frac{-D_{sh}}{(1-D_{sh})^3}V_{dc}$	$I_{L3}=\frac{1}{1-2D_{sh}}I_{dc}$	$V_{D2}=\frac{-1}{(1-D_{sh})^3}V_{dc}$	$I_{D1}=I_{D2}=I_{D3}=\frac{1}{1-2D_{sh}}I_{dc}$
$V_{C4}=\frac{-D_{sh}}{(1-D_{sh})^2}V_{dc}$	$I_{L4}=\frac{1}{(1-D_{sh})(1-2D_{sh})}I_{dc}$	$V_{D3}=\frac{-2D_{Sh}}{(1-2D_{Sh})(1-D_{Sh})^3}V_{dc}$	$I_{D4}=I_{D5}=\frac{1}{(1-D_{sh})(1-2D_{sh})}I_{dc}$
$V_{C5}=\frac{-D_{sh}}{1-D_{sh}}V_{dc}$	$I_{L5}=\frac{1}{(1-D_{sh})^2(1-2D_{sh})}I_{dc}$	$V_{D4}=\frac{-1}{(1-D_{sh})^2}V_{dc}$	$I_{D6}=I_{D7}=\frac{1}{(1-D_{sh})^2(1-2D_{sh})}I_{dc}$
-	-	$V_{D5}=\frac{2D_{sh}^2-3D_{sh}}{(1-2D_{sh})(1-D_{sh})^3}V_{dc}$ $V_{D6}=\frac{-1}{1-D_{sh}}V_{dc}$ $V_{D7}=\frac{-2D_{sh}^3+5D_{sh}^2-4D_{sh}}{(1-2D_{sh})(1-D_{sh})^3}V_{dc}$	-

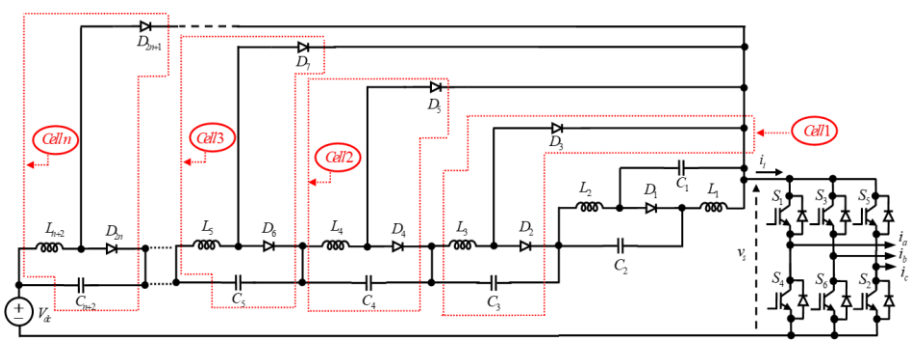

Fig. 7. The developed QZSI power circuit with discontinuous current

P. Computation of Boost Factor and Capacitor Voltage Stress

By contrasting the capacitor voltage stress values from (48) to (50) in the two-cell DDAQZSI with equivalent equations in Table III of the three-cell DDAQZSI, it is drawn that the factor of $1/1-D_{sh}$ affects the capacitor voltage stress equation when the number of the cells used is increased by one. Moreover, the voltage stresses of the capacitors in the previous and new structures are equivalent. That is to say that the voltage stress of capacitor C_3 in the two-cell DDAQZSI is

equivalent to the voltage stress of capacitor C_4 in the three-cell DDAQZSI.

As previously stated, adding two diodes to the basic structure increases the number of the cells used. These diodes are connected in parallel and series. In the main section of the circuit, inductors and one diode are connected in series whiles the remaining diode is parallel-connected. Furthermore, evaluating the diode voltage stress equations of Table III with (54) to (58), it is clear that the series-connected diodes are affected by a factor of $1/1-D_{sh}$.

Moreover, there are the same explanations for the inductors' current. In other words, by contrasting two-diode-cell-based QZSI inductors' current equations from (59) to (62) to three-diode-cell-based QZSI inductors' current equations from Table III, it results that the inductors' current values are affected by a factor of $1/1-D_{sh}$ when the number of the cells used are increased. Additionally, by evaluating diodes' current equations from (63) to (65) and the equivalent equations in Table III, it is drawn that the current equations of diodes D_1, D_2 and D_3 are equivalent and constant when the number of the diode-cells used are increased. Moreover, the current equations of other diodes are affected by a factor of $1/1-D_{sh}$ in comparison to the diode current equation. Finally, Table IV shows the n-cell summarized element equations for current and voltage in DDAQZSI.

Based on Table IV, the current values of diodes in individual cells are the same while the peak dc input voltage is equivalent to:

$$v_{s,\max} = V_{dc} - \sum_{i=1}^{n+2} V_{Ci} = \frac{1}{(1-2D_{Sh})(1-D_{Sh})^n} V_{dc} = BV_{dc} \qquad (71)$$

Obviously, it is drawn from (71) that the boost factor value of DDAQZSI is increased by a factor of $1/1-D_{sh}$ when the number of the used cells is also increased. It is obvious that the required value of the boost factor is achievable for this topology by using the equivalent D_{sh} value when juxtaposed to traditional ZSI. This characteristic is the major merit of the proposed developed DDAQZSI.

III. Comparison of the Proposed Topology with the Conventional ZSIs

In this section, to investigate the advantages and disadvantages of the proposed topologies (DDAQZSI and CDAQZSI), these topologies will be compared with several ZSIs. In this comparison, the values of the boost factor based on the number of the elements used are considered. Table I shows this comparison by considering the same value of the ST state duty cycle.

In this table, D shows the value of the ST state duty cycle and n is the number of the units used. As it is clear from the above table, the proposed topologies can obtain a higher value of the boost factor in comparison to other topologies by the same value of D. In addition, it is possible to develop the proposed topologies by increasing only the passive elements that lead to decreasing the losses of the converters in comparison to others. In other words, the value of the boost factor is however increased and the number of the used elements are increased but because of using passive elements, the power losses will not increase while to receive the same value of the boost factor by using other topologies, the power losses will be increased.

IV. Experimental Results

In this section, the correct performance of the proposed CDAQZSI is reconfirmed. To obtain these results, the experimental prototype of the proposed topology with two basic units shown in Fig. 2 is considered. Table V indicates the parameter values utilized for laboratory investigation. Additionally, a simple boost control technique is used and all components are assumed to be ideal.

TABLE VI
EXPERIMENTAL PARAMETERS

$100\,V$	*Input voltage* (V_i)
$5kHz$	*Switching frequency*
150Ω	R_L
6.3 mH	L_f
6 mH	$L_1 = L_2 = L_3 = L_4$
680 μF	$C_1 = C_2 = C_3 = C_4$
0.15	D_{ST}
50 Hz	f_o

Fig. 8 illustrates the experimental waveform of the proposed inverter's input source voltage of which the peak value is 200 V , which is equivalent to 197.6 V derived by computing Eq. (13). The experimental boost factor value is approximately 2, which is equivalent to 1.976 derived by computing Eq. (15). The proposed diode-cells are utilized in the proposed topology to obtain this increase.

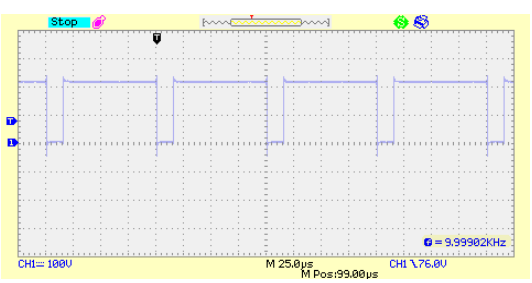

Fig. 8. The input voltage waveform of CDAQZSI

TABLE IV

VOLTAGE AND CURRENT EQUATIONS OF ALL ELEMENTS USED IN n-CELL DDAQZSI

Capacitors' Voltage Equations	Inductors' Current Equations	Diodes' Voltage Equations	Diodes' Current Equations
$V_{C1}=V_{C2}=\frac{-D_{sh}}{(1-2D_{sh})(1-D_{sh})^{n}}V_{dc}$	$I_{L1}=I_{L2}=\frac{1-D_{sh}}{1-2D_{sh}}I_{dc}$	$V_{D1}=\frac{-1}{(1-2D_{sh})(1-D_{sh})^{n}}V_{dc}$	$i_i=I_{dc}$
$V_{C3}=\frac{-D_{sh}}{(1-D_{sh})^{n}}V_{dc}$	$I_{L\,j+2}=\frac{1}{(1-D_{sh})}I_{L\,j+1}$ for $j=1,2,3,4,\cdots,n$	$V_{D2}=\frac{-1}{(1-D_{sh})^{n}}V_{dc}$	$I_{D1}=I_{D2}=I_{D3}=\frac{1}{1-2D_{sh}}I_{dc}$
$V_{C\,j+2}=(1-D_{sh})^{j-1}V_{C3}$ for $j=1,2,3,\cdots,n$	-	$V_{D\,2\,j+1}=\frac{-2D_{sh}}{(1-2D_{sh})(1-D_{sh})^{j}}V_{dc}+\sum_{j=2}^{n}\frac{-D_{sh}}{(1-D_{sh})^{j}}$ for $j=1,2,3,\cdots,n$	$I_{D\,2\,j}=I_{D\,2\,j+1}=\frac{1}{(1-D_{sh})^{j-1}(1-2D_{sh})}I_{dc}$ for $j=2,3,4,\cdots,n$
-		$V_{D\,2\,j}=(1-D_{sh})^{j-1}V_{D2}$ for $j=1,2,3,\cdots,n$	-

TABLE V

COMPARISON OF NUMBER OF ELEMENTS AND BOOST FACTOR FOR PROPOSED TOPOLOGY WITH CONVENTIONAL ZSIs

No.	Topologies	Value of Boost Factor	No. of Diode	No. of Capacitors	No. of Inductors
1	Proposed (DDAQZSI and CDAQZSI)	$1/(1-2D)(1-D)^{m}$ for $m=1,2,3,\cdots,n$	$N_D=2n+1$	$N_C=n+2$	$N_L=n+2$
2	[25]	$1/(1-2D)$	1	3	2
3	[26]	$(1+D)/(1-3D)$	1	2	4
3	[14]	$(1+D)/(1-D)$	3	0	2
5	[18]	$1/(1-2D)(1-D)$	2	3	3

The experimental capacitors' voltage waveforms are illustrated in Fig. 9. Capacitors C_1 and C_2 have equivalent voltage values, which is $32\,V$ as is depicted in Fig. 9(a). Approximately, this value is equivalent to $29.66\,V$, which is derived by computing Eq. (10). Fig. 9(b) illustrates the waveform of capacitor C_3 's voltage value. The voltage magnitude from this waveform is $140\,V$, which is almost approximately equivalent to $138.4\,V$ obtained from computing Eq. (11). Fig. 10 illustrate the voltage waveform values of diodes D_1 to D_5. The voltage magnitudes of these diodes D_1 to D_5 are equivalent to $200\,V$, $140\,V$, $60\,V$, $120\,V$, and $82\,V$, respectively. These values are almost equivalent to $197.7\,V$, $138.4\,V$, $59.3\,V$, $117.6\,V$, and $80.07\,V$, respectively, derived by computing Eq. (16) to (20).

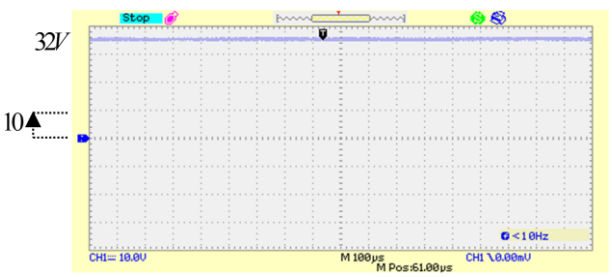

(a)

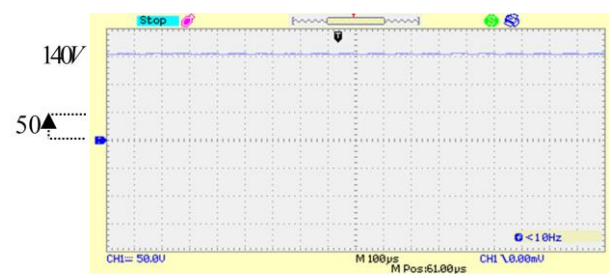

(b)

Fig. 9. Capacitors' voltage waveforms; (a) $V_{C1}=V_{C2}$; (b) V_{C3}

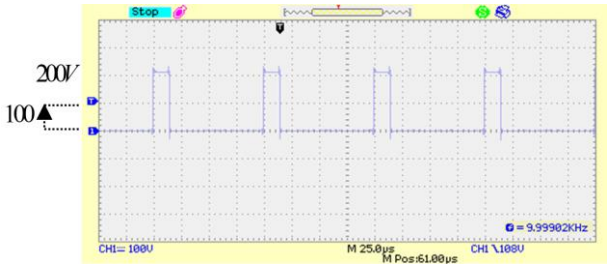

(a)

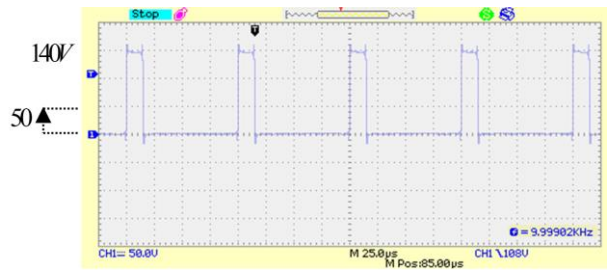

(b)

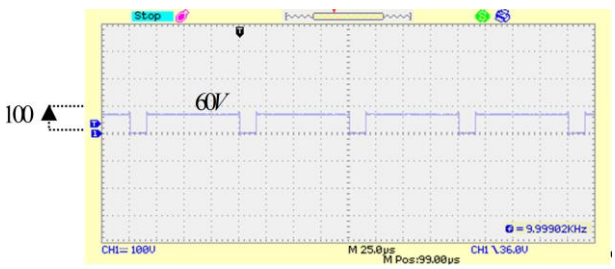

(c)

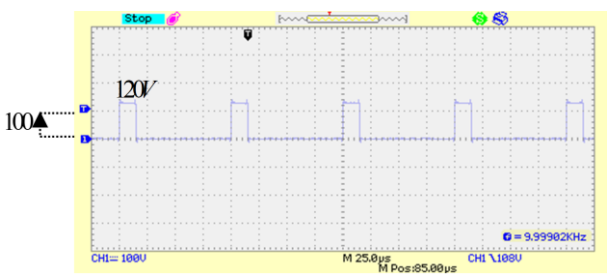

(d)

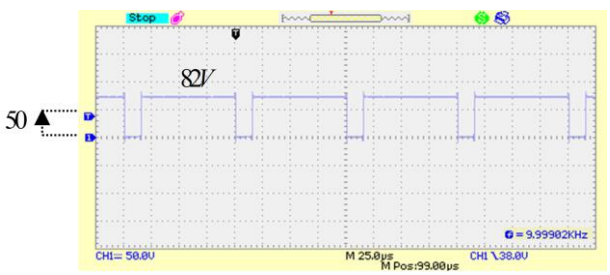

(e)

Fig. 10. Diodes' voltage waveforms; (a) V_{D1} ; (b) V_{D2} ; (c) V_{D3} ; (d) V_{D4} ; (e) V_{D5}

V. CONCLUSION

Two newly developed QZSIs created on two novel diode-cells are proposed. These topologies, which are called DDAQZSI and CDAQZSI, are capable of increasing the boost factor to the required magnitude without increasing the number of the active elements used. The proposed QZSIs are examined in three conditions: a two-diode-cell QZSI, a three-diode-cell QZSI, and lastly, an -diode-cell developed QZSI. The main difference between these topologies is related to the input dc current, which is continuous in CDAQZSI and is discontinuous in DDAQZSI. These inverters are thoroughly scrutinized in the ST and non-ST states. The current and voltage equations of the used elements, namely capacitors, diodes, and inductors, are computed. According to the acquired equations, the boost factor values are increased by a factor of $1/1-D_{sh}$ when the number of the diode-cells used is increased in the two proposed QZSIs. In addition, in the CDAQZSI, dc-link, diodes, and inductors' current values are reduced by a factor of $1-D_{sh}$ when the same ST duty cycle value (D_{sh}) with more diode-cells are utilized. Moreover, in the DDAQZSI, by increasing the number of basic units, the value of inductors' current will be constant. Lastly, the accuracy operation of the CDAQZSI is reconfirmed through experimental results in the laboratory on two diode-cells.

REFERENCES

[1] F.Z. Peng, "Z-source inverter," *IEEE Trans. Power Electron*., Vol. 39, No. 2, pp. 504-510, March/April 2003.

[2] S. Laali and Ebrahim Babaei, "New capacitor assisted quasi Z-source inverter," in *Proc. IECON*, pp. 8021-8026, 2017.

[3] R. Motiur, K. Avneet, Y.wang, M. Raghuram, N.K. Pilli, S. K. Singh, X. Pan, X. Xiong, "High Gain Quasi-Switched Boost Inverter With Optimal Performance Parameters," *IEEE Trans. Transportation Electrification*, Vol. 6, No. 2, pp. 554-567, March 2020.

[4] S. Laali, Ebrahim Babaei, and Vida Ranjbarzad, "New hybrid quasi Z-source inverter based on diode-capacitor basic unit," in *Proc. ELECO*, pp.335-339, 2017.

[5] Sh. Dong, Q. Zhang, and Z. Chunbo, "Switched-coupled-inductor Z-source inverter with a high boost inversion capability," *IET Power Electron.*, Vol. 13, No. 12, pp. 2580-2588, 2020.

[6] E. Babaei, M. Shadnam Zarbil, and M. Sabahi, "A new structure of quasi Z-source based cascaded multilevel inverter," *Journal of Circuits, Systems, and Computers*, Vol. 26, No. 12, pp. 1-26, Dec. 2017.

[7] E. Babaei, E. Shokati Asl, and M. Hasan Babayi, "Steady-state and small-signal analysis of high voltage gain half-bridge switched-boost inverter," *IEEE Trans. Ind. Electron.*, Vol. 63, No. 6, pp. 3546-3553, June 2016.

[8] A. Ho; Tae-Won Chun, Hong-Hee Lee, and Heung-Geun Kim, "Active switched quasi-Z-source inverter with high-boost ability for low-voltage renewable energy sources," in *Proc. ICCEP*, pp. 627-632, 2015.

[9] A. Sarikhani, M. H. Ghaderi, and M. Hamzeh, "A common-ground quazi-Z-source single-phase inverter suitable for

photovoltaic applications," *IEEE Trans. Energy Conversion*, Vol. 36, No. 2, pp. 594-601, June 2021.
[10] M. Hanif, M. Basu, and K. Gaughan, "Understanding the operation of a Z-source inverter for photovoltaic application with a design example," *IET Power Electronics*, Vol. 4, No. 3, pp. 278-287, 2011.
[11] C.Qin, C. Zhang, A. Chen, X. Xing and G. Zhang, "A Space Vector Modulation Scheme of the Quasi-Z-Source Three-Level T-Type Inverter for Common-Mode Voltage Reduction," *IEEE Transactions on Industrial Electronics*, Vol. 65, No. 10, pp. 8340-8350, Jan 2018.
[12] M. Shen, J. Wang, A. Joseph, F.Z. Peng, L.M. Tolbert, and D.J. Adams "Constant boost control of the Z-source inverter to minimize current ripple and voltage stress," *IEEE Trans. Ind. Appl.*, Vol. 42, No.3, pp. 770-778, May/June 2006.
[13] A.V. Ho, T.W. Chun and H.G. Kim, "Extended boost active-switched-capacitor/switched-inductor quasi-Z-source inverters," *IEEE Trans. Power Electron.*, Vol. 30, No. 10, pp. 5681–5690, May. 2015.
[14] L. Pan, "Γ-Z-Source inverters," *IEEE Trans. Power Electron*., Vol. 29, No. 12, pp. 6534-6543, 2014.
[15] H.F. Ahmed, H. Cha, S. Kim and H. Kim, "Switched-Coupled-Inductor Quasi-Z-Source Inverter," *IEEE Trans. Power Electron*., Vol. 31, No. 2, pp. 1241-1254, 2016.
[16] M.K. Nguyen, Y.C. Lim and S.J. Park, "A comparison between single-phase quasi-Z-source and quasi-switched boost inverters," *IEEE Trans. Ind. Electron.*, Vol. 62, No. 10, pp. 6336-6344, Oct. 2015.
[17] A. Ho and T. Chun, "Single-Phase Modified Quasi-Z-Source Cascaded Hybrid Five-Level Inverter," *IEEE Transactions on Industrial Electronics*, Vol. 65, No. 6, pp. 5125-5134, Jun 2018.
[18] C.J. Gajanayake, F.L. Luo, H.B. Gooi, P.L. So, and L.K. Siow, "Extended-boost Z-source inverters," *IEEE Trans. Power Electron*., Vol. 25, No. 10, pp. 2642-2652, Oct. 2010.
[19] M. Ghodsi and S. M. Barakati, "A new switched boost inverter using transformer suitable for the microgrid-connected PV with high boost ability," in *Proc. PEDSTC*, pp. 123-128, 2016.
[20] M. Ghodsi, S. M. Barakati and B. Wu, "Extended switched-inductor quasi-Z-source inverter: Modeling and prototype realization", *Int Trans Electr Energ Syst*, Vol. 29, No.3, March 2019 .
[21] M. Ghodsi and S. M. Barakati, "A new switched-inductor quasi-Z-source inverter," in *Proc. PEDSTC*, pp. 177-184, 2016.
[22] Z. Aleem, H-K. Yang, H.F. Ahmed, S. Winberg, and J.-W. Park, "A class of single-phase Z-source AC-AC converters with magnetic coupling and safe-commutation strategy," *IEEE Trans. Ind. Electron.*, Vol. 68, No. 9, pp. 8104- 8115, Sept. 2021.
[23] Sara Laali, Ebrahim Babaei, Concettina Buccella, and Carlo Cecati, "Diode assisted quasi Z-source inverter with discontinuous current: Analysis and simulation," in *Proc. 2018 AEIT International Annual Conference*, 2018.
[24] Sara Laali, Ebrahim Babaei, Concettina Buccella, and Carlo Cecati, "Developed quasi Z-source inverter based on diode-cells: Analysis and simulation," in *Proc. 2018 AEIT International Annual Conference*, 2018.
[25] J. G. Cintron, Y. Li, S. Jiang, and F. Z. Peng, "Quasi-Z-source inverter with energy storage for photovoltaic power generation systems," in Proc. *26th Annual IEEE Appl. Power Electron. Conf. Expo*., pp. 401–406, 2011.
[26] M. Zhu, K. Yu, and F.L. Luo, "Switched inductor Z-source inverter," *IEEE Trans. Power Electron.*, Vol. 25, No. 8, pp. 2150-2158, Aug. 2010.

Sara Laali was born in Tehran, Iran in 1984. She received the B.S. degree in electronics engineering from Islamic Azad University, Tabriz Branch, and the M.S. degree in electrical engineering from Islamic Azad University, South Tehran Branch, Iran, in 2008 and 2010, respectively. She has been joined to the Department of Electrical Engineering, Adiban Higher Education Institute from 2010 to 2015. She received her Ph.D. in Electrical Engineering from the Department of Electrical and Computer Engineering, University of Tabriz, Tabriz, Iran, in 2015. In Oct 2016, she has been joined to the Department of Electrical and computer Engineering, Islamic Azad University, North Tehran Branch. In addition, she managed several industry projects on energy storage systems specially on elevator and new inverters in renewable energy systems. Her major fields of interest include the analysis and control of power electronic converters, multilevel converters, and FACTS devices.

Ebrahim Babaei received his Ph.D. degree in Electrical Engineering from the University of Tabriz in 2007. In 2007, he joined the Faculty of Electrical and Computer Engineering, University of Tabriz. He has been a Professor since 2015. He is the author and co-author of one book and more than 600 journal and conference papers. He also holds 25 patents in the field of power electronics. His current research interests include analysis, modeling, design, and control of power electronics converters and their applications, renewable energy sources, and FACTS devices. Prof. Babaei has been the Editor-in-Chief of Tabriz Journal of Electrical Engineering since 2013. He is also currently an Associate Editor of the IEEE Transactions on Industrial Electronics, IEEE Transactions on Power Electronics, Open Journal of the Industrial Electronics Society, and Iranian Journal of Science and Technology, and Transactions of Electrical Engineering. He has been the corresponding guest editor for two special issues in the IEEE Transactions on Industrial Electronics. In addition, Prof. Babaei has been the technical program chair, track chair, organizer of different special sessions, and technical program committee member in the most important international conferences organized in the field of power electronics.

International Journal of Industrial Electronics, Control and Optimization © 2022 IECO
Vol. 5, No. 1, pp. 63-76, Jan (2022)

A Novel Meta-heuristic Framework for Solving Power Theft Detection Problem: Cheetah Optimization Algorithm

Hassan Ghaedi[1], Seyed Reza Kamel Tabbakh[2,†] , and Reza Ghaemi[3]
[1] Department of Computer, Neyshabur Branch, Islamic Azad University, Neyshabur, Iran
[2] Department of Computer, Mashhad Branch, Islamic Azad University, Mashhad, Iran
[3] Department of Computer, Quchan Branch, Islamic Azad University, Quchan, Iran

ABSTRACT

In this paper, a two-level stacking technique with feature selection is used to detect power theft. The first level of this technique uses base classifiers such as support vector machine (SVM), naïve Bayes (NB), and AdaBoost selected by evaluating the F-score and diversity criteria. The appropriate features of the base classifiers are selected using a new feature selection algorithm based on the cheetah optimization algorithm (CHOA). This algorithm ensures diversification and intensification in each step of running by adjusting the Attention parameter of the cheetahs. In the second level, a single-layer perceptron (SLP) model is used to obtain the weight of the base classifiers and combine their predictions. The proposed framework is evaluated on the Irish Social Science Data Archive (ISSDA) dataset, and MATLAB R2020b is used for simulation and evaluation. The results of the accuracy, recall, precision, and F-score, specificity, and receiver operating characteristic (ROC) criteria indicated the high efficiency of the proposed framework in detecting power theft.

Article Info

Keywords:
Cheetah optimization algorithm, Classification, Feature selection, Machine learning, Power theft detection
Article History:
Received 2021-08-13
Accepted 2021-12-06

I. INTRODUCTION

Nowadays, electricity theft is one of the major challenges faced by power companies all over the world. Early detection of power theft can minimize the financial losses of these companies. Various methods have been used to detect power theft. Many researchers have used data mining techniques and modeling by using customers' consumption patterns for theft detection.

Passos Júnior et al. [1] used the optimum-path forest (OPF) clustering algorithm to identify normal and abnormal customer profiles in their research. They also provided a model for identifying non-technical losses (NTL) when there was little or no information about unauthorized customers. Jokar et al. [2] provided a consumption pattern-based power theft detector that uses distribution transformer meters to list areas with a high probability of theft in a short time and monitors abnormal uses to identify suspicious customers. They also used clustering and classification techniques to detect theft. In their review, Ahmad et al. [3] focused on different models for identifying non-technical losses. In their study, several methods of power theft detection were examined and discussed such as the SVM [4] model, optimum-path forest clustering process, real-time estimation techniques, SVM model with a genetic algorithm, decision trees (DT), NB network [5], etc, and their advantages were mentioned. Zheng et al. [6] presented a density-based power theft detection method to detect abnormal consumption patterns and used several malicious types for validation testing. The method was compared with several clustering algorithms. Xiao and Ai [7] developed a data-driven theft

†Corresponding Author: Rezakamel@ieee.org
Tel: +98-9151237429, Department of Computer, Mashhad Branch, Islamic Azad University, Mashhad

detector that uses random matrix theory with a wide range of smart meters. The use of matrix theory as a data source is one of the key steps in this method, in which areas with a high probability of theft and customers suspected of theft are quickly listed. Zheng et al. [8] proposed a method of power theft detection based on the wide and deep convolutional neural network (CNN). This method can accurately determine the non-periodic and periodic thefts of normal customers and store the general characteristics of the consumed data in one dimension. Ghasemi and Gitizadeh [9] discussed a combined method for detecting unauthorized customers. In this method, based on the probabilistic neural network and Levenberg-Marquardt method, a classification method of customer consumption pattern and a mathematical model are designed in which distributed generation (DG) resources are analyzed on unauthorized consumption. Guerrero et al. [10] proposed a two-module framework for reducing non-technical losses. The first module filters customers based on text mining and a complementary artificial neural network. The second module uses a data mining process including classification and regression tree and self-organization map (SOM). By using these modules, non-technical losses are significantly reduced. Messinis and Hatziargyriou [11] reviewed the recent research papers on the detection of non-technical losses and focused on algorithms, data types and size, features, evaluation metrics, and response times of the NTL detection system. Besides, they provided a comprehensive list of performance metrics and their importance. Maamar and Benahmed [12] provided an overview of machine learning research to detect power theft using smart meter data and studied the challenges of electrical theft detection. Learning models were compared in terms of performance metrics, analytics and simulation environments, and datasets used. Singh et al. [13] employed relative entropy to measure the similarity between possible distributions derived from the reconstructed consumption dataset. When power theft attacks are injected into advanced metering infrastructure (AMI), the energy consumption probability distribution is derived from the consumption history, resulting in greater relative entropy. Nazmul Hasan et al. [14] proposed a hybrid power theft detection system that combines CNN with long short-term memory (LSTM). Since power consumption is time-series data, the CNN-LSTM model was used for classification, and a technique based on local values was employed to calculate missing items. In their study, Li et al. [15] proposed a hybrid model based on CNN and random forest (RF) to detect power theft. In this model, CNN was first used to learn features between different hours of the day and different days extracted from smart meter data. A dropout layer and a back-propagation algorithm were used in this model to reduce over-fitting and update network parameters in the training phase, respectively. The RF was then trained based on the characteristics obtained to determine whether the customer was robbing or not. Konstantinos and Georgios [16] proposed a combined data mining method to identify abnormal customers. In this method, a combination of principal component analysis (PCA) technique and mean shift algorithm were used for different theft scenarios, which detected theft with high efficiency. In their paper, Maamar and Benahmed [17] proposed a hybrid approach based on k-means and deep neural networks to detect power theft anomalies. K-means was used to identify a group of customers with similar power consumption patterns in order to know the different types of normal behavior, and a deep neural network was used to build an anomaly detection model. Chandel and Thakur [18] developed an electrical theft detection methodology based on the detection of abnormal readings of voltage, current, and power factor sent to the center every 15 minutes at regular intervals by smart meters. High detection rate (DR) and low false positive rate (FPR) indicated the high efficiency of the presented method. Razavi et al. [19] provided a feature engineering framework for detecting power theft in smart grades. The framework combined the finite mixture model clustering for customer segmentation and the genetic programming algorithm to identify new features. In this framework, the gradient boosting algorithm was used, which significantly improved the detection rate. Feng et al. [20] presented an algorithm for detecting abnormal power consumption patterns based on local matrix reconstruction (LMR). Five daily load characteristics were used instead of high daily amplitude load curves and PCA technique to calculate weighted regeneration errors. Zhang et al. [21] proposed a feature engineering-based method for detecting abnormal power consumption behavior. First, the main feature set was created by brainstorming. Then, the optimal feature set, which reflected the consumption behavior of customers, was obtained based on the variance and similarity between the selected features. In the abnormal detection stage, a density-based clustering algorithm was used to detect abnormal consumption behaviors.

Ghaedi et al. [22] used a combination of clustering and classification to detect power theft. The improved crow search algorithm was used for optimal customer clustering and the two-stage stacking technique was used to classify electricity consumers.

The effectiveness of any classification technique depends on the features used in the training and testing patterns. Feature selection [23][24] is a technique for selecting the appropriate subset of features that enhances the capabilities and robustness of the models. Indeed, the purpose of feature selection is to improve the performance of models. Over the last few years, many researchers have used ensemble classifiers to increase the efficiency of models. In fact, the methods of ensemble classifiers combine the prediction results of several classifiers to fix the problems related to the base classifiers in order to achieve a better result. In ensemble

classifiers, each classifier gives a different solution to the problem according to its performance and it is expected that by combining these answers, prediction accuracy increases [14]. Two different classifiers may have a variety of errors when patterns that are incorrectly classified are different. The difference in the errors of base classifiers is caused by classifiers covering each other's errors. Important challenges are the proper selection of base classifiers and how to combine them.

In our study, the stacked ensemble technique [25], which is a two-level technique, is used to predict power theft. One of the most important and effective factors in ensemble methods is the correct selection of the base classifiers. To optimally select the base classifiers, the *F-score* and diversity criteria are used together. To improve the prediction of the stacking technique, the performance of the base classifiers is improved by selecting the appropriate features using the CHOA algorithm. The results of the base classifiers are combined based on weighted voting. Each model has a different role in decision-making based on its capabilities. The model used in the second level of stacking is the SLP model, which has generalized properties and is never over-fit. Experiments are performed on the ISSDA dataset [26].

This paper is organized as follows. The cheetah optimization algorithm is described in Section II. Section III reviews the cheetah algorithm for feature selection. Section IV explains the proposed framework for power theft detection. The performance evaluation criteria are explained in Section V. Section VI presents the results and evaluation followed by some concluding points in Section VII.

II. CHEETAH OPTIMIZATION ALGORITHM (CHOA)

Cheetahs are expert hunters built for speed. They have small heads, long legs, and muscular tails to maintain balance. Their hearts and lungs are larger than usual to supply oxygen to the running muscles. Half of their muscle mass is placed around the spine so that they can be as flexible as a spring. This lengthens their strides, which helps them reach their maximum speed [27]. For cheetahs, only three strides are enough to reach a speed from zero to 65 km/h, and it only takes 3 seconds to reach a speed of 110 km/h. Cheetahs need coordinated senses to hunt. Although cheetahs are very fast, they must be close enough to their *victim* before attacking. When they see *victim*, they are completely focused [28]. Teamwork increases the likelihood of success in hunting. When one gets tired, the other continues to chase. Male cheetahs usually hunt in groups [29]. Fig. 1 shows photos of group hunting by cheetahs.

The CHOA algorithm is a population-based meta-heuristic algorithm in which the location and velocity of the $object_i$ ($cheetah_i$ or $victim_i$) in the search space are specified as follows:

$$(location_{object_i} = [location_{object}{}_1^i, location_{object}{}_2^i, \dots, location_{object}{}_d^i]$$
$$velocity_{object_i} = [velocity_{object}{}_1^i, velocity_{object}{}_2^i, \dots, velocity_{object}{}_d^i]$$

where d is the dimension of the search space.

Fig. A1 in Appendix A shows the steps of the CHOA algorithm. All cheetahs choose a direction according to the movement of the *victim*, and the *victim* chooses its direction according to the $cheetah_{leader}$. Based on the current velocity of a cheetah and its distance from the *victim*, a new velocity is calculated for a cheetah. To find the best solution by $cheetah_{leader}$, firstly, all of the *N* cheetahs and *M* victims are initialized at random locations in the search space. Because the cheetahs are not far apart in a group, they are located in a range with a radius $R_{Hunting}$(10 meters).

Fig. 1. Photos of group hunting by cheetahs

At the beginning of the movement (first step), the velocity of all cheetahs and *victim* is considered zero. In the next steps, the velocities and locations are updated. Fig. 2 shows the vectors that determine the movement path of the cheetahs.

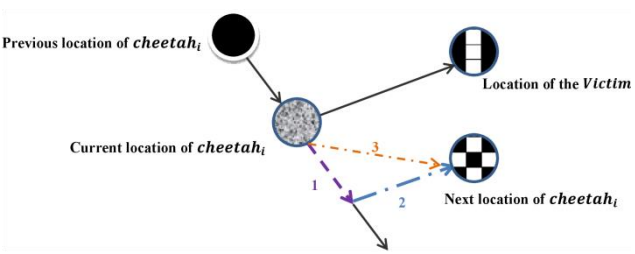

Fig. 2. The direction of the cheetah movement

As shown in Fig. 2, vector 1 represents the coefficient of the previous movement of the $cheetah_i$. Vector 2 represents the coefficient of the vector of the current location to the *victim*. Finally, based on the results of the two vectors, the new velocity of the $cheetah_i$ is determined as vector 3.

For each cheetah, the fitness of the new location is evaluated, and depending on the obtained value, the

$\text{cheetah}_{\text{Leader}}$ may be updated. If the $cheetah_{Leader}$ improves, the *victim* will escape and its velocity and location will be updated.

Fig. 3 also illustrates the movement pattern of the *victim* with respect to the changes in the movement of the $cheetah_{leader}$.

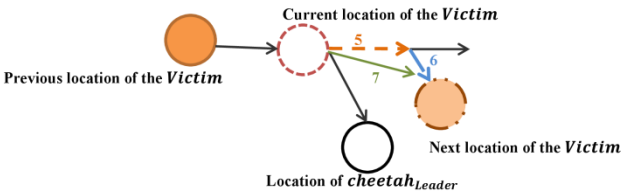

Fig. 3. The direction of the $victim$ movement

As shown in Fig. 3, vector 5 represents the coefficient of the previous movement of the *victim*. Vector 6 represents the coefficient of the vector of the current location to the $cheetah_{Leader}$. Finally, based on the result of the two vectors, the new velocity of the *victim* is determined as vector 7.

To attack, the distance of the cheetahs to the $victim$ must reach a certain threshold. The best distance is between 30 to 100 meters. Therefore, the locations of the victims are randomly adjusted in the mentioned range. One of the important criteria for starting an attack is *Attention*. The $Attention$ of each object (*cheetah* or *victim*) is calculated as follows:

$$Attention_{object_i} = \frac{Fitness(object_i)}{\sum_{i=1}^{N} MAX(Fitness(object_i))} \quad (1)$$

where $Fitness(object_i)$ is the fitness value of $object_i$ and $\sum_{i=1}^{N} MAX(Fitness(object_i))$ represents the highest amount of fitness among objects. In fact, values of the *Attention* are between 0 and 1. To attack, the $cheetah_{Leader}$ must have more *Attention* than *victim*. The cheetah with the highest fitness is known as the $cheetah_{Leader}$. The movement of each cheetah is affected by the movement of the *victim* and is updated as follows:

$$velocity_{cheetah_i} = \omega * velocity_{cheetah_i} + rand1() * \alpha * \left(location_{victim} - location_{cheetah_i}\right) \quad (2)$$

$$New - location_{cheetah_i} = location_{cheetah_i} + velocity_{cheetah_i} \quad (3)$$

where ω is the inertia weight. The weight of inertia controls the effect of past velocities on present velocities. In this study, the weight of inertia decreases linearly. The algorithm usually starts moving with a large amount of the weight inertia, which causes a large search space at the beginning of the algorithm, and this weight decreases over time, which causes the search within a small space at the final steps. In fact, inertia indicates how much the cheetah wants to maintain its current state of motion. A lower amount of inertia results in faster convergence of the algorithm, and increasing the amount of inertia increases the number of sudden movements of the cheetahs. $velocity_{cheetah_i}$ represents the velocity of the $cheetah_i$. α indicates the influence of the location of the $location_{victim}$ on the location of the $cheetah_i$. $location_{victim}$ shows the location of the *victim.* $\text{Location}_{\text{cheetah}_i}$ represents the current location of the cheetah_i. *rand1()* is a random function with a uniform distribution between 0 and 1 that is used to increase random search and maintain the random nature of the algorithm.

During the hunting process, if $cheetah_{Leader}$ improves his fitness, it will not be able to catch the *victim* and the new location of the *victim* will be updated as follows:

$$velocity_{victim} = \gamma * velocity_{victim} + rand2() * \beta * \left(location_{victim} - location_{cheetah_{Leader}}\right) \quad (4)$$

$$New - location_{victim} = location_{victim} + velocity_{victim} \quad (5)$$

where γ is the inertia weight, $location_{victim}$ is the current location of the *victim*,. β is the change percentage in the fitness improvement of $\text{cheetah}_{\text{Leader}}$,. and *rand2()* is a random function with a uniform distribution between 0 and 1. The fact that $cheetah_{Leader}$ is selected based on the distance and attention factors prevents the algorithm from falling into the local optimization. The two most important factors in meta-heuristic algorithms are diversification and intensification. In the CHOA algorithm, with increasing the attention of the *victim*, the cheetah has to search a wider space, and diversification increases. Also, if the attention of the *victim* is low, the cheetah will hunt locally, which means that the intensification will increase.

III. CHEETAH ALGORITHM FOR FEATURE SELECTION

Feature selection is a method of dimension reduction that is used in various fields such as data mining, machine learning, pattern recognition, and so on. In fact, feature selection is a technique of selecting an effective feature subset from an original feature set to increase prediction accuracy. Datasets contain many redundant, irrelevant, and noisy features. Eliminating these features by selecting the important features reduces computational costs so that important information is not lost and learning efficiency is increased. Although many methods have been proposed to solve the problem of selecting important features, most are suffering from the problem of high complexity, high computational cost, and early convergence. Therefore, the use of meta-heuristic algorithms to solve these challenges has received much attention so that today it is one of the most efficient methods and can extract the best subset of features

by maintaining the accuracy of the model and creating more generalizable models [30].

Meta-heuristic search algorithms are inspired by physical, biological, and natural processes, and most of them operate as a population. Unlike classical methods, meta-heuristic search methods operate on a random basis and search space in parallel. These types of methods only use the fitness function to direct the search, but because of their collective intelligence, they can discover the solution.

Various studies have been conducted on feature selection using meta-heuristic algorithms. Pandey et al. [31] used the binary cuckoo binominal search algorithm to select the feature subset. Different versions of the cuckoo search have also been used to select important features [32]–[34]. Naik et al. [35] employed a binary version of the bat algorithm (BBA) with a generalized one-pass neural network to estimate the number of selected features. In some studies [36]–[38], modified versions of BBA have been used to solve various classification problems along with the feature selection strategy. Xu et al. [39] used a combination of a binary firefly algorithm with an opposition-based learning algorithm to select important features. Selvakumar and Muneeswaran [40] used a combination of the firefly algorithm with the Bayesian network and C4.5 with feature selection to detect network intrusion. In one study [41], a modified firefly algorithm was used along with the chaos theory used to select the effective features in medical data. Yan et al. [42] used an improved version of the flower pollination algorithm considering group strategy to select effective features in biomedical data. Zhang et al. [43] improved the krill herd algorithm and used it in high dimensional microarray datasets to extract important features. Pathak et al. [44] used the Levy flight gray wolf optimizer (GWO) to select the appropriate features from original datasets. Al-Tashi et al. [45] used the GWO algorithm to select the best features.

In this paper, the CHOA meta-heuristic algorithm is proposed for feature selection due to its outstanding performance in ensuring diversification and intensification, as well as the use of the dynamic Attention factor for each cheetah.

Each cheetah is represented by a binary string as $F = F_1, F_2, \dots F_n \quad n = 1,2,\dots,2$. $F_i$specifies the consumption for the hour *i* that the consumer sends to the center. Values of the features are considered in the range of 0-1. If the corresponding bit value is more than 0.5, it indicates that the feature is selected; otherwise, it indicates that the feature is not selected.

In fact, each cheetah represents a subset of features that is the candidate solution. The fitness of each cheetah is evaluated using base classifiers and cheetah with the highest fitness selected as the $cheetah_{Leader}$. If cheetah fitness is greater than the $\text{cheetah}_{\text{Leader}}$ fitness, then the location vector for the $cheetah_{Leader}$ is saved and the $\text{cheetah}_{\text{Leader}}$ is updated. Finally, after satisfying the algorithm termination conditions, the optimal features that the $\text{cheetah}_{\text{Leader}}$ has stored for each base classifier are extracted.

According to Algorithm B1 in Appendix B, after loading the data, the parameters related to the cheetahs, including locations and velocities, are set. The initial location of the cheetahs is set within a radius of 10 meters and their initial velocity is set to 0. The initial locations of the *victim* are also determined randomly and their initial velocities are set to 0. Then, according to the number of iterations of the algorithm, the location and velocity of the cheetahs, as well as the *victim*, are updated according to Equs. (2)-(5). At each iteration, the fitness(cost) function of each cheetah is evaluated, and the leader may change during the attack. In fact, the location and velocity of the cheetahs are affected by the movement and velocity of the *victim* .To evaluate the fitness of a cheetah, its location and the data are sent to the cost function of the feature selection. To evaluate the performance of the proposed feature selection algorithm, the results are compared with the actual data label of the dataset and the performance criteria are evaluated.

IV. PROPOSED FRAMEWORK FOR POWER THEFT DETECTION

Fig. C1 in Appendix C shows the steps of the proposed framework. According to Fig. C1, the reference dataset is normalized by the Min-Max method [46] to increase the prediction efficiency.

After data normalization, to make a balance between normal and abnormal samples of the dataset and increase the rate of correct theft detection, abnormal samples have been added to the original dataset according to equations in [2]. The sampling rate and reading of meters have been reduced and done every hour to increase the privacy of customers. For each sample $x = \{x_1, \dots, x_{t \quad t=1,2,\dots,24}\}$, six types of artificial attacks are generated as follows:

in which the function $h_1(x_t)$ multiplies all samples in a random value and the function $h_2(x_t)$ multiplies each sample in different random values.

$$h_1(x_t) = \alpha x_t \tag{6}$$

$$\alpha = random(0.1,0.8)$$

$$h_2(x_t) = y_t x_t \quad = random(0.1,0.8) \tag{7}$$

$$h_3(x_t) = \begin{cases} 0 & \forall t \in [ts, tf] \\ x_t & else \end{cases} \tag{8}$$

$$h_4(x_t) = \quad y_t mean(x) \tag{9}$$

$$y_t = random(0.1,0.8)$$

$$h_5(x_t) = \quad mean(x) \tag{10}$$

$$h_6(x_t) = x_{24-t} \tag{11}$$

The function $h_3(x_t)$ is a by-pass attack that sends a value of 0 at a specified time interval [ts, tf](ts: t start, tf: t final); otherwise, it sends the actual amount of consumption. ts and

tf are the beginning and ending of the theft period, respectively.

The functions $h_4(x_t)$ and $h_5(x_t)$ focus on sending the average daily consumption. The function $h_6(x_t)$ reverses the order of the readings in a day.

To select the best base classifiers of the staking technique, the *F-score* values of all classifiers are first measured to predict power theft on the dataset. The classifier with the highest *F-score* is selected as the first base classifier. Then, to select the other base classifiers, the triple combinations of the classifier with the highest *F-score* and other classifiers are created. This combination is obtained based on diversity criteria. Diversity criteria include *disagreement*, *Kappa* and *Matthews correlation coefficient* (*MMC*). These criteria are explained in Section V. Each combination with the highest *F-score* is selected as the final combination of the base classifiers.

After identifying base classifiers, the two-level stacking technique is used for training. In the first level of the training, the base classifiers are trained with the same data (56% of the total data) to learn and solve the final problem. According to the ISSDA dataset and to reduce the sampling rate, the number of features is reduced to 24 features. To better train these classifiers, the effective features of each classifier are automatically selected by the CHOA algorithm in this level of training. Features, with values greater than 0.5, are selected. The base classifiers are trained with selected features and their fitness functions are obtained to evaluate. In the second level of training, the meta-model is trained to calculate the weight of each base classifier. These weights determine the degree of importance of the votes of the base classifiers in the final decision. The model used in the second level of training is the single-layer perceptron model, which is characterized by generalizability and is not over-fitted. This model assigns a weight to the output of each base classifier. In fact, the output of the training phase of the meta-model is the weight of each base classifier. After training the base classifiers, the validation data (24% of the total data) and the trained base classifiers are used to generate the training data ($\mathrm{Xtrain_i}$) of the meta-model. Then, the trained meta-model and the weight ($\mathrm{W_i}$) of each base classifier are determined. Finally, the trained model is tested using test data, and the performance of the proposed framework is evaluated.

V. PERFORMANCE EVALUATION CRITERIA

To evaluate the diversity of the classifiers, the average values of all classifier pairs are used as a criterion to compare the diversity of the classifiers. These criteria are obtained based on Table I.

In Table I, X and W are the number of cases in which both classifiers D_i and D_j have correct and incorrect predictions, respectively, Y is the number of cases that classifiers D_i and D_j have negative and positive values, respectively, and Z is the number of cases that classifiers D_i and D_j have positive and negative values, respectively.

Table I

A 2× 2 MATRIX OF THE RELATIONS BETWEEN CLASSIFIERS D_i AND D_j

	D_j correct(1)	D_j wrong(0)
D_i correct(1)	X	Z
D_i wrong(0)	Y	W

Matthews correlation coefficient (MMC):

MMC [47] is one of the metrics related to the correlation measurement between the observed values by the two classifiers and their predicted values. *MMC* values are between -1 and +1. Values close to +1 indicate an ideal prediction and a strong positive correlation between true labels and prediction. The strong correlation indicates that the predicted values are very similar to the actual values. A value of 0 indicates random data prediction.

$$MMC_{ij} = \frac{xw - yz}{\sqrt{(x+z)(x+y)(y+w)(z+w)}} \tag{12}$$

A lower value of this criterion shows more diversity between the two classifiers.

Disagreement measure:

Disagreement [41][48] represents the ratio between the number of observations that one classifier is correct and the other is incorrect according to the total number of observations. A greater value of this criterion shows more diversity between the two classifiers.

$$D_{ij} = \frac{z+y}{x+y+z+w} \tag{13}$$

Kappa coefficient:

Kappa is one of the important criteria to evaluate the diversity between the two observers from the perspective of agreement [49]. *Kappa*'s main purpose is to evaluate the degree of agreement or disagreement of two observers from a similar event. In fact, *Kappa* is based on the idea of measuring agreement between true and predicted labels and has been proposed to remove chance agreement from overall *accuracy*.

$$K_{ij} = \frac{\Theta_1 - \Theta_2}{1 - \Theta_2} \tag{14}$$

where Θ_1 is overall accuracy (observed agreement) and Θ_2 is the chance agreement (agreement expected only by chance).

$$\Theta_1 = \frac{TP + TN}{N} \quad (15)$$

$$\Theta_2 = \frac{(TP + FN)(TP + FP) + (TN + FP)(TN + FN)}{N^2} \quad (16)$$

In calculating the kappa coefficient, in addition to the data that are observed correctly, the data that are observed incorrectly are also included. Then, it is a good measure for comparing the results of two classifiers. The *kappa* coefficient can be between -1 and +1. A lower value shows lower agreement and higher diversity.

To evaluate the efficiency of the proposed framework, several performance criteria have been used, i.e., *accuracy*, *recall*, *precision*, *F-score*, specificity, and receiver operating characteristic (*ROC*) curve. These criteria are based on the confusion matrix presented in Table II.

Table II

CONFUSION MATRIX

		Predicted	
		Positive	Negative
Actual	Positive	TP	FN
	Negative	FP	TN

Abbreviations in the confusion matrix are true positive (*TP*), true negative (*TN*), false positive (*FP*), and false negative (*FN*). In general, $N = TP + TN + FN + FN$.

Accuracy:

Accuracy is the correct detection rate of the classifier in the total of the classes:

$$Accuracy = \frac{(TP + TN)}{N} \quad (17)$$

Recall (sensitivity):

Recall represents the ratio of the number of positive data in a particular class that is correctly classified to the number of data that should be classified in that particular class.

$$Recall = \frac{TP}{TP + FN} \quad (18)$$

Precision:

This criterion expresses the ratio of the number of correct predictions made for samples of a particular class to the total number of predictions for samples of the same class.

$$Precision = \frac{TP}{TP + FP} \quad (19)$$

F-score:

This criterion combines precision and recall parameters to better evaluate the performance of a classification model. This criterion provides a more accurate description of how the classification model works on all existing classes in the data.

$$F - score = 2 \times \frac{Recall \times Precision}{Recall + Precision} \quad (20)$$

Specificity:

Specificity indicates the ratio of the number of negative data in a particular class that is correctly classified to the number of data that should be classified in that particular class.

$$Specificity = \frac{TN}{TN + FP} \quad (21)$$

Receiver operating characteristic (ROC) curve:

An excellent prediction is a prediction in which the values of both sensitivity and specificity criteria are 1. These two criteria are always in competition with each other. Increasing one is accompanied by decreasing the other. This situation led to the production of the *ROC* curve, which expresses the relationship between the two criteria of sensitivity and specificity. The vertical axis of this curve indicates *sensitivity* and the horizontal axis represents *1-specificity*. The area under this curve (*AUC*) is used as a measure to evaluate the performance of the classifier. Ideally, the area under the *ROC* curve is 1.

VI. RESULTS AND EVALUATION

In this section, the results of the proposed framework are evaluated on the ISSDA dataset. In all experiments, the average of different runs was used to measure the evaluation criteria. The ISSDA dataset contains consumption data of 5,000 Irish home and business customers from 2009 to 2010, published in January 2012. For each customer, consumption information is stored for 535 days so that each day contains 24 features. Table III shows the information stored in this dataset.

Table III

INFORMATION OF ISSDA DATASET

Meter ID	Consumption time (day-hour)	Consumption amount (Kwh)

Table IV shows the information of a meter, including the meter ID, consumption value in each hour (kWh), and consumption date that are sent to the center.

Table IV

CONSUMPTION INFORMATION OF A METER

Date	Hour1(kWh)	…	Hour24(kWh)	Meter ID
2009/29/8	0.094	…	0.149	1184

For example, Hour1(kWh) represents the amount of consumption electricity at 01:00 a.m.

Base classifiers are selected among the classifiers of SVM, neural network (NN), NB, AdaBoost [50], RF, and KNN. According to Table V, the *F-score* criterion of these classifiers was obtained to predict power theft. The final base classifiers of the stacking technique are considered to be three classifiers. According to Table V, the SVM classifier has the highest *F-score*. To select base classifiers, the triple combinations of the SVM classifier with the highest *F-score* and other classifiers are created. The values of diversity

criteria are calculated based on the average values of each pair of classifiers. As shown in Table VI, according to the *Kappa* and *MMC* criteria, the SVM-NB-AdaBoost combination has the best diversity.

Table V

F-SCORE CRITERION OF THE BASE CLASSIFIERS (NO-FEATURE SELECTION)

Classifier / Criterion	SVM	NN	NB	AdaBoost	RF	KNN
F-score	0.897	0.893	0.864	0.877	0.862	0.871

Also according to the disagreement criterion, this combination has the best diversity after the SVM-NB-RF combination. Given that the SVM-NB-AdaBoost combination has the highest diversity, this combination is used for base classifiers.

According to Table V, the SVM, NN, and AdaBoost classifiers have the highest *F-score*. If their combination is used as the base classifier in the proposed framework, they are less efficient than when both the *F-score* and diversity criteria are used.

Table VI

F-SCORE AND DIVERSITY VALUES OF THE SVM AND OTHER CLASSIFIERS

Subset classifiers	AVG Kappa ↓	AVG disagreement ↑	AVG MMC ↓	F-score ↑
SVM-NB-KNN	0.8941	0.0085	0.8985	0.8918
SVM-NB- RF	0.8497	0.0126	0.8556	0.9245
SVM-NN-KNN	0.9026	0.0074	0.9270	0.8732
SVM-NN-RF	0.8736	0.0101	0.8796	0.9113
SVM-KNN-RF	0.8720	0.0105	0.8776	0.9137
SVM-RF-AdaBoost	0.9057	0.0074	0.9095	0.8862
SVM-NN-AdaBoost	0.8994	0.0074	0.9008	0.8720
SVM-KNN-AdaBoost	0.8923	0.0085	0.8953	0.9144
SVM-NB-AdaBoost	0.8474	0.0126	0.8525	0.9624
SVM-NB-NN	0.8911	0.0085	0.8953	0.9045

As is seen in Table VI, the SVM-NB-AdaBoost combination, which has better diversity, also has the highest *F-score*. After selecting the SVM, NB, and AdaBoost classifiers as the base classifiers, out of 3745 data in the dataset, 80% were randomly selected for training and 20% for testing. Out of the total training data, 80% were used for training the base classifiers and 20% as validation data to train and produce data for Meta classifier. The model used in the second level of the stacking technique is SLP, which has the generalization property and is never over-fit.

After training the second level classifier, weights of the base classifiers are obtained. The results of the first-level classifiers are combined based on the weighted voting.

A. *Experiment 1*

In this experiment, to increase the prediction performance of the proposed framework, the CHOA algorithm was used to select the features of the SVM, NB, and AdaBoost classifiers.

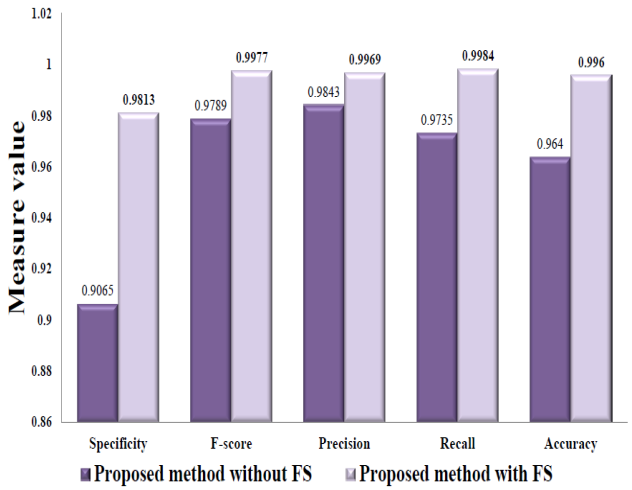

Fig. 4. Values of the *accuracy*, *recall*, *precision*, *F - score*, and *specificity* criteria for both conditions of feature and no-feature selection

The values of *accuracy*, *recall*, *precision*, *F-score*, and *specificity* criteria were evaluated for feature selection/no feature selection conditions.

Fig. 4 presents the values of the mentioned criteria for both conditions of feature selection and no-feature selection. According to the results in Fig. 4, it can be seen that the values of evaluation criteria are higher when the feature selection strategy is used. For example, the accuracy criterion value is 0.996 for the feature selection method and 0.964 for the strategy of no-feature selection.

In fact, with the feature selection strategy, abnormal power customers were identified with fewer features and higher efficiency. The selected features of the classifiers are:

AdaBoost: Hour8, Hour9, Hour10, Hour11, Hour12, Hour13, Hour14, Hour15, Hour16, Hour20, Hour21, Hour22, Hour23, Hour24.

NB: Hour7, Hour8, Hour9, Hour10, Hour11, Hour12, Hour13, Hour14, Hour15, Hour19, Hour20, Hour21, Hour22, Hour23.

SVM: Hour6, Hour7, Hour8, Hour9, Hour10, Hour11, Hour12, Hour13, Hour14, Hour15, Hour16, Hour17, Hour20, Hour21, Hour22, Hour23, Hour24.

B. *Experiment 2*

In this experiment, the *ROC* curves of the proposed framework were illustrated for situations without or with feature selection.

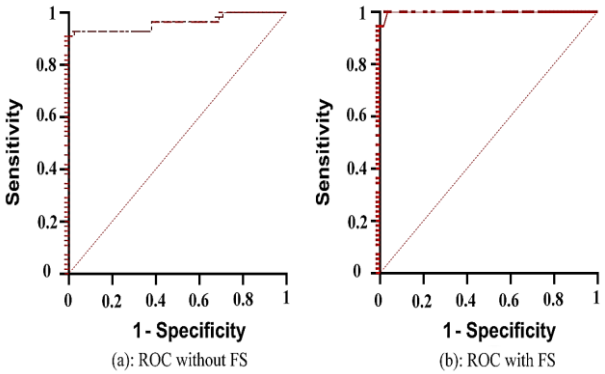

Fig. 5. The *ROC* curves for both conditions of the feature selection and without feature selection

According to Fig. 5, it can be seen that the proposed framework for the situation where the feature selection algorithm is used to detect power theft shows a higher efficiency. According to the *ROC* curves in Figs. 5(a) and 5(b), the values of the *AUC* parameter for situations without feature selection and with feature selection are 0.9632 and 0.9982, respectively. The obtained *AUC* value for the feature selection situation indicates the high performance of the proposed framework in detecting abnormal power customers.

C. Experiment 3

In this experiment, the results of the proposed framework were compared with the results reported in [22] and an average of 20 different runs used to evaluate the results and measure the criteria. In each independent run, the maximum iteraion is set to 100. The attacks of the research [2] have been used to evaluate the results. For all the methods in Table VII, plan 1 (all attacks) and scenario of 80% of the data for training and 20% for testing were used. Table VII shows the values of the *accuracy* criterion for this experiment. According to Table VII, it can be seen that the *accuracy* value of the proposed framework is 0.996, which indicates the higher efficiency of the proposed framework to detect power theft.

Table VII

COMPARISON OF THE ACCURACY CRITERION OF THE PROPOSED FRAMEWORK AND RESEARCHES [22]

Research \ Criterion	*Accuracy*
ICSA-Stacking [22]	0.9835
Proposed framework	0.996

D. Experiment 4

In this experiment, the results of the proposed framework were compared with the results of the research [15].

Table VIII shows the values of the *recall*, *precision*, and *F-score* criteria for both frameworks.

Table VIII

COMPARISON OF RECALL, PRECISION, AND F – SCORE CRITERIA OF THE PROPOSED FRAMEWORK AND RESEARCH [15]

Criterion \ Method	CNN-RF	Proposed Framework
Recall	0.97	0.9984
Precision	0.97	0.9969
F-score	0.97	0.9977

According to Table VIII, it can be seen that the values of $recall$, $precision$, and F-score criteria for the proposed framework are higher than the results reported in [15]. With these results, we find that the proposed method identifies unauthorized electricity customers with higher efficiency.

E. Experiment 5

In this experiment, the prediction results of the proposed framework were compared with different feature selection algorithms. PSO, crow search algorithm (CSA) [51], and improved CSA (ICSA) [22] feature selection algorithms were used to compare the results.

According to Table IX, it can be seen that the proposed framework with the CHOA feature selection algorithm is more efficient in detecting abnormal consumers.

Table IX

COMPARISON OF DIFFERENT FEATURE SELECTION ALGORITHMS IN COMBINATION WITH THE PROPOSED FRAMEWORK

Criterion \ Method	PSO	CSA	ICSA	CHOA
Accuracy	0.9017	0.922	0.942	0.996

According to Fig. 6, CHOA can converge the fastest due to its low complexity, and in the ISSDA dataset, none exceeds 10 iterations. This illustrates why it is applied for the feature selection algorithm.

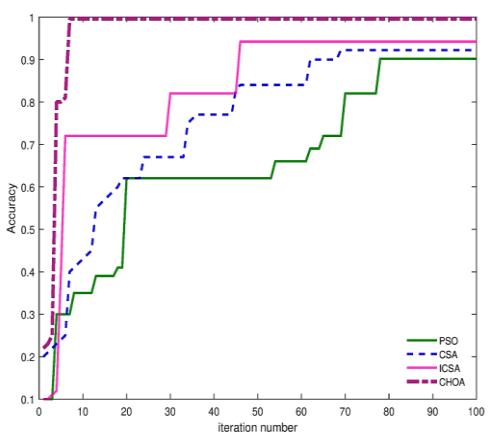

Fig. 6.The converged curves for different feature selection algorithms

Other algorithms converge very slowly, requiring at least 80 iterations to converge. The proposed algorithm also converges very fast, and basically, 10 iterations are sufficient to get a good solution and detect power theft. Figs. 6 illustrates the converged curves for PSO, CSA, ICSA, and CHOA feature selection algorithms.

VII. CONCLUSION

In this research, a two-level stacking technique was used to detect power theft. The base classifiers of the first level of this technique were selected using *F-score* and diversity criteria. The *disagreement*, *Kappa* and *Matthews correlation coefficient* criteria were used to evaluate the diversity of the classifiers. Among the SVM, NN, NB, AdaBoost, RF, and KNN classifiers, the base classifiers of SVM, NB, and AdaBoost were selected. To increase the correct detection rate of this technique, the CHOA algorithm was used to select the features of the base classifiers. The results of the proposed framework were compared with the results of various studies, which showed that the efficiency of the proposed framework was higher than other studies.

Appendix A:

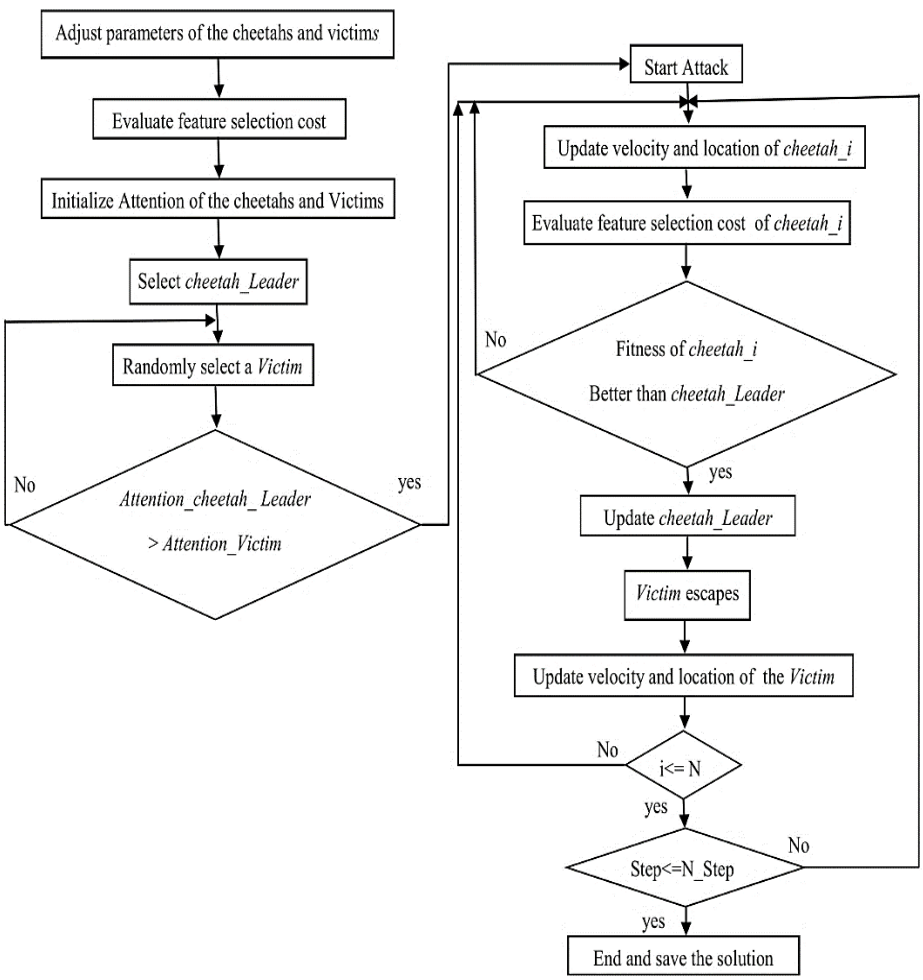

Fig. A1. Steps of the CHOA algorithm

Appendix B:

- **Load data**
- **Adjust parameters of the cheetahs and victims**

Randomly initialize the location of N cheetahs in the search space with radius $R_{hunting}$(10 meters);
Randomly initialize the location of M victims in the distance of 30 to 100 meters from the area of cheetahs;
Adjust the velocity of cheetahs and victims to 0;

- **Evaluate the fitness of each cheetah (feature selection cost)** ;
- **Calculate the *Attention* of each cheetah and *victim***;
- **Select cheetah with highest fitness as** $cheetah_{Leader}$;
- **Randomly select one of the victims as *victim***;

if $Attention_{cheetah_{Leader}} > Attention_{victim}$ **then**
  Attack is start;
end
else
  select another *victim*;
end
Set step=1;
while $step < Nsteps$ **do**
  • On the way to *victim*, the velocity and location of each cheetah are updated as follows:
  for i=*1 to* N **do**
    $velocity_{cheetah_i} = \omega \times velocity_{cheetah_i} + rand1() \times \alpha \times (location_{victim} - location_{cheetah_i})$;
    $New - location_{cheetah_i} = location_{cheetah_i} + velocity_{cheetah_i}$;
    • Evaluate the fitness of $cheetah_i$ (feature selection cost);
    if *fitness of* $cheetah_i$ *is better than* $cheetah_{Leader}$ **then**
      •Update the $cheetah_{Leader}$;
      • *victim* escapes and its velocity and location are updated as follows:
      $velocity_{victim} = \gamma \times velocity_{victim} + rand2() \times \beta \times (location_{victim} - location_{cheetah_{Leader}})$;
      $New - location_{victim} = location_{victim} + velocity_{victim}$;
    end
  end
end

Algorithm B1. The pseudo-code of the feature selection using the CHOA algorithm

Appendix C:

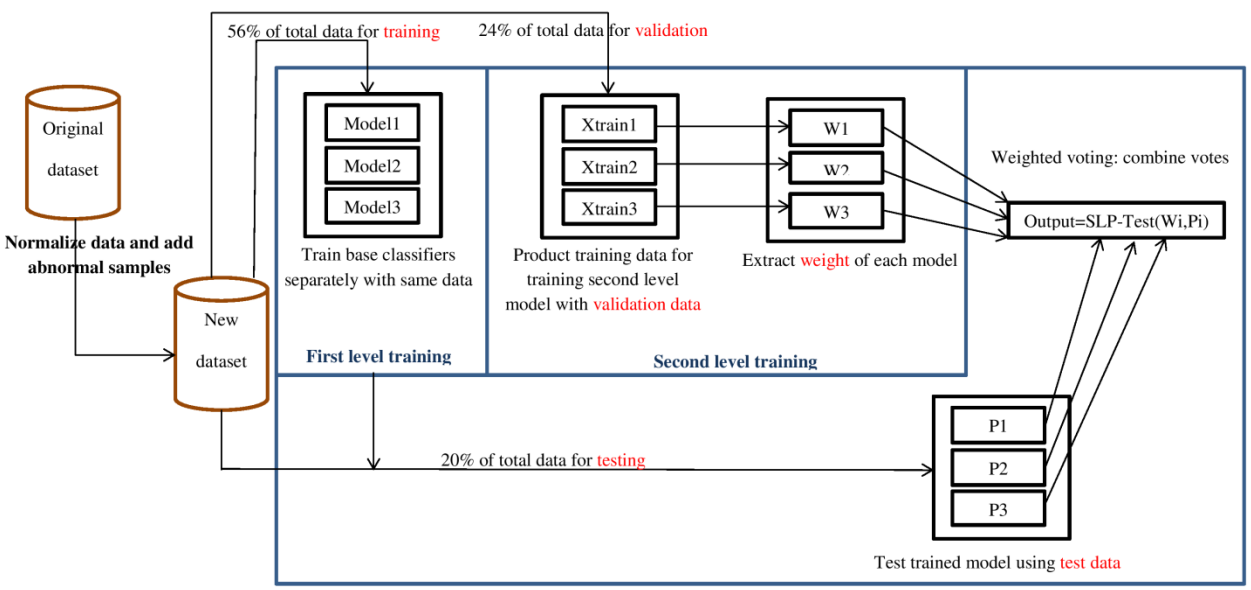

Fig. C1. flowchart of the proposed framework

Mode1= train(FS-AdaBoost(datatrain, dtrain))
Model2= train(FS-NB(datatrain, dtrain))
Model3= train(FS-SVM(datatrain, dtrain))
Xtrain1= Predict(Model1, datavalid)
Xtrain2= Predict(Model2, datavalid)
Xtrain3= Predict(Model3, datavalid)
W1 = Train-SLP(Xtrain1, dvalid)
W2 = Train-SLP(Xtrain2, dvalid)
W3 = Train-SLP(Xtrain3, dvalid)
P1= Predict(Model1, datatest)
P2= Predict(Model2, datatest)
P3= Predict(Model3, datatest)

FS:feature selection
dtatrain: train data for base classifier
dtrain: label of the train data
datavalid: validation data to train second level model
dvalid: label of the validation data
datatest: the test data

REFERENCES

[1] L. A. Passos Júnior *et al.*, "Unsupervised non-technical losses identification through optimum-path forest," *Electric Power Systems Research*, vol. 140, pp. 413–423, 2016, doi: 10.1016/j.epsr.2016.05.036.

[2] P. Jokar, N. Arianpoo, and V. C. M. Leung, "Electricity theft detection in AMI using customers' consumption patterns," *IEEE Transactions on Smart Grid*, vol. 7, no. 1, pp. 216–226, 2016, doi: 10.1109/TSG.2015.2425222.

[3] T. Ahmad, H. Chen, J. Wang, and Y. Guo, "Review of various modeling techniques for the detection of electricity theft in smart grid environment," *Renewable and Sustainable Energy Reviews*, vol. 82, no. November 2016, pp. 2916–2933, 2018, doi: 10.1016/j.rser.2017.10.040.

[4] C. Cortes and V. Vapnik, "Support-vector networks," *Chem. Biol. Drug Des.*, vol. 297, pp. 273–297, Jan. 2009, doi: 10.1007/%2FBF00994018.

[5] D. D. Lewis, "Naive (Bayes) at Forty: The Independence Assumption in Information Retrieval," 1998.

[6] K. Zheng, Y. Wang, Q. Chen, and Y. Li, "Electricity theft detecting based on density-clustering method," *2017 IEEE Innovative Smart Grid Technologies - Asia: Smart Grid for Smart Community, ISGT-Asia 2017*, pp. 1–6, 2018, doi: 10.1109/ISGT-Asia.2017.8378347.

[7] F. Xiao and Q. Ai, "Electricity theft detection in smart grid using random matrix theory," *IET Generation, Transmission and Distribution*, vol. 12, no. 2, pp. 371–378, 2018, doi: 10.1049/iet-gtd.2017.0898.

[8] Z. Zheng, Y. Yang, X. Niu, H. N. Dai, and Y. Zhou, "Wide and Deep Convolutional Neural Networks for Electricity-Theft Detection to Secure Smart Grids," *IEEE Transactions on Industrial Informatics*, vol. 14, no. 4, pp. 1606–1615, 2018, doi: 10.1109/TII.2017.2785963.

[9] A. A. Ghasemi and M. Gitizadeh, "Detection of illegal consumers using pattern classification approach combined with Levenberg-Marquardt method in smart grid," *International Journal of Electrical Power and Energy Systems*, vol. 99, no. December 2017, pp. 363–375, 2018, doi: 10.1016/j.ijepes.2018.01.036.

[10] J. I. Guerrero, I. Monedero, F. Biscarri, J. Biscarri, R. Millan, and C. Leon, "Non-Technical Losses Reduction by Improving the Inspections Accuracy in a Power Utility," *IEEE Transactions on Power Systems*, vol. 33, no. 2, pp. 1209–1218, 2018, doi: 10.1109/TPWRS.2017.2721435.

[11] G. M. Messinis and N. D. Hatziargyriou, "Review of non-technical loss detection methods," *Electric Power Systems Research*, vol. 158, pp. 250–266, 2018, doi: 10.1016/j.epsr.2018.01.005.

[12] A. Maamar and K. Benahmed, "Machine learning techniques for energy theft detection in AMI," *ACM International Conference Proceeding Series*, pp. 57–62, 2018, doi: 10.1145/3178461.3178484.

[13] S. K. Singh, R. Bose, and A. Joshi, "Energy theft detection in advanced metering infrastructure," *IEEE World Forum on Internet of Things, WF-IoT 2018 - Proceedings*, vol. 2018-Janua, pp. 529–534, 2018, doi: 10.1109/WF-IoT.2018.8355148.

[14] M. Nazmul Hasan, R. N. Toma, A. Al Nahid, M. M. Manjurul Islam, and J. M. Kim, "Electricity theft detection in smart grid systems: A CNN-LSTM based approach," *Energies*, vol. 12, no. 17, pp. 1–18, 2019, doi: 10.3390/en12173310.

[15] S. Li, Y. Han, X. Yao, S. Yingchen, J. Wang, and Q. Zhao, "Electricity Theft Detection in Power Grids with Deep Learning and Random Forests," *Journal of Electrical and Computer Engineering*, vol. 2019, 2019, doi: 10.1155/2019/4136874.

[16] B. Konstantinos and S. Georgios, "Efficient Power Theft Detection for Residential Consumers Using Mean Shift Data Mining Knowledge Discovery Process," *International Journal of Artificial Intelligence & Applications*, vol. 10, no. 01, pp. 69–85, 2019, doi: 10.5121/ijaia.2019.10106.

[17] A. Maamar and K. Benahmed, "A Hybrid Model for Anomalies Detection in AMI System Combining K-means Clustering and Deep Neural Network," *Computers, Materials and Continua*, vol. 60, no. 1, pp. 15–39, 2019, doi: 10.32604/cmc.2019.06497.

[18] P. Chandel and T. Thakur, "A novel rule based technique to detect electricity theft in India," *Advances in Science, Technology and Engineering Systems*, vol. 4, no. 2, pp. 413–421, 2019, doi: 10.25046/aj040251.

[19] R. Razavi, A. Gharipour, M. Fleury, and I. J. Akpan, "A practical feature-engineering framework for electricity theft detection in smart grids," *Applied Energy*, vol. 238, no. December 2018, pp. 481–494, 2019, doi: 10.1016/j.apenergy.2019.01.076.

[20] Z. Feng, J. Huang, W. H. Tang, and M. Shahidehpour, "Data mining for abnormal power consumption pattern detection based on local matrix reconstruction," *International Journal of Electrical Power and Energy Systems*, vol. 123, no. February, p. 106315, 2020, doi:

10.1016/j.ijepes.2020.106315.

[21] W. Zhang, X. Dong, H. Li, J. Xu, and D. Wang, "Unsupervised Detection of Abnormal Electricity Consumption Behavior Based on Feature Engineering," *IEEE Access*, vol. 8, pp. 55483–55500, 2020, doi: 10.1109/ACCESS.2020.2980079.

[22] H. Ghaedi, S. R. Kamel Tabbakh Farizaniv, and R. Ghaemi, "Improving power theft detection using efficient clustering and ensemble classification," *International Journal of Electrical and Computer Engineering (IJECE)*, vol. 11, no. 5, pp. 3704–3717, 2021, doi: 10.11591/ijece.v11i5.pp3704-3717.

[23] H. Liu and H. Motoda, *Feature Extraction, Construction and Selection: A Data Mining Perspective*. USA: Kluwer Academic Publishers, 1998.

[24] H. Liu and L. Yu, "Toward integrating feature selection algorithms for classification and clustering," *IEEE Transactions on Knowledge and Data Engineering*, vol. 17, no. 4, pp. 491–502, 2005, doi: 10.1109/TKDE.2005.66.

[25] D. H. Wolpert, "Stacked generalization," *Neural Networks*, vol. 5, no. 2, pp. 241–259, 1992, doi: https://doi.org/10.1016/S0893-6080(05)80023-1.

[26] "Irish Social Science Data Archive," 2012. https://www.ucd.ie/issda/data/commissionforenergyregulationcer/.

[27] J. W. Wilson *et al.*, "Cheetahs, Acinonyx jubatus, balance turn capacity with pace when chasing prey," *Biology letters*, vol. 9, no. 5, p. 20130620, Sep. 2013, doi: 10.1098/rsbl.2013.0620.

[28] L. K. Van der Weyde, T. Y. Hubel, J. Horgan, J. Shotton, R. McKenna, and A. M. Wilson, "Movement patterns of cheetahs (Acinonyx jubatus) in farmlands in Botswana," *Biology Open*, vol. 6, no. 1, pp. 118–124, Dec. 2016, doi: 10.1242/bio.021055.

[29] M. S. Farhadinia *et al.*, "Feeding ecology of the Asiatic cheetah Acinonyx jubatus venaticus in low prey habitats in northeastern Iran: Implications for effective conservation," *Journal of Arid Environments*, vol. 87, pp. 206–211, 2012, doi: https://doi.org/10.1016/j.jaridenv.2012.05.002.

[30] P. Agrawal, H. F. Abutarboush, T. Ganesh, and A. W. Mohamed, "Metaheuristic Algorithms on Feature Selection: A Survey of One Decade of Research (2009-2019)," *IEEE Access*, vol. 9, pp. 26766–26791, 2021, doi: 10.1109/ACCESS.2021.3056407.

[31] A. Pandey, D. Rajpoot, and M. Saraswat, "Feature selection method based on hybrid data transformation and binary binomial cuckoo search," *Journal of Ambient Intelligence and Humanized Computing*, vol. 11, Feb. 2020, doi: 10.1007/s12652-019-01330-1.

[32] S. Sarvari, N. F. M. Sani, Z. M. Hanapi, and M. T. Abdullah, "An Efficient Anomaly Intrusion Detection Method With Feature Selection and Evolutionary Neural Network," *IEEE Access*, vol. 8, pp. 70651–70663, 2020, doi: 10.1109/ACCESS.2020.2986217.

[33] R. Shetty, S. Alangar, and P. Pai, "An efficient online sequential extreme learning machine model based on feature selection and parameter optimization using cuckoo search algorithm for multi-step wind speed forecasting," *Soft Computing*, vol. 25, Jan. 2021, doi: 10.1007/s00500-020-05222-x.

[34] S. Marso and M. El Merouani, "Predicting financial distress using hybrid feedforward neural network with cuckoo search algorithm," 2020.

[35] A. Naik, V. Kuppili, and D. Edla, "Efficient feature selection using one-pass generalized classifier neural network and binary bat algorithm with a novel fitness function," *Soft Computing*, vol. 24, Mar. 2020, doi: 10.1007/s00500-019-04218-6.

[36] T. Niu, J. Wang, K. Zhang, and P. Du, "Multi-step-ahead wind speed forecasting based on optimal feature selection and a modified bat algorithm with the cognition strategy," *Renewable Energy*, vol. 118, pp. 213–229, 2018, doi: https://doi.org/10.1016/j.renene.2017.10.075.

[37] S. Jeyasingh and M. Veluchamy, "Modified Bat Algorithm for Feature Selection with the Wisconsin Diagnosis Breast Cancer (WDBC) Dataset," *Asian Pacific journal of cancer prevention : APJCP*, vol. 18, pp. 1257–1264, May 2017, doi: 10.22034/APJCP.2017.18.5.1257.

[38] S. Fei, "Fault diagnosis of bearing based on relevance vector machine classifier with improved binary bat algorithm for feature selection and parameter optimization," *Advances in Mechanical Engineering*, vol. 9, p. 168781401668529, Jan. 2017, doi: 10.1177/1687814016685294.

[39] H. Xu, S. yu, J. Chen, and X. Zuo, "An Improved Firefly Algorithm for Feature Selection in Classification," *Wireless Personal Communications*, vol. 102, pp. 1–12, Oct. 2018, doi: 10.1007/s11277-018-5309-1.

[40] S. B and M. K, "Firefly algorithm based Feature Selection for Network Intrusion Detection," *Computers & Security*, vol. 81, Nov. 2018, doi: 10.1016/j.cose.2018.11.005.

[41] S. Dash, R. Thulasiram, and P. Thulasiraman, "Modified Firefly Algorithm With Chaos Theory for Feature Selection: A Predictive Model for Medical Data," *International Journal of Swarm Intelligence Research*, vol. 10, pp. 1–20, Apr. 2019, doi: 10.4018/IJSIR.2019040101.

[42] C. Yan, J. Ma, H. Luo, G. Zhang, and J. Luo, "A Novel Feature Selection Method for High-Dimensional Biomedical Data Based on an Improved Binary Clonal Flower Pollination Algorithm," *Human Heredity*, vol. 84, pp. 1–13, Sep. 2019, doi: 10.1159/000501652.

[43] G. Zhang, J. Hou, J. Wang, C. Yan, and J. Luo, "Feature Selection for Microarray Data Classification Using Hybrid Information Gain and a Modified Binary Krill Herd Algorithm," *Interdisciplinary Sciences: Computational Life Sciences*, vol. 12, May 2020, doi: 10.1007/s12539-020-00372-w.

[44] Y. Pathak, K. V Arya, and S. Tiwari, "Feature selection for image steganalysis using levy flight-based grey wolf optimization," *Multimedia Tools and Applications*, vol. 78, no. 2, pp. 1473–1494, 2019, doi: 10.1007/s11042-018-6155-6.

[45] Q. Al-Tashi, H. Rais, and S. Jadid Abdulkadir, *Feature Selection Method Based on Grey Wolf Optimization for Coronary Artery Disease Classification*. 2018.

[46] J. Han, M. Kamber, and J. Pei, "3 - Data Preprocessing," in *The Morgan Kaufmann Series in Data Management Systems*, J. Han, M. Kamber, and J. B. T.-D. M. (Third E. Pei, Eds. Boston: Morgan Kaufmann, 2012, pp. 83–124.

[47] L. I. Kuncheva and C. J. Whitaker, "Measures of

Diversity in Classifier Ensembles and Their Relationship with the Ensemble Accuracy," *Machine Learning*, vol. 51, no. 2, pp. 181–207, 2003, doi: 10.1023/A:1022859003006.

[48] D. B. Skalak, "The Sources of Increased Accuracy for Two Proposed Boosting Algorithms," 1996.

[49] M. L. McHugh, "Interrater reliability: the kappa statistic," *Biochemia medica*, vol. 22, no. 3, pp. 276–282, 2012, [Online]. Available: http://europepmc.org/abstract/MED/23092060.

[50] Y. Freund, "Boosting a Weak Learning Algorithm by Majority," *Information and Computation*, vol. 121, no. 2, pp. 256–285, 1995, doi: https://doi.org/10.1006/inco.1995.1136.

[51] A. Askarzadeh, "A novel metaheuristic method for solving constrained engineering optimization problems: Crow search algorithm," *Computers and Structures*, vol. 169, pp. 1–12, 2016, doi: 10.1016/j.compstruc.2016.03.001.

Hassan Ghaedi received the M.S. degrees in software engineering from islamic azad University, Arak branch, iran. He is currently pursuing the Ph.D. degree in the Department of Computer Engineering, islamic azad University, Neyshabur branch, iran. His research interests include data mining (classification and clustering).

Seyed Reza Kamel Tabbakh is with the Department of Software Engineering, Faculty of Engineering, Islamic Azad University Mashhad branch, Mashhad, Iran. He received his PhD in communication and network engineering from University Putra Malaysia (UPM) in 2011. He received his BSc and MSc in software engineering from Islamic Azad University, Mashhad branch and Islamic Azad University, South Tehran branch, Iran respectively. His research interests include IPv6 networks, routing and security.

RezaGhaemi received his Ph.D. degree in Computer Engineering and Artificial Intelligence from National University Putra Malaysia in 2011. He is currently an Associate Professor at Islamic Azad University, Quchan Branch. His research interests include Machine Learning, Data Mining and Soft Computing.

International Journal of Industrial Electronics, Control and Optimization © 2022 IECO
Vol.5, No. 1, pp. 77-87, Jan (2022)

Adaptive Fuzzy Fractional-order Fast Terminal Sliding Mode Control for a Class of Uncertain Nonlinear Systems

Amir Razzaghian[1], Reihaneh Kardehi Moghaddam[2,†] and Naser Pariz[3]

[1,2] Department of Electrical Engineering, Mashhad Branch, Islamic Azad University, Mashhad, Iran
[3] Department of Electrical Engineering, Ferdowsi University of Mashhad, Mashhad, Iran

ABSTRACT

The paper introduces a novel adaptive fuzzy fractional-order (FO) fast terminal sliding mode control procedure for a class of nonlinear systems in the presence of uncertainties and external disturbances. For this purpose, firstly, using fractional calculus, a new FO nonlinear sliding surface is proposed and then, the corresponding FO fast terminal sliding mode controller (FOFTSMC) is designed to satisfy the sliding condition in finite time. Next, to eliminate the chattering phenomenon, a fuzzy system is constructed to design a continuous switching control law. The finite-time stability of the proposed adaptive fuzzy FOFTSMC (AFFOFTSMC) is proved using the concept of Lyapunov stability theorem. Finally, to illustrate the effectiveness of the proposed AFFOFTSMC, three examples are given as case studies. The numerical simulation results confirm the superiority of the proposed controller, which are the better robust performance, faster convergence, finite-time stability of the closed-loop control system, and a chattering free control effort compared to other mentioned control methods.

Article Info

Keywords:
Adaptive control, Fractional calculus, Fuzzy systems, Nonlinear systems, Terminal sliding mode control.

Article History:
Received 2021-06-07
Accepted 2022-02-09

I. INTRODUCTION

In fractional calculus, non-integer and complex orders are applied in definitions of derivative and integral which are called the FO derivative and FO integral, respectively [1]. FO derivatives are widely-applied in both pure and applied mathematics. Recently, some new extensions on FO derivatives are introduced in [2]. Fractional calculus widely used in control engineering because of useful properties to improve the performance of integer-order (IO) controller. Using fractional calculus, provides more accuracy in system modeling and describing real phenomena behaviors [3]. Hence, in [4], a FO model has presented for the hybrid power source system. [5], has proposed a novel FO hyperchaotic economic system. It is also proved that some FO dynamical systems show chaotic behaviors. Many articles investigate FO chaotic systems [6]. The authors in [7] have proposed a FO model for COVID-19. The results show that the FO model has less root-mean-square error than the classical one, and in [8], FO model using the Caputo–Fabrizio derivative is introduced for the same purpose.

Various FO controllers have been introduced by researchers for different purposes such as FOPID [9], FO optimal control [10], FO adaptive control [11] and FO sliding mode control [12]. Stability analysis of FO systems with some new features is investigated in [13-15].

Sliding mode control (SMC) is a well-known and useful controller with many benefits such as simple design, robustness against uncertainties, and disturbance rejection which has been widely used for control of nonlinear systems in the presence of structured and unstructured uncertainties [16]. Convectional SMC designed based on a linear switching manifold which can guarantee the asymptotic stability of the closed-loop control system. To improve the convectional SMC, terminal sliding mode control (TSMC) was developed to

[†]**Corresponding Author:** r_k_moghaddam@mshdiau.ac.ir
Department of Electrical Engineering, Mashhad Branch, Islamic Azad University, Mashhad, Iran

obtain finite-time stability and faster closed-loop control behavior [17]. However, TSMC suffered from singularity problem. To avoid this problem, nonsingular terminal sliding mode controller (NTSMC) is proposed [18].

Chattering phenomenon is another problem that exists in both the conventional SMC and TSMC. These undesirable high-frequency oscillations can stimulate the unmodelled high-frequency dynamics of the system.

To reduce or eliminate the chattering, various techniques have been proposed, such as higher-order SMC [19], Dynamic SMC [20], and boundary layer method which defines a boundary layer around the sliding surface and using a continuous control within the boundary layer [21]. Although, this method reduces the chattering, but it no longer drives the system state to the origin, and steady-state error will be increased. Recently, intelligent approaches such as fuzzy-based SMC [22-24] and neural network-based SMC [25-26] have been designed for reducing chattering.

To deal with structured and unstructured uncertainties, SMC-based techniques have utilized two main approaches: disturbance observer-based SMCs [27-28] and intelligent SMCs [29-30].

Many researches have been using the fractional calculus in the design of FO sliding mode control methods for uncertain nonlinear systems to improve the performance of them [31-34]. However, proposed methods demonstrate robustness against structured and unstructured uncertainties, unknown upper bound of lumped uncertainty forces the designer to choose a large switching gain that results chattering phenomenon. In order to overcome this problem, a FO adaptive neuro-fuzzy sliding mode H_∞ controller is proposed in [35] that neuro-fuzzy system used to estimate the matched uncertainty. In [36], an adaptive neural network FO nonsingular TSMC is introduced. The proposed method uses RBF neural network to estimate lumped uncertainty. An adaptive fuzzy neural network FO sliding mode control technique for micro gyroscope has been presented in [37]. A new multi-layer fuzzy neural network is introduced to improve the control performance and then, the proposed controller is derived to guarantee the trajectory tracking performance. In [38], adaptive FO NTSMC based on fuzzy wavelet neural networks for mobile robots has been investigated. The proposed method uses a fuzzy wavelet neural network to estimate the model uncertainty of the system. The effectiveness of the proposed technique is verified by simulation results. The author in [39], has designed a fuzzy neural network-based FO robust control approach based on the nonlinear SMC for exoskeleton robots. The article has designed a fuzzy neural network compensator to approximate the lumped uncertainty. The simulation results confirm the superiority of the proposed intelligent robust controller. Although, the proposed methods show high robustness in the presence of lumped uncertainty, but in most of them, high computational complexity and guarantee the closed-loop control system stability is a challenging problem.

Finally, several disturbance observer-based FOSMCs for nonlinear systems are proposed in various articles [40-43]. In [40], a FO command filtered backstepping SMC based on a FO nonlinear disturbance observer for the nonlinear systems has been introduced. The controller applied a FO disturbance observer to obtain fast and improved disturbance estimation performance. FO disturbance observer-based adaptive SMC for an uncertain fractional-order nonlinear time-delayed system has investigated in [41]. The numerical simulations have verified the effectiveness of the proposed method. The authors in [42-43] have studied disturbance observer-based FO SMC for a class of nonlinear systems in the presence of the matched and mismatched disturbances. In [42], a finite-time disturbance observer is introduced to estimate the matched and mismatched disturbances and then a FO nonsingular TSMC based on the disturbance observer is designed. The simulation results have demonstrated the superiority of the proposed control method. Also in [43], a FO nonlinear SMC based on an extended nonlinear disturbance observer for the uncertain FO nonlinear systems is presented. The simulation results have confirmed the effectiveness of the proposed controller in the presence of both of the matched and mismatched uncertainties.

Motivated by the above discussion, in this research, based on Lyapunov stability concept and universal approximation theorem using fuzzy systems, we design a novel AFFOFTSMC for a class of uncertain nonlinear systems. The proposed AFFOFTSMC has some superiorities such as: robust performance in the presence of uncertainties, finite-time convergence, faster response with higher accuracy, coping with singularity problem, the chattering elimination in control signal, and higher precision control performance using FO nonlinear sliding surface instead IO one.

The rest of this paper is organized as follows: Preliminaries of fractional calculus are introduced in Section 2. Section 3, presents the problem formulation. In Section 4, the FOFTSMC is introduced. Section 5, designs the proposed AFFOFTSMC for a class of uncertain nonlinear systems. In Section 6, the effectiveness of the proposed controller is illustrated by the several numerical simulations and the results are compared with FOFTSMC and integer-order terminal sliding mode controller (IOTSMC) methods. Finally, conclusions are given in Section 7.

II. PRELIMINARIES

In this section, some basic definitions of fractional calculus are given. Three of the most commonly used definitions of fractional-order derivatives are Caputo, Riemann–Liouville and Grünwald–Letnikov. In this paper, we use the Caputo definition and the simplified notation D^α to denote the Caputo fractional-order derivative.

Definition 1. [44] The αth-order fractional integral of function $f(t)$ is defined as follows

$$ {}_{t_0}I_t^{\alpha} f(t) = \frac{1}{\Gamma(\alpha)} \int_{t_0}^{t} (t-\tau)^{\alpha-1} f(\tau) d\tau, \quad \alpha \in \mathbb{R}^+ \tag{1} $$

where $\Gamma(.)$ is the Gamma function, which is defined as $\Gamma(r) = \int_0^{\infty} e^{-\tau} \tau^{r-1} d\tau$.

Definition 2. [44] The αth-order Caputo fractional derivative of function $f(t)$ is defined as follows

$$ D^{\alpha} f(t) = {}_{t_0}^{C}D_t^{\alpha} f(t) = \begin{cases} \frac{1}{\Gamma(m-\alpha)} \int_{t_0}^{t} \frac{f^{(m)}(\tau)}{(t-\tau)^{\alpha-m+1}} d\tau, & m-1 < \alpha < m \\ \frac{d^m}{dt^m} f(t), & \alpha = m \end{cases} \tag{2} $$

where m is the smallest integer number, larger than or equal to α.

Property 1. [44] The following equality holds for fractional-order integral for $m = 1$.

$$ D^{\alpha}\left({}_{t_0}I_t^{\alpha} f(t)\right) = f(t) \tag{3} $$

Property 2. [44] The following equality holds for the Caputo fractional-order derivative for $m = 1$.

$$ {}_{t_0}I_t^{\alpha} f(t)(D^{\alpha} f(t)) = f(t) - f(t_0) \tag{4} $$

Property 3. [45] Let $f(t)$ is $p \in \mathbb{N}$ times continuously differentiable. If there exists $l \in \mathbb{N}$ such that $l \le p$ and $\beta, \alpha + \beta \in [l-1, l]$, then $D^{\alpha}\left(D^{\beta} f(t)\right) = D^{\alpha+\beta} f(t)$ (5)

Lemma 1. [46] Let $y(t) \in \mathbb{R}^n$ be a differentiable vector. Then, for any time instant $t \ge 0$

$$ \frac{1}{2} D^{\alpha}(y(t)^T P y(t)) \le y(t)^T P D^{\alpha} y(t), \forall\ \alpha \in (0,1] \tag{6} $$

where $P \in \mathbb{R}^{n \times n}$ is a positive definite constant matrix.

Lemma 2. [47] Let $x = 0$ be an equilibrium point of the following non-autonomous fractional-order system

$$ D^{\alpha} x(t) = f(x,t) \tag{7} $$

where $\alpha \in (0,1)$ and $f(x,t)$ satisfies the Lipschitz condition with Lipschitz constant $M > 0$. Suppose that there exists a Lyapunov function $V(t, x(t))$ and a class-K functions ι_1, ι_2 and ι_3 satisfying

$$ \iota_1(\|x\|) \le V(t,x) \le \iota_2(\|x\|) \tag{8} $$

$$ D^r V(t,x) \le -\iota_3(\|x\|) \tag{9} $$

where $r \in (0,1)$. Then the equilibrium point of system (7) is asymptotically stable.

III. System Description

Consider the following class of uncertain high-order nonlinear systems

$$ \begin{cases} \dot{x}_1 = x_2 \\ \dot{x}_2 = x_3 \\ \dots \\ \dot{x}_{n-1} = x_n \\ \dot{x}_n = f(\boldsymbol{x},t) + b(\boldsymbol{x},t)u(t) + d(\boldsymbol{x},t) \end{cases} \tag{10} $$

where $\boldsymbol{x} = [x_1, x_2, \dots, x_n]^T$ indicates the system state vector, $f(\boldsymbol{x},t) = f_n(\boldsymbol{x},t) + \Delta f(\boldsymbol{x},t)$ and $\Delta f(\boldsymbol{x},t)$ is an uncertain term representing the un-modeled dynamics or structural variation of the system, $b(\boldsymbol{x},t) = b_n(\boldsymbol{x},t) + \Delta b(\boldsymbol{x},t)$ and $\Delta b(\boldsymbol{x},t)$ is the input uncertainty, $u(t)$ is the control input, and $d(x,t)$ is the external disturbance.

Assumption 1. The matrices $f_n(\boldsymbol{x},t)$ and $b_n(\boldsymbol{x},t)$ are known, smooth nonlinear functions and $b_n(\boldsymbol{x},t) \neq 0$ for of all possible $\boldsymbol{x}$ and $t \ge 0$.

Assumption 2. $L(x,t)$ called the lumped uncertainty and defined as

$$ L(\boldsymbol{x},t) = \Delta f(\boldsymbol{x},t) + \Delta b(\boldsymbol{x},t)u(t) + d(\boldsymbol{x},t) \tag{11} $$

It is supposed that $L(\boldsymbol{x},t)$ is bounded $\|L(\boldsymbol{x},t)\| \le \sigma$, where σ is a known positive constant.

The controlling aim is to design a novel chattering free FO fast terminal sliding mode controller using switching fuzzy systems for stabilizing state variables of the system in the presence of uncertainties in finite time.

IV. FOFTSMC Design

The novel fractional-order fast terminal sliding surface is defined as

$$ s(t) = D^{1-\alpha} x_n + \gamma_n \mathrm{sig}(x_n)^{\zeta_n} + \gamma_{n-1}\mathrm{sig}(x_{n-1})^{\zeta_{n-1}} + \dots + \gamma_1 \mathrm{sig}(x_1)^{\zeta_1} \tag{12} $$

where $s = [s_1, \dots, s_n]^T$, γ_i $(i = 1, 2, \dots, n)$ are designed positive constants and choose such that the polynomial $\Lambda^n + \gamma_n \Lambda^{n-1} + \dots + \gamma_2 \Lambda + \gamma_1$ is Hurwitz.

$$ \zeta_{i-1} = \zeta_i \zeta_{i+1} / (2\zeta_{i+1} - \zeta_i)\ (i = 2, \dots, n), \zeta_{i+1} = 1, \zeta_n = \zeta_0 \in (1-\epsilon, 1), \epsilon \in (0,1), \text{ and } \mathrm{sig}(.)^{\zeta_i} = |.|^{\zeta_i}\mathrm{sign}(.) \tag{13} $$

[18].

$$ D^{\alpha} s = \dot{x}_n + D^{\alpha}(\gamma_n \mathrm{sig}(x_n)^{\zeta_n} + \gamma_{n-1}\mathrm{sig}(x_{n-1})^{\zeta_{n-1}} + \dots + \gamma_1 \mathrm{sig}(x_1)^{\zeta_1}) = f_n(\boldsymbol{x},t) + b_n(\boldsymbol{x},t)u(t) + L(\boldsymbol{x},t) + D^{\alpha}(\gamma_n \mathrm{sig}(x_n)^{\zeta_n} + \gamma_{n-1}\mathrm{sig}(x_{n-1})^{\zeta_{n-1}} + \dots + \gamma_1 \mathrm{sig}(x_1)^{\zeta_1}) $$

Theorem 1. For the nonlinear system (10) with the fractional-order nonlinear sliding surface (12), if control law is designed as

$$ u(t) = -b_n^{-1}(f_n + D^{\alpha}(\gamma_n \mathrm{sig}(x_n)^{\zeta_n} + \gamma_{n-1}\mathrm{sig}(x_{n-1})^{\zeta_{n-1}} + \dots + \gamma_1 \mathrm{sig}(x_1)^{\zeta_1}) + \sigma + k_1 s + k_2 \mathrm{sign}(s)) \tag{14} $$

where k_1 and k_2 are known positive constants, then the system states will converge to zero in finite time.

Proof. Let the Lyapunov function is selected as

$$ V_1(t) = \frac{1}{2} s^T s \tag{15} $$

Taking the FO derivative of $V_1(t)$ and based on Lemma 1, one obtains

$$D^{\alpha}V_1(t) \le sD^{\alpha}s \tag{16}$$

Substituting (13) into (16) yields

$$\begin{aligned} D^{\alpha}V_1(t) \le s\Big(& f_n(\boldsymbol{x},t) + b_n(\boldsymbol{x},t)u(t) + L(\boldsymbol{x},t) \\ & + D^{\alpha}(\gamma_n \mathrm{sig}(x_n)^{\zeta_n} \\ & + \gamma_{n-1}\mathrm{sig}(x_{n-1})^{\zeta_{n-1}} + \cdots \\ & + \gamma_1 \mathrm{sig}(x_1)^{\zeta_1})\Big) \end{aligned} \tag{17}$$

Applying the control law (14) into (17) results in

$$\begin{aligned} D^{\alpha}V_1 &\le s(L(\boldsymbol{x},t) - \sigma - k_1 s - k_2 \mathrm{sign}(s)) \\ &\le s(|L(\boldsymbol{x},t)| - \sigma - k_1 s \\ &\quad - k_2 \mathrm{sign}(s)) \\ &\le s(-k_1 s - k_2 \mathrm{sign}(s)) \\ &\le -k_1 s^2 - k_2|s| \\ &\le -k(s^2 + |s|) \le -k|s| \end{aligned} \tag{18}$$

where $k = \min\{k_1, k_2\}$

Consequently, the system states will converge to sliding surface $s(t) = 0$ asymptotically. Next, we show that convergence occurs in finite time.

Let the reaching time, the time for the system states to reach the sliding surface, be t_r. Using Property 2 and taking the fractional integral of both sides of (18) from 0 to t_r, one obtains

$$V_1(t_r) - V_1(0) \le -\frac{k}{\sqrt{1/2}\,\Gamma(\alpha)} \int_0^t {V_1}^{1/2}(\theta)(t-\theta)^{\alpha-1} d\theta \tag{19}$$

Since $V_1(t_r) - V_1(0) = \int_0^{t_r} \dot{V}_1(\theta)d\theta$, we can write

$$\int_0^{t_r} \frac{\dot{V}_1(\theta)}{{V_1}^{1/2}(\theta)} d\theta \le -\frac{k}{\sqrt{1/2}\,\Gamma(\alpha)} \int_0^{t_r} (t-\theta)^{\alpha-1} d\theta \tag{20}$$

$$2{V_1}^{1/2}(t)\Big|_0^{t_r} \le -\frac{k t_r^{\alpha}}{\sqrt{1/2}\,\Gamma(\alpha+1)} \tag{21}$$

Noting that $V_1(t_r) = 0$, it yields

$$t_r \le \left(\frac{2\sqrt{1/2}\,\Gamma(\alpha+1){V_1}^{1/2}(0)}{k}\right)^{1/\alpha} \tag{22}$$

Thus, it can be concluded that the system states will converge to sliding surface $s(t) = 0$ in finite time and the proof is completed.

V. Main Results

In this section, a fuzzy system is used to estimate the switching control signal $k_2\mathrm{sign}(s)$. Therefore, the switching term in the control law becomes continuous, and chattering phenomenon can be alleviated.

Based on universal the approximation theorem, fuzzy systems with singleton fuzzifier, center average defuzzifier, and product inference engine, can approximate every function in the domain. First, we define fuzzy sets $\psi_i^{\varsigma_i}$, $\varsigma_i = 1,2,\dots,\rho_i$ for input vector x_i $(i = 1,2,\dots,n)$. Next, use $\prod_{i=1}^{n}\rho_i$ fuzzy rules to construct fuzzy system $\hat{h}(\boldsymbol{x}|\omega_h)$, where j-th fuzzy rule is:

R^j: If x_1 is $\psi_1^{\varsigma_1}$ and … and x_n is $\psi_n^{\varsigma_n}$ then $\hat{h}$ is $B^{\varsigma_1,\dots,\varsigma_n}$

Hence, the output of fuzzy system is

$$\hat{h}(\boldsymbol{x}|\omega_h) = \frac{\sum_{\varsigma_1=1}^{\rho_1}\cdots\sum_{\varsigma_n=1}^{\rho_n} \bar{y}_h^{\varsigma_1\cdots\varsigma_n}\left(\prod_{i=1}^{n}\mu_{\psi_i^{\varsigma_i}}(x_i)\right)}{\sum_{\varsigma_1=1}^{\rho_1}\cdots\sum_{\varsigma_n=1}^{\rho_n}\left(\prod_{i=1}^{n}\mu_{\psi_i^{\varsigma_i}}(x_i)\right)} \tag{23}$$

where $\mu_{\psi_i^{\varsigma_i}}(x_i)$ is the Gaussian membership function of x_i and defined as

$$\mu_{\psi_i^{\varsigma_i}}(x_i) = \exp\left(-\frac{(x_i - c_i)^2}{2\varrho_i^2}\right) \tag{24}$$

where c_i and ϱ_i are the center and width of the i-th fuzzy set $\psi_i^{\varsigma_i}$, respectively.

If $\bar{y}_h^{\varsigma_1\cdots\varsigma_n}$ select as the free parameter, and put it in the set $\hat{\omega} \in R^{\prod_{i=1}^{n}\rho_i}$. Fuzzy basis function column vector $\xi(\boldsymbol{x})$ in introduced such as

$$\hat{h}(\boldsymbol{x}|\omega_h) = \hat{\omega}_h^T \xi(\boldsymbol{x}) \tag{25}$$

where

$$\xi(\boldsymbol{x}) = \frac{\prod_{i=1}^{n}\mu_{\psi_i^{\varsigma_i}}(x_i)}{\sum_{\varsigma_1=1}^{\rho_1}\cdots\sum_{\varsigma_n=1}^{\rho_n}\left(\prod_{i=1}^{n}\mu_{\psi_i^{\varsigma_i}}(x_i)\right)} \tag{26}$$

Now, we use fuzzy system $\hat{\eta}(s|\omega_\eta)$ in the form of (25) to approximate the $k_2\mathrm{sign}(s)$.

Replacing $k_2\mathrm{sign}(s)$ by $\hat{\eta}(s|\omega_\eta)$, the control law is rewritten as

$$\begin{aligned} u(t) = -b_n^{-1}\Big(& f_n + D^{\alpha}(\gamma_n \mathrm{sig}(x_n)^{\zeta_n} + \\ & \gamma_{n-1}\mathrm{sig}(x_{n-1})^{\zeta_{n-1}} + \cdots + \gamma_1 \mathrm{sig}(x_1)^{\zeta_1}) + \sigma + \\ & k_1 s + \hat{\eta}(s|\omega_\eta)\Big) \end{aligned} \tag{27}$$

$$\hat{\eta}(s|\omega_\eta) = \hat{\omega}_\eta^T \phi(s) \tag{28}$$

where $\hat{\eta}(s|\omega_\eta)$ is the output of the fuzzy system and $\phi(s)$ is fuzzy vector.

Let the define the optimal parameters of fuzzy system as

$$\omega_\eta^* = \arg\min_{\omega_\eta \in \Omega_\eta}\left[\sup_{x\in R^n}|\hat{\eta}(s|\omega_\eta) - k_2\mathrm{sign}(s)|\right] \tag{29}$$

where Ω_η is constraint set of ω_η, and can be defined as

$$\Omega_\eta = \{\omega_\eta \in R \mid |\omega_\eta| \le M_\eta\} \tag{30}$$

where M_η is a positive constant.

The ideal $\hat{\eta}(s|\omega_\eta)$ is

$$\hat{\eta}(s|\omega_\eta^*) = k_2\mathrm{sign}(s) \tag{31}$$

The block diagram of proposed adaptive fuzzy fractional-order fast terminal sliding mode controller with switching fuzzy system is shown in Fig. 1.

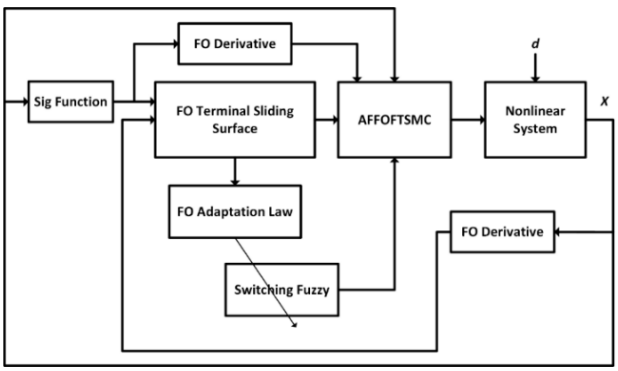

Fig. 1. Block diagram of the proposed AFFOFTSMC

Theorem 2. For the nonlinear system (10) with the fractional-order nonlinear sliding surface (12), if control law is chosen as (27) and adaptive law is designed as (32), then the system states will converge to zero in finite time.

$$D^{\alpha}\omega_{\eta} = \frac{1}{\delta}s\phi(s) \tag{32}$$

where $\delta > 0$.

Proof. Let the Lyapunov function is selected as

$$V_2(t) = \frac{1}{2}s^T s + \frac{1}{2}\delta\tilde{\omega}_{\eta}^T\tilde{\omega}_{\eta} \tag{33}$$

where $\tilde{\omega}_{\eta} = \omega_{\eta}^{*} - \omega_{\eta}$.

Taking the FO derivative of $V_2(t)$ and based on Lemma 1, one obtains

$$D^{\alpha}V_2(t) \le sD^{\alpha}s + \delta\tilde{\omega}_{\eta}^T D^{\alpha}\tilde{\omega}_{\eta} \tag{34}$$

Substituting (13) into (33) yields

$$\begin{aligned} D^{\alpha}V_2(t) \le s\Big(& f_n(\boldsymbol{x},t) + b_n(\boldsymbol{x},t)u(t) + L(\boldsymbol{x},t) \\ & + D^{\alpha}(\gamma_n \mathrm{sig}(x_n)^{\zeta_n} \\ & + \gamma_{n-1}\mathrm{sig}(x_{n-1})^{\zeta_{n-1}} + \cdots \\ & + \gamma_1 \mathrm{sig}(x_1)^{\zeta_1})\Big) + \delta\tilde{\omega}_{\eta}^T D^{\alpha}\tilde{\omega}_{\eta} \end{aligned} \tag{35}$$

Applying the control law (27) into (35) results in

$$\begin{aligned} D^{\alpha}V_2 \le s\Big(& L(\boldsymbol{x},t) - \sigma - k_1 s - \hat{\eta}\big(s|\omega_{\eta}\big) \\ & + \hat{\eta}\big(s|\omega_{\eta}^{*}\big) - \hat{\eta}\big(s|\omega_{\eta}^{*}\big)\Big) \\ & + \delta\tilde{\omega}_{\eta}^T D^{\alpha}\tilde{\omega}_{\eta} \\ \le s\Big(& L(\boldsymbol{x},t) + \tilde{\omega}_{\eta}^T\phi(s) - \sigma \\ & - k_1 s - \hat{\eta}\big(s|\omega_{\eta}^{*}\big)\Big) \\ & + \delta\tilde{\omega}_{\eta}^T D^{\alpha}\tilde{\omega}_{\eta} \\ \le \delta\tilde{\omega}_{\eta}^T\Big(& \frac{1}{\delta}s\phi(s) - D^{\alpha}\omega_{\eta}\Big) \\ & + s\Big(L(\boldsymbol{x},t) - \sigma - k_1 s \\ & - \hat{\eta}\big(s|\omega_{\eta}^{*}\big)\Big) \end{aligned} \tag{36}$$

where $D^{\alpha}\tilde{\omega}_{\eta} = -D^{\alpha}\omega_{\eta}$.

Using the adaptive law (32), we have

$$\begin{aligned} D^{\alpha}V_2 &\le s(L(\boldsymbol{x},t) - \sigma - k_1 s - k_2\mathrm{sign}(s)) \\ &\le s(|L(\boldsymbol{x},t)| - \sigma - k_1 s \\ &\quad - k_2\mathrm{sign}(s)) \\ &\le s(-k_1 s - k_2\mathrm{sign}(s)) \\ &\le -k_1 s^2 - k_2|s| \\ &\le -k(s^2 + |s|) \le -k|s| \end{aligned} \tag{37}$$

where $k = \min\{k_1, k_2\}$

Therefore, the system states converge to zero asymptotically. Similar to Theorem 1, it is proved that the system states converge to zero in finite time and the proof is completed.

VI. Simulation Results

In this section, in order to verify superiority of the proposed AFFOFTSMC, three examples are given: a second-order dynamical system, a third-order dynamical system and a chaotic system. Also, the proposed method is compared with FOFTSMC, and IOTSMC in [19].

A comparative analysis based on the integral absolute value (IAV) index using different controllers for each example is presented in Tables I-III, respectively.

$$IAV = \int_0^t |V(t)|\,dt.$$

Example 1. Consider the dynamical equation of an inverted pendulum as follows [48]:

$$\begin{cases} \dot{x}_1 = x_2 \\ \dot{x}_2 = f(\boldsymbol{x}) + b(\boldsymbol{x})u + d \end{cases} \tag{38}$$

where $f(\boldsymbol{x}) = \frac{\mathrm{g}\sin x_1 - (mlx_2\cos x_1 \sin x_1)/(m+m_c)}{l(4/3 - m\cos^2 x_1/(m+m_c))}$,

$b(\boldsymbol{x}) = \frac{\cos x_1/(m+m_c)}{l(4/3 - m\cos^2 x_1/(m+m_c))}$,

$\boldsymbol{x} = [x_1 \quad x_2]$, x_1 and x_2 are the angular position and velocity of the pole, respectively, u is the control input, $\mathrm{g} = 9.8$ m/s^2, $m_c = 1$ kg and $m = 0.1$ kg are the mass of the vehicle and the mass of the pendulum, respectively, $l = 0.5$ m is the half length of the pendulum, and $d = 1 + \sin \pi t/2$ is an external disturbance where $|d| \le 2$.

From (12) and (27), the sliding surface and the control effort are determined as:

$$s(t) = D^{1-\alpha}x_2 + \gamma_2\mathrm{sig}(x_2)^{\zeta_2} + \gamma_1\mathrm{sig}(x_1)^{\zeta_1} \tag{39}$$

$$\begin{aligned} u(t) = -b^{-1}\Big(& f + D^{\alpha}(\gamma_2\mathrm{sig}(x_2)^{\zeta_2} + \gamma_1\mathrm{sig}(x_1)^{\zeta_1}) \\ & + \sigma + k_1 s + \hat{\eta}\big(s|\omega_{\eta}\big)\Big) \end{aligned} \tag{40}$$

The membership function of the sliding surface defined as

$$\begin{cases} \mu_{NM}(s) = \dfrac{1}{\big(1 + \exp\big(5(s+3)\big)\big)} \\ \mu_{ZO}(s) = \dfrac{1}{(1 + \exp(-s^2))} \\ \mu_{PM}(s) = \dfrac{1}{\big(1 + \exp\big(5(s-3)\big)\big)} \end{cases} \tag{41}$$

The control parameters are given as: $\gamma_1 = 10$, $\gamma_2 = 7$, $\zeta_1 = 9/23$, $\zeta_2 = 9/16$, $\sigma = 2$, $\alpha = 0.6$, $k_1 = 2$, $\delta = 120$, and in FOFTSMC, $k_2 = 3$. The initial condition is $\boldsymbol{x}(0) = [\pi/9 \quad 0]^T$.

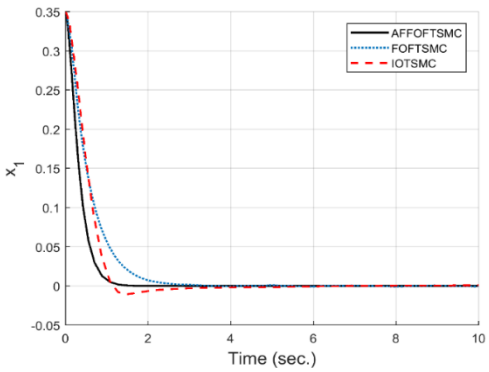

(a)

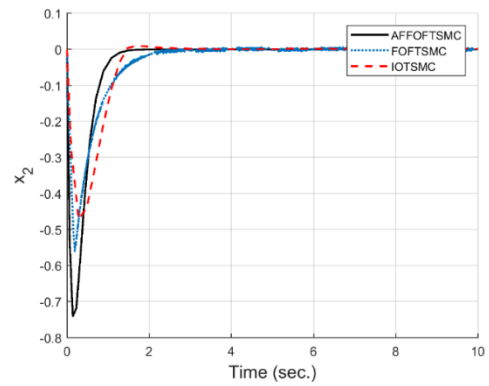

(b)

Fig. 2. State responses of inverted pendulum under the mentioned controllers

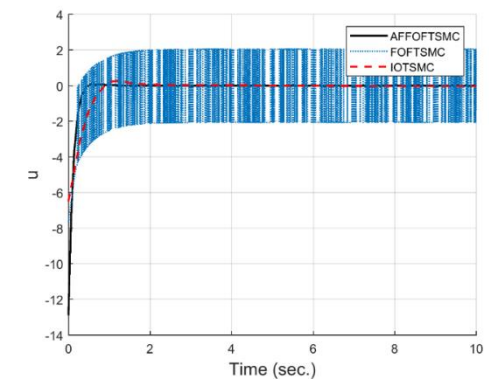

Fig. 3. The time responses of control signals for inverted pendulum

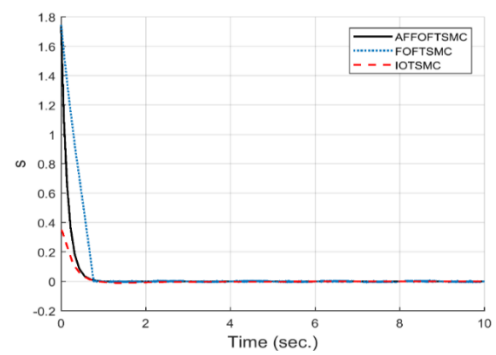

Fig. 4. The time responses of sliding surfaces for inverted pendulum

TABLE I
INTEGRAL OF THE ABSOLUTE VALUES FOR INVERTED PENDULUM

Controller	x_1	x_2	u
AFFOFTSMC	0.119	0.289	1.428
FOFTSMC	0.145	0.454	2.375
IOTSMC	0.194	0.369	2.361

In Figs. 2-4, the state responses, control inputs and sliding surfaces of the inverted pendulum system under the maintained controllers are shown, respectively. Based on Fig. 2, the state responses of the inverted pendulum system under the proposed controller have faster convergence and smaller reaching time respect to the other mentioned controllers.

It is observed from Fig. 3 that the chattering phenomenon is completely removed by the proposed AFFOFTSMC due to applying switching fuzzy, while the sign function in FOFTSMC produces serious chattering. However, control signal in IOTSMC can significantly reduce chattering due to the continuous control law, but has an overshoot and longer reaching time.

As it is seen in Fig. 4, sliding surface of AFFOFTSMC converge to the zero quicker than other sliding surfaces.

Example 2. Consider the nonlinear system as follow [49]:

$$\begin{cases} \dot{x}_1 = x_2 \\ \dot{x}_2 = x_3 \\ \dot{x}_3 = -(1+0.3\sin t)x_1^2 - (1.5+0.2\cos t)x_2 \\ \quad -(1+0.4\sin t)x_3 + (3+\cos x_1)u + d \end{cases} \tag{42}$$

where disturbance d is a random noise with a mean value of 0.5 and $|d| \le 0.1$.

From (12) and (27), the sliding surface and the control effort are determined as:

$$s(t) = D^{1-\alpha}x_3 + \gamma_3 \mathrm{sig}(x_3)^{\zeta_3} + \gamma_2 \mathrm{sig}(x_2)^{\zeta_2} + \gamma_1 \mathrm{sig}(x_1)^{\zeta_1} \tag{43}$$

$$\begin{aligned} u(t) = (3+\cos x_1)^{-1}\Big(& (1+0.3\sin t)x_1^2 \\ & + (1.5+0.2\cos t)x_2 \\ & + (1+0.4\sin t)x_3 \\ & - D^{\alpha}(\gamma_3 \mathrm{sig}(x_3)^{\zeta_3} \\ & + \gamma_2 \mathrm{sig}(x_2)^{\zeta_2} + \gamma_1 \mathrm{sig}(x_1)^{\zeta_1}) \\ & - \sigma - k_1 s - \hat{\eta}\big(s|\omega_\eta\big)\Big) \end{aligned} \tag{44}$$

The membership function of the sliding surface is defined as (41).

The control parameters are given as: $\gamma_1 = 80$, $\gamma_2 = 66$, $\gamma_3 = 15$, $\zeta_1 = 7/16$, $\zeta_2 = 7/13$, $\zeta_3 = 7/10$, $\sigma = 0.1$, $\alpha = 0.35$, $k_1 = 3$, $\delta = 150$, and in FOFTSMC, $k_2 = 5$. The initial condition is $\boldsymbol{x}(0) = [0.3 \quad -1 \quad 0.5]^T$.

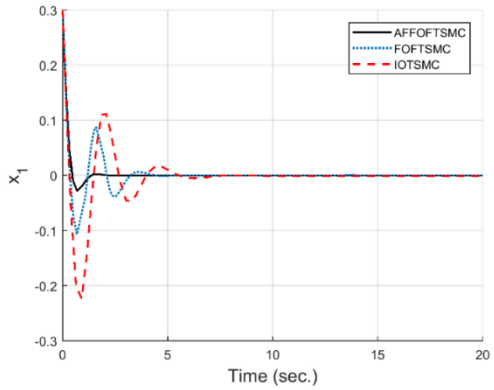

(a)

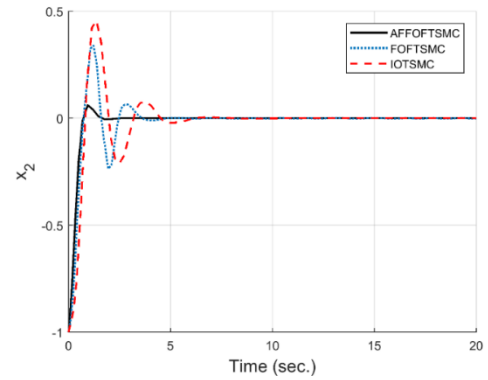

(b)

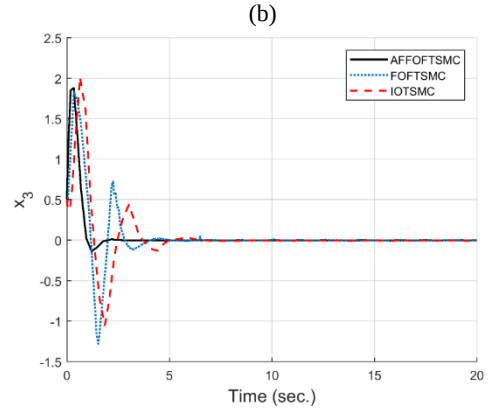

(c)

Fig. 5. State responses of the nonlinear system under the mentioned controllers

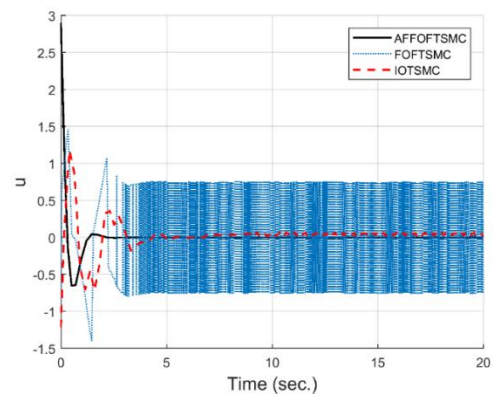

Fig. 6. The time responses of control signals for the nonlinear system

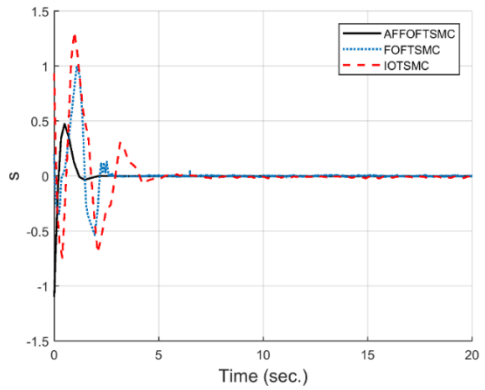

Fig. 7. The time responses of sliding surfaces for the nonlinear system

TABLE II

INTEGRAL OF THE ABSOLUTE VALUES FOR THE SYSTEM 2

Controller	x_1	x_2	x_3	u
AFFOFTSMC	0.069	0.361	1.135	0.789
FOFTSMC	0.166	0.674	1.865	1.087
IOTSMC	0.361	1.142	2.547	1.596

The time responses of system states, control inputs and sliding surfaces are shown in Figs. 5-7, respectively.

Based on Fig. 5, using proposed AFFOFTSMC, the state variables of the system have faster convergence and high robustness against uncertainties compared to other mentioned controllers. Also, state response curves of FOFTSMC and IOTSMC methods have large overshoots and undershoots, and much longer reaching times compared to the proposed method.

Fig. 6, illustrates that control input obtained by the proposed AFFOFTSMC is smooth and free of chattering. It is obvious, though chattering existing in the control input obtained by IOTSMC is significantly lesser compared to that in FOFTSMC, but as it observes in Fig. 5, the time that the system states converge to zero is much longer.

It can be seen from Fig.7 that the proposed sliding surface converge to zero faster than other sliding surfaces. On the other hand, sliding surface in IOTSMC is oscillated around the origin.

Example 3. Consider the uncertain chaotic Genesio system described as [50]:

$$\begin{cases} \dot{x}_1 = x_2 \\ \dot{x}_2 = x_3 \\ \dot{x}_3 = -6x_1 - 2.92x_2 - 1.2x_3 + x_1^2 + \Delta f(\boldsymbol{x}, t) + u + \end{cases} \quad (45$$

The uncertain term $\Delta f(\boldsymbol{x}, t) = 0.1\sin(\pi x_1)\sin(2\pi x_2)\sin(3\pi x_3)$, where $|\Delta f(\boldsymbol{x})| \leq 0.1$ and $d = 0.1\cos(3t)$, where $|d| \leq 0.1$.

From (12) and (27), the sliding surface and the control effort are determined as:

$$s(t) = D^{1-\alpha}x_3 + \gamma_3 \mathrm{sig}(x_3)^{\zeta_3} + \gamma_2 \mathrm{sig}(x_2)^{\zeta_2} + \gamma_1 \mathrm{sig}(x_1)^{\zeta_1} \quad (46)$$

$$u(t) = 6x_1 + 2.92x_2 + 1.2x_3 - x_1^2 - \sigma - D^{\alpha}(\gamma_3 \mathrm{sig}(x_3)^{\zeta_3} + \gamma_2 \mathrm{sig}(x_2)^{\zeta_2} + \gamma_1 \mathrm{sig}(x_1)^{\zeta_1}) - k_1 s - \hat{\eta}(s|\omega_\eta) \quad (47)$$

In (40), the membership function of the sliding surface is described.

The control parameters are given as: $\gamma_1 = 80$, $\gamma_2 = 66$, $\gamma_3 = 15$, $\zeta_1 = 7/16$, $\zeta_2 = 7/13$, $\zeta_3 = 7/10$, $\sigma = 0.2$, $\alpha = 0.85$, $k_1 = 5$ and $\delta = 200$, and in FOTSMC, $k_2 = 10$. The initial condition is $\boldsymbol{x}(0) = [-1 \quad 1 \quad 0]^T$.

The state responses of the chaotic Genesio system are shown in Fig. 8. It is evident that the state trajectories of the chaotic system under the proposed AFFOFTSMC reach the equilibrium point in finite time. Although, other mentioned controllers can suppress chaos and stabilize the system states around the equilibrium point, but it is occurring in much longer time.

Fig. 9, shows the time response of the control inputs and the time response of the sliding surfaces are depicted in Fig. 10. Clearly, the proposed control method eliminated chattering while achieving small reaching time. Finite-time and smaller sliding surface of the proposed AFFOFTSMC confirmed excellent performance of the method compared with the other mentioned controllers.

TABLE III

INTEGRAL OF THE ABSOLUTE VALUES FOR THE GENESIO SYSTEM

Controller	x_1	x_2	x_3	u
AFFOFTSMC	0.416	1.069	2.139	9.877
FOFTSMC	0.642	1.856	4.365	17.19
IOTSMC	0.804	1.997	3.558	10.64

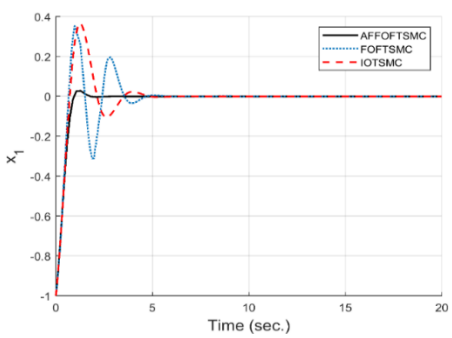

(a)

Fig.8. Continued

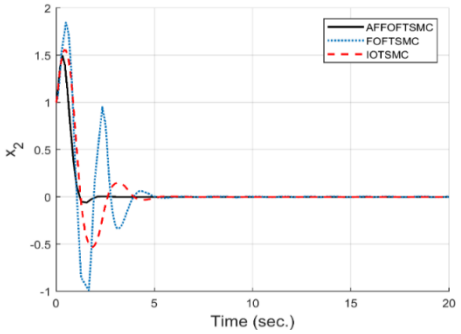

(b)

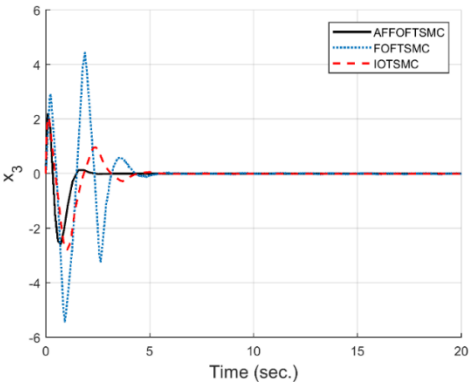

(c)

Fig. 8. State responses of chaotic Genesio system under the mentioned controllers

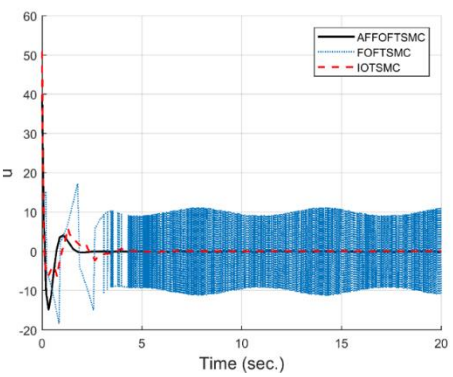

Fig. 9. The time responses of control signals for chaotic Genesio system

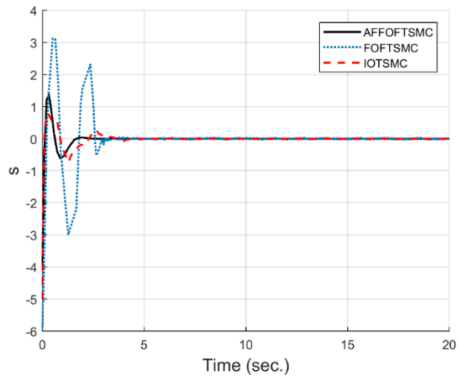

Fig. 10. The time responses of sliding surfaces for chaotic Genesio system

VII. CONCLUSIONS

This paper studies a procedure for the design of a FO robust controller using a combination of sliding mode control technique and fuzzy systems to stabilize the state variables and the finite-time convergence of a class of nonlinear systems in the presence of model uncertainty and external disturbances.

The finite-time stability of the closed-loop control system using Lyapunov stability theorem has been proved and the fuzzy system through the online adaptive learning laws is utilized to approximate the switching control term. Unlike integer-order fast terminal sliding mode controller, the FO controller has more degree of freedom to increase control performance accuracy. Furthermore, applying the fuzzy system helps to achieve a chattering free control signal.

The proposed control method was successfully applied to the three nonlinear systems. The numerical simulation results have been confirmed the superior performance of the proposed control method comparing to the other mentioned controllers.

REFERENCES

[1] H. G. Sun, Y. Zhang, D. Baleanu, W. Chen, and Y. Chen, "A new collection of real world applications of fractional calculus in science and engineering," *Communications in Nonlinear Science and Numerical Simulation*, Vol. 64, pp. 213-231, Nov. 2018.

[2] X. J. Yang, *General fractional derivatives: theory, methods and applications*, New York: CRC Press, 2019.

[3] O. Naifar, and A. Ben Makhlouf, *Fractional Order Systems—Control Theory and Applications*, Springer, Chap. 3, pp. 29-47, 2022.

[4] Y. Wang, G. Gao, X. Li, and Z. Chen, "A fractional-order model-based state estimation approach for lithium-ion battery and ultra-capacitor hybrid power source system considering load trajectory," *Journal of Power Sources*, Vol. 449, pp. 227543, Feb. 2020.

[5] A. Yousefpour, H. Jahanshahi, J. M. Munoz-Pacheco, S. Bekiros, and Z. Wei "A fractional-order hyper-chaotic economic system with transient chaos," *Chaos, Solitons & Fractals*, Vol. 130, pp. 109400, Jan. 2020.

[6] M. S. Tavazoei "Fractional order chaotic systems: history, achievements, applications, and future challenges," *The European Physical Journal Special Topics*, Vol. 229, No. 6, pp. 887-904, Mar. 2020.

[7] K. Rajagopal, N. Hasanzadeh, F. Parastesh, I. I. Hamarash, S. Jafari, and I. Hussain. "A fractional-order model for the novel coronavirus (COVID-19) outbreak," *Nonlinear Dynamics*, Vol. 101, No. 1, pp. 711-718, Jul. 2020.

[8] A. Boudaoui, Y. El hadj Moussa, Z. Hammouch, and S. Ullah, "A fractional-order model describing the dynamics of the novel coronavirus (COVID-19) with nonsingular kernel," *Chaos, Solitons & Fractals*, Vol. 146, pp. 110859, May 2021.

[9] S. Zhang, L. Liu, and X Cui, "Robust FOPID controller design for fractional-order delay systems using positive stability region analysis," *International Journal of Robust and Nonlinear Control*, Vol.29, No. 15, pp. 5195-5212, Oct. 2019.

[10] M. H. Heydari, and Z. Avazzadeh, "A computational method for solving two-dimensional nonlinear variable-order fractional optimal control problems," *Asian Journal of Control*, Vol. 22, No. 3, pp. 1112-1126, May 2020.

[11] Q. Zhu, M. Xu, W. Liu, and M. Zheng, "A state of charge estimation method for lithium-ion batteries based on fractional order adaptive extended kalman filter," *Energy*, Vol. 187, pp. 115880, Nov. 2019.

[12] C. Hua, J. Chen, and X. Guan, "Fractional-order sliding mode control of uncertain QUAVs with time-varying state constraints," *Nonlinear Dynamics*, Vol. 95, No. 2, pp. 1347-1360, Jan. 2019.

[13] X. Yang, C. Li, T. Huang, and Q. Song, "Mittag–Leffler stability analysis of nonlinear fractional-order systems with impulses," *Applied Mathematics and Computation*, Vol. 293, pp. 416-422, Jan. 2017.

[14] V. N. Phat, and N. T. Thanh, "New criteria for finite-time stability of nonlinear fractional-order delay systems: A Gronwall inequality approach," *Applied Mathematics Letters*, Vol. 83, pp. 169-175, Sep. 2018.

[15] L. Liu, S. Zhang, D. Xue, and Y. Chen, "Robust stability analysis for fractional-order systems with time delay based on finite spectrum assignment," *International Journal of Robust and Nonlinear Control*, Vol. 29, No. 8, pp. 2283-2295, May 2019.

[16] Y. Shtessel, C. Edwards, L. Fridman, and A. Levant, *Sliding mode control and observation*, New York: Springer, 2014.

[17] S. Kamal, J. A. Moreno, A. Chalanga, B. Bandyopadhyay, and L. M. Fridman, "Continuous terminal sliding-mode controller," *Automatica*, Vol. 69, pp. 308-314, Jul. 2016.

[18] H. Wang, L. Shi, Z. Man, J. Zheng, S. Li, M. Yu, C. Jiang, H. Kong, and Z. Cao, "Continuous fast nonsingular terminal sliding mode control of automotive electronic throttle systems using finite-time exact observer," *IEEE Trans. Ind. Electron.*, Vol. 65, No. 9, pp. 7160-7172, Sep. 2018.

[19] Y. Feng, F. Han, and X. Yu, "Chattering free full-order sliding-mode control," *Automatica*, Vol. 50, No. 4, pp. 1310-1314, Apr. 2014.

[20] B. Sahoo, S. K. Routray, and P. K. Rout, "Execution of robust dynamic sliding mode control for smart photovoltaic application," *Sustainable Energy*

Technologies and Assessments, Vol. 45, pp. 101150, Jun. 2021.

[21] I. Sami, S. Ullah, N. Ullah, and J. S. Ro, "Sensorless fractional order composite sliding mode control design for wind generation system," *ISA transactions*, Vol. 111, pp. 275-289, May 2021.

[22] P. S. Londhe, and B. M. Patre, "Adaptive fuzzy sliding mode control for robust trajectory tracking control of an autonomous underwater vehicle," *Intelligent Service Robotics*, Vol. 12, No. 1, pp. 87-102, Jan. 2019.

[23] M. Bekrani, M. Heydari, and S. T. Behrooz, "An Adaptive Control Method Based on Interval Fuzzy Sliding Mode for Direct Matrix Converters," *International Journal of Industrial Electronics Control and Optimization*, Vol. 3, No. 2, pp. 159-172, Apr. 2020.

[24] E. Liu, Y. Yang, and Y. Yan, "Spacecraft attitude tracking for space debris removal using adaptive fuzzy sliding mode control," *Aerospace Science and Technology*, Vol. 107, pp. 106310, Dec. 2020.

[25] A. Razzaghian, and R. K. Moghaddam, "Robust Adaptive Neural Network Control of Miniature Unmanned Helicopter," *26th Iranian Conference on Electrical Engineering (ICEE 2018): IEEE*, pp. 801-805, 2018.

[26] C. Liu, G. Wen, Z. Zhao, and R. Sedaghati, "Neural-network-based sliding-mode control of an uncertain robot using dynamic model approximated switching gain," *IEEE Trans. Cyberne.*, Vol. 51, No. 5, pp. 2339-2346, May 2021.

[27] A. Razzaghian, "Robust Nonlinear Control Based on Disturbance Observer for a Small-Scale Unmanned Helicopter," *Journal of Nonlinear Analysis and Application*, Vol. 2017, No. 2, pp. 122-131, Sep. 2017.

[28] O. Mofid, M. Momeni, S. Mobayen, and A. Fekih, "A disturbance-observer-based sliding mode control for the robust synchronization of uncertain delayed chaotic systems: application to data security," *IEEE Access*, Vol. 9, pp. 16546-16555, Jan .2021.

[29] X .Yin, L. Pan, and S. Cai, "Robust adaptive fuzzy sliding mode trajectory tracking control for serial robotic manipulators," *Robotics and Computer-Integrated Manufacturing*, Vol. 72, pp. 101884, Dec. 2021.

[30] X. Su, Y. Xu, and X. Yang, "Neural network adaptive sliding mode control without overestimation for a maglev system," *Mechanical Systems and Signal Processing*, Vol. 168, pp. 108661, Apr. 2022.

[31] Y. Wang, G. Luo, L. Gu, and X. Li, "Fractional-order nonsingular terminal sliding mode control of hydraulic manipulators using time delay estimation," *Journal of Vibration and Control*, Vol. 22, No. 19, pp. 3998-4011, Nov. 2016.

[32] G. Sun, and Z. Ma, "Practical tracking control of linear motor with adaptive fractional order terminal sliding mode control," *IEEE/ASME Trans. Mechatro.*, Vol. 22 No. 6, pp. 2643-2653, Dec. 2017.

[33] Y. Wang, S. Jiang, B. Chen, and H. Wu, "A new continuous fractional-order nonsingular terminal sliding mode control for cable-driven manipulators," *Advances in Engineering software*, Vol. 119, pp. 21-29, May 2018.

[34] X. Zhou, W. Wang, Z. Liu, C. Liang, and C. Lai, "Impact angle constrained three-dimensional integrated guidance and control based on fractional integral terminal sliding mode control," *IEEE Access*, Vol. 7, pp. 126857-126870, Sep. 2019.

[35] S. Song, B. Zhang, X. Song, Y. Zhang, Z. Zhang, and W. Li, "Fractional-order adaptive neuro-fuzzy sliding mode H∞ control for fuzzy singularly perturbed systems," *Journal of the Franklin Institute*, Vol. 356, No. 10, pp. 5027-5048, Jul. 2019.

[36] A. Razzaghian, R. Kardehi Moghaddam, and N. Pariz, "Adaptive neural network conformable fractional-order nonsingular terminal sliding mode control for a class of second-order nonlinear systems," *IETE Journal of Research*, to be published, doi: 10.1080/03772063.2020.1791743.

[37] J. Fei, Z. Wang, X. Liang, Z. Feng, and Y. Xue, "Fractional sliding mode control for micro gyroscope based on multilayer recurrent fuzzy neural network," *IEEE Trans. Fuzz. Syst.*, to be published, doi: 10.1109/TFUZZ.2021.3064704.

[38] X. Wu, and Y. Huang, "Adaptive fractional-order non-singular terminal sliding mode control based on fuzzy wavelet neural networks for omnidirectional mobile robot manipulator," *ISA transactions*, to be published, doi: 10.1016/j.isatra.2021.03.035.

[39] A. Razzaghian, "A fuzzy neural network-based fractional-order Lyapunov-based robust control strategy for exoskeleton robots: Application in upper-limb rehabilitation," *Mathematics and Computers in Simulation*, Vol. 193, pp. 567-583, Mar. 2022.

[40] S. Han, "Fractional-Order Command Filtered Backstepping Sliding Mode Control with Fractional-Order Nonlinear Disturbance Observer for Nonlinear Systems," *Journal of the Franklin Institute*, Vol. 357, No. 11, pp. 6760-6776, Jul. 2020.

[41] Z. Wang, X. H. Wang, J. W. Xia, H. Shen, and B. Meng, "Adaptive sliding mode output tracking control based-FODOB for a class of uncertain fractional-order nonlinear time-delayed systems," *Science China Technological Sciences*, Vol. 63, No. 9, pp. 1854-1862, Sep. 2020.

[42] A. Razzaghian, R. Kardehi Moghaddam, and N. Pariz, "Fractional-order nonsingular terminal sliding mode control via a disturbance observer for a class of nonlinear systems with mismatched disturbances," *Journal of Vibration and Control*, Vol. 27, No. 1-2, pp. 140-151, Jan. 2021.

[43] A. Razzaghian, R. Kardehi Moghaddam, and N. Pariz, "Disturbance observer-based fractional-order nonlinear sliding mode control for a class of fractional-order systems with matched and mismatched disturbances," *International Journal of Dynamics and Control*, Vol. 9, No. 2, pp. 671-678, Jun. 2021.

[44] I. Podlubny, *Fractional differential equations*, New York, NY: Academic Press, 1999.

[45] K. Diethelm, *The analysis of fractional differential equations*, Berlin: Springer, 2010.

[46] N. Aguila-Camacho, M. A. Duarte-Mermoud, and J. A. Gallegos, "Lyapunov functions for fractional order systems," *Communications in Nonlinear Science and Numerical Simulation*, Vol. 19, No. 9, pp. 2951-2957, Sep. 2014.

[47] Y. Li, Y. Chen, and I. Podlubny, "Mittag–Leffler stability of fractional order nonlinear dynamic systems," *Automatica*, Vol. 45, No. 8, pp. 1965-1969, Aug. 2009.

[48] F. Sheikholeslam, and M. Zekri, "Design of adaptive fuzzy wavelet neural sliding mode controller for uncertain nonlinear systems," *ISA transactions*, Vol. 52, No. 3, pp. 342-350, May 2013.

[49] Y. J. Huang, T. C. Kuo, S. H. Chang, "Adaptive sliding-mode control for nonlinearsystems with uncertain parameters," *IEEE Trans. Syst., Man, Cybern., Part B (Cybernetics)*, Vol. 38, No. 2, pp. 534-539, Mar. 2008.

[50] S. Dadras, H. R. Momeni, "Adaptive sliding mode control of chaotic dynamical systems with application to synchronization," *Mathematics and Computers in Simulation*, Vol. 80, No. 12, pp. 2245-2257, Aug. 2010.

Amir Razzaghian received his M.Sc. degree in Control Engineering from the Department of Electrical Engineering, Islamic Azad University of Mashhad, Iran in 2015. He completed his Ph.D. in Control Engineering at Islamic Azad University of Mashhad, Iran in 2020. His main research interests include Nonlinear Control, Fractional-order Systems, Fuzzy Systems and Neural Networks.

Reihaneh Kardehi Moghaddam received her B.Sc. degree in Bioelectric Engineering from Amirkabir University of Technology, Tehran, Iran in 2001. She received her M.Sc. and Ph.D. degrees in Control Engineering from Ferdowsi University of Mashhad, Iran in 2004 and 2010, respectively. Currently, she is an Associate Professor at Islamic Azad University of Mashhad, Iran. Her main research interests include Nonlinear Control and Optimal Control.

Naser Pariz received his B.Sc. and M.Sc. degrees in Electrical Engineering from Ferdowsi University of Mashhad, Iran in 1988 and 1991, respectively, and Ph.D. degree from the Department of Electrical Engineering, Ferdowsi University of Mashhad, Iran in 2001. From 1991 to 1995, he was a Lecturer at Ferdowsi University of Mashhad, where he is currently a Full Professor. His main research interests include Nonlinear Control, Hybrid Systems and Applied Mathematics.

IECO

This page intentionally left blank.

International Journal of Industrial Electronics, Control and Optimization IECO
Vol. 5, No. 1, pp. 89-98, Jan (2022)

An Improved Fuzzy Controlled Back-to-Back Electric Spring Using Hybrid Structure of ES-1 and Shunt-APF to Improve Power Quality in Microgrids

Hamed Sadeghi[1], and Hamid Reza Mohammadi[2,†]

[1,2] Faculty of Electrical and Computer Engineering, University of Kashan, Kashan, Iran

ABSTRACT

Electric spring (ES) is a new technology that can be used for fast demand-side management to balance the power between generation and consumption in smart grids. In this paper, the back-to-back structure of electric spring is controlled to operate simultaneously as electric spring and shunt active power filter (shunt-APF). That means, the series part of the back-to-back electric spring regulates the critical load voltage and applies the demand-side management and the parallel part operates as a shunt active power filter capable of power factor correction and current harmonic compensation. In the proposed structure, due to harmonic compensation and power factor improvement by the parallel inverter, the output power capacity of the electric spring is increased compared with the first and second generation of electric springs (ES-1 and ES-2), and the performance is improved in critical conditions. Additionally, to improve the robustness of the control system against uncertainties in the grid system, two fuzzy logic controllers are designed to control the voltage of the electric spring and the DC link voltage. The theoretical analysis is validated by simulation results using MATLAB/SIMULINK software.

Article Info

Keywords:
Active power filter, Back-to-Back converter, Electric spring, Fuzzy controller, Microgrid.

Article History:
Received 2021-10-18
Accepted 2021-02-21

I. INTRODUCTION

Nowadays, economic and environmental benefits cause increasing attention to renewable energy resources such as solar and wind energy. Because of intermittent feature of these resources, the generated power will be uncertain and unpredictable. Additionally, widespread application of these resources, causes uncertainty in power quality and instability of the power system [1-3]. So far, various approaches such as reactive power compensation equipment [4], energy storage devices [5], direct load control such as load shaving, on/off non-critical loads have been proposed to improve voltage fluctuation. Some of traditional approaches are not compatible with the future power networks [6-8]. Electric spring (ES) is a new integrated technology that combines with non-critical loads to make smart loads. This technology is capable of voltage regulation through power consumption control of non-critical loads. In a smart load, an electric spring is connected in series with a non-critical load. Using electric spring, the power fluctuations in the grid are applied to the non-critical

[†]**Corresponding Author**: mohammadi@kashanu.ac.ir
Tel: +98-031-55913463, University of Kashan
Faculty of Electrical and Computer Engineering, University of Kashan, Kashan, Iran

load which does not require high power quality, and in this way the critical load voltage is stabilized. Smart load is an adaptive structure that can automatically maintain the power balance between the supply-side and the demand-side. In [9-11], it was shown that the demand side response (DSR) is achievable in non-critical resistive loads. Using DSR, the grid voltage regulation and active power management is done by managing electrical loads.

So far, four versions of ES have been suggested. The first version (ES-1), which has a capacitor on its DC link, can only inject/absorb reactive power [12]. While, the second version (ES-2) can manage both the active and reactive power as the capacitor in the DC link is replaced with a voltage source such as a battery pack [13]. The third version (ES-3) is a new type of ES without non-critical load (NCL) [14]. As mentioned, the ES-2 has a wider operating range than the ES-1, which shows the importance of the active power exchange capability in the DC link. In [15] a new generation of electric springs was introduced that uses two converters in the form of back-to-back converters with a capacitor in the DC link (Fig. 1).

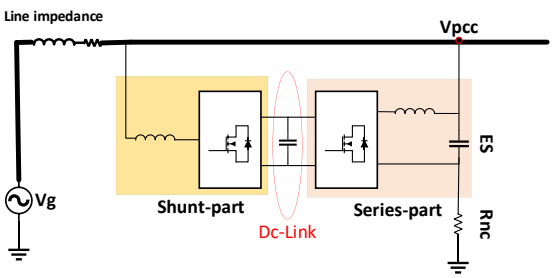

Fig. 1. Circuit structure of a back-to-back electric spring

The main function of the back-to-back electric spring is to maintain a stable voltage for a critical load. In [16] the back-to-back electric spring is introduced for main voltage stabilization and reactive power control. Due to uncertainties in the grid system such as load changes, the PI controller cannot operate properly [17]. In this condition, a fuzzy controller can be used to solve the problem. The detail of the fuzzy controller design method is discussed in [17, 18].

On the other hand, widespread application of renewable energy sources such as photovoltaic and wind energy which are connected to the grid through power electronic converters, along with an increasing application of power electronic devices to improve the efficiency and productivity in different industries, are new challenges for the grid power quality. Therefore, power quality improvement using active power filters attracts more attention. A shunt active power filter has the capability of harmonic compensation as well as reactive power compensation leading to power quality improvement.

In this paper, by using the back-to-back converters a new hybrid structure is proposed combining the first generation of electric springs (ES-1) and shunt active power filter to improve the power quality in microgrids. In this structure, the active power exchange capability is added to the ES-1 and the current harmonics and reactive power of the nonlinear load are compensated. Using an improved fuzzy controller, the robustness of the system is enhanced and the critical load voltage is adaptively stabilized.

II. HYBRID STRUCTURE OF ES-1 AND SHUNT ACTIVE POWER FILTER

In the proposed structure, the series part is a full-bridge inverter and is connected in series with the non-critical load, which forms a smart load (Fig. 2). The control system of the series part, adjusts the non-critical load voltage through comparison of the PCC voltage with its reference value. In this way, the power consumption of the non-critical load is adjusted adaptively, and as a consequence, the voltage of the critical load is regulated to its reference value using fast load demand response. In other words, to stabilize the critical load voltage at reference value, the power balance between the supply and demand side can be quickly controlled by adjusting the non-critical load voltage.

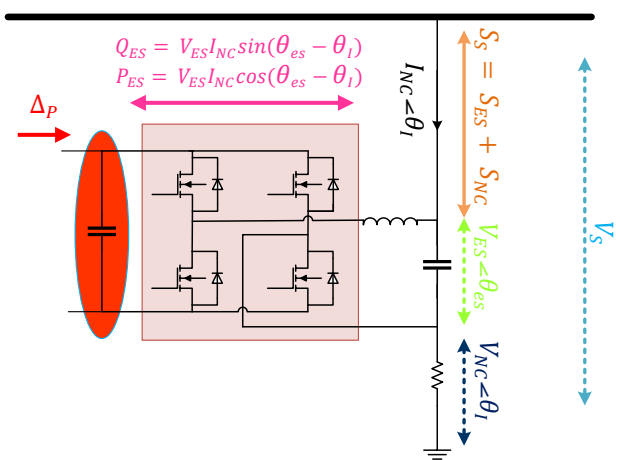

Fig. 2. Series part of the proposed structure

The shunt part of the proposed structure is a full-bridge inverter that connects to the grid through a passive filter (Fig. 3). The most important function of this inverter is to stabilize the DC link voltage. Indeed, this converter provides the possibility of active power exchange through the DC link. In addition, other capabilities such as current harmonics and reactive power compensation can also be provided by separating the active and reactive power from each other.

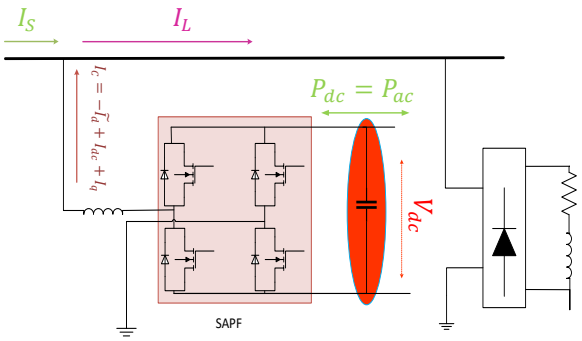

Fig. 3. Shunt part of the proposed structure

The ES-1 is connected to a capacitor in the DC link and can only exchange the reactive power at its output. Therefore, the output voltage of the ES-1 must be controlled so that it is perpendicular with the non-critical load voltage. This reduces the operating range of the electric spring. The ES-2 is connected to a battery in the DC link and can exchange active power as well as reactive power in its output. To increase the power exchange capability, the battery storage capacity must be increased which increases the cost and maintenance issues. Furthermore, for better performance, the state of charge (SoC) of the battery must be controlled which increases the control complexity. In the back-to-back structure introduced in [15], the power factor improvement and current harmonic compensation were not considered in the control system design. In the proposed hybrid structure, besides the load demand response capability of the electric spring, the power factor improvement and current harmonic compensation capabilities are provided. Also, using a fuzzy controller for the electric spring, the control performance such as robustness, can greatly be improved and the voltage stability and power quality can be improved significantly in microgrid systems.

III. THE PRINCIPLE OF OPERATION

A. Series Part

The series part of the proposed structure can exchange the active power as well as the reactive power in its output. Therefore, the output voltage phase angle of the series inverter can be controlled at any desired value. Although a capacitor is used in the DC link, but the required active power is provided by the shunt part. In a full H-bridge converter, if the loss is neglected, the power in dc and ac sides would be equal as (1).

$$P_{dc} = P_{ac} \quad (1)$$

Therefore, due to the possibility of providing active power in the DC link, it can be expected that the output voltage of the series part (ES) can be modulated with the desired angle and magnitude irrespective of the output current. This property provides four main operating modes for the ES:

1) Capacitive mode ($-jQ_{es}$): The ES injects pure reactive power and performs reactive power compensation. Therefore, the equivalent load will be more capacitive (V_{ES} 90 lagging V_{NC}) as in Fig. 4(a). Consequently, the line current is decreased and the critical load voltage is increased.

2) Inductive mode ($+jQ_{es}$): The ES absorbs pure reactive power and performs reactive power increment. Therefore, the equivalent load will be more inductive (V_{ES} 90 leading V_{NC}) as in Fig. 4(b). Consequently, the line current is increased and the critical load voltage is decreased.

3) Positive resistive mode ($+P_{es}$): The ES voltage is positive and absorbs active power (V_{ES} in phase with the V_{NC}) as in Fig. 4(c). Consequently, the line current decreases due to the non-critical load voltage decrement. Thus, the critical load voltage is increased.

4) Negative resistive mode ($-P_{es}$): The ES voltage is negative and injects an active power (180° phase difference between V_{ES} and V_{NC}) as in Fig. 4(d). Consequently, the line current increases due to the non-critical load voltage increment. Thus, the critical load voltage is decreased.

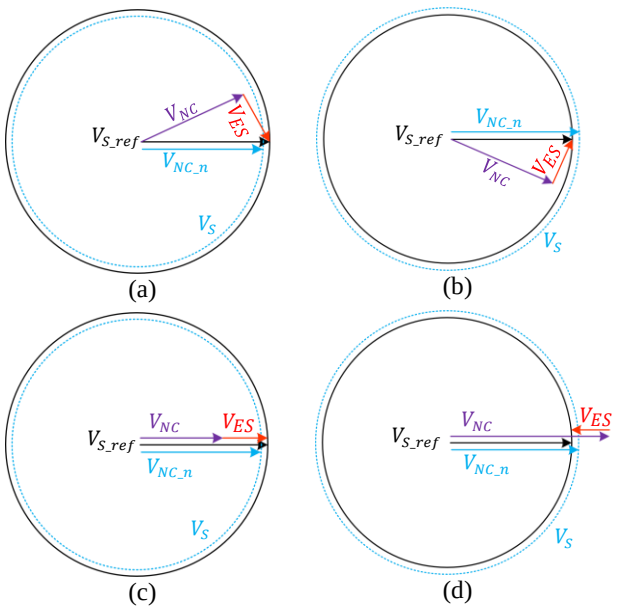

Fig. 4. Four main operational modes of the back-to-back ES

The other operational modes of the back-to-back electric spring are as follows:

5) Inductive-positive resistive mode ($P_{es} + jQ_{es}$) as in Fig. 4(e).

6) Inductive-negative resistive mode ($-P_{es} + jQ_{es}$) as in Fig. 4(f).

7) Capacitive-positive resistive mode ($P_{es} - jQ_{es}$) as in Fig. 4(g).

8) Capacitive-negative resistive mode ($-P_{es} - jQ_{es}$) as in Fig. 4(h).

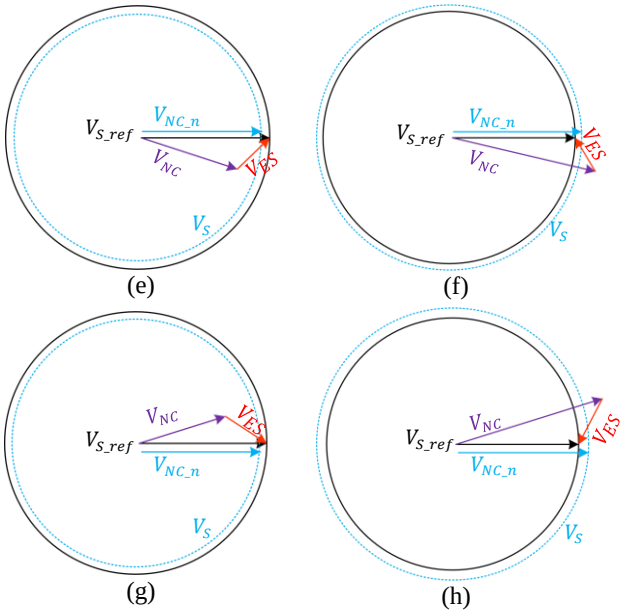

Fig. 5. Four other operational modes of the back-to-back ES

In all modes, the non-critical load is assumed to be a resistance load, and therefore its voltage (V_{NC}) and current (I_{Nc}) are in phase.

The relationship between the ES voltage (V_{ES}), line voltage (V_S), and non-critical load voltage (V_{NC}) is given by:

$$|V_s|\angle 0^\circ = |V_{ES}|\angle\theta_{es} + |V_{NC}|\angle\theta_{nc} \quad (2)$$

The non-critical load current I_{Nc} can be expressed as:

$$I_{Nc} = |I_{Nc}|\angle\theta_I \quad (3)$$

Where $|I_{Nc}|$ and θ_I are magnitude and phase angle of the non-critical load current, respectively.

The apparent power at the PCC in steady-state condition can be expressed as follows:

$$|S_S|\angle\delta_s = |S_{ES}|\angle\delta_{es} + |S_{NC}|\angle\delta_{nc} \quad (4)$$

Where, $|S_S|$, $|S_{ES}|$, and $|S_{NC}|$ are magnitudes of the apparent powers exchanged at the PCC, electric spring, and non-critical load, respectively. Also, $\angle\delta_s$, $\angle\delta_{es}$, and $\angle\delta_{nc}$ are phase angles of the above- mentioned apparent powers with respect to the voltage $V_S\angle 0^\circ$. The apparent powers can be expressed as follows:

$$\begin{cases} |S_S|\angle\delta_S = |V_S|\cdot|I_{Nc}|\angle -\theta_I \\ |S_{ES}|\angle\delta_{es} = |V_{ES}|\cdot|I_{Nc}|\angle(\theta_{es}-\theta_I) \\ |S_{NC}|\angle\delta_{nc} = |V_{NC}|\cdot|I_{Nc}|\angle(\theta_{nc}-\theta_I) \end{cases} \quad (5)$$

Generally, the apparent power can be written as:

$$S\angle\emptyset = |S|\,Cos(\emptyset) + j\cdot|S|\,Sin(\emptyset) = P + jQ \quad (6)$$

Assuming the load reactive power is controlled by the shunt active power filter. Therefore, the electric spring only control the exchanged active power which is expressed by (7).

$$P_S = P_{ES} + P_{NC} \quad (7)$$

Using (5) and (6), the active powers can be expressed as follows:

$$\begin{cases} P_{ES} = |I_{NC}|.|V_{ES}|.Cos(\theta_{es}-\theta_I) \\ P_{NC} = |I_{NC}|.|V_{NC}|.Cos(\theta_{nc}-\theta_I) \\ P_S = |I_{NC}|.|V_S|.Cos(-\theta_I) \end{cases} \quad (8)$$

Substituting (8) into (7), P_{NC} can be written as follows:

$$P_{NC} = |I_{NC}|.|V_S|.Cos(-\theta_I) - |I_{NC}|.|V_{ES}|.Cos(\theta_{es}-\theta_I) \quad (9)$$

In accordance to (9), the magnitude and phase angle of the ES voltage ($|V_{ES}|$ and θ_{es}) can be used to control the active power of the non-critical load. In the case of the PCC voltage higher than its reference value, the series part (ES) controls the active power of the non-critical load in such a way that the line current increases as a result of increasing the power consumption by the non-critical load. Therefore, the voltage drop across the line impedance is increased and the critical load voltage regulates. For this purpose, the electric spring works in negative resistance mode. That is, by generating a voltage in the opposite sign of the V_{NC}, the non-critical load voltage is increased and caused the increment of the non-critical load current. To generate the negative voltage, the electric spring must absorb the active power from the DC link.

In the case of the PCC voltage lower than its reference value, the series part (ES) controls the active power of the non-critical load in such a way that the line current decreases as a result of decreasing the power consumption by the non-critical load. Therefore, the voltage drop across the line impedance is decreased and consequently, the critical load voltage is regulated. For this purpose, the electric spring works in positive resistance mode. That is, by generating a voltage in phase with V_{NC}, the non-critical load voltage is decreased and caused the decrement of the non-critical load current. To generate the positive voltage, the electric spring must inject the active power into the DC link.

B. Shunt Part

Fig. 6 shows the hybrid structure of the electric spring and shunt active power filter. In this figure, the exchanged active and reactive power between the grid and the shunt active power filter are shown. The active power exchanged by the shunt active power filter (P_c) consists of two terms:

$$P_c = P_h - \Delta_P \quad (10)$$

Where, P_h is the active power exchange due to the current harmonic components which are injected by the shunt active

power filter. Also, the Δ_P can be written as:

$$\Delta_P = P_{loss} + P_{ES} \quad (11)$$

Where, P_{loss} is the switching loss and P_{ES} is the active power exchanged by the electric spring. Δ_P is used to generate the appropriate reference voltage. The exchanged power of the ES (P_{ES}) can be positive or negative.

In this paper, the instantaneous power theory or PQ theory is used to generate the reference current for the shunt active power filter. In the PQ theory, the single-phase voltage (V_C) and current (I_L) are converted into αβ frame using eq. (12).

$$\begin{bmatrix} X_\alpha \\ X_\beta \end{bmatrix} = \begin{bmatrix} X(\omega t) \\ X(\omega t - 90^\circ) \end{bmatrix} \quad (12)$$

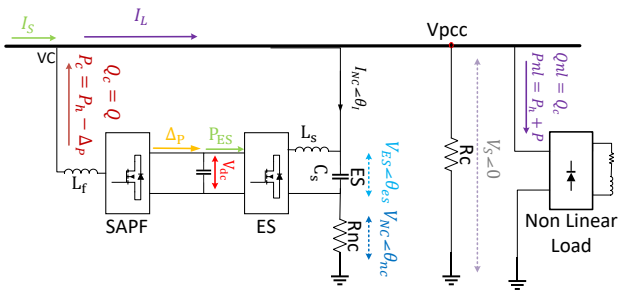

Fig. 6. Hybrid structure of the electric spring (ES-1) and shunt active power filter

IV. CONTROL DESIGN OF IMPROVED BACK-TO-BACK ELECTRIC SPRING

A. *Electric Spring*

The proposed hybrid structure regulates the PCC voltage using series part (ES-1) and compensates for the current harmonics and reactive power of the nonlinear load using the shunt part (shunt active power filter). A fuzzy controller is designed to control the series part which simulates the behavior of a PI controller to ensure the regulation of the PCC voltage to its reference value. Using the fuzzy controller, the robustness of the system will be improved and in case of uncertainty in the system parameters, the control system works properly.

At first, the PCC voltage is measured and compared with its reference value and the error signal (e) is obtained. The error signal and its changes are fed as inputs to the fuzzy controller. The fuzzy controller determines the modulation index 'm' as its output to reduce the error signal to zero. Then the modulation index 'm' is converted into a sinusoidal signal by the sinusoidal block, which is in phase or out of phase with the main voltage. Fig. 7 shows the control block diagram of the improved fuzzy controlled back-to-back electric spring.

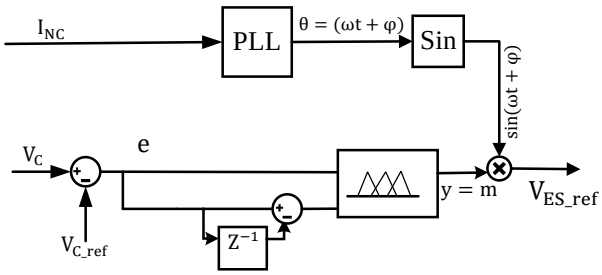

Fig. 7. Control block diagram of the improved fuzzy controlled back-to-back electric spring

Fuzzy logic is a data analysis method based on using non-precise values over a range to determine the correct correspondence to a particular group. It works by translating the experienced human's inference into fuzzy rules that determines what output should be produced for a particular range of input. The structure of a fuzzy controller is shown in Fig. 8.

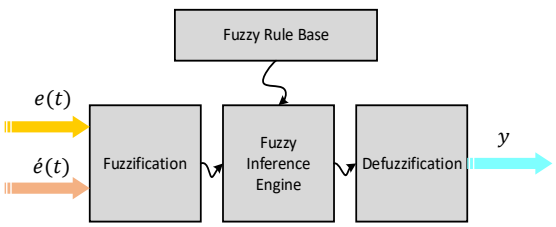

Fig. 8. Fuzzy controller

As shown in fig. 9, the values of the input error and change of error are normalized by an input scaling factor. To make the designed fuzzy controller universal, the ranges of the inputs $(e(t), \acute{e}(t))$ and the output (y) have been designed between [-1,1]. For this case, input variables comprise of error, $e(t)$, and change of error, $\acute{e}(t)$, are both defined by triangular membership functions with seven fuzzy subsets as {NL, NM, NS, Z, PS, PM, PL}, and the output y is represented as {NL, NM, NS, Z, PS, PM, PL}.

As shown in Table I, 49 fuzzy rules are defined to increase the fuzzy output accuracy. One of the fuzzy rules in this table is described for example. The last rule "if e=PL and é=PL, then y=PL" means that: if the difference between the measured and the reference voltages is a positive large value and the rate of change of this difference is also a positive large value, the electric spring output voltage will also be a large value. In this way, the behavior of a PI controller can be simulated using the fuzzy controller. The fuzzy inference system is Mamdani type and the defuzzification method is centroid.

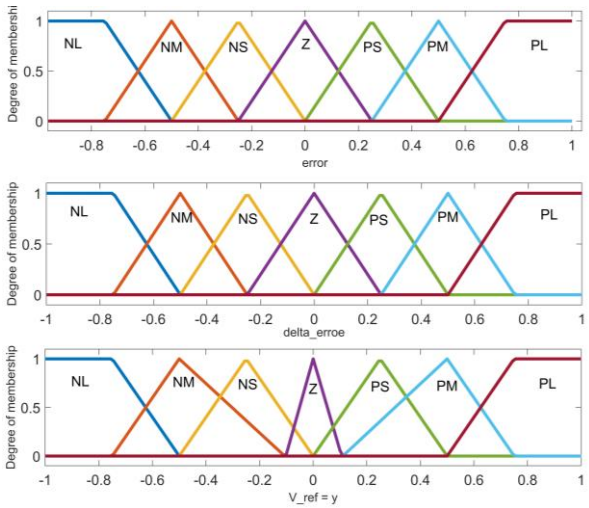

Fig. 9. Membership functions of the input and output

TABLE I
FUZZY RULES

e / é	NL	NM	NS	Z	PS	PM	PL
NL	NL	NL	NL	NL	NM	NS	Z
NM	NL	NM	NL	NM	NS	Z	PS
NS	NL	NL	NS	NS	Z	PS	PM
Z	NL	NM	NS	Z	PS	PM	PL
PS	NM	NS	Z	PS	PS	PL	PL
PM	NS	Z	PS	PM	PL	PM	PL
PL	Z	PS	PM	PL	PL	PL	PL

B. *Shunt Active Power Filter*

The current reference for the shunt active power filter is obtained from the PQ theory. The block diagram of this method is shown in Figure 10.

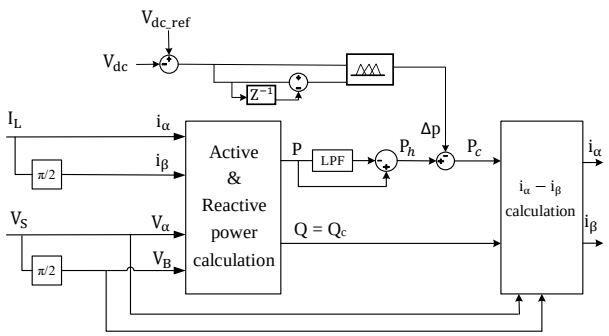

Fig. 10. Current reference extraction using pq method

The PQ theory determines instantaneous active and reactive powers based on α-β components as:

$$\begin{bmatrix} P \\ Q \end{bmatrix} = \begin{bmatrix} V_\alpha & V_\beta \\ V_\beta & -V_\alpha \end{bmatrix} \begin{bmatrix} I_\alpha \\ I_\beta \end{bmatrix} = \begin{bmatrix} P_h \\ Q_h \end{bmatrix} + \begin{bmatrix} P_f \\ Q_f \end{bmatrix} \quad (13)$$

Where P_h is the harmonic active power component, P_f is the fundamental active power component, Q_h is the harmonic reactive power component and Q_f is the fundamental reactive power component. After calculating the active power, a low-pass filter is used to separate the harmonic active power component from the fundamental active power component. Also, the DC link voltage control loop is used to compensate for the switching power loss (Δ_P). To calculate the reference currents, the power loss must be considered. Finally, the reference currents in the αβ reference frame are calculated using the values of the active and reactive powers as given by (14).

$$\begin{bmatrix} i_\alpha \\ i_\beta \end{bmatrix} = \begin{bmatrix} V_\alpha & V_\beta \\ V_\beta & -V_\alpha \end{bmatrix}^{-1} \begin{bmatrix} P_h - \Delta_P \\ Q \end{bmatrix} \quad (14)$$

Also, a fuzzy controller is designed to control the DC link voltage which increases the robustness of the control system against parameter changes. Due to abbreviation, the similar explanations are omitted. The membership functions and fuzzy rules are given in Fig.11 and TABLE II, respectively.

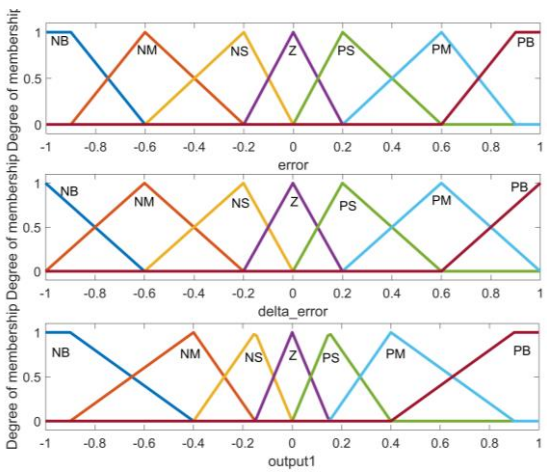

Fig. 11. Membership functions of the input and output

TABLE II
FUZZY RULES

e / é	NB	NM	NS	Z	PS	PM	PB
NB	NB	NB	NB	NB	NM	NS	Z
NM	NB	NB	NB	NM	NS	Z	PS
NS	NB	NB	NM	NS	Z	PS	PM
Z	NB	NM	NS	Z	PS	PM	PB
PS	NM	NS	Z	PS	PM	PB	PB
PM	NS	Z	PS	PM	PB	PB	PB
PB	Z	PS	PM	PB	PB	PB	PB

V. SIMULATION RESULTS AND DISCUSSIONS

In this section, the performance of the improved fuzzy controlled back-to-back electric spring is simulated using MATLAB/Simulink software. The simulation parameters are given in Table III.

A microgrid consisting of a critical load, a non-critical load and the proposed hybrid structure of electric spring (ES-1) and shunt active power filter is connected to a programmable power source through a transmission line.

The performance of the proposed system is evaluated under voltage suppression and voltage support conditions when a nonlinear local load is connected. The main voltage is set to 110 V and is increased or decreased in different time intervals.

A. Voltage Support Performance

In this experiment, the critical load voltage is assumed to be 105 V. Also, due to the nonlinear local load connection, the grid current is non-sinusoidal and contains harmonics and the power factor is not unity. The critical load voltage, ES voltage, and non-critical load voltage are shown in Fig. 12. Initially, the back-to-back electric spring is bypassed. The shunt active power filter is activated at t=0.2s to stabilize the DC link voltage and compensate the current harmonics. At t=0.6s, the series part (ES) is activated to regulate the PCC voltage to 110V. It can be seen that the voltage regulation function is performed well. The ES produces a voltage in phase with the PCC voltage to voltage support purpose and as a consequence, the non-critical load voltage decreases.

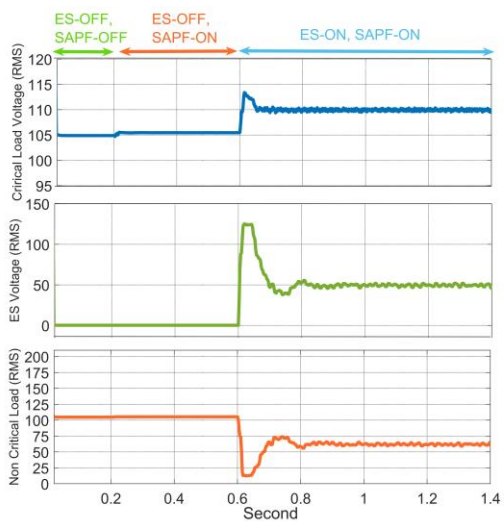

Fig. 12. Cririal load voltag (upper trace), electric spring voltage (middle trace) and non-critical load voltage (lower trace)

The simulation results of the shunt part (shunt active power filter) are shown in Figures 13 to 17. The shunt part activates at t=0.2s and compensates for the current harmonics and the reactive power of the nonlinear local load. Also, the series part is activated at t=0.6s. The compensation current generated by the shunt part is shown in Fig. 13.

The DC link voltage and the load power factor are shown in Figs. 14 and 15, respectively. Also, the source current THD is shown in Fig. 16. The THD value is reduced from 10% to less than 5% when the shunt active power filter is activated at t=0.2s and remains less than 5% after activating the series part (ES-1) at t=0.6s. Also, Fig. 15 shows that the PF improves after activating the shunt active power filter and the electric spring.

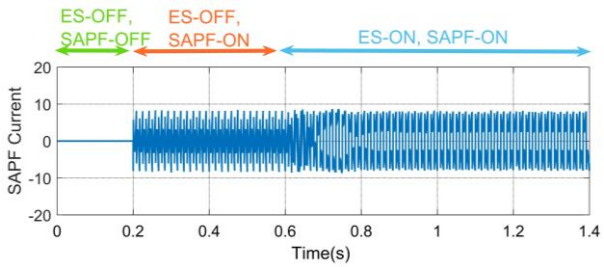

Fig. 13. The compensation current of the shunt active power filter

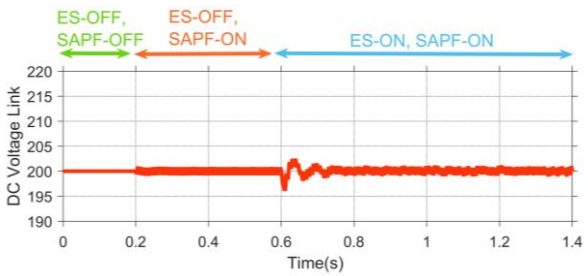

Fig. 14. The DC link voltage

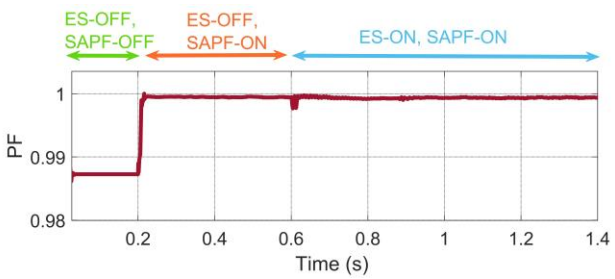

Fig. 15. The load power factor (PF)

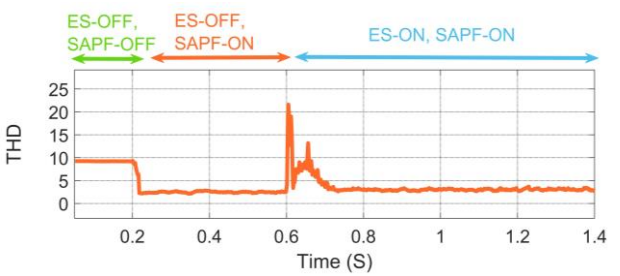

Fig. 16. THD of the source current

Fig. 14 shows that in the voltage support mode, after activation of the ES at t = 0.6s, it injects the active power into the DC link and the DC link voltage is increased. The shunt active power filter section absorbs the active power from the DC link and injects it back into the grid.

B. Voltage Suppression Performance

In the next experiment, the critical load voltage is assumed to be 115V. Also, due to the nonlinear load connection, the grid current contains harmonics and the power factor is not unity. The critical load voltage, ES voltage, and non-critical load voltage are shown in Fig. 17. Initially, the back-to-back electric spring is bypassed. The shunt part (shunt active power filter) is activated at t=0.2s to stabilize the DC link voltage and to compensate for the current harmonics. At t=0.6s, the series part (ES) is activated and regulates the PCC voltage to 110 V. The ES produces a voltage with 180° phase difference with the PCC voltage to voltage suppression purpose and as a consequence the non-critical load voltage increases.

The simulation results for the shunt part (shunt active power filter) are shown in Figs. 18 to 21. The shunt part activates at t=0.2s and compensates for the current harmonics and the reactive power of the nonlinear local load. Also, the series part is activated at t=0.6s. The compensation current generated by the shunt part is shown in Fig. 18.

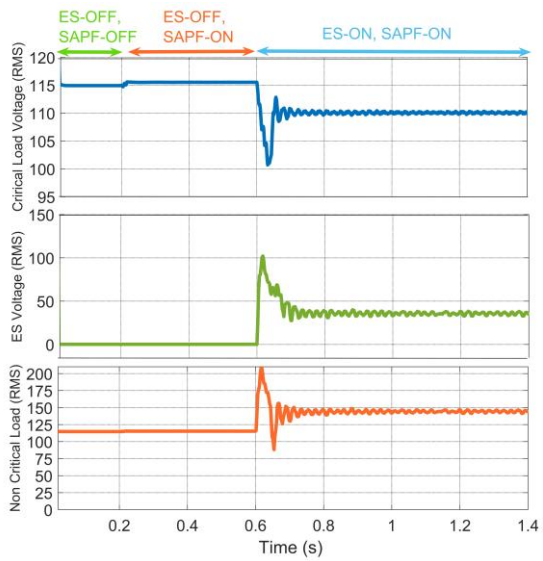

Fig. 17. Cririca load voltag (upper trace), electric spring voltage (middle trace) and non-critical load voltage (lower trace)

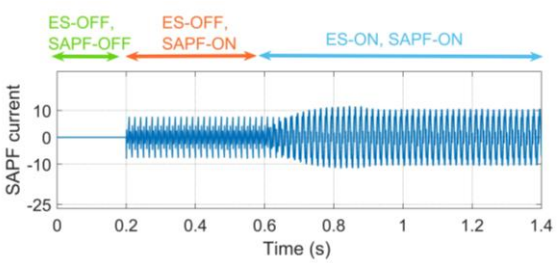

Fig. 18. Shunt active power filter compensation current

The DC link voltage and the load power factor are shown in Figs. 19 and 20, respectively. Also, the source current THD is shown in Fig. 21. The THD value is reduced from 10% to less than 5% when the shunt active power filter is activated at t=0.2s and remains less than 5% after activating the series part (ES-1) at t=0.6s. Also, Fig. 20 shows that the PF improves after activating the shunt active power filter and the electric spring.

Fig. 19 shows that in the voltage suppression mode, after activation of the ES at t = 0.6s, it absorbs the active power from the DC link and the DC link voltage is decreased. The shunt active power filter section absorbs the active power from the grid and injects it back into the DC link.

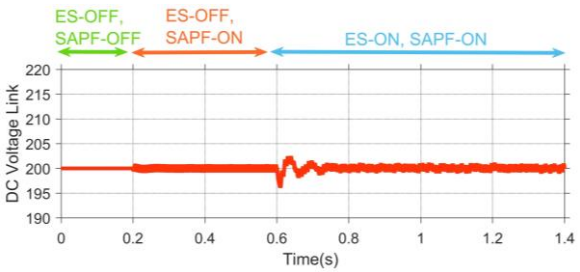

Fig. 19. The DC link voltage

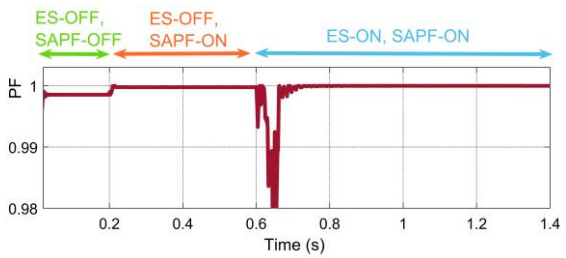

Fig. 20. The load power factor (PF)

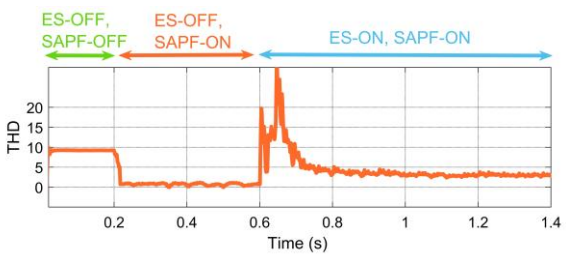

Fig. 21. The source current THD value

C. Robustness of the Fuzzy Conrol System of Electric Spring Against Parameter Variation

In this subsection, the performance of the fuzzy controller of the electric spring against the changes in the non-critical load parameter is shown.

In this experiment, the non-critical load resistance is changed as 20, 30, 40, and 50Ω. Simulation results for both PI and fuzzy controllers are shown in Fig. 22. In both methods, the electric spring is activated at t = 0.6S.

As shown in Fig. 22, when the non-critical load is equal to 50Ω, the PI controller is unable to adjust the PCC voltage. But, the fuzzy controller is capable of maintaining the PCC voltage in 110V regardless to the value of non-critical load. The resuts show that in the proposed structure, the fuzzy controller increases the robustness of the electric spring against parameter variations.

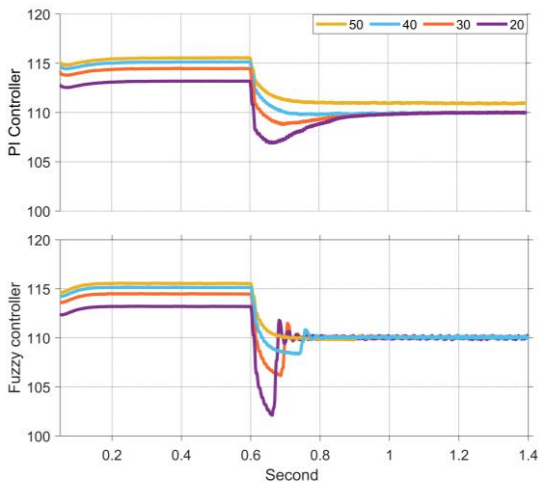

Fig. 22. The critical load voltage in case of parameter variation, PI controller (upper trace) and fuzzy controller (lower trace)

D. *Robustness of the Fuzzy Conrol System of the DC Link Voltage Against Parameter Variation*

In this experiment, the robustness of the DC link voltage control system is tested. The performance of the fuzzy controller against load parameter changes is compared with the PI controller.

For this purpose, the non-critical load resistance is changed to 30, 40 and 50Ω at t=0.6S. As shown in Fig. 23, both PI and Fuzzy controllers, control the DC link voltage and regulate it to 200V.

controller (upper trace) and fuzzy controller (lower trace)

However, by changing the non-critical load parameters, the performance of the PI controller is deteriorated in some cases and the overshoot and settling time are increased. But, using the fuzzy controller the control system performance is very good in all cases and the overshoot and settling time are acceptable.

The simulation results show that in case of using fuzzy controller, the robustness of the control system is increased and the DC link voltage is more stable than the case of using PI controller.

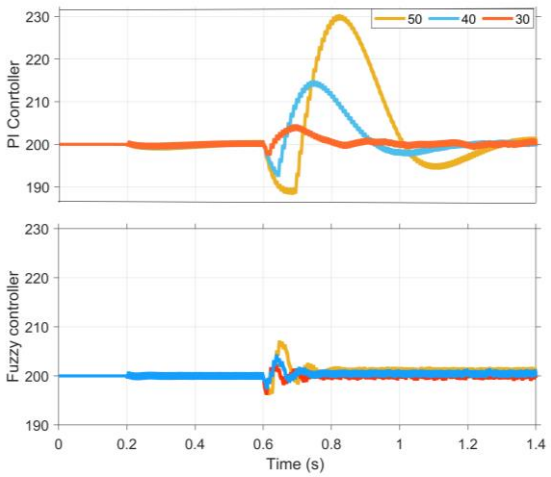

Fig. 23. The DC link voltage in case of parameter variation, PI controller (upper trace) and fuzzy controller (lower trace)

TABLE III
SIMULATION PARAMETERS

System and Loads	
Frequency	60HZ
Nominal System Voltage (V_S)	110V
Line Impedance	0.7Ω
	9mH
R/X Ratio of the System	0.02
Non-critical Load R_C	60Ω
Critical Load	50Ω
Voltage Limitation of Non-Critical Loads	35%
Nonlinear Load (Diode bridge with RL load)	13.34Ω
	50mH
Rating of the inverters	2 kVA
Electric Spring Specifications	
Inverter Type	Single Phase Full Bridge Inverter
Switching Frequency	8KHZ
Low-pass Filter Inductance L_S	3.1mH
Low-pass Filter Capacitor C_S	21µF
Shunt Active Power Filter Specifications	
Inverter Type	Single Phase Full Bridge Inverter
Switching Frequency	8KHZ
Regulated DC Bus Voltage	200V
DC Bus Capacitance	4500µF
Low-pass Filter Inductance L_f	8.3mH

VI. CONCLUSION

In this paper, an improved structure of a back-to-back electric spring is used capable of demand-side management and stabilizing the critical load voltage. This structure also

works as a shunt active power filter and compensates for the current harmonics caused by the nonlinear load and improves the power factor. Two robust fuzzy controllers are designed to control the voltage of the electric spring and the DC link voltage which have good performances in case of grid uncertainties such as load or line impedance changes. Using simulation results, the robustness of the improved fuzzy controlled back-to-back electric spring is shown against parameter variation.

REFERENCES

[1] I. Koutsopoulos, and L. Tassiulas, "Challenges in demand load control for the smart grid," *IEEE Network,* vol. 25, no. 5, pp. 16-21, 2011.

[2] X. Liang, "Emerging Power Quality Challenges Due to Integration of Renewable Energy Sources," *IEEE Transactions on Industry Applications,* vol. 53, no. 2, pp. 855-866, 2017.

[3] S. A. Shirmardi, M. Joorabian, and H. Barati, "Green Micro-Grid Operation Constrained to Reliability and Flexibility Indices in the Presence of Distributed Generations and Energy Storage Systems," *International Journal of Industrial Electronics Control and Optimization,* vol. 4, no. 4, pp. 397-407, 2021.

[4] L. Wang, C. Lam, and M. Wong, "Hybrid Structure of Static Var Compensator and Hybrid Active Power Filter (SVC//HAPF) for Medium-Voltage Heavy Loads Compensation," *IEEE Transactions on Industrial Electronics,* vol. 65, no. 6, pp. 4432-4442, 2018.

[5] C. Ju, P. Wang, L. Goel, and Y. Xu, "A Two-Layer Energy Management System for Microgrids With Hybrid Energy Storage Considering Degradation Costs," *IEEE Transactions on Smart Grid,* vol. 9, no. 6, pp. 6047-6057, 2018.

[6] Z. Bao, W. Qiu, L. Wu, F. Zhai, W. Xu, B. Li, and Z. Li, "Optimal Multi-Timescale Demand Side Scheduling Considering Dynamic Scenarios of Electricity Demand," *IEEE Transactions on Smart Grid,* vol. 10, no. 3, pp. 2428-2439, 2019.

[7] X. Kong, C. Li, F. Zheng, and C. Wang, "Improved Deep Belief Network for Short-Term Load Forecasting Considering Demand-Side Management," *IEEE Transactions on Power Systems,* vol. 35, no. 2, pp. 1531-1538, 2020.

[8] M. A. A. Pedrasa, T. D. Spooner, and I. F. MacGill, "Scheduling of Demand Side Resources Using Binary Particle Swarm Optimization," *IEEE Transactions on Power Systems,* vol. 24, no. 3, pp. 1173-1181, 2009.

[9] G. Buja, S. Giacomuzzi, Q. Wang, and M. Bertoluzzo, "Demand-Side Power Paradigm-Oriented Analysis of Reactive Electric Spring Stabilization Capabilities," *IEEE Access,* vol. 8, pp. 213662-213670, 2020.

[10] Y. Qi, T. Yang, J. Fang, Y. Tang, K. R. R. Potti, and K. Rajashekara, "Grid Inertia Support Enabled by Smart Loads," *IEEE Transactions on Power Electronics,* vol. 36, no. 1, pp. 947-957, 2021.

[11] J. Zhang, G. Ma, X. Lyu, M. Li, J. Xu, and X. Wu, "Research on Scheduling Control Strategy of Large-Scale Air Conditioners Based on Electric Spring," *International Journal of Electrical Power & Energy Systems,* vol. 124, pp. 106398, 2021.

[12] S. Y. Hui, C. K. Lee, and F. F. Wu, "Electric Springs—A New Smart Grid Technology," *IEEE Transactions on Smart Grid,* vol. 3, no. 3, pp. 1552-1561, 2012.

[13] S. Tan, C. K. Lee, and S. Y. Hui, "General Steady-State Analysis and Control Principle of Electric Springs With Active and Reactive Power Compensations," *IEEE Transactions on Power Electronics,* vol. 28, no. 8, pp. 3958-3969, 2013.

[14] C. K. L. a. S. Y. R. Hui, "Input AC Voltage Control Bi-directiobal Power Converters " *U.S.patent,* 2013.

[15] S. Yan, C. Lee, T. Yang, K. Mok, S. Tan, B. Chaudhuri, and S. Y. R. Hui, "Extending the Operating Range of Electric Spring Using Back-To-Back Converter: Hardware Implementation and Control," *IEEE Transactions on Power Electronics,* vol. 32, no. 7, pp. 5171-5179, 2017.

[16] Z. Rui, F. Shi, D. Shu, Z. Yan, and X. Luo, "A Flexible Multi-objective Coordinated Control Strategy for Smart Loads Based on Electric Springs." *IEEE/IAS Industrial and Commercial Power System Asia (I&CPS Asia),* pp. 1344-1349, 2020.

[17] M. S. Javaid, U. B. Irshad, A. Hussein, and M. A. Abido, "A Novel Fuzzy Logic Controller for Smart Load Voltage Regulation." *International Conference on Clean Electrical Power (ICCEP),* pp. 620-624, 2017.

[18] S. Disha, "Designing and Modeling Fuzzy Control Systems," *International Journal of Computer Applications,* vol. 16, 02/28, 2011.

Hamed Sadeghi was born in shahrekord, Iran, in 1996. He recived the B.S degree from IAUN, Isfahan, Iran in 2018 and the M.S degree from University of Kashan, Kashan, Iran in 2021 all in electrical engineering. His research interest include power electronics, power quality, system automation, renewable energies, energy management.

Hamid Reza Mohammadi was born in Qom, Iran, in 1971. He received the B.S. degree from Sharif University of Technology, Tehran, Iran, in 1993, the M.S. degree from the University of Tabriz, Tabriz, Iran, in 1995, and the Ph.D. degree from Tarbiat Modares University, Tehran, Iran, in 2008 all in electrical engineering. Currently, he is an Associate Professor in the Electrical Engineering Department at the University of Kashan, Kashan, Iran. His research interests include power electronics, power quality, active filters, and different microgrid aspects including modeling and control of power converters, power quality, and energy management.

International Journal of Industrial Electronics, Control and Optimization © 2022 IECO
Vol.5, No. 1, pp. 99-108, Jan (2022)

Design of Low Power Full-Adder Circuit Using Quantum-dot Cellular Automata

Faezeh Motalebi[1] ,and Samira Sayedsalehi[2, †]

[1]Department of Computer and IT Engineering, Qazvin Branch, Islamic Azad University, Qazvin, Iran
[2]Department of Computer Engineering, South Tehran Branch, Islamic Azad University, Tehran, Iran

ABSTRACT

Quantum-dot Cellular Automata (QCA) is a new technology for eliminating some of the problems of existing technologies such as CMOS. Some of the key advantages of QCA are an intersection of wires in the same plane, high speed, small area, power consumption, complexity and low cost. Employing a three-input majority gate, a five-input majority gate and three logic gates, this study presents a full-adder circuit in a single layer which for higher efficiency and avoiding much complexity and based on the function of the intended full-adder circuit, the five-input gate is proposed. The proposed full-adder circuit and the proposed ripple adder circuit are compared with previous designs regarding complexity, number of cells, and area and the results are reported. Moreover, proposed circuits' power consumption has been calculated by using QCApro. These results indicate that the proposed full adder design in comparison with previous similar design achieved 36%, 20% and 4.4% reduction in the number of cells, latency and power consumption, respectively.

Article Info

Keywords:
Computational circuits, Full adder, Majority gate, Quantum cellular automata.

Article History:
Received 2021-11-12
Accepted 2022-02-04

I. INTRODUCTION

In recent decades, Metal Oxide Semiconductor (MOS) has been the current technology. The remarkable rise in integration of integrated circuits has raised issues such as an increase in power consumption, limited integration density and limitation in system scaling [1]. As CMOS transistors' size reduced to Nano scale, this technology encountered serious problems and challenges such as high leakage current, reduction in gateway control, high power consumption, high lithography cost, etc. These problems slow the process of reduction of the size and therefore challenge the ability of CMOS technology for creating structures with high density and efficiency in the near future. To overcome this limitation, Quantum cellular automata (QCA), which is one of the solid state Nano-electronic devices and a member of quantum dot, is proposed as an alternative to replace the existing CMOS circuits. The basic element of QCA is a cell which consists of four quantum dots and two electrons. In this technology most of the circuits are produced based on three-input majority gates, five-input majority gates and logic gates [2], [3]. One of the most important circuits which is examined in any technology is adders. So far, many adders have been introduced in QCA [4]-[11]. The most important factor in an efficient design is designing one layer with minimum cells and power level. In this study, by employing a three-input majority gate, a five-input majority gate, and three logic gates a circuit in one layer was proposed; simplicity of design resulted in high efficiency in wider computational circuits. Moreover, after calculating its power consumption, it could be said that the proposed design was more functional and with more favorable outcomes. In section 2, we present a brief description of material, structure, and components of QCA circuits. In section 3, we introduce former QCA full adder circuits. In section 4, we introduce our proposed circuits. In section 5, we simulate the circuits and examine the results. And in the last section the findings are presented.

[†]**Corresponding Author**: s_sayedsalehi@azad.ac.ir
Tel: +982188830826, Islamic Azad University, South Tehran Branch
Faculty of Electrical and Computer Engineering, Islamic Azad University, South Tehran Branch, Tehran, Iran

II. A REVIEW OF QCA

A. *Preliminary materials and devices*

Quantum Cellular Automata was first presented by professor Lent at The University of Notre Dame in 1993. The two existing arrangements in Quantum Cellular Automata are one with polarization of P=+1 as logic 1 and one with polarization P=-1 as logic 0. In QCA two wiring methods, standard and inverter, are used (Fig. 1) [12]. The wires cross over each other in several ways such as coplanar-based wiring method, multilayer-based wiring method, and clocking-based method in which two wires can cross each other without affecting each other (Fig. 2) [13].

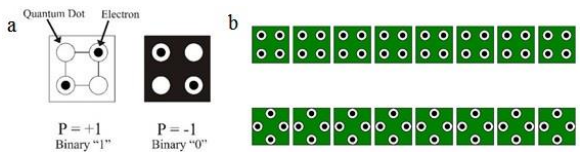

Fig. 1. (a) Basic QCA Cell and Binary encoding; (b) Standard and inverting wiring.

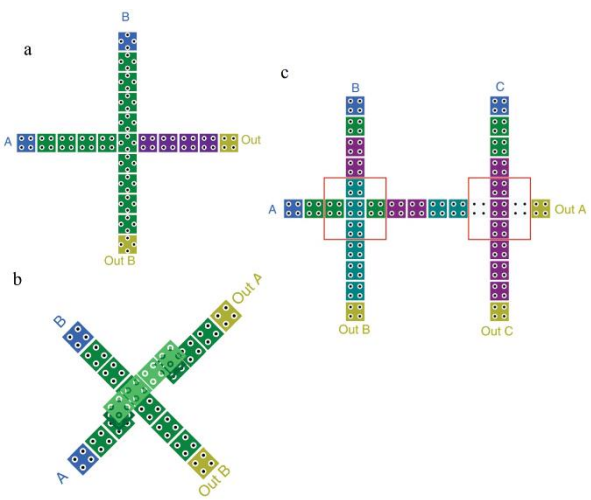

Fig. 2. (a) Crossover based on coplanar-based wiring, (b) Crossover based on multilayer-based, (c) Crossover based on clocking-based wiring [4].

B. *Basic elements in QCA*

The basic elements in QCA circuits are logic gates, three-input majority gate, and five-input majority gate.

1) Logic Gate: It is the simplest way for placing a cell obliquely next to another cell; other methods are also based on it. Another method is the inverting signal in layers (Fig. 3(a)) [14].

2) Three-input majority gate: A three-input majority gate or majority voting includes three inputs and one output in which the polarization of the output cell is determined by the polarization of input cells (Fig. 3(b)) [15].

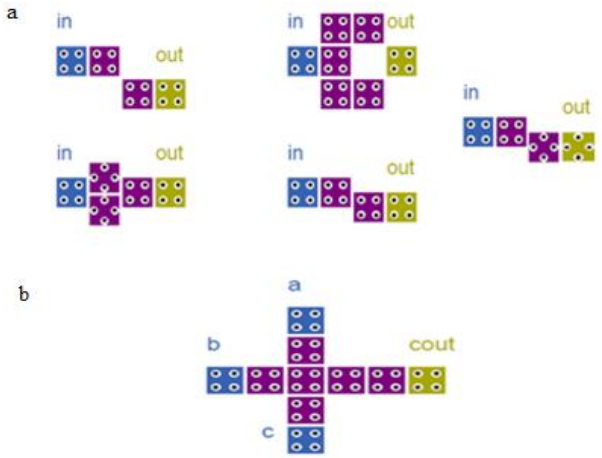

Fig. 3. (a) Some inverting structures, (b) Three-input majority gate.

3) Five-input majority gate: In order to decrease the number of consumption majority gates and to optimize circuits, scientists began to design a five-input majority gate. The first designs were proposed by Navi et al in 2010. In 2011, Akeela and Wagh, and in 2014 Roohi et al proposed their own designs to improve the previous methods. The five-input gate proposed by Sheikhfaal et al, called PM5, was presented in 2015 (Fig. 4).

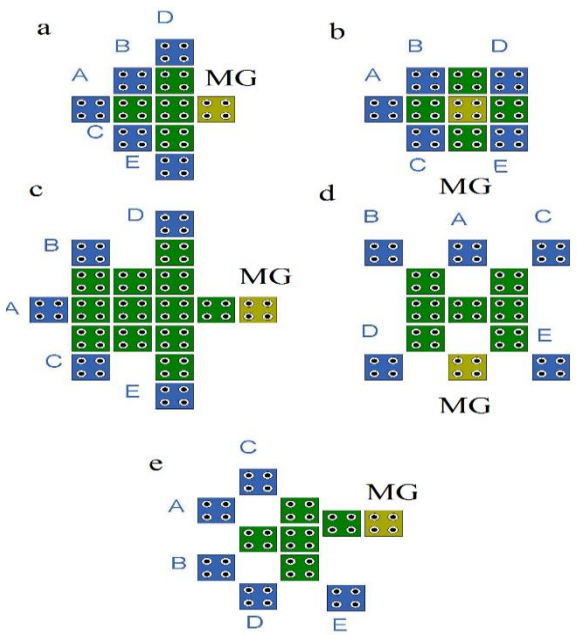

Fig. 4. Four proposed designs for five-input majority gate: (a) The structure proposed by Navi et al [5], (b) The structure proposed by Navi et al [6], (c) The structure proposed by Akeela and Wagh [16], (d) The structure proposed by Roohi et al [17], (e) QCA five-input gate [18].

C. Power Consumption

Since there is no electricity flow in computations of QCA, power consumption is far less than CMOS. The most precise models for calculating power dissipation were proposed by Lent and Timler in 2002. Moreover, Liu et al proposed upper bound power dissipation in 2012. At first, the formula of power was expanded by Lent and Timler, the total power and energy from QCA cells could be calculated by using a Hamiltonian matrix in which for each array of QCA cells, Hartree-Fock approximation is used [19], by taking into account the Coulombic interaction effect among them, a mean square approach, like refer to Equ. (1), is introduced [20], [21]:

$$H = \begin{bmatrix} \frac{-E_k}{2}\sum_i c_i f_{i,j} & -\gamma \\ -\gamma & \frac{E_k}{2}\sum_i c_i f_{i,j} \end{bmatrix} = \begin{bmatrix} \frac{-E_k}{2}(c_{j-1}+c_{j+1}) & -\gamma \\ -\gamma & \frac{E_k}{2}(c_{j-1}+c_{j+1}) \end{bmatrix} \quad (1)$$

Here, γ is tunneling and c_i is the polarization taken from cell ith, and $f_{i,j}$ is the geometric model that determines the electrostatic interaction between cells (i, j) with regard to geometric distance. With regard to the distance of adjacent cells, the factor $f_{i,j}$ is included in King's energy definition (E_k). This energy, with the energy cost of 2 QCA cells with opposing polarization, is calculated in referring to Equ. (2) [17]:

$$E_{i,j} = \frac{1}{4\pi\varepsilon_0\varepsilon_r}\sum_{n-1}^{4}\sum_{m=1}^{4}\frac{q_{i,n}q_{j,m}}{|r_{i,n}-r_{j,m}|} \quad (2)$$

QCA cell energy in each clock cycle is calculated in referring to Equ. (3):

$$E = \langle H \rangle = \frac{\hbar}{2}.\vec{\Gamma}.\vec{\lambda} \quad (3)$$

$\vec{\Gamma}$ is the vector of the energy area from a cell affected by its adjacent cell. $\hbar$ is the reduced Planck's constant and $\vec{\gamma}$ indicates coherence. The Hamiltonian vector is presented as corresponding to the Hamiltonian definition (Refer to Equ. (4)):

$$\vec{\Gamma} = \frac{1}{\hbar}[-2\gamma, 0, E_k(c_{j-i}+c_{j+1})] \quad (4)$$

$(c_{j-i} + c_{j+1})$ is the total of adjacent polarizations. As shown in Fig. 5, the power flow of a QCA cell, which has been placed in a binary wire, has been classified into 4 major signal flow [20], [22]. Horizontal signal powers are equal, in which the input power is the signal power taken from the left neighbor and the output signal is the freed signal power to the right-hand cell. During the switch, the gradual increase of inter dot barriers results in transference of the intended amount of the energy to the cell (switch phase) and these barriers decrease in P_{clock}; therefore, the energy returns to a clocking circuit and negligible power dissipation in the clocking circuit is called P_{diss} [21].

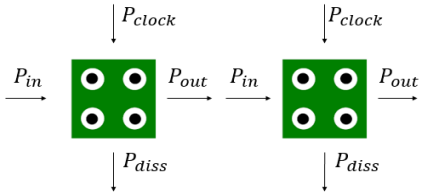

Fig. 5. Power flows in a pair of adjacent cells

The equation for the total power could be calculated this refer to Equ. (5):

$$P_t = \frac{dE}{dt} = \frac{\hbar}{2}\left[\frac{d\vec{\Gamma}}{dt}.\vec{\lambda}\right] + \frac{\hbar}{2}\left[\vec{\Gamma}.\frac{\vec{\lambda}}{dt}\right] = P_1 + P_2 \quad (5)$$

In Equ. (5), P_1 includes two major components: first, the power increase is the result of the difference between the input signal and the output signal. Second, clocking power transferred to a cell (P_{clock}). P_2 indicates dissipated power, P_{diss} [22]. Power dissipation during a cycle-hour T_{cc}= (-T, T) could be defined as Hamiltonian terms and correlation vectors (refer to Equ. (6)):

$$E_{diss} = \frac{\hbar}{2}\int_{-T}^{T}\vec{\Gamma}.\frac{d\vec{\lambda}}{dt} = \frac{\hbar}{2}\left(\left[\vec{\Gamma}.\vec{\lambda}\right] - \int_{-T}^{T}\vec{\lambda}.\frac{d\vec{\Gamma}}{dt}\right) \quad (6)$$

It is worth mentioning that the highest energy dissipation occurs when the rate of the change of $\vec{\Gamma}$ is at its highest. Therefore, $\vec{\Gamma}$ + is shown as $\vec{\Gamma}$ (+T) and $\vec{\Gamma}$- is shown as $\vec{\Gamma}$(-T). The upper bound of power dissipation can be calculated in referring to Equ. (7):

$$P_{diss} = \frac{E_{diss}}{T_{cc}} < \frac{\hbar}{2T_{cc}}\vec{\Gamma}_+ \times \left[-\frac{\vec{\Gamma}_+}{|\vec{\Gamma}_+|}\tanh\left(\frac{\hbar|\vec{\Gamma}_+|}{K_BT}\right) + \frac{\vec{\Gamma}_-}{|\vec{\Gamma}_-|}\tanh\left(\frac{\hbar|\vec{\Gamma}_-|}{K_BT}\right)\right] \quad (7)$$

K_B is Boltzmann constant and T shows heat. In one array of similar QCA cells, the total power dissipation is the sum of power dissipations of all the cells as shown power dissipation is the same for each QCA cell [21]. Using this information, Srivastava et al in 2011 proposed a power dissipation model for QCA circuits based on dividing the total power into leakage main component and switching. The power dissipated during clock changes (from top to bottom and from bottom to top) brings about power leakage and the power dissipated due to a period of change results in power change. Based on this model an assessment device called QCApro has been designed. This device assesses the maximum, the minimum and the average of power dissipation in QCA structure under a change without deadlock. In addition, this device can be used to investigate the efficiency of the circuit based on Bayesian network analysis [23].

III. Previous Research (Literature Review)

Different quantum cellular automata designs can be compared with each other based on occupation area, consumed cell count in the model's structure, examining the kind of wiring, delay in the release of the model in terms of used clock cycle (the number of clocking zones), and output polarization. Full-adder circuits are from combined circuits which have a variety of functions in digital circuits. In quantum cellular automata technology, there are three major structures for designing full-adder circuits whose differences lie in their elements and the arrangement of their elements. Since 1994, various models have been proposed based on logical gates and three-input majority gates. In 2007, Azghadi designed a full adder using a five-input majority gate for the first time in which most of the structures were designed multi-layers [24]. In 2012 and 2015, Hashemi et al. along with Navi, using Azghadi's model, presented two structures with multi-layer rule and clocking rules for designing [7], [8]. In 2010, Navi et al. presented two five-input majority gates (Fig. 4.(a) and 4.(b)) and proposed their suggested circuits based on them [5], [6]. Moreover, in 2016, Newaz Bahar and Waheed, like other designs, proposed their own design in three levels [11]. In 2011, Sayedsalehi et al. proposed two new implementations for multi-layer design which, be compared with all other designs, had lower cell counts and smaller occupation area [9]. In 2016, Labrado and Thapliyal designed a model in a single layer which in terms of cell count, delay, and environment, compared with other designs, has a better performance [10]. In 2016, Angizi et al. (Fig. 6) proposed a model which has a new quantum cellular automata design based on XOR [4].

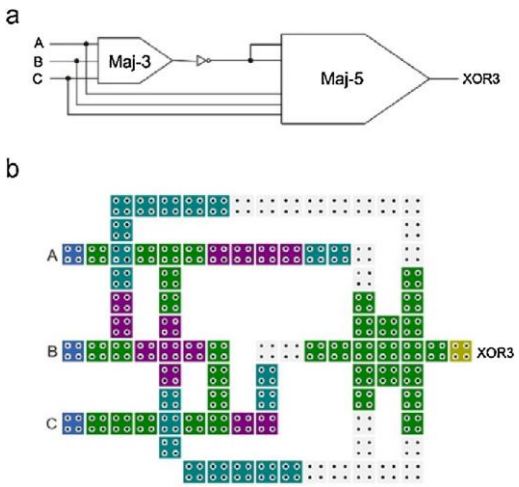

Fig. 6. (a) The logical schema of full adder by, (b) The circuit proposed in [4].

IV. The Proposed Design

The proposed circuit is based on the full-adder circuit of Angizi et al. in tools 2-0-3, QCADesigner; this tool was developed by Walus et al. in ATIPS laboratory for drawing arrangement and simulating quantum cellular automata digital circuits [25] and consists of one five-input majority gate, one three-input majority gate and three logical gates [4]. In Fact, the carry out function of full-adder is output of the three-input majority gate.

A. The Proposed Five-input Majority Gate

Since the five-input majority gate designs that have so far been proposed are not satisfactory, with studies and research we have suggested different changes in the location of inputs which can be observed in Fig. 7. The inputs of the proposed five-input gate are a, b, c, and d in which the input b is somehow considered as two inputs.

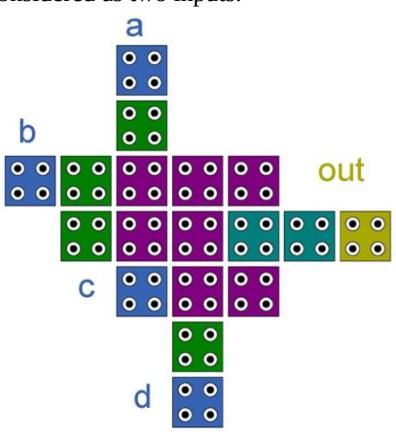

Fig. 7. The proposed five-input gate

B. The proposed full-adder circuit

In this circuit we use three logical gates of which two are simple logical gates and the other is the logical gate shown in Fig. 3 (a). In the next step, for crossing wires we employ clocking rules so that two wires with different hour-phases cross without affecting each other; this is an efficient way for wire-crossing in a single layer (Fig. 2 (c)). In the end, the proposed plan is presented based on the given explanations. At first, three inputs a, b, and c enter the three-input majority gate and generate Cout, then by reversing Cout and by double reversing of wire a, which is used because of adjacency of two input cells of five-input majority gate and because of the attempt to keep the circuit single layer, we produce five-input majority gate and acquire output sum. The results of output sum and Cout after one output are displayed, as shown in Fig. 8. This design includes 59 quantum cells in a space of 0.07 square micrometer, in this design release delay is one cycle-hour which, be compared with Angizi's design, has smaller occupation area and lower delay. One of the reasons for efficiency of this design is its single layer design which reduces the power consumption considerably and results in higher efficiency of wider computational circuits; inputs are at one end and outputs are at the other end of and outside the circuit which accelerates wider computational operations (Fig. 8.). Moreover, because it is a single layer and inputs and outputs are not enclosed, we can easily calculate its power by using QCAPro software. Compared with all other single layer designs which have been presented until now, this design is more efficient in terms of area, delay, and cell count which, in turn, reduces the costs be compared with other single layer designs.

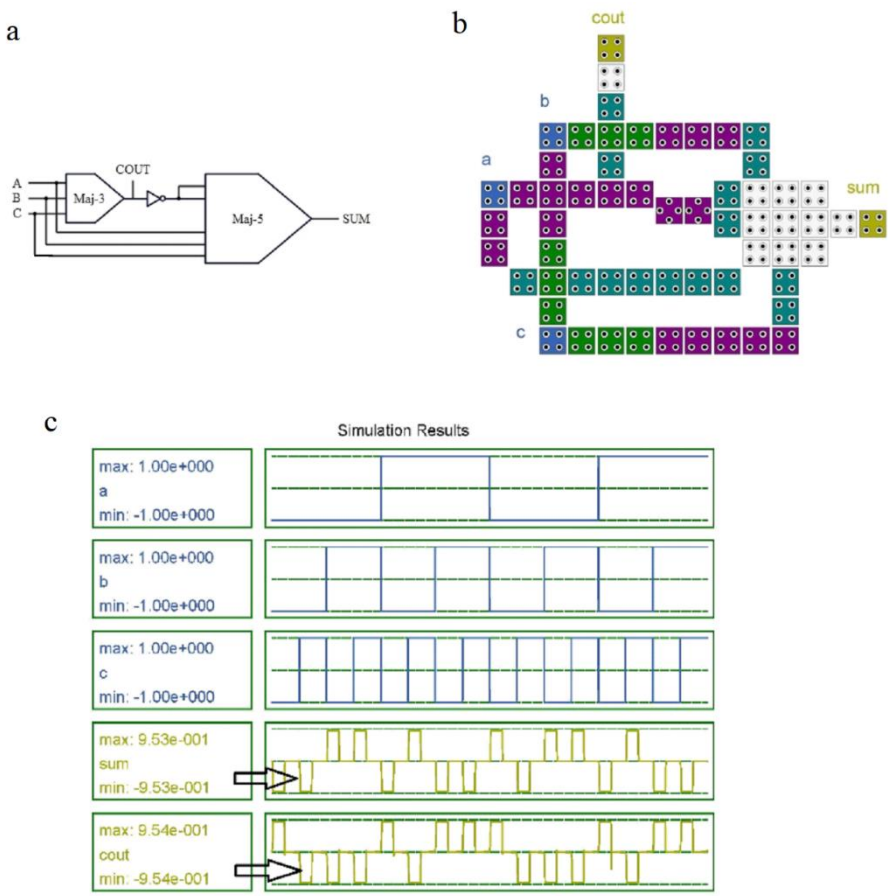

Fig. 8. (a) Schematic design based on Angizi's design, (b) cell layout in the proposed plan, (c) Output result of simulation of the proposed plan.

C. The Proposed Four-bit Ripple Adder Circuit

By placing four adders near each other, we design a four-bit ripple adder in a way that the first adder includes three inputs a_0, b_0, and c_0 and two outputs $Cout_0$ and sum_0 and $Cout_0$ is also the input c1 for the adjacent circuit; this process continues up to the fourth circuit (Fig. 9). Here, the important point is that for the purpose of synchronization it is necessary that outputs and inputs enter the circuit at the same time; it is, therefore, essential that we add to our design some cells with appropriate timing. As can be seen in Fig. 9, in the first full adder the inputs enter without any delay and the output occurs after a 4 cycle-phases delay. In this way, the next full adder, one of whose

inputs results from the first circuit's output and enter after one cycle-phases delay and the output is displayed after a three cycle-phases delay; the third cycle, one of whose inputs is from the second circuit's output, enters after a two cycle-phases delay and the output exits after a two cycle-hour delay. Eventually, in the fourth full adder, one of whose inputs like other full adders is from the previous full adder, i.e., the third full adder, the inputs enter after a three cycle-phases delay and the output exit after one cycle-phases delay. This timing in four-bit ripple design brings about synchronization of the inputs and outputs of the proposed four-bit ripple adders.

In order to show the output result of simulation better, we classify the inputs and the outputs into three groups based on the Bus Layout option. Then, in order to show the accuracy of the result of the output of the simulation, we assign values to the inputs, for example, the sum of 1101 and 0011 is 10000 and as can be seen in the Fig. 10, through marking the result of the simulated output occurs like the figure in one column. Our proposed four-bit ripple adder design includes 379 quantum cells in a space of 1 square micrometer; in this design there is a four cycle-phases release delay; it is compared with the previous four-bit ripple adders in the table which is more efficient in terms of area, cell count, delay, and cost.

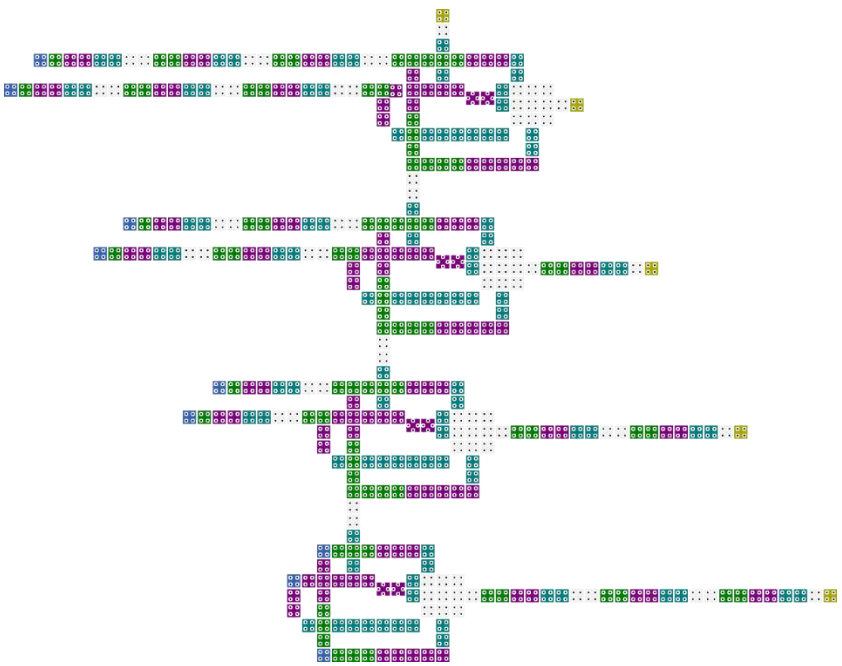

Fig. 9. The layout of four-bit ripple adder circuit

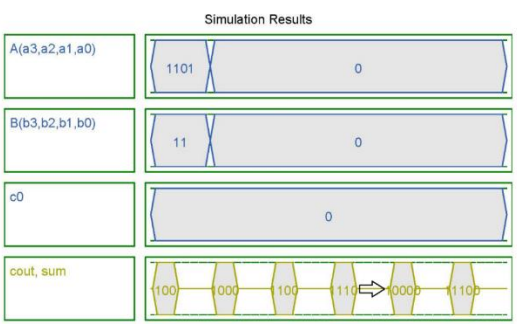

Fig. 10. The simulated output after initialization.

V. Simulation and Comparing the Results

A. *Simulation of Power*

To calculate power, version 1.4-1 of QCApro tools is required which operates through QCADesigner 1.1-4 software using C ++ / C programming language in Linux environment or using Ubuntu in the Windows operating system which is a set of techniques for analysis of configured data based on INUS theory. This simulation can be a quick design for checking the value of the outputs of all the inputs; in single-layer adder circuits if there is an error, it will create the error message, therefore it is a modeling tool for probable error and power dissipation in circuits. QCApro estimates the minimum,

the mean, and the maximum of power dissipation [23], [26]. All the input majority gate designs introduced in Fig. 4 are examined through three different tunneling energy levels (0.5 E_k, 1 E_k and 1.5 E_k) in heat of 2K and power dissipation is shown by 0.5 E_k in Fig. 11.

Obviously high power dissipation cells are shown by using heat points with darker colors. It is obvious that in presented designs the mid-cells or voter cells have higher power dissipation than other cells and thus the set position of input cells is like other cells and their effect on the voter cell can be taken as one of the significant functions in increasing power dissipation. Compared with previous designs, the proposed five-input majority gate design includes fewer cells with dark colors (Fig. 12); it is a standard design [18].

Moreover, in the proposed design we observe fewer dark-colored cells be compared with Angizi's design which, as was mentioned earlier, is indicative of the proposed model's standard design in lower level of energy dissipation in a single layer (Fig. 13).

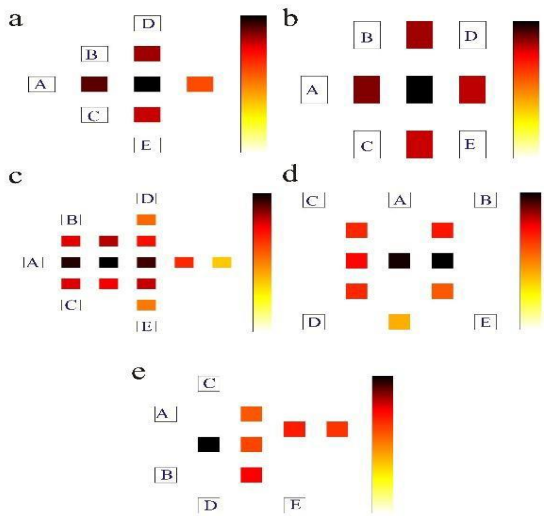

Fig. 11. Power dissipation map for five-input majority gates in heat 2K and with 0.5 E_k, [18] (a) The structure presented by Navi et al., (b) The structure presented by Navi et al., (c) The structure presented by Akeela and Wagh, (d) The structure presented by Roohi et al., (e) The structure presented by Sheikhfaal et al.,

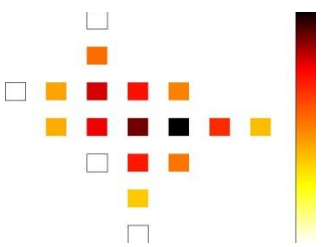

Fig. 12. Power dissipation map for proposed five-input majority gate in heat 2K and 0.5 E_k.

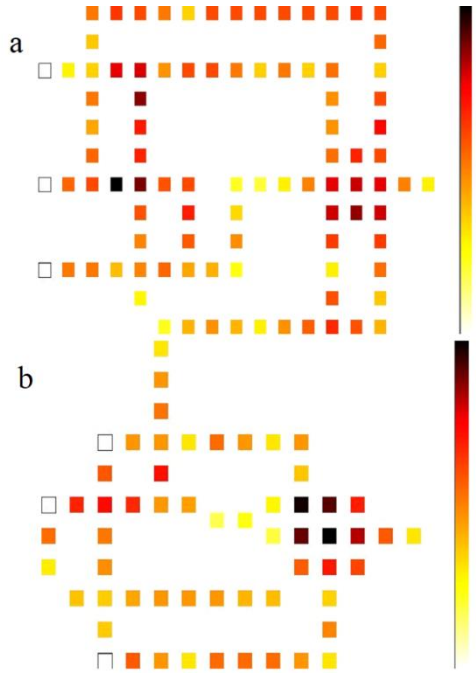

Fig. 13. (a) Power dissipation map for Angizi's full-adder design in heat 2K and with 0.5 E_k, (b) Power dissipation map for the proposed full-adder design in heat 2K and with 0.5 E_k

B. Comparing Circuits' Results

Now, we compare the implementations carried out in research papers. Table I compares the structures proposed for one-bit full-adder circuits and four-bit ripple adder circuits according to occupation area, cell count, and release delay in terms of the cycle-hour and the number of layers.

C. Comparing Power Consumption

All consumption power maps for five-input majority gates are examined through three different tunneling energy levels (0.5 E_k, 1 E_k and 1.5 E_k) in heat 2K. Table II compares the structure proposed for five-input majority gates and average leakage energy dissipation, average switch energy dissipation and total energy consumption at three levels. Since the inputs are applied from one side and with appropriate distance (Fig. 13(b)), cell count in its single-layer direction is more than previous designs too which increases total energy consumption compared with designs with lower cell count. It should be noted that the proposed design includes fewer dark-colored cells compared with other designs which is indicative of standard design of the proposed design at lower level of energy dissipation at one level.

Since the proposed circuit is a single layer, it was examined using QCApro and its power consumption was implemented; examining Table II we observe low power consumption and fewer cells with dark colors. Table III compares leakage energy values, switch energy, and total energy consumption in the proposed full-adder circuit with Angizi's design at three different tunneling energy levels of (0.5 E_k, 1 E_k and 1.5 E_k).

It is clear from Table III that be compared with Angizi's design, the proposed design has lower power consumption at three different tunneling energy levels. This is indicative of an optimal design in comparison with full-adder circuits in one level. These results indicate that the proposed full adder design in comparison with pervious similar design [4] is achieved 36%, 20% and 4.4% reduction in the number of cells, latency and power consumption, respectively.

VI. Conclusion

This study was concerned with designing an efficient full-adder circuit by using quantum cellular automata technology. The cell count and occupation area of a particular design in QCA technology directly affect the cost of building circuits based on this technology. Avoiding the problems of previous circuits, this paper proposed an effective design that enhanced efficiency, simplicity, and regularity of full-adder circuits inquantum cellular automata technology. Due to its occupation area, the proposed circuit was capable of performing in different heats. Another advantage of this design is that the circuit's inputs and outputs were not located in the center of the design in two opposite positions. Therefore, it could be used to build multi-bit adder circuits and wider computational circuits. Since it was a single layer, its consumption power can be calculated. Be Compared with all the other single layer designs, this design was more efficient in terms of area, delay and cell counts which, in turn, help to reduce the costs. Finally, it could be said that this design had a better function, produced more satisfactory results.

TABLE I

COMPARISON BETWEEN THE STRUCTURES PROPOSED FOR ONE-BIT FULL-ADDER CIRCUITS AND FOUR-BIT RIPPLE ADDER CIRCUITS IN QUANTUM CELLULAR AUTOMATA TECHNOLOGY

Circuits	Types of circuits	Cell count	Area (nm^2)	Latency (clock cycle)	Single layer	Circuits	Types of circuits	Cell count	Area (nm^2)	Latency (clock cycle)	Single layer
Design in [7]	FA[1]	79	0.05	1.25	No	Design in [9]	FA	33	0.02	0.75	No
	RA[2]	308	0.29	2	No		RA	-	-	-	-
Design in [8]	FA	71	0.06	1.25	Yes	Design in [4]	FA	93	0.07	1.25	Yes
	RA	442	1	4	Yes		RA	-	-	-	-
Design in [5]	FA	73	0.04	0.75	No	Design in [10]	FA	63	0.05	0.75	Yes
	RA	-	-	-	-		RA	-	-	-	-
Design in [6]	FA	61	0.03	0.75	No	Design in [11]	FA	48	0.03	0.75	No
	RA	-	-	-	-		RA	-	-	-	-
Design in [9]	FA	31	0.02	0.75	No	Propoed Design	FA	59	0.07	1	Yes
	RA	178	0.17	2.4	No		RA	379	1	4	Yes

TABLE II

COMPARING THE PRESENTED STRUCTURE FOR FIVE-INPUT MAJORITY GATES, THE RESULT OF ANALYZING AVERAGE LEAKAGE ENERGY DISSIPATION, SWITCH ENERGY DISSIPATION, AND TOTAL ENERGY CONSUMPTION

circuits	cell count	Area (nm^2)	Single layer	Avg. leakage energy dissipation (mev)			Avg. switching energy dissipation (mev)			Total energy consumption (mev)		
				$0.5E_k$	$1E_k$	$1.5E_k$	$0.5E_k$	$1E_k$	$1.5E_k$	$0.5E_k$	$1E_k$	$1.5E_k$
Design in [5]	10	0.007	NO	1.28	4.14	7.69	11.53	10.37	9.16	12.81	14.51	16.85
Design in [6]	10	0.004	NO	1.35	4.25	7.8	10.94	9.84	8.7	12.29	14.09	16.5
Design in [16]	18	0.02	YES	3.44	10.67	19.52	32.66	29.89	27.01	36.1	40.56	46.53
Design in [17]	13	0.01	YES	3.38	8.95	15.03	9.23	7.7	6.41	12.61	16.65	21.44
Design in [18]	11	0.01	YES	2.99	7.73	12.35	3.69	2.77	2.15	6.68	10.5	14.5
Proposed design	18	0.02	YES	3.74	11.67	21.38	33.63	30.57	27.04	37.37	42.25	48.78

[1] Full Adder
[2] Ripple Adder

TABLE III
THE RESULT OF ANALYZING AVERAGE LEAKAGE ENERGY, SWITCH ENERGY, AND TOTAL ENERGY CONSUMPTION IN THE PROPOSED FULL-ADDER CIRCUIT

circuits	Avg. leakage energy dissipation (mev)			Avg. switching energy dissipation (mev)			Total energy consumption (mev)		
	$0.5E_k$	$1E_k$	$1.5E_k$	$0.5E_k$	$1E_k$	$1.5E_k$	$0.5E_k$	$1E_k$	$1.5E_k$
Design in [4]	26.27	80.93	146.71	160.23	141.55	122.8	186.49	222.49	269.51
Proposed design	24.19	75.21	135.78	154	135.71	117.96	178.19	210.92	253.73

REFERENCES

[1] R. Compano, L. Molenkamp and D. Paul, "Roadmap for nanoelectronics," *European Commission IST Programme, Future and Emerging Technologies*, 2000.

[2] C. Lent, P. Tougaw, W. Porod and G. Bernstein, "Quantum cellular automata", *Nanotechnology*, vol. 4, no. 1, pp. 49-57, 1993. Available: 10.1088/0957-4484/4/1/004.

[3] S. Sarmadi, S. Sayedsalehi, M. Fartash and S. Angizi, "A Structured Ultra-Dense QCA One-Bit Full-Adder Cell", *Quantum Matter, vol. 5, no. 1, pp. 118-123, 2016. Available:* 10.1166/qm.2016.1263.

[4] S. Angizi, E. Alkaldy, N. Bagherzadeh and K. Navi, "Novel Robust Single Layer Wire Crossing Approach for Exclusive OR Sum of Products Logic Design with Quantum-Dot Cellular Automata", *Journal of Low Power Electronics*, vol. 10, no. 2, pp. 259-271, 2014. Available: 10.1166/jolpe.2014.1320.

[5] K. Navi, R. Farazkish, S. Sayedsalehi and M. Rahimi Azghadi, "A new quantum-dot cellular automata full-adder", *Microelectronics Journal*, vol. 41, no. 12, pp. 820-826, 2010. Available: 10.1016/j.mejo.2010.07.003.

[6] K. Navi, S. Sayedsalehi, R. Farazkish and M. Azghadi, "Five-Input Majority Gate, a New Device for Quantum-Dot Cellular Automata", *Journal of Computational and Theoretical Nanoscience*, vol. 7, no. 8, pp. 1546-1553, 2010. Available: 10.1166/jctn.2010.1517.

[7] S. Hashemi, M. Tehrani, K. Navi, and Essays, "An efficient quantum-dot cellular automata full-adder," *Scientific Research and Essays*, vol. 7, no. 2, pp. 177-189, 2012.

[8] S. Hashemi and K. Navi, "A Novel Robust QCA Full-adder", *Procedia Materials Science*, vol. 11, pp. 376-380, 2015. Available: 10.1016/j.mspro.2015.11.133 [Accessed 13 February 2022].

[9] S. Sayedsalehi, M. Moaiyeri and K. Navi, "Novel Efficient Adder Circuits for Quantum-Dot Cellular Automata", *Journal of Computational and Theoretical Nanoscience*, vol. 8, no. 9, pp. 1769-1775, 2011. Available: 10.1166/jctn.2011.1881.

[10] C. Labrado and H. Thapliyal, "Design of adder and subtractor circuits in majority logic-based field-coupled QCA nanocomputing", *Electronics Letters*, vol. 52, no. 6, pp. 464-466, 2016. Available: 10.1049/el.2015.3834.

[11] A. Bahar and S. Waheed, "Design and implementation of an efficient single layer five input majority voter gate in quantum-dot cellular automata", *SpringerPlus*, vol. 5, no. 1, 2016. Available: 10.1186/s40064-016-2220-7.

[12] K. Kim, K. Wu and R. Karri, "The Robust QCA Adder Designs Using Composable QCA Building Blocks", *IEEE Transactions on Computer-Aided Design of Integrated Circuits and Systems*, vol. 26, no. 1, pp. 176-183, 2007. Available: 10.1109/tcad.2006.883921.

[13] A. Gin, P. Tougaw and S. Williams, "An alternative geometry for quantum-dot cellular automata", *Journal of Applied Physics*, vol. 85, no. 12, pp. 8281-8286, 1999. Available: 10.1063/1.370670.

[14] I. Hanninen and J. Takala, "Robust Adders Based on Quantum-Dot Cellular Automata", *2007 IEEE International Conf. on Application-specific Systems, Architectures and Processors (ASAP)*, 2007. Available: 10.1109/asap.2007.4459295 [Accessed 13 February 2022].

[15] P. Tougaw and C. Lent, "Logical devices implemented using quantum cellular automata", *Journal of Applied Physics*, vol. 75, no. 3, pp. 1818-1825, 1994. Available: 10.1063/1.356375.

[16] R. Akeela, and M. D. Wagh, "A five-input majority gate in quantum-dot cellular automata." *NSTI Nanotech*, pp. 978-981.

[17] A. Roohi, H. Khademolhosseini, S. Sayedsalehi and K. Navi, "A symmetric quantum-dot cellular automata design for 5-input majority gate", *Journal of Computational Electronics*, vol. 13, no. 3, pp. 701-708, 2014. Available: 10.1007/s10825-014-0589-5.

[18] S. Sheikhfaal, S. Angizi, S. Sarmadi, M. Hossein Moaiyeri and S. Sayedsalehi, "Designing efficient QCA logical circuits with power dissipation analysis", *Microelectronics Journal*, vol. 46, no. 6, pp. 462-471, 2015. Available: 10.1016/j.mejo.2015.03.016.

[19] P. Tougaw and C. Lent, "Dynamic behavior of quantum cellular automata", *Journal of Applied Physics*, vol. 80, no. 8, pp. 4722-4736, 1996. Available: 10.1063/1.363455.

[20] J. Timler and C. Lent, "Power gain and dissipation in quantum-dot cellular automata", *Journal of Applied Physics*, vol. 91, no. 2, pp. 823-831, 2002. Available: 10.1063/1.1421217.

[21] W. Liu, S. Srivastava, L. Lu, M. O'Neill and E. Swartzlander, "Are QCA cryptographic circuits resistant to power analysis attack?", *IEEE Transactions on Nanotechnology*, vol. 11, no. 6, pp. 1239-1251, 2012. Available: 10.1109/tnano.2012.2222663.

[22] S. Srivastava, S. Sarkar and S. Bhanja, "Estimation of Upper Bound of Power Dissipation in QCA Circuits", *IEEE Transactions on Nanotechnology*, vol. 8, no. 1, pp. 116-127, 2009. Available: 10.1109/tnano.2008.2005408.

[23] S. Srivastava, S. Sarkar and S. Bhanja, "Estimation of Upper Bound of Power Dissipation in QCA Circuits", *IEEE Transactions on Nanotechnology*, vol. 8, no. 1, pp. 116-127, 2009. Available: 10.1109/tnano.2008.2005408.

[24] M. Rahimi Azg, O. Kavehei and K. Navi, "A Novel Design for Quantum-dot Cellular Automata Cells and Full Adders", *Journal of Applied Sciences*, vol. 7, no. 22, pp. 3460-3468, 2007. Available: 10.3923/jas.2007.3460.3468.

[25] K. Walus, T. Dysart, G. Jullien and R. Budiman, "QCADesigner: A Rapid Design and Simulation Tool for Quantum-Dot Cellular Automata", *IEEE Transactions On Nanotechnology*, vol. 3, no. 1, pp. 26-31, 2004. Available: 10.1109/tnano.2003.820815.

[26] A. Thiem, "Qcapro: Professional functionality for performing and evaluating qualitative comparative analysis, r package version 1.1-0," URL: http://www. alrikthiem. net/software, 2016.

Faeze Motalebi recieved her bachelor Degree in software computer engineering in 2013 from Islamic Aazad University Malard Branch, and her M.Sc. degree in computer architecture engineering in 2017 from Islamic Azad University Qazvin Branch. Her M.Sc thesis was about Full_Adder Circuit using Quantum-dot Cellular Automata. Her research interests include Quantum-dot Cellular Automata, nanolectronic.

Samira Sayedsalehi received her M.Sc. degree in computer architecture engineering in 2008, and her Ph.D. in computer architecture engineering in 2012 from Science and Research Branch of Islamic Azad University, Tehran, Iran. She is currently Assistant Professor in Faculty of Computer Engineering of South Tehran Branch, Islamic Azad University. Her research interests include Nano electronics with emphasis on Quantum-dot Cellular Automata, CNFET, Computer Architecture, and Computing.